DarkSide : Searching for dark matter with liquid argon

Julie Rode

Thèse préparée
à SORBONNE UNIVERSITÉ
École doctorale STEP'UP - ED N°560
Laboratoire de Physique Nucléaire et des Hautes Énergies
Laboratoire Astro-Particules et Cosmologie

DarkSide: Searching for Dark Matter with Liquid Argon

par **Julie Rode**

Thèse de doctorat de Physique de l'Univers dirigée par
Dr. Claudio Giganti et Dr. Davide Franco, présentée et soutenue
publiquement le 30 septembre 2022
devant un jury composé de :

Claudio Giganti Chargé de recherche (CNRS - LPNHE)	Directeur de thèse
Davide Franco Directeur de recherche (CNRS - APC)	Directeur de thèse
Claudia Nones Ingénieur de Recherche (CEA - IRFU)	Rapporteur
Jacob Lamblin Maitre de Conférences (Université Grenoble Alpes - LPSC)	Rapporteur
Corinne Augier Professeur (Université Claude Bernard Lyon 1 - IP2I-Lyon)	Examinatrice
Bertrand Laforge Professeur (Sorbonne Université - LPNHE)	Président du jury

Acknowledgements

I would like to acknowledge the inestimable help of Alessandra Tonazzo without who I may not have had the opportunity to make this PhD. Thank you for remembering my existence two years after I left the NPAC master and for recommending me to Claudio Giganti and Davide Franco who were looking for a PhD on dark matter. You gave me the opportunity to contribute to this very fascinating work!

Then, I would like to thank Claudio and Davide for accepting me as their PhD and training me in dark matter detection physics, computing, data analysis, and improved a lot my abilities to present scientific works. I deeply thank Davide for his support in coding techniques and for all the knowledge he teach me in detector and dark matter physics as well as his rigorousness, kindness and scientific enthusiasm.

I would also like to greet Pascal Pralavorio et Fabrice Hubaut for their scientific help, which was very useful several times during these three years. I also deeply thank them for rescuing me from loneliness at the first DarkSide general meeting with their cheerful company.
I would like to thank Emmanuel Le Guirec who also helped me in many technical computing methods and from who I learned a lot about python tools. I also acknowledge all the other members of DarkSide experiment and more particularly Paolo Agnes for his help is many issues and Michael Poehlmann for its useful insights. I also thanks Miguel Campos for taking the time to look back at its old paper and code to answer my (many) questions about his work.

I would also like to acknowledge both LPNHE and APC laboratories for welcoming me in their teams. Thank you to Jean-Philippe Lenain, my LPNHE god-father, for regularly checking on me and to my thesis committee members, Véronique Van Elewyck and Frederic Derue, for their time and useful comments.
I also thank my jury, Corinne Augier, Bertrand Laforge, Claudia Nones and Jacob Lamblin, and particularly the last two for their careful reviewing of the manuscript, helpful corrections and insights.

Je tiens également à remercier mes parents pour m'avoir toujours poussé en avant. Le résumé simplifié en annexe t'es dédiée maman, toi qui n'a jamais rien compris à la physique, en espérant qu'il t'apporte quelques éclairsissements sur l'utilisation de mes journées de ces trois dernières années !
Une pensée également pour feu mes grands-pères qui depuis toute petite ont eu un oeil sur la bonne conduite de mes études. J'aurais aimé qu'ils puissent en voir l'achèvement et que je puisse voir leur sourire au fond de la salle (que dis-je, au premier rang derrière le jury

!). A défaut, ce manuscrit leur est dédié. Un grand merci également à mes grands-mères pour leur soutien, parfois de loin, même si elles ne savent pas toutes trop ce que je fais (elles non plus).
Je ne saurais oublier Nicolas, pour son soutien quotidien, ses petites suggestions de packages pythons "plus efficaces" et sa relecture des paragraphes sur les réseaux de neurones. Mais également, Joëlle et Philippe pour leur gentillesse et leur soutien, Titounette pour ses reportages sur la meute familiale (de chats), et puis aussi Louise pour son agréable compagnie en confèrence et Timothée pour sa bonne humeur au labo !

I would like to finish this section by these few words that means so much to me, and even more in these challenging times:

> *"Try and leave this world a little better than you found it, when your turn comes to die, you can die happy in feeling that at any rate, you have not waste your time but have done your best."* Robert Baden-Powell (1941)

Résumé

Les observations astrophysiques et les mesures cosmologiques ont soulevé l'existence d'une masse manquante invisible dans l'Univers qui a été nommée matière noire. Les principaux candidats actuels pour cette matière inconnue sont les WIMPs, particules massives à faible interaction, les ALPs, particules similaires à des axions, et les neutrinos stériles de masse entre 7 et 36 keV/c^2.
L'expérience DarkSide a pour but la détection directe des particules de matière noire à l'aide d'une chambre à projection temporelle à double phase utilisant de l'argon liquide. Le détecteur principal actuel, DarkSide-50 de masse active 50 kg, a permis de tracer les meilleures limites de détection à faible masse. Le prochain détecteur, DarkSide-20k, de masse fiducielle 20 tonnes, est en préparation avec notamment plusieurs prototypes en cours testant de nouvelles technologies ou de nouvelles méthodes de détection afin de réussir ce changement d'échelle. Proto-0 et ReD sont deux de ces prototypes ; Proto-0 teste de nouvelles technologies tandis que ReD est destiné à tester la possibilité de mesures de directionalité.

Dans cette thèse, nous allons d'abord examiner quelques améliorations dans le calcul des contributions de certains bruits de fond ainsi que l'étalonnage en énergie de DarkSide-50. Ces résultats ont contribué à affiner les limites du modèle concernant les WIMPs avec et sans effet Migdal. Nous étudierons également de nouveaux modèles de matière noire, les ALPs solaires et galactiques ainsi que les neutrinos stériles dans une gamme de masse de 7 à 36 keV/c^2. Les limites atteintes pour les ALPs et les neutrinos stériles ne sont pas compétitives par rapport aux travaux déjà existants. Nous nous pencherons ensuite sur le logiciel de reconstruction de données dévelopé à l'aide des données des expériences Proto-0 et ReD ainsi que des simulations réalisées pour DarkSide-20k. Finalement, les données reconstruites nous permettrons de déterminer la stabilité de l'épaisseur de la poche de gaz de l'expérience ReD, d'étudier l'impact de plusieurs configurations et paramètres du futur détecteur DarkSide-20k sur la discrimination de la forme des impulsions et donc sur sa future sensibilité à la matière noire, de reconstruire la position du signal de scintillation pour DarkSide-20k et d'évaluer la performance de l'association entre les signaux de scintillation et d'ionisation dans le détecteur DarkSide-20k.

Abstract

Astrophysical observations and cosmological measurements have raised the existence of an invisible missing mass in the Universe that has been called Dark Matter. Current main candidates for this unknown matter are WIMPs, Weakly Interacting Massive Particles, ALPs, Axion-Like Particles, and sterile neutrinos between 7 and 36 keV/c^2.
The DarkSide experiment has for aim direct detection of dark matter particles using a dual-phase liquid argon time projection chamber. The actual main detector, DarkSide-50 with 50 kg of active mass, has allowed raising the best detection limits at low mass. The next one, DarkSide-20k with 20 ton of fiducial mass, is in preparation with notably several prototypes testing new technologies or methods of detection to perform successfully the change in scale. Proto-0 and ReD are two of these prototypes; Proto-0 is testing new technologies while ReD is meant for testing the possibility of directionality measurements.

In this work, we will first look at some improvements in the background contribution and energy scales of DarkSide-50. This contributed to refining the overall limits on WIMPs with and without the Migdal effect. We will also study additional dark matter models, solar and galactic ALPs and sterile neutrinos in the 7 to 36 keV/c^2 mass range. Limits found for ALPs and sterile neutrinos are not competitive with already existing work.
Secondly, we will look at the data reconstruction software developed with Proto-0 and ReD data and with DarkSide-20k simulations. Finally, this data reconstruction will allow us to assess the stability of the gas pocket thickness inside the ReD experiment, to study the impact of several configurations and parameters of the design of DarkSide-20k on the pulse shape discrimination and thus on its sensitivity to dark matter, to reconstruct the position of the scintillation signal inside DarkSide-20k and to assess the performance in associating the scintillation and ionisation signals in DarkSide-20k.

Table of Contents

Introduction

Generations of scientists have contributed raising humanity general knowledge up to understand a part of the structures and dynamics around us. By deepening the understanding of the Universe, they were able to look at new aspects of it or to start looking at it in different ways, finding for instance that around 80% of the mass of the Universe was missing. With this new mystery, a quest for the invisible, for the unreachable, began. It was not the first time, and would certainly not be the last, that one was looking for something they could not understand, they could not see or directly measure yet. Everything was possible. It could have been some kind of astrophysical object, a new particle, a set of new particles that were very weakly interacting with ordinary matter, or even just the evidence that current models were not describing the Universe precisely enough. To this day, dark matter is one of the biggest puzzles in cosmology and fundamental physics and even if a part of possible candidates have been discarded, there is still much to test and to discover.

Hypothetical dark matter candidates can be observed in several ways and many experiments were launched or adapted to try detecting them. DarkSide experiment is one of them and has for main purpose to search for Weakly Interacting Massive Particles (WIMPs), one of the most promising dark matter candidates. Its detection principle is simple: nuclear scattering on argon nucleus inside a dual-phase (liquid and gaseous) argon time projection chamber.
The current main detector of the DarkSide experiment, DarkSide-50 allowed improving significantly limits on WIMP-nucleon cross-section at low-mass, giving the world's best limits, and is able to make background free searches at higher masses. However, to improve this limit, or better, find some dark matter, the experiment is increasing its target mass from 50 kg to 20 ton to gain a larger exposure. This new detector is called DarkSide-20k. To succeed in this change in scale, the involved technology also needs upgrading, with notably the introduction of silicon photo-multipliers (SiPMs) instead of usual photo-multipliers. Thus, the Proto-0 prototype was built in order to calibrate the SiPM response and was running at CERN in November 2019. Another detector, ReD was built to test for the possibility to detect directionality, one of the WIMPs' signatures, which would be helpful for searches below the neutrino floor.

During this PhD, I participated in two different axes of study. First, the re-analysis of DarkSide-50 low-mass analysis, contributing to the description of the backgrounds and to the calibration. This allowed improving WIMPs limits, with and without the Migdal effect. I also implemented inside the framework solar and galactic axion-like particles and keV-sterile neutrinos models in order to compute their limits with DarkSide-50 data. I also looked at the hypothesis of annual modulation with the same data-set (Chapter III). Secondly, I contributed to the optimisation of the data reconstruction process using data

from ReD, Proto-0 and simulations for DarkSide-20k (Chapter IV). This optimisation allowed to study the gas pocket thickness of the ReD experiment (Chapter V) and making a precise Pulse Shape Discrimination, one of the most valuable features of argon detectors (Chapter VI). Finally, I implemented the reconstruction of the position of particle interactions inside DarkSide-20k using the scintillation channel only (Chapter VII) that allowed assessing the performance of the association between the scintillation and ionisation deposits of energy (Chapter VIII).
To give the context of these studies, Chapter I will go through a short review of the history of dark matter and its main candidates with a highlight on WIMPs and their direct detection. The second chapter will detail the DarkSide experiment in terms of collaboration, goals, detectors and technologies involved.

Chapter I

Into Dark Matter

> It is the unknown that excites the ardor of scholars, who, in the known alone, would shrivel up with boredom.
>
> Wallace Stevens (1957)

The search for dark matter is relatively recent as the first hints of this hidden mass can be traced back to the beginning of the 20th century, less than a hundred years ago. Since then, more and more observations and experiments have allowed strengthening the general belief in this additional matter even though its precise nature is still widely unknown and no direct detection was performed.

In this first chapter, we will retrace the main pieces of evidence of the existence of dark matter (Section I.1). Then we will go through the main physical constraints applied to it in Section I.2. Resulting candidates whether astrophysical objects, particles or alternative theories will then be developed (Section I.3). We will conclude with an overview of dark matter direct detection (Section I.4).

I.1 Main Dark Matter Evidences

I.1.1 First evidences

The first indication of a possible none-baryonic matter, the so-called dark matter, dates back to 1932 with a study of Doppler shifts of stars near the Milky Way plane by the Dutch astronomer Jan Hendrik Oort[1].
It can be considered that stars dynamics are only affected by gravity. By only considering Newtonian gravity, their velocity v is such as:

$$v(r) = \sqrt{\frac{GM(r)}{r}} \tag{I.1}$$

where r is the radial distance between the star and its galactic centre, G is the gravitational constant and M is the total mass. However, Oort observed that the gravitational force due to luminous masses was too small to maintain stars in their observed trajectories. Hence, he postulated the presence of an additional invisible matter located on the galaxy plane as a possible explanation [1]. However, he believed there was a mistake: the

underestimation of the dust between the observer and the galactic center.

Soon after, in 1933, another astronomer, Fritz Zwicky studied individual galaxy velocities dispersion in the Coma cluster considering classical mechanics and came to the same conclusion of a missing mass in the cluster [2] [3].

In 1983, Vera Rubin *et al.* continued the work started by Jan Hendrik Oort using Doppler shifts to assess the rotational velocity of 60 isolated spiral galaxies. They notably observed that the orbital velocity remained constant from a given distance to the galactic centre (Figure I.1), a fact in contradiction with Newtonian dynamics (Equation (I.1)). They came to the same conclusion: most matter is not in the galaxy centre and does not emit light [1] [4].

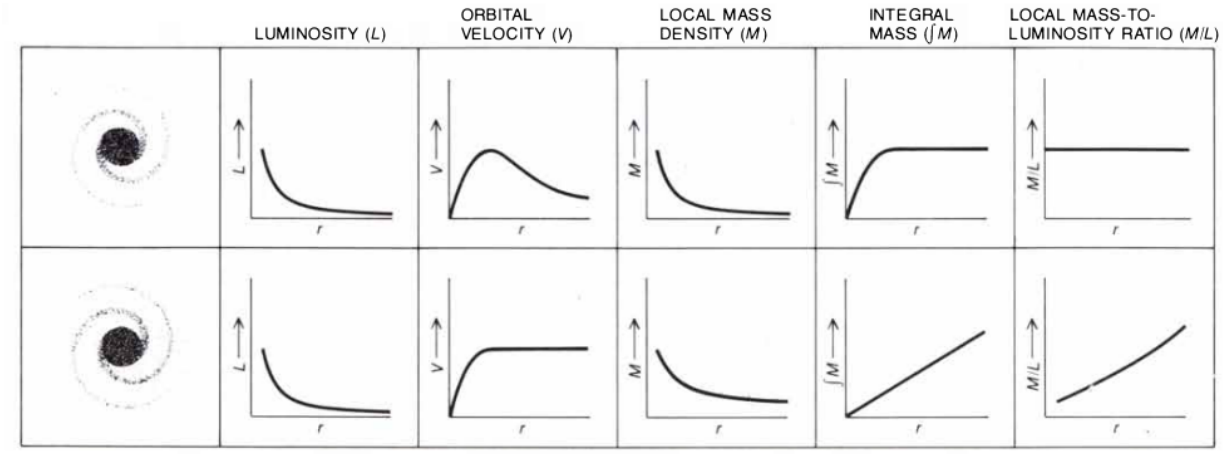

Figure I.1 – Expected (top) and observed (bottom) galaxies properties, from Rubin et al. [4]. At the exception of luminosity, all other properties are different, highlighting the widely different mass behavior between observation and theory.

I.1.2 Gravitational Lensing

General relativity theory states that masses affect the curvature of space-time, meaning that the trajectory of light is deviated by large masses - such as stars, galaxies, clusters of galaxies - and so, bends when passing near them [5]. Hence, if a large mass is placed between an observer and a given structure this last can be distorted, shifted or duplicated; this phenomenon is called gravitational lensing [6]. The observation in 1979 by Dennis Walsh, Robert Carswell and Ray Weymann of QSO 0957 + 561, also called the "Twin Quasar", was the first observational evidence of gravitational lensing [7]. Indeed, what they thought to be a double pair of resembling quasars turned out to be a single quasar. Its image was observed twice due to a gravitational lens from the YGKOW G1 galaxy situated between Earth and the quasar [7].

As it is a purely gravitational interaction, the distortion depends on the mass of the lens M_L. By measuring the bend using the radius of an arclet Θ (Equation (I.2)), it is possible to derive the total amount of matter present in the gravitational lens and compare it to

the visible mass [6] [8]:

$$\Theta = \sqrt{\frac{4GM_L d_{LS}}{c^2 d_L d_S}} \tag{I.2}$$

where G is the gravitational constant, c is the speed of light, d_L, d_S and d_{LS} are respectively distances to the lens, to the source and between the lens and the source.

Among other examples, Abell 370 and Cluster 2244-02 galaxy clusters are both displaying very luminous arcs from gravitational lenses which were well-resolved enough to allow studying the cluster's mass distribution [9]. In both cases, a large amount of additional invisible matter was needed to match the inferred total mass from the lens: 10^2 to 10^3 solar mass-to-light ratio [9].

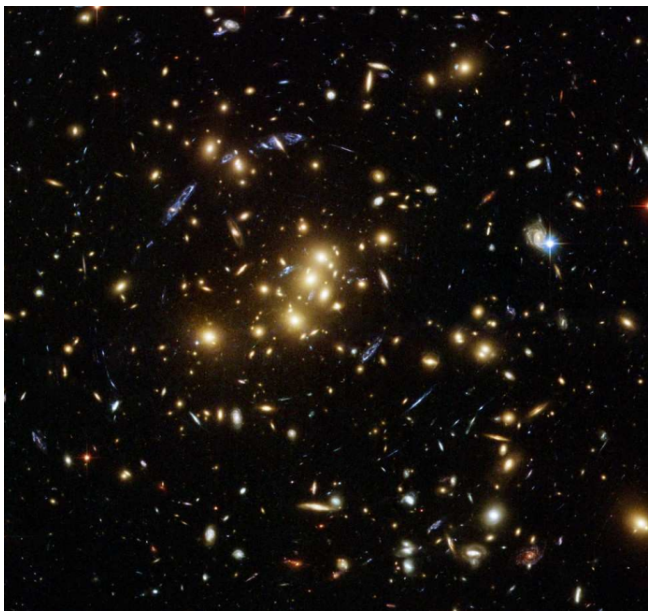

Figure I.2 – Gravitational lensing near galaxy cluster CL0024+17. Credit : NASA/ESA/M.J. Jee (John Hopkins University)

I.1.3 Galaxy Clusters Collisions

Observation of galaxy cluster collisions gave another hint of the nature of dark matter [10]. The first observation was performed in 2006 by Douglas Clowe et al. [10] on 1E 0657-56 cluster, also called the "Bullet Cluster". During this collision of actually two clusters, the hot intergalactic gas holding most of visible matter emitted X-ray by compression and shock. Using gravitational lensing, dark matter was mapped and both X-ray distribution and dark matter were found at strictly separated positions inside the cluster: X-ray emissions at the center and dark matter at both opposite sides [10] [11]. This means that during the collision visible matter and hypothetical dark matter interact differently and that dark matter did not actually interact, but passed through, collision-less. This effect is shown on Figure I.3 for the galaxy cluster MACS J0025.4-1222 - also called "Baby Bullet" (2008) - with X-ray emissions highlighted in pink and reconstructed dark matter with gravitational lensing in blue. This kind of observation was repeated several times

with more than 72 other galaxy cluster collisions, all showing similar behaviors [12].

Figure I.3 – Collision of the galaxy cluster MACS J0025.4-1222 pictured by Hubble Space Telescope and Chandra X-ray observatory. In pink are X-ray emissions and in blue dark matter reconstruction from gravitational lensing. Visible structures such as galaxies are visible in yellow. Credit: NASA, ESA, CXC, M. Bradac (University of California, Santa Barbara), and S. Allen (Stanford University)

I.1.4 Cosmological Evidences

The largest source of deuterium (^{2}H) in the Universe has been produced during the Big Bang Nucleosynthesis (BBN) during the first 20 minutes after the Big Bang [13]. Deuterium produced in stars during stellar nucleosynthesis is almost destroyed instantaneously by fusion into ^{4}He. It is consequently possible to probe the deuterium-to-hydrogen ratio just after BBN by looking in primordial-like areas with elements with lower masses than Lithium [8]. This ratio depends on the relative density of the baryon [8] with the total matter density. This last can be inferred from the Cosmic Microwave Background (CMB)[14]. This method gives a baryon density of around 20% of the total matter [15], which again points out the presence of a missing mass.

Primordial perturbations are creating potential wells in which baryons are falling. This creates acoustic peaks inside the CMB anisotropies [16] [17]. At the recombination epoch, 380,000 years after the Big Bang, the Universe becomes transparent to photons and baryons stop interacting with photons. They are frozen inside their wells which are most likely made of dark matter. Thus, the CMB which dates from this recombination period allows estimating baryon abundance as it reflects the dynamics of the photon-baryon fluid. COBE, WMAP and Planck experiments estimate baryonic matter abundance around 20% of the total mass [14] [18].
More, CMB fluctuations are too small to have allowed the formation of current large scales structures because it lacked time to achieve their formation. Indeed, baryonic matter only became charged neutral at recombination, a necessary condition for it to fall into gravitational wells and start to form structures. Today's structures need another form of matter electrically neutral and present before recombination to account for observations [19] [8].

I.2 General Constraints on Dark Matter

Evidences developed in the previous section provide some constraints that would help grasp the main properties of dark matter.
First, dark matter is around five times more abundant than baryonic matter in the Universe [6] [18]. It interacts according to gravitation theory [6], is collision-less [12], have a small electro-weak cross section [6] and a small self-interaction cross-section [6] [12].
In addition, dark matter is cold, meaning that it behaves in a none relativistic manner [20] [21]. It is not formed as planet-like bodies [6] and is an electrically neutral form of matter [19].
Finally, dark matter should have a livetime larger than the age of the Universe, so be extremely stable in order to be consistent with observations [22]. It should also have the correct relic abundance found in the Universe [23] [24].
Other more precise numerical constraints have been measured by several experiments. Details can be found in many collaboration papers as for instance [25] [26] [27].

I.3 Dark Matter Candidates

We will now go through several types of dark matter candidates. First, we will present astrophysical bodies, then particle candidates, namely Weakly Interacting Massive Particles, Axion-Like Particles, keV-sterile neutrinos, and some other alternative particles. Finally, we will briefly discuss the possibility of the non-existence of dark matter; discrepancies between observations and models being explained by inaccurate models.

I.3.1 Astrophysical Objects

It was hypothesized that a large part of dark matter could be MACHOs - MAssive Compact Halo Objects - including neutron stars, black holes, brown dwarfs, unassociated planets [28] [29]. This was ruled out by MACHO and EROS-2 collaborations which looked for microlensing events in the Magellan clouds with these objects and found very few candidates [30]. So, MACHOs could only account for a small amount of the missing mass. In addition, CMB studies pointed out the none baryonic nature of dark matter [14] [18].

However, in 1966, Yakov Borisovich Zel'dovich and Igor Dmitriyevich Novikov theorised the existence of primordial black holes (PBH) which would have been created at the beginning of the Universe in a region dense enough for a gravitational collapse on itself [31]. This theory was later notably developed by Stephen Hawking [32]. PBHs would date back from the beginning of the universe, would be by nature cold, collision-less and none luminous. The reconstructed PBH mass spectrum using LIGO merging results falls into the allowed range for dark matter [33] [34]. Recently, through gravitational waves, LIGO/VIRGO observed black holes whose parameters are compatible with PBHs [35]. The PBH theory is hence considered as a serious candidate for a part of dark matter and more observations should be able to either validate or rule out this theory [34]. The PBH contribution to dark matter could however not be more than around 10% due to constraints based on underlying physics phenomena, PBH mass function and abundance [36].

I.3.2 Particles

Another type of candidates would be another, or a set of others, not yet detected particles. These hypothetical particles are not included in the Standard Model that does not contain any relevant candidate [37]. We will develop here the most important candidates at this day.

I.3.2.1 Weakly Interacting Massive Particles

Weakly Interacting Massive Particles (WIMPs) with a mass range from the GeV/c^2 to the TeV/c^2 are one of the most popular candidates for cold dark matter notably because of the so-called "WIMP miracle" [38] [37].

The standard scenario of WIMP production dates back to the beginning of the Universe, during the radiation dominated period. WIMPs would have been the result of particle-antiparticle collisions inside the thermal plasma which was hot enough to allow such pair creations. WIMPs were in this hot and dense Universe in thermal equilibrium with baryonic matter. Then, with the Universe expansion, dark matter production decreased exponentially with the decreasing temperature following a Boltzmann factor of $e^{\frac{-m_\chi}{T}}$ with m_χ the WIMP mass and T its temperature. In addition, as the Universe is expanding, dark matter is scattered away until it became diluted enough to make the annihilation rate negligible. When this annihilation rate became smaller than the Hubble expansion rate - this event is called "freeze out" - WIMP production stopped [39]. The Boltzmann equation (Equation I.3) describes this phenomenon [38]:

$$\frac{dn_\chi}{dt} = -3Hn_\chi - \langle\sigma_a v\rangle(n_\chi^2 - n_{eq}^2) \tag{I.3}$$

with n_χ the number density of WIMPs, n_{eq} the number density of WIMPs in thermal equilibrium, H the Hubble constant and $\langle\sigma_a v\rangle$ the WIMPs averaged annihilation cross-section.

By solving the Boltzmann equation (Equation I.3) the frozen density of WIMPs at the origin, so what is called the thermal relic density Ω_χ (Equation (I.4)) can be derived [39]:

$$\Omega_\chi h^2 \sim \frac{3 \times 10^{-27} c m^3 s^{-1}}{\langle\sigma_a v\rangle} \tag{I.4}$$

with h the reduced Hubble constant.

From this expression we expect the effective annihilation cross-section of WIMPs $\langle\sigma_a v\rangle$ to be around 10^{26} cm^{3}s^{-1}. This is also the typical order of magnitude of the weak interaction cross-section [40]. This would mean that WIMPs could interact via electro-weak interaction and is often referred as the "WIMP miracle". In addition, the WIMP miracle is model-independent: it does not necessitate any assumptions on the WIMP mass [38]. Thermal relic density evolution is shown on Figure I.4.
WIMPs also arise naturally in several Beyond the Standard Model theories [38] [37].

Three detection methods are explored for WIMPs searching, and more generally for dark matter: high-energy colliders, indirect detection and direct detection [41]. Colliders have not the search of WIMPs for first purpose, however, it is possible to look for their production by looking for missing transverse momentum inferred from momentum conservation

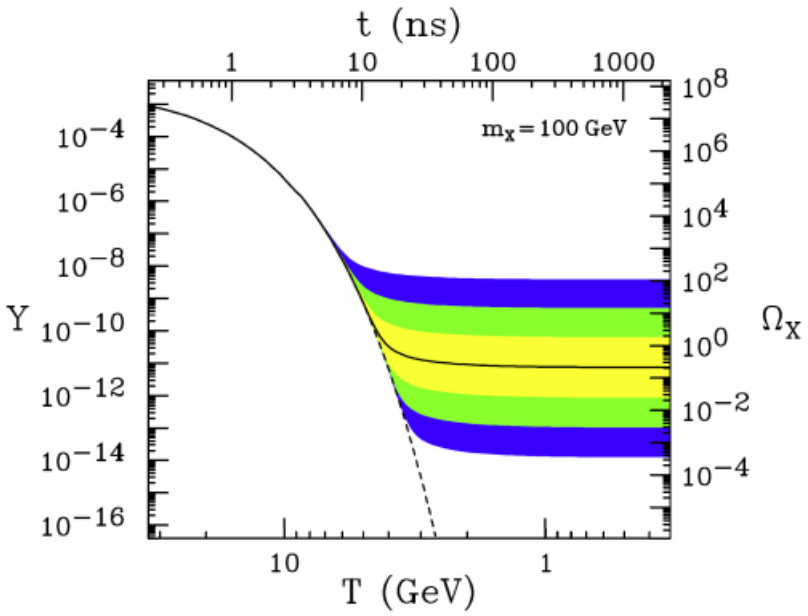

Figure I.4 – Comoving number density Y and resulting thermal relic density Ω_X of a 100 GeV, P-wave annihilating dark matter particle depending on temperature T and time t. The solid contour is for an annihilation cross section that yields the correct relic density, shaded regions are for cross sections that differ by 10, 10^2, and 10^3 from this value and the dashed contour is the number density of a particle that remains in thermal equilibrium. From [38].

[42] [43]. This is notably done at the LHC with the ATLAS and CMS experiments [42] [41] [44].
Indirect searches of WIMPs are based on the search for annihilation or decaying products of dark matter in cosmic rays [45] [46]. For instance, data collected by the Fermi Large Area Telescope can be used for this purpose [47]. Super-Kamiokande collaboration also performed such indirect measurements without imposing strong limits until now [48] [49] [50].
Finally, the main experiments performing direct searches are either using noble liquids such as xenon (LUX, Xenon1T, PANDA-X experiments) and argon (DEAP, DarkSide) or bolometers (CDMS, CRESST, EDELWEISS). We will discuss further direct detection which will interest us in the scope of the DarkSide experiment in Section I.4 of this chapter.

I.3.2.2 Axion-Like Particles

The possibility of the existence of a global $U(1)_A$ symmetry was introduced in 1977 by Roberto Peccei and Helen Quinn in order to solve the CP symmetry violation present in quantum chromodynamics [52]. This spontaneously broken symmetry produces a Nambu-Goldstone boson [53] that was called "axion" by Frank Wilczek after the detergent product as "it cleans the CP violation problem" [54]. Two theories are acknowledged for axion production, either vacuum realignment mechanism or radiation from topological strings [55].
Axions, or more generally axion-like particles (ALPs), are possible candidates for cold dark matter. They would be very light neutral non thermally produced pseudo-scalar

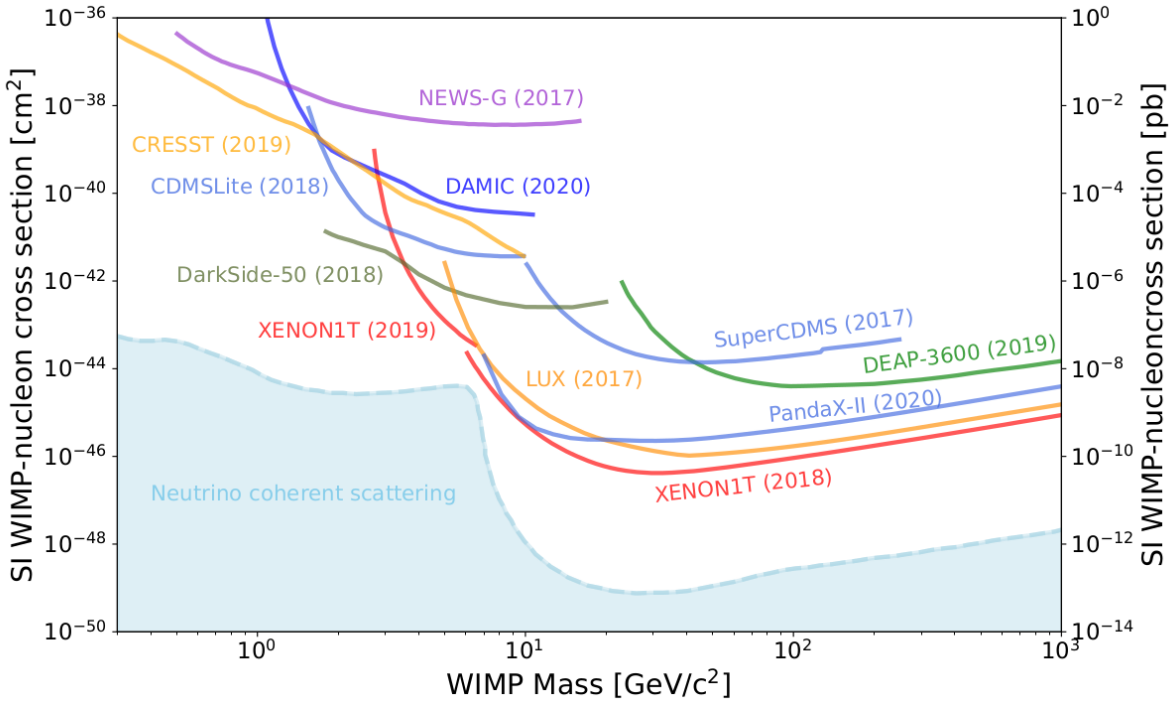

Figure I.5 – State of the art on upper limits on WIMPs-nucleon cross section from [51]

bosons, collision-less, with masses between few μeV and few meV [52] [53] [55].
Two different axion models are explored, the DFSZ (Dine, Fishehler, Srednicki, Zhitnitsky) [56] [57] and the KSVZ (Kim, Shifman, Vainshtein, Zakharov) [58] [59] models with their own predictions and constraints.

Dark matter ALPs search is currently performed by several dedicated experiments using mostly haloscopes like for instance ADMX (Axion Dark Matter eXperiment) and MADMAX (Magnetized Disc and Mirror Axion Experiment). The basic detection principle of ADMX, the actual most sensitive experiment for axion search, consists of converting axions into photons thanks to a microwave resonant cavity inside a magnetic field induced by a superconducting magnet. This cavity can be tuned to different frequencies depending on the axion mass searched [60] [61]. ADMX set exclusion limits on axion-photon coupling for the mass range around 2.6 to 3.4 μeV [61].
MADMAX would also be using axion photon conversion as axion would be producing electromagnetic radiation at the transition between materials. Hence the detector is composed of multiple layers of dielectric media inside a strong magnetic field. Their area of interest would be the mass range 40-400 μeV [62].
Several other experiments using different techniques are also constraining the phase-space as it is shown in Figure I.6.

I.3.2.3 keV-Sterile Neutrinos

In the Standard Model, the only massive candidates which are both electrically neutral and stable enough are neutrinos. However, due to their very low mass, they have a relativistic behaviour and so, could only account for hot dark matter. In addition, a neutrino dominated cosmology would not have allowed the structures to form the way they did,

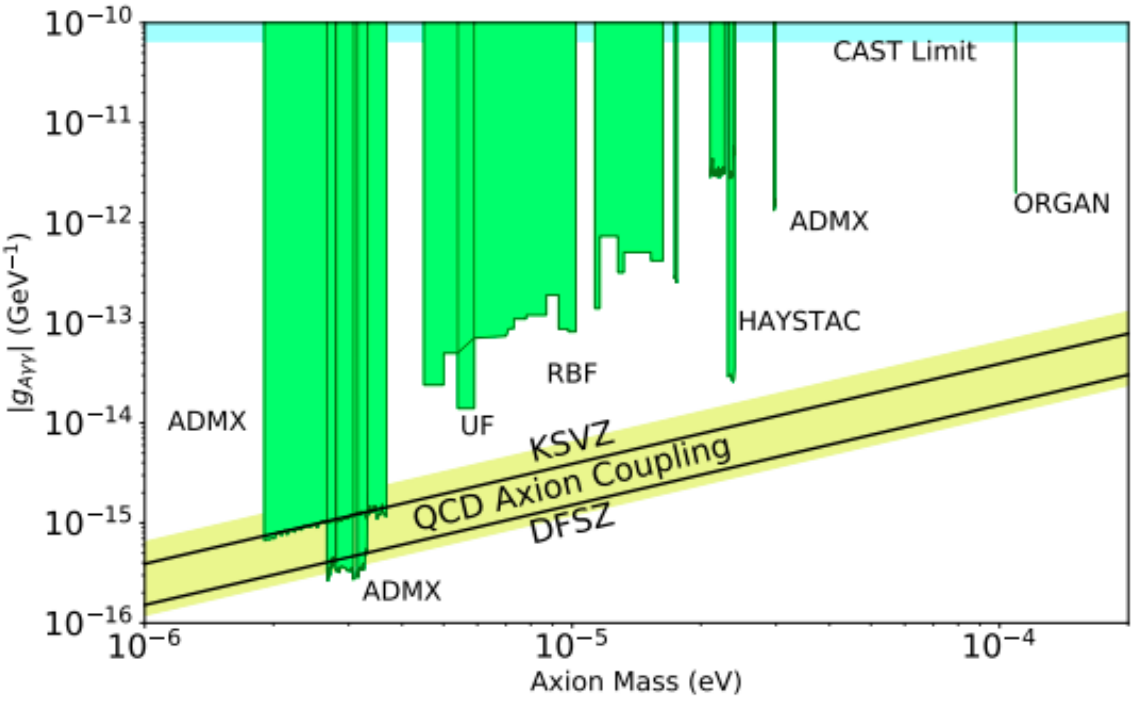

Figure I.6 – Exclusion plot for ALPs from [63] (2019)

ruling out neutrinos as possible candidates for dark matter [64] [65] [66].
However, even if standard neutrinos are not acceptable candidates, it is possible to postulate the existence of a different kind of neutrinos that would be able to fulfil interaction and cosmological requirements such as heavy neutrinos with weaker interactions than standard neutrinos and masses of a few keV.

Sterile neutrinos are $SU(2) \times U(1)$-singlet leptons interacting by weak interaction only by their mixing with active neutrinos [65]. They are stable on long-time scales even if they can decay by mixing [65]. At the keV-scale, they could account either for cold or warm dark matter depending on their mass. However, a mass range of 7 to 36 keV/c^2 corresponds to the natural range for cold dark matter candidates [67] [68] and sterile neutrinos with masses larger than around 5 keV can be considered as behaving like relatively cold dark matter [69] [68]. Hence, in the mass range of interest for dark matter, sterile neutrinos are considered as cold dark matter.
This candidate presents a large number of constraints that can be found in the review [66].

Search for keV sterile neutrinos can be performed in several ways as for instance:

- Using noble atoms (argon, xenon) and time projection chambers as for Xenon100, Xenon1T [70] or DarkSide-50.
- With tritium beta decay as Troitsk nu-mass [71] and TRISTAN [72] experiments
- With a stable dysprosium target [73]

The constrain on their mixing is given by the mixing matrix element $|U_{e4}|^2 = \sin^2(2\theta)$ with θ the mixing angle. This mixing element is part of an extension of the PMNS standard framework for neutrino mixing with three families, adding a fourth sterile neutrino. The best constrain for now was given by indirect astrophysical measurements (cf. Figure I.7).

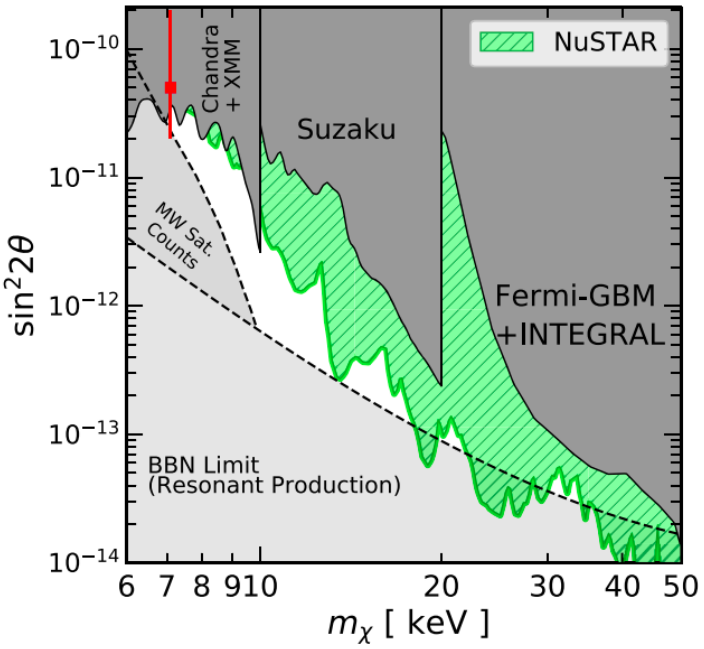

Figure I.7 – Exclusion plot for keV-sterile neutrinos from [74]

I.3.2.4 Other Candidates

WIMPs derivative such as Super WIMPs [75] or WIMPZILLAS [76] are also studied. Super WIMPs would inherit the relic density of classical WIMPs, but have a weaker interaction strength and are not detectable through experiments, only in the early Universe cosmological signatures such as BBN and CMB [77].
WIMPZILLAS are stable non-thermal WIMPs with masses at the inflation scale, 10^{12} to 10^{16} GeV. They could decay into ultra high energy cosmic rays which is not explained yet and would be a way to detect them [76].

Super symmetry (SUSY) is mathematically speaking an extension of the Poincaré symmetry and in terms of application to particle physics the super-symmetric extension of the Standard Model in which each particle has a supersymmetric partner (same quantum numbers, gauge interaction, 1/2 spin difference) [78]. From the additional super-symmetric partner it brings, few can be dark matter candidates as notably the neutralino, gravitino, axino or sneutrino. These particles are often hypothesized as WIMPs candidates.
In all four cases, no experimental data is going in either direction, phase-space is however more and more constrained thanks to diverse experiments.

Many other candidates exists such as the ELDERs (ELastically DEcoupling Relic) [79] or the closely related SIMPs (Strongly-Interacting Massive Particle) [80]. A basic summary of these candidates depending on their mass range is presented in Figure I.8.

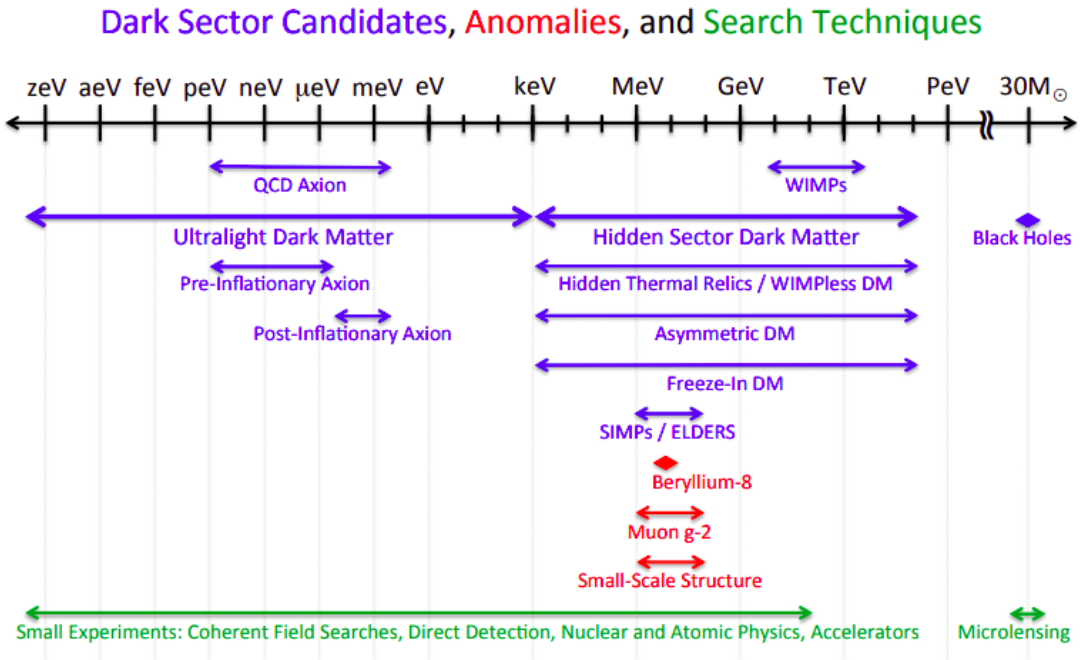

Figure I.8 – Dark matter candidates, detection techniques and anomalies depending on the mass range from [81] (2017)

I.3.3 Alternative Theories

This missing mass issue could also be due to a misunderstanding of the physics and so, to issues in theoretical models. Taking this direction, a large number of alternative models without addition matter were derived, as for instance the well-known MOdified Newtonian Dynamics (MOND) theories. MOND is an alternative set of theories built to explain the rotation curve of spiral galaxies highlighted by Zwicky [2] without dark matter [82]. It was initiated by Mordehai Milgrom in 1983 who hypothesized that the theory used to made this hidden mass observation was wrong and so, proposed a modification of the law of inertia inside Newton's theory [82]. In 2004, introducing a tensor-vector scalar field theory, Jacob Bekenstein opened the door to relativistic variants of MOND theories [83]. More recently, mixed approaches combining both MOND and a small number of dark matter particles were developed [84] [85]. The whole set of these theories can be found in many reviews such as [86] [87].

I.4 Direct Detection Dark Matter Signatures

Direct searches, which interests us in the scope of the DarkSide experiment, attempt to detect dark matter by looking for the scattering between these particles and atomic nuclei [41]. For this purpose, we look for one or several dark matter signatures that can be measured inside a detector. DarkSide experiment is currently using energy spectra. Efforts are made to develop directionality as we will see with the ReD experiment in Section II.4.2.

Energy spectrum. The most used signature is the energy spectrum. Indeed, many experiments are using detectors in which dark matter particles are interacting with the nuclei or electrons of the detector by respectively nuclear or electronic recoil. The energy deposited by the particle recoil is the signature we are looking for. These experiments necessitate a very good control of the backgrounds, the reason why they are almost always underground, well shielded and using low-radiation materials.

Annual modulation. As Earth is in motion around the Sun, and assuming an isotropic and smooth halo, Earth is not in co-rotation with dark matter causing an annual modulation [88]. Indeed, the galactic disk, the Sun and Earth are rotating in a basically static dark matter halo. This causes Earth to receive what is called a "WIMP wind" which is different along the year because of the annual Earth motion [88]. Its maximum speed would be in June and minimum in December with a small difference between both of around 3%.

Due to this modulation, the differential rate in direct detection experiments should display a cosine dependence as:

$$\frac{dR}{dE}(E,t) \simeq S_0(E) + S_m \cos\left(\frac{2\pi(t-\phi)}{T}\right) \tag{I.5}$$

with the time averaged rate S_0, the modulation amplitude S_m, period T and phase ϕ. The amplitude modulation is very small in front of the time averaged rate. The theory gives us that we expect a period of a year, so of 365.24 days and a phase that points to a maximum around the 2^{nd} of June, so of 152.5 days.

The main asset of this kind of signature is that it is easily recognizable among the different backgrounds.

The DAMA/LIBRA experiment claimed the observation of an annual modulation compatible in frequency and phase with 8.9σ [89]. Their results are compatible with 10 or 80 GeV WIMP candidates, but the cross-sections needed to explain the DAMA/LIBRA signal in these mass ranges are excluded by every other dark matter experiment [88]. This modulation could in fact be due to other phenomena, like for instance a seasonal effect of cosmic rays. CoGENT has also shown some abnormalities going in this direction but at less than 5σ [90]. More recently, the COSINE experiment carried out an independent test to verify DAMA/LIBRA claim which excluded it [91].

Directionality. Dark matter candidates such as WIMPs are doing elastic scattering with baryonic matter nuclei. A useful property of elastic scattering is that it keeps in memory the incoming direction. In addition, as seen for an annual modulation, the Earth receive a sort of "WIMP wind" because of the motion of the Sun in the Galaxy. Consequently, dark matter flux would arrive in Earth in the direction of solar motion, hence nuclear recoil should be in the direction of solar motion [92], towards the Cygnus constellation [93]. Furthermore, the daily rotation of Earth causes the detector to see the WIMP wind with different angles along the day at a given point on Earth (cf. Figure I.9). Most known backgrounds are isotropic. Hence, looking for this angular distribution anisotropy of nuclear recoils would be a powerful discrimination between the expected signal and backgrounds [93].

It is also worth noting that directionality is supposed to be a stronger phenomenon than annual modulation, as the Sun motion induces a forward-backward motion asymmetry of more than an order of magnitude [93].

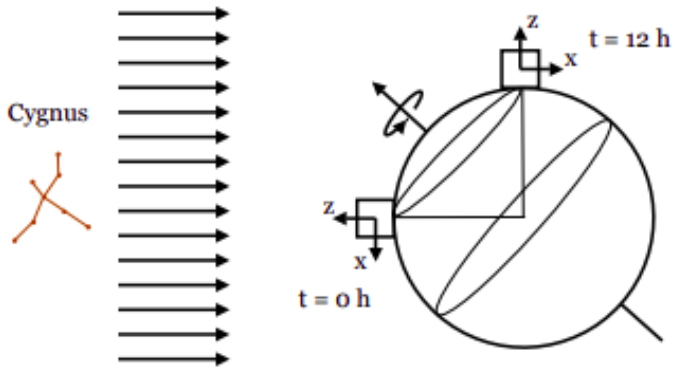

Figure I.9 – Earth daily rotation induces a recoil angle modulation when measured in the laboratory frame, from [93]

This property could refine direct detection for elastic scattering candidates and in the case of WIMPs search, go beyond the neutrino floor. The neutrino floor is defined as the cross-section at which nuclear recoils induced by solar or atmospheric neutrinos constitute an irreducible background to WIMP searches.

Chapter II

The DarkSide Experiment

> It doesn't matter how beautiful your theory is, it doesn't matter how smart you are. If it doesn't agree with experiment, it's wrong.
>
> Richard Feynman (1960s)

The DarkSide experiment is part of the Global Argon Dark Matter Collaboration (GADMC) which aims at bringing together with a common plan of action all experiments searching for WIMPs, one of the most promising dark matter candidates, using argon-based detectors. Collaborations involved inside GADMC are ArDM (Laboratorio Subterraneo de Canfranc (LSC) in Spain), DarkSide-50 (Laboratori Nazionali del Gran Sasso (LNGS) in Italy), DEAP-3600 and MiniCLEAN (both at SNOLab in Canada). They are planning together DarkSide-20k which aims at reaching a higher sensitivity to dark matter. It is meant to be the same kind of detector as DarkSide-50 but with a fiducial mass of 20 ton instead of 20 kg.

To manage this change in scale, several technological upgrades are necessary. They are studied and tested in different intermediary prototypes: Proto-0, Proto-1T and followings that are for now located at the European Organization for Nuclear Research (CERN) in Switzerland.
In this chapter we will go through the characteristics and functioning of DarkSide experiment detectors used for searching dark matter (Section II.1). We will then look at the design of DarkSide-50 in Section II.2 and to its coming upgrade, DarkSide-20k in Section II.3. Two prototypes were designed to prepare the scaling up to 20 ton, Proto-0 and ReD, presented in Sections II.4.1 and II.4.2, respectively.

II.1 Main Features of Detection

The properties of dark matter candidates, and in particular their low interaction probability with matter, set some stringent requirements for detectors aiming at its direct detection. These requirements are low backgrounds - meaning that detectors have to be built with radio-pure materials and operated in underground laboratories with efficient

shielding-, large masses, low energy thresholds, and eventually the possibility of discriminating between signal and background.

Detectors using noble liquids based dual-phase time projection chambers (TPC) satisfy all these requirements: it is possible to build multi-ton detectors underground that are sensitive to scattering of few keV or smaller. They can distinguish between nuclear and electronic recoils using the ratio of their ionization and scintillation components. The best limits in the search for WIMPs with masses from 1 GeV/c^2 to hundreds of TeV/c^2 are set by noble liquids.
The detection principle of noble liquids based dual-phase TPC is developed in details in Section II.1.1. Roughly, a dark matter particle interacts with a nucleon in the TPC inducing a scintillation signal s_1. Ionization electrons produced by the interaction drift towards the top of the TPC and interacts with the gaseous phase inducing a ionization signal s_2. The s_2/s_1 ratio depends on the recoil type.

Among the different noble liquids xenon and argon are the most suitable targets for dark matter. Xenon is heavier so has a larger cross-section with dark matter particles. It means that at a same detector size, same WIMP mass and same interaction probability, xenon based experiments will observe more dark matter candidates than argon-based ones. Xenon is radio-pure while argon is contaminated by cosmogenic radioactive ^{39}Ar. Xenon also has a larger stopping power for neutrons. Xenon based experiments (XENON, LUX, PANDA-X) have currently the best limits on WIMPs above 10 GeV/c^2.

However, in addition to the s_2/s_1 ratio, at high mass ($>$ 10 GeV/c^2) argon allows to reduce further the background thanks to the pulse-shape discrimination which as a higher discrimination power than s_2/s_1 (cf. Section II.1.2) whereas xenon cannot. More, at low mass ($<$ 10 GeV/c^2), contrary to xenon, argon enables for higher transferred momentum due to its low atomic mass. Hence, it performs well on analyses using only its ionisation signal as it will be shown in Chapter III. Finally, it is possible to reduce strongly the ^{39}Ar component using underground argon (cf. Section II.1.2).
For these reasons, the choice of GADMC went to liquid argon based detectors with the challenge to build very large detectors to compensate the lower cross-section of argon.

II.1.1 Dual-phase Time Projection Chamber

DarkSide experiment uses a dual-phase TPC with liquid and gaseous argon. Its basic principle is schemed on Figure II.1. A dark matter candidate interacts inducing a nuclear recoil, which deposits energy. This ionizes argon atoms and excites meta-stable argon states.
Argon atom excited states are emitting photons in singlet and triplet states via the following reaction chain:

$$Ar* + Ar \rightarrow Ar_2^* \rightarrow 2Ar + h\nu \tag{II.1}$$

The excited state forms excited di-argon molecules by combining with another argon atom in its fundamental state. This excited di-argon de-excite by emitting a 128 nm photon. Both singlet and triplet states contribute to the scintillation signal called s_1.

In parallel, after ionisation, electron-ion pairs recombination leads to the formation of excited molecules that also emit scintillation light when de-exciting. The emitted photon is the same as the one coming from scintillation as it comes from the same de-excitation of excited di-argon. It is consequently part of the scintillation signal s_1. The detailed reaction chain is the following:

$$Ar^+ + Ar \rightarrow Ar_2^+ \tag{II.2}$$

$$Ar_2^+ + e^- \rightarrow Ar_2^* \rightarrow 2Ar + h\nu \tag{II.3}$$

Ionisation electrons that escape recombination will be drifted to the top of the TPC thanks to a uniform electric field. These electrons are accelerated by a high voltage electric field when they reach the gaseous phase producing electro-luminescence light in the gas. This induces what is called the ionisation signal s_2. Indeed, only free electrons that escape recombination are contributing to the ionisation signal. Those who recombine contribute to the scintillation signal.

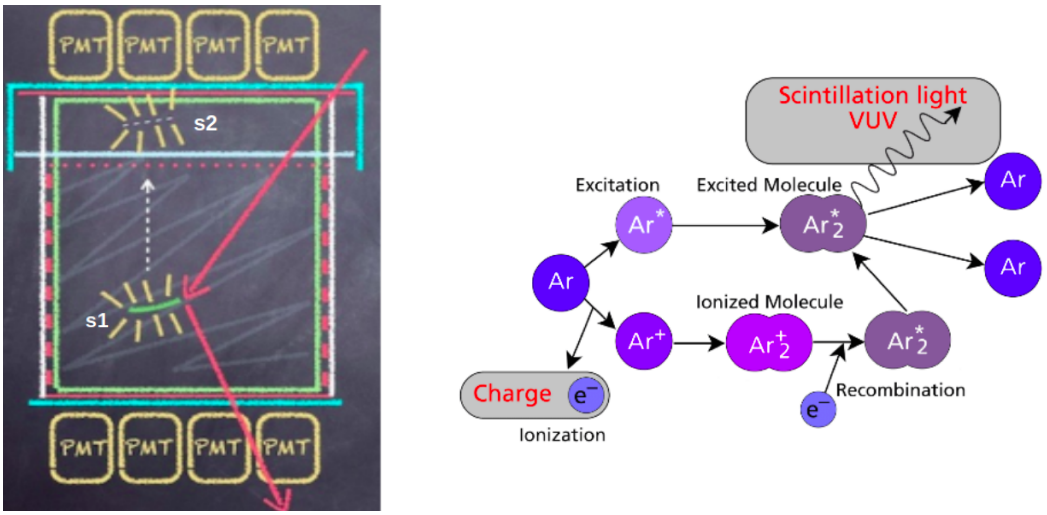

Figure II.1 – Scheme of (left) DarkSide-50 TPC highlighting its working principle with an incoming particle represented by red arrows and both s_1 and s_2 respectively scintillation and ionization signals, adapted from [94] and (right) ionization and scintillation mechanisms in dual phase argon TPC [95].

In s_1, photons are immediately (few tens of ns) collected by photo multipliers. Due to the drift time inside the detector, the s_2 signal is collected after a time-scale of several microseconds depending on the interaction position. The time difference between s_1 and s_2 allows Z reconstruction. X and Y reconstructions are done by exploiting the location of the s_2 interaction on the grid of photo multipliers positioned at the top of the detector. Indeed, depending on the location of the interaction they would not be receiving the same amount of light.

The energy deposited in both s_1 and s_2 is reconstructed following Equation II.4 [96]:

$$E_{dep} = w\left(\frac{s_1}{g_1} + \frac{s_2}{g_2}\right) \tag{II.4}$$

with $w = 19.5$ eV the mean energy to produce a quantum and g_1 and g_2 respectively s_1 and s_2 detection amplification factors. Both g_1 and g_2 are dependent on the electric field

value. In DarkSide-50, $g_1 = 0.16$ and $g_2 = 23$.

II.1.2 Backgrounds and Pulse Shape Discrimination

The main source of backgrounds are electronic recoils (from β and γ decays) and nuclear recoils from neutrons and α decays. Electronic recoils account for the large majority of them.
These experiments are built with low-radioactivity materials and are operated in underground facilities to shield them as much as possible from external backgrounds.

However, to reduce even more background sources and make dark matter studies possible, underground argon (UAr) is used. Indeed, ^{40}Ar is the most abundant isotope in the atmospheric argon, but there is also a non-negligible component of ^{39}Ar of around 1 Bq/kg. This is a β emitter with an endpoint of 565 keV and hence a direct source of background. However, ^{39}Ar is cosmogenic, so underground argon which lied a long time without any interaction with cosmic rays has a very low ^{39}Ar production rate. For DarkSide experiments, UAr is extracted from an underground argon reservoir in Colorado (USA). It is purified in a plant in Cortez (Colorado, USA). This facility, called Urania, will be able to provide 330 kg/day of UAr at a purity of 99.99%. For the next detector, DarkSide-20k, to reduce even more ^{39}Ar isotopic abundance, Aria device is being installed in Seruci (Italy). Aria is a 350 m cryogenic distillation column to separate isotopes. It allows reducing ^{39}Ar in UAr by 10 per pass [97].

The main advantage of argon is that, thanks to pulse shape discrimination (PSD), it is possible to perform background free searches at high WIMP mass in argon and reject electronic recoils with a discrimination factor above 10^8 making possible to built multi-ton detectors that can search for WIMP-induced nuclear recoils with no backgrounds coming from electronic recoils. The principle is the following. During scintillation, the excited state of the argon atom is emitting photons in singlet and triplet states (cf. Section II.1.1). When a nuclear recoil occurs, a larger number of singlet states are produced, contrary to an electronic recoil for which a larger number of triplet states are produced. The de-excitation time of the singlet state is very short (around 7 ns) while the de-excitation time of the triplet state is quite large (around 1600 ns). The electronic recoil rejection is based on the time difference of the pulse shape distributions.
For xenon, the singlet and triplet de-excitation times are very close (respectively around 2 ns and 27 ns) so pulse shape discrimination cannot be used for background rejection.
Figure II.2 reports the pulse shape discrimination plot for DarkSide-50 underground argon: the distribution of events (electronic recoils from ^{39}Ar) depending on f_{90} (fraction of photo-electrons in the first 90 ns of the pulse) and s_1. It allows to delimiter a portion of the (s_1, f_{90}) plane in which there is not any electronic recoil event, thus background free. Chapter VI will describe the pulse shape discrimination computation in details in the scope of DarkSide-20k.

An additional way to discriminate electronic and nuclear recoils is to look at the ratio between ionization and scintillation signals. This method is also used in xenon experiments and typically allows background rejection with a discrimination factor of $10^2 - 10^3$. Figure II.3 displays for XENON-10 experiment the difference of s_2/s_1 ratio depending on

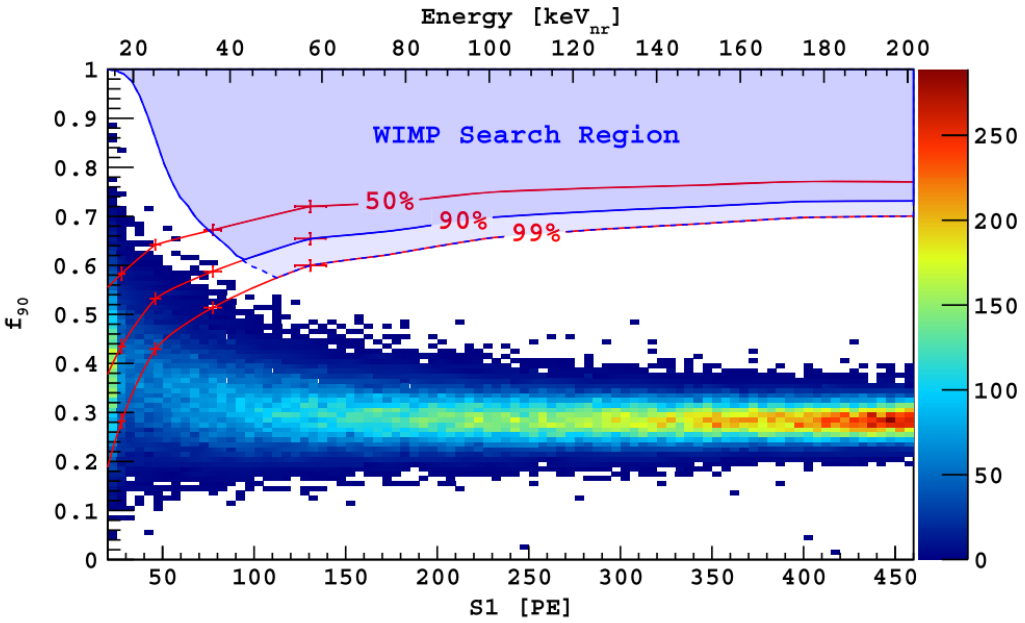

Figure II.2 – Pulse shape discrimination variable f_{90} versus s_1 for DarkSide-50 events. The red line shows the f_{90} acceptance contours, the shaded blue area the electron background free WIMP search area. Taken from [98]. See Chapter VI for more details on pulse shape discrimination.

either nuclear or electronic recoils depending on the energy.

As we will show in the following chapter, DarkSide-50 proved to be a competitive detector for searches at low-mass WIMPs (<10 GeV/c^2) by exploiting the s_2 only signal. For low mass WIMPs, releasing energies of few hundred of eV in the TPC, s_1 detection efficiency is low and PSD cannot be used. Thus, the background has to be modelled. The main components of this background are coming from the PMTs and cryostat radioactive contaminants and from ^{39}Ar and ^{85}Kr contaminants in liquid argon. PMT and cryostat backgrounds are ^{232}Th, ^{40}K, ^{60}Co, ^{238}U and ^{235}U. Their activities are summarised in Table 1 [100]. To reduce the emission of γ-rays and neutron backgrounds from external contamination, only events in the core of the TPC (for Dark-Side-50: 21.6 cm high, 2 cm radius area) are selected [96]. In addition, multi-scatter events (events with more than one s_2) are rejected as they do not correspond to the expected signature [96]. Dark matter candidates have a too low cross-section to be able to do multiple scattering.

II.2 DarkSide-50 Experiment

DarkSide-50 experiment was built to perform WIMP direct detection of dark matter using liquid argon. First results were published in 2015 [25] resulting in best limits for WIMP interactions on argon. DarkSide-50 was operated first with atmospheric argon and it demonstrated the power of the pulse shape discrimination with a large amount of ^{39}Ar. Then, using underground argon instead of atmospheric argon, it demonstrated that underground argon is depleted in ^{39}Ar by a factor 1400±200 [98]. The combination of the pulse shape discrimination performance and underground argon allows to be able

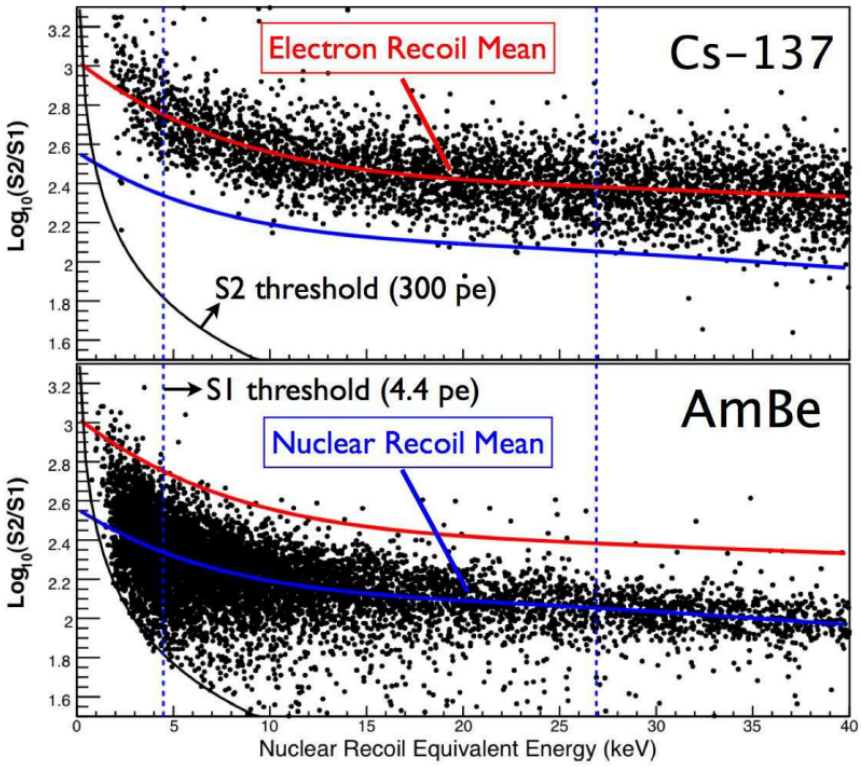

Figure II.3 – XENON-10: $\log(s_2/s_1)$ versus energy from calibration data for (top) electronic recoils and (bottom) nuclear recoils. Dashed blue lines are delimiting the energy range used by XENON-10. From [99].

to reach background-free search for high mass WIMPs [98]. In 2018, a blind analysis on the full dataset, with underground argon inside the detector, was performed in order to improve high-mass WIMPs limits [100].

Also in 2018, an analysis exploiting the s_2 only signal allowed to reach the best sensitivity between 1.8 and 6 GeV/c^2 [101]. As we will show in Chapter III, a part of this thesis was devoted to a more refined analysis of calibration and different backgrounds allowed improving these limits [96] and additional dark matter candidates were studied.
In this section, we will present the detector setup, electronic, data acquisition and calibrations.

II.2.1 Detector Setup

The DarkSide-50 experiment is located in Italy, at the underground Laboratori Nazionali del Gran Sasso in Hall C. The detector is placed in the large water tank that was used by Borexino collaboration for their Counting Test Facility. This water tank is used by DarkSide-50 as a Water Cerenkov Detector (WCD). It is the outer layer of the overall detector whose structure is similar to Matriochkas with three different layers. The water equivalent depth of the detector is 3,800 m [102]. At this depth, the muon flux is reduced by a factor around 10^6 thanks to the rock shielding [103].

The WCD is a cylindrical tank with a height of 10 m and a diameter of 11 m filled with

1 kiloton of high purity water. Its goal is to shield the inner parts of the detector from γ radiation both from the capture of neutrons at the proximity of the experiment and from the radioactivity of the detector materials [104] [105]. It also serves as anti-coincidence for cosmic muons [25] [105]. This part of the detector is based on the Cerenkov effect and hence detect Cerenkov photons from relativistic particles - and mostly muons - crossing the water [104] [25]. The emitted light is captured by 80 photo-multipliers at the bottom of the water tank [25] [106]. The working principle of this detector is to detect photons emitted by charged particles crossing the water at a speed higher than the speed of light in water (Cerenkov effect).

Inside the WCD is located the Liquid Scintillator Veto (LSV): 30 ton of an organic liquid scintillator loaded with boron are contained inside a 4 m diameter sphere in stainless steel [25] [105]. The scintillator is a mixture of pseudocumene (PC) for the primary scintillator, trimethyl borate (TMB,B(OCH3)3) for boron loading and with 2,5-diphenyloxazole (PPO) as a wavelength shifter. Boron is used for its high cross-section to thermal neutron capture. Scintillation photons are detected by an array of 110 photo-multipliers located on the sphere inside the surface [105]. The LSV light yield is (0.54 ± 0.04) photo-electrons per keV and was measured by using ^{14}C and ^{60}Co sources [25].
The LSV is designed to identify and veto neutrons that might enter or exit the liquid argon TPC. Neutrons thermalize by scattering on protons in the liquid scintillator and are efficiently captured by ^{10}B nuclei. Hence, the LSV is with the WCD what is called the neutron veto whose aim is to shield the inner detector from backgrounds, and mostly from neutron backgrounds. These backgrounds can be coming from either cosmic ray muons or radioactivity of both the external environment and detector materials [105]. The LSV also serves as anti-coincidence for these radiogenic and cosmogenic neutrons, but also γ-rays and cosmic muons [25]. Events still passing through the WCD and LSV to the inner part are tagged in order to be vetoed in the analysis [105].

The last and most inner layer of the detector, placed inside a stainless steel cryostat and supported by a levelling rod system at the centre of the LSV is the liquid-argon dual phase Time Projection Chamber (TPC) [25]. This TPC is a 36 cm diameter and 36 cm-high cylinder in which is placed a large active volume of liquid argon above which is located a 1 cm thick argon gas layer [106]. The cold liquid argon mass is (46.4 ± 0.7) kg [25]. A uniform electric field is applied on the TPC thanks to the high voltage applied between the TPC anode and cathode [107]. Thirty-eight PMTs divided into two arrays of nineteen are respectively placed at both extremities of the TPC to collect emitted light (cf. Figure II.4) [25]. Scintillation photons are emitted at 128 nm and pass through a TetraPhenylButadiene wavelength-shifter to be detected at 420 nm by photo-multipliers [25]. The general mechanism of the TPC is detailed in Section II.1.1.

II.2.2 Electronics and Data Acquisition

Two different electronic and data acquisition systems are present, one for the neutron veto, WCD and LSV, and the other for the TPC. Their synchronisation is however provided by a high precision time-stamp with a precision of 20 ns provided by the Laboratori Nazionali del Gran Sasso GPS [107].

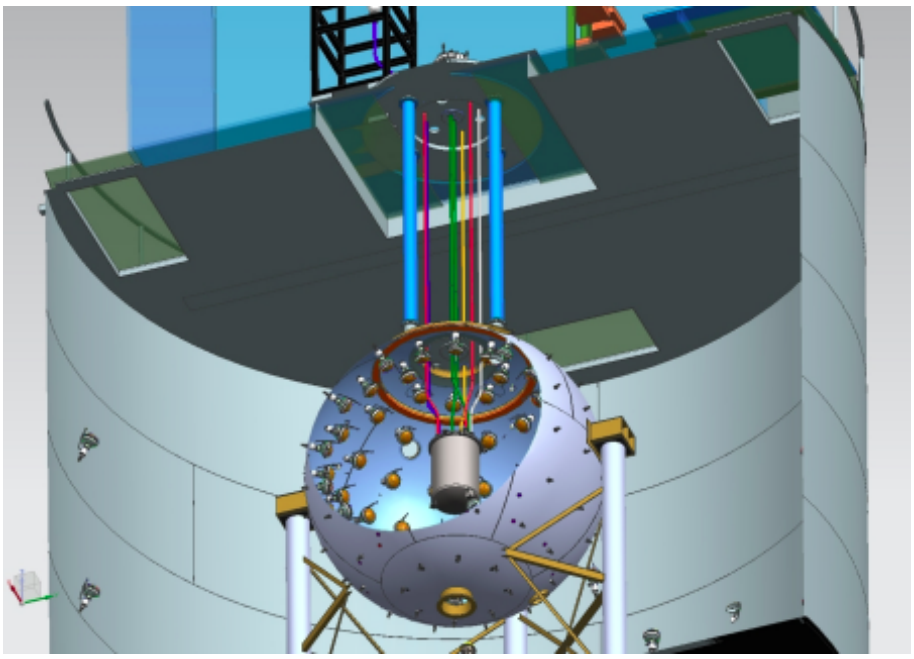

Figure II.4 – DarkSide-50 detector with for the inner part of the detector to the outer: the TPC cryostat at the centre of the LSV sphere inside the WCD tank from [25]

TPC electronic connections are made of 5 to 10 m of vacuum-tight pipes [107]. To avoid sporadic light emission while keeping a high signal-to-noise ratio, PMTs are operated at a low gain (around 10^5). The anode signal for each one of them is consequently first amplified by a cryogenic pre-amplifier placed at the PMT base inside liquid argon, hence working at a temperature around 87 K [25] [107]. This pre-amplifier is constructed to be as radio-pure as possible to avoid additional background and consequently used Cirlex circuit board [107]. Its active internal gain is 3V / V [107]. At room temperature, another amplification by a factor 10 is performed using one amplifier module for five channels [107]. Each PMT is associated to a single channel. The signal is filtered and then split: one copy is sent to a discriminator for the TPC trigger while another is sent to a digitizer with two choices for low and high gain: a 12-bit 250MHz waveform digitizer CAEN V1720 if the signal has a high gain and to a 14 bit 100MHz CAEN V1724 if the signal as a low gain [25] [107]. In each case, a module is dealing with eight channels [107].

Vetoes electronic connections are made of low dispersion 40 m coaxial cables [107]. Signals received by the veto PMTs are amplified 10 times before being split and send to NI PXIe-5162 digitizers [25] [107]. One module operates on 16 channels [107]. To reduce the quantity of stored data, a zero suppression algorithm is performed. Only peaks above 0.25 times the amplitude of a single photo-electron pulse are kept [25] [107].

Data acquisition is managed by trigger boards CAEN V1495, one for each detector [25]. Each sub-system has an independent trigger and share a common global trigger mastered by the TPC data acquisition system [25] [107]. Physics runs need TPC and veto synchronisation, thus are using the global trigger which has an efficiency above 99% for s_1 larger than 60 photo-electrons [25]. To save disk space, the high energy part of the ^{39}Ar energy spectrum is rejected thanks to a specific trigger condition [25].
The acquisition window for TPC data was taken at 440 μs with an inhibit time after each

trigger of 810 μs [25]. The veto has two possible acquisition windows, a short one of 6.5 μs and a long one of 70 μs to include possible delayed neutron captures; the last is used for physics runs [25] [107].

II.2.3 Calibrations

Single photo-electron response of PMTs. Photo-multipliers are used in all three detectors. To retrieve the single-electron response for each channel, laser calibration is used. Light from 405 nm wavelength pulsed laser diodes is injected through optical fibres in each detector. The acquisition window used for these calibration runs is 3 μs [25]. For each channel, it is possible to retrieve the gain, charge and pedestal of the received signal. As we assume a Poisson distribution of the number of photo-electrons we can retrieve a calibration relation between the measured mean charge and the mean number of photo-electrons produced for each laser pulse. The variance is determined the same way. The systematic uncertainty of this method on the single-photo-electron mean is estimated inferior to 2.5% [25]. This procedure is detailed in Chapter IV where we implemented the same kind of procedure for Proto-0 and ReD.
PMTs from both WCD and LSV are going through a similar experimental procedure, but a single Gaussian fit is used on each channel to retrieve the single-photo-electron mean response [25].

TPC light yield. To evaluate the TPC light yield, gaseous ^{83m}Kr is injected inside the detector. When it decays, it emits two conversion electrons so close in time that this double emission is recorded as a single one with a reference energy of 41.5 keV. Its mean decay lifetime is 1.83 hours [108]. In the TPC, the light yield is measured at this 41.5 keV line with a fit of the s_1 spectrum (cf. example of Figure II.5 for a zero-field run which gives a light yield of (7.9 $\pm$ 0.4) photo-electrons) [25]. The main systematic uncertainty on the light yield measure comes from the PMTs mean single-photo-electron response (cf. previous paragraph) [25].

TPC response. The calibration of the TPC response to both electronic and nuclear recoil was performed using a combination of in-situ sources thanks to CALIS [109] and external experiments like ARIS [110] and SCENE [111] [112]. ARIS is a small dual-phase LAr TPC which aimed at characterizing LAr response to nuclear recoils using a collimated neutron beam produced by the Licorne source (ALTO facility, Orsay, France) [110]. SCENE is a dual-phase LAr TPC which aimed at studying nuclear recoil scintillation yield using low energy pulses from a neutron beam (Notre Dame Institute for Structure and Nuclear Astrophysics, USA) [111].

CALIS (CALibration source Insertion System) apparatus is used to position inside the liquid argon veto radioactive sources, such as γ sources (^{57}Co, ^{133}Ba, ^{137}Cs and ^{22}Na) and neutron sources (AmC or AmBe, with different isotopes) to calibrate the LSV detector response and the TPC electronic and nuclear recoil detector response [109]. Both γ and neutron sources were placed inside the LSV against the TPC cryostat to avoid rate losses thanks to an articulated arm and measurements were performed positioning sources at

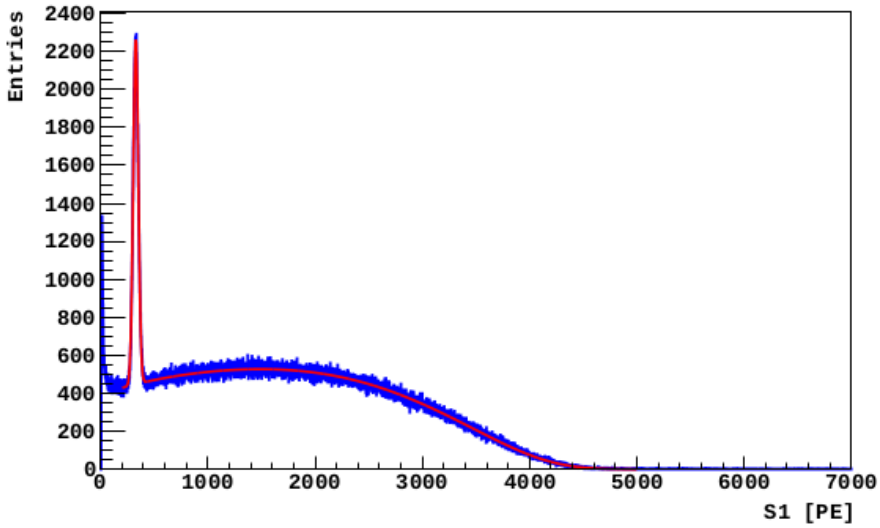

Figure II.5 – Scintillation spectrum at zero-field inside DarkSide-50 TPC with atmospheric argon, so presence of ^{39}Ar. Blue: ^{83m}Kr injected in the detector with a sum of conversion electrons at 41.5 keV. Red: fit of the ^{83m}Kr and ^{39}Ar spectrum. From [25]

different places around the cryostat [109].

Additional external calibration of the liquid argon response was performed thanks to two external experiments, SCENE [111] [112] and ARIS [110]. They allowed to determine nuclear recoil energy scale and ionization yields [101]. Both were as well used for measuring scintillation yield and scintillation nuclear and electronic recoil response for low mass analyses [101] [110].
The advantage of external experiments using a neutron beam is that it is possible to calibrate the liquid argon response to a recoil of a known energy while in in-situ calibration for nuclear recoil relies on spectral shapes that need additional Monte-Carlo simulations to model them.

II.3 DarkSide-20k Prospect

The future detector of the DarkSide program will be DarkSide-20k, a 20-ton detector with advanced technologies to allow the scale-up from the previous detector of 50 kg. The construction of this detector will start in 2022 and the first data-taking is expected for 2026. In the meantime, its design and characteristics are largely discussed and refined to achieve the best detector possible. A large part of this thesis has been devoted to optimize the detector design and develop the reconstruction algorithms for DarkSide-20k as it will be shown in Chapters IV, VI and VII.

II.3.1 Detector Setup

As with every detector of the DarkSide program, the active part will be a dual-phase TPC (Scheme Figure II.6). It will be located at 3,800 m deep in the Gran Sasso underground laboratory in Italy. As DarkSide-50, its structure is like Matriochkas.

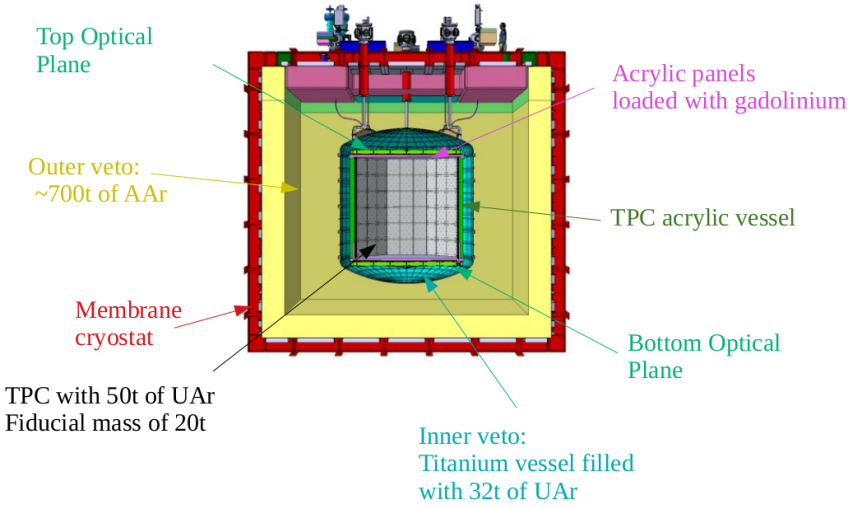

Figure II.6 – Scheme of the main elements of DarkSide-20k future detector.

The most outer layer is a membrane cryostat as the one designed for Proto-DUNE with a width of 8.5 m and a height of 7.9 m which contains the whole detector. Inside it, the outer veto is formed by a ∼700 ton of AAr buffer which shields from external radiations, cosmogenic neutrons and acts as a muon veto.

Then, a titanium vessel seals the inner veto filled with 32t of UAr. The inner veto shields the TPC from neutron backgrounds. On its inner surface, it encapsulates the TPC with 424 ultra-pure panels of 10 cm thick acrylic loaded with gadolinium. Reflectors with wavelength shifters are deposited on all the surfaces to convert photons in the range that can be detected by a total of 5 m^2 surface of SiPMs deployed in the veto. Front end boards are then used to digitize and amplify detected signals. They are mounted in parallel to the tiles. Optical transmitters are driving the signals.

The neutron veto works as schemed in Figure II.7. Neutrons are captured by the gadolinium loaded acrylic placed between the TPC and the inner veto for its high interaction cross-section with neutrons. The gadolinium emits γ rays up to 8 MeV that interact with the UAr of the inner veto. The wavelength of the emitted scintillation light is then shifted using TPB and detected inside the inner veto SiPMs.

Finally, the most inner layer is an ultra pure sealed acrylic TPC filled with 51.1 ton of UAr (active mass of 49.7 ton). This TPC has an octagonal shape with a drift length of 350 cm with an octagonal inscribed circle diameter of 355 cm. The fiducialisation of the TPC, so the removal of the section too close to the edges and so, that can be subject to an additional background, gives a fiducial LAr mass of 20.2 ton with a vertical fiducial cut of 70 cm from the walls and a radial fiducial cut of 30 cm from the walls. The gas pocket thickness will be equal to (7.0±0.5) mm. The grid wire spacing will be 3 mm, its optical transparency 97% and its operating voltage -3.8 kV.

The cathode and anode will be coated with a Clevios transparent conductor. Their operating voltage will be set at respectively, -73.8 kV and ground. The drift field will be set

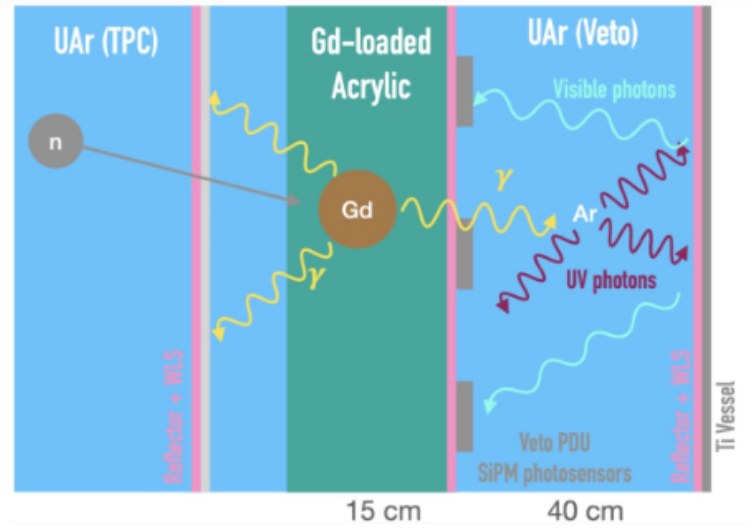

Figure II.7 – Scheme of the inner veto working principle in DarkSide-20k

at 200 V/cm, the extraction field at 2.8 kV/cm and the luminescence field at 4.2 kV/cm. Instead of copper rings like in DarkSide-50, this detector will use Clevios grooves to conduct the electric field.
The sides of the TPC are covered by multilayer polymeric reflectors and wavelength shifters to convert 128 nm photons into 420 nm photons that can be detected thanks to a 28 m^2 coverage of SiPMs, arranged in 4140 channels on the top of the TPC and 4140 on the bottom. Each SiPM has an active area of 1 cm^2 and 24 SiPMs are grouped together into a PDM (Photo Detector Module). Finally, a motherboard will gather 25 PDMs, a steering module (that can disable individual PDMs) and optical linear transmitters.

Projections of the sensitivity of DarkSide-20k are shown in Figure II.8.

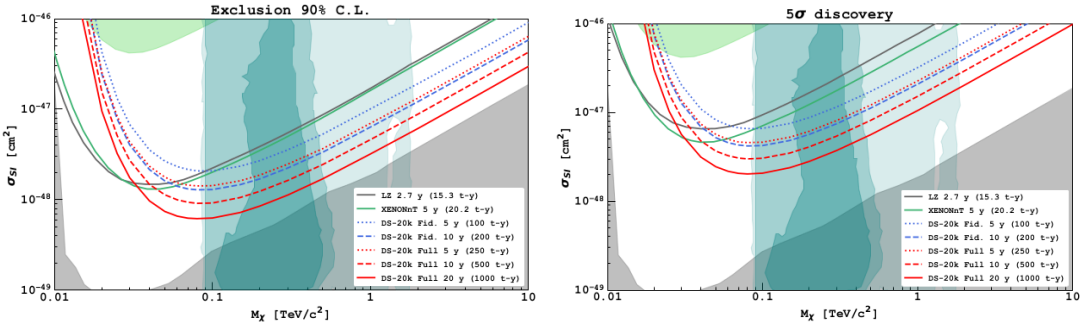

(a) (b)

Figure II.8 – DarkSide-20k expected sensitivities to spin independent WIMPs future detector for (a) 90% C.L. exclusion and (b) 5σ discovery. Different exposures as well as detector configurations are tested. It is compared to LZ and XENONnT sensitivities. Taken from [113].

II.3.2 Silicon Photo-Multipliers

One of the main technological improvement planned for DarkSide-20k is the use of silicon photo-multipliers (SiPMs). This technology is already largely used in several particle physics experiments [114]. Basically, SiPMs are photo-multipliers (PMTs) which have as assets a higher photo-detection efficiency, high gain, fast response, small size, insensitivity to magnetic fields, low light detection, blue sensitivity, a better single-photon resolution, a lower background, a lower operating voltage and a lower cost [115] [114]. DarkSide-20k will need 28 m^2 of them.

SiPMs are silicon-based solid-state sensors [115] composed of 2-D arrays of pixels (single photon avalanche diodes) summed in parallel working in Geiger mode [116]. It returns a signal proportional to the number of detected primary photons. For the DarkSide experiment, they were developed for liquid argon by the Fondazione Bruno Kessler (FBK) with some specific properties following DarkSide-20k requirements listed in Table II.1. They are clustered in tiles called PDM (photo detection modules); each PDM regroups 24 1-cm^2 SiPMs (cf. Figure II.9).

Table II.1 – Properties of PDMs provided by FBK following DarkSide-20k requirements. PDE stands for the photon detection efficiency.

Surface	Power dissipation	PDE	Noise Rate	Time Resolution	Dynamic Range
24 cm^2	$\sim$ 170 mW	45%	0.004 cps/mm^2	16 ns	$\sim$ 100

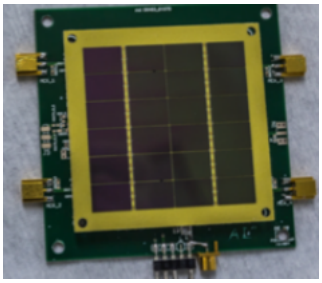

Figure II.9 – Picture of a PDM with 24 SiPMs developed by FBK for the DarkSide experiment

Several tests have already been performed with SiPMs in order to test DarkSide-20k requirements [113]. For example, the performance of the photo-electron charge spectrum through ASIC amplifiers at 7 VoV (Figure II.10a) or the photon detection efficiency, for instance depending on the over-voltage in Figure II.10b. Complete details are available in [113].

Thermal electrons can induce avalanches inside SiPMs causing dark count rate (DCR). DCR is dependent on the temperature over-voltage and active area [115]. It is a source of noise at the single-photon level. SiPM's exposition to radiations increases the DCR [117].

Another source of noise in SiPMs is due to optical cross-talk. Cross-talk happens when an avalanche produces a photon which initiates an avalanche in the neighbour pixel. Consequently, the detected number of photo-electrons is higher than the real one: single

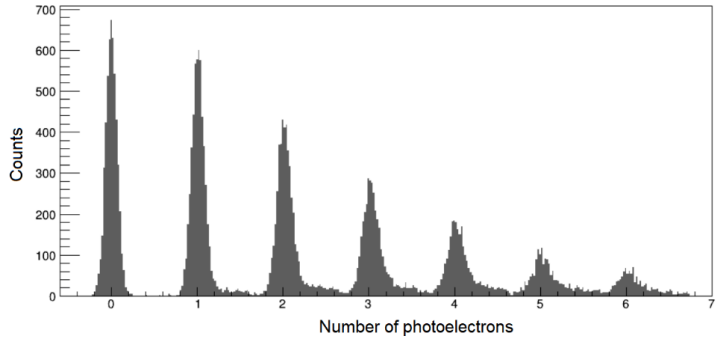

(a)

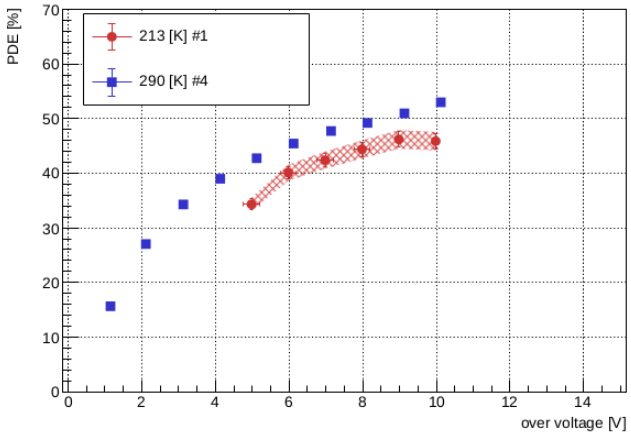

(b)

Figure II.10 – (a) Photo-electron charge spectrum using laser and ASIC amplifiers at 7 VoV, (b) photo detection efficiency of DarkSide SiPMs depending on the over-voltage at different temperatures. From [113].

photons will create a signal of more than one avalanche. It can be either internal - when the avalanche is produced on the same SiPM - or external - when produced in another one. The cross-talk increases with over-voltage [115].

Another common phenomenon inducing noise is after-pulses. Indeed, electrons from the avalanche are captured by impurities and released with some delay. The size of the resulting secondary avalanches depends on the recovery time of the SiPM (from 300 to 600 ns). If they happen before the end of the recovery time they will be weaker than the usual ones [118]. Once again, over-voltage increases after-pulses as it increases the probability of inducing avalanches [115].

These different components of the noise response can be clearly identified as it can be observed in Figure II.11 [119].

II.4 Prototypes for DarkSide-20k

In order to prepare the construction of DarkSide-20k and test all the critical components the collaboration has engaged in several prototypes, and notably on Proto-0 and ReD on which some of the work of this thesis was based. Their description is discussed in the

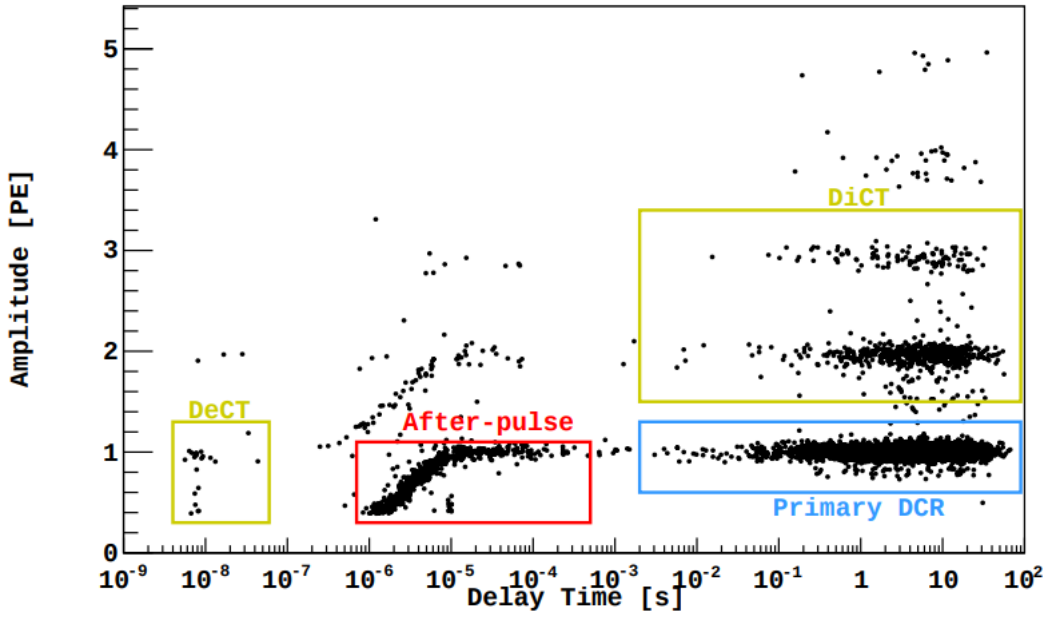

Figure II.11 – Delay time response of SiPMs at 77K versus amplitude in absence of light stimulation [119]

following sections.

II.4.1 Proto-0 Prototype

Proto-0 is one of the first prototypes built to prepare DarkSide-20k. Its goal is manifold. First, one of the main technological improvements that will allow the change in scale is the use of SiPMs (cf. Section II.3.2) instead of generic photomultipliers. Hence, a first aim of Proto-0 is to characterise the functioning of SiPMs with a full motherboard. Secondly, this change to SiPMs requires to develop an appropriate reconstruction software (laser calibration, xy reconstruction, light yields, pulse finding, etc.) which will then be adapted to coming prototypes and to DarkSide-20k. Finally, this prototype is also a test of the gas pocket formation. Consequently, Chapter IV on data reconstruction will be partly based on data from this experiment. In this section, we will present the detector setup, electronic and data acquisition system.

II.4.1.1 Detector Setup

Proto-0 prototype is located at CERN, in Switzerland. It is composed of a dual phase liquid argon TPC with a mechanical mock-up on a support structure. The TPC is 0.12 m^3 square-section volume with a full drift length of 12 cm. The active liquid argon mass inside the TPC is around 10 kg. The gas pocket thickness is 7 mm with a xy dimension of (352×352) mm^2. A field cage is present around the TPC to provide an electric field. The whole system is placed in a cryostat. The cryogenic system used is the ICARUS/WARP cryogenic R&D setup system of building 182-2-001 at CERN. Some pictures are shown in Figure II.12.

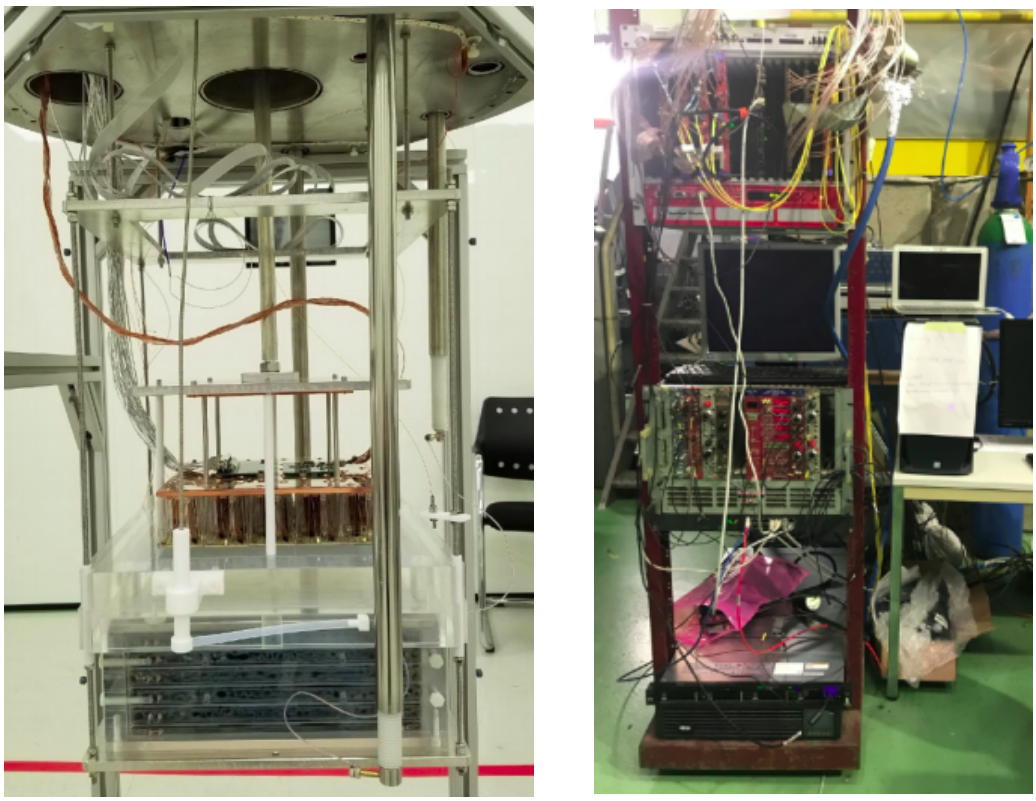

Figure II.12 – Pictures of Proto-0 TPC inside its structure in the cleanroom (left) and data acquisition system (right) taken at CERN

II.4.1.2 Electronics and Data Acquisition

As will DarkSide-20k, Proto-0 uses SiPMs gathered in PDMs (Photo-Detector Modules). Each PDM is a (5×5) cm^2 array of 24 SiPMs. This first prototype has only one motherboard which contains 25 PDMs displayed in a 5×5 array. Thus, a motherboard is around $(25 \times 25 \times 5)$ cm^3. A system with additional motherboards will be tested with the next prototype. Each PDM corresponds to a single channel. The correspondence between both is:

$$\begin{aligned} \text{tile } 0 : \text{channel} &= 2 \times \text{PDM} - 2 \\ \text{tile } 1 : \text{channel} &= 2 \times \text{PDM} \\ \text{tile } 2 : \text{channel} &= 2 \times \text{PDM} + 4 \\ \text{tile } 3 : \text{channel} &= 2 \times \text{PDM} + 8 \end{aligned} \tag{II.5}$$

with each tile corresponding to a 250 Ms, 14 bit ADC CAEN V1725 which digitize waveforms for each channel. They are linked by optical links of 80 MB/s. They are able to read 16 channels, but one is reading 7 channels and the three others 6 (tile 0 : PDM 1 to 7, tile 1: PDM 8 to 13, tile 2: PDM 14 to 19, tile 3: PDM 20 to 25).

The acquisition window is 200 μs with 100 μs pre-trigger. Trigger synchronization is performed thanks to a 'chronobox', a DE-10 nano evaluation card with a Cyclone-V SoC FPGA. When taking physics runs, the trigger is set at a 5 PDMs coincident signal in an 80 ns window with a threshold from 200 to 1600 ADC counts below the baseline. For each event, the baseline is computed on the first 200 ns.

II.4.2 ReD Experiment

ReD (Recoil Directionality) experiment has for aim to study the feasibility of measuring nuclear recoil dark matter directionality in a dual phase argon TPC. Directionality signature was discussed in Section I.4. It could be useful in DarkSide experiment both for background discrimination and to find dark matter candidates or to draw limits below the neutrino floor. The technique that is intended to be used for directionality measurements is columnar recombination which is developed in Section II.4.2.1. The experiment is thus measuring the dependence of scintillation and ionisation signals as a function of the recoil path and the electric field of the TPC.

Chapters IV and V are using data from this experiment, respectively for developing data reconstruction and for evaluating the gas pocket thickness. In this section, we will describe the settings of the detector and its calibration.

II.4.2.1 Columnar Recombination

The phenomenon of recombination happens when a freed electron from an energetic ionizing particle is captured by an ion. In a time projection chamber, the freed ionization electrons are drifted by a uniform electric field to its top (cf. Section II.1.1). However, as we have already seen, all the electrons do not reach the top, some recombine with argon ions from the ionisation track to produce ion-electron pairs. It is called columnar recombination as this kind of recombination has a columnar shape and recombination increases when the electric field is parallel to the column [120]. This means that the intensity of the recombination changes depending on the angle between the particle direction and the electric field. Recombination magnitude is maximal when the particle path and the electric field are parallel and minimal when they are perpendicular. This could be used to determine the nuclear recoil direction [121].

Recombination happens when a freed electron gets sufficiently close to an ion. The electron capture distance, called Onsage radius, r_O, is such as [121]:

$$r_O = \frac{e^2}{\epsilon E} \tag{II.6}$$

with e the electron charge, ϵ the dielectric constant of the medium and $E = kT$ the thermal electron kinetic energy. It corresponds to the distance from which the electrostatic potential is balanced by kinetic energy [121].
Measuring a directional signal via columnar recombination is possible when the recoil path exceeds the Onsager radius. In liquid argon, at T = 87 K, the Onsager radius is around 80 nm. This corresponds to a recoil energy around 30 keV, so compatible with direct dark matter searches inside the region of interest [122].

Columnar recombination is taken into account inside s_1 signals. In addition, the more recombination occurs, the less electron reaches the top of the TPC and thus, the smaller the s_2 signals. Hence, directionality can be measured by comparing the ratio between the recombination signal and the remaining ionisation events [121].

Columnar recombination was not observed on ReD results yet [123].

II.4.2.2 Detector Setup

ReD experiment is located at Laboratori Nazionali del Sud (LNS) in Catania, Italy. It was previously (before December 2019) in Naples. The general design of the experiment is the following. A monochromatic neutron beam passes through a dual phase argon TPC and the direction of scattered neutrons is detected by a time-of-flight spectrometer (cf. Figure II.13) [123]. We will see briefly the three main parts of the experimental setup (neutron production, liquid argon TPC and neutron spectrometer). The strict alignment of the three devices was a challenge of this setup.

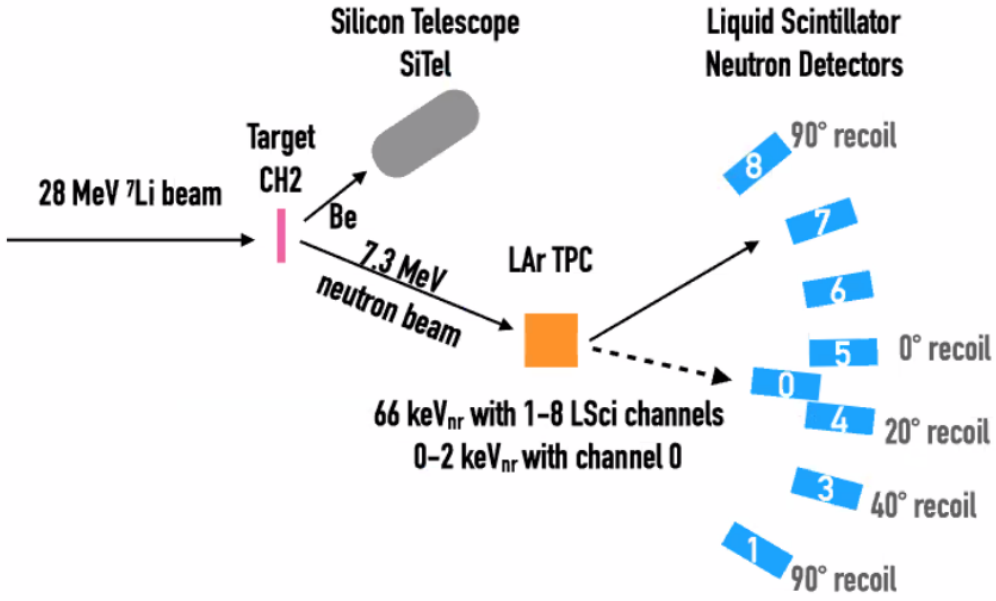

Figure II.13 – Scheme of the ReD experimental setup at LNS for a 28 MeV incoming beam [From ReD internal communication]. This incoming beam is generated by the Tandem accelerator. It is going through a scattering chamber where it interacts with a CH_2 target to produce a very collimated neutron beam. This neutron beam interacts with the liquid argon TPC and then, a neutron spectrometer composed of liquid scintillator neutron detectors is measuring the azimuth angle and time-of-flight of scattered neutrons.

In order to produce neutrons, ReD experiment is using the electrostatic Tandem accelerator at LNS. Tandem can be operated at different energies. For ReD, a mono-energetic ^{7}Li beam with energies from 18 to 34 MeV is launch in direction of the apparatus with an 80° angle.
The beam first reaches a stainless steel cylindrical scattering chamber: 55 cm high, 30 cm radius, 2 cm thickness. In the scattering chamber, the beam interacts with a CH_2 target which allows very collimated neutron production by inverse kinematics of $^7\mathrm{Li} + p \rightarrow {}^7\mathrm{Be} + n$. Neutron energies are included between 3 and 10 MeV depending on the beam incoming energy. A silicon detector is used to monitor the beam current. Two others are arranged to form a telescope to identify particles, respectively through δE - E measurements. Outside the scattering chamber, signals are amplified by three ORTEC-142 amplifiers, one for each silicon detector. They retrieve a fast and a slow signal. The fast one is sent to a CAEN data acquisition board and used for the trigger.

Indeed, Tandem cannot send pulsed beams, so a hardware trigger is needed [124] [125] [123].

The heart of the experiment is the dual-phase TPC with an active mass of 185 g. This TPC displays a different geometry than the one of DarkSide-50. This geometry is a smaller version of the one expected for DarkSide-20k. It is a $(5 \times 5 \times 6)$ cm^3 square-section volume [123]. Thick acrylic windows of 4.5 mm are displayed at the top and bottom and a reflecting acrylic structure is present on the four inner walls. As in DarkSide-50, a tetraphenyl butadiene wavelength shifter is present to convert the 128 nm emitted photons into ultraviolet visible light (around 420 nm). A field cage on the outside of the TPC with nine copper shaped rings at 0.5 cm from each other is present to establish an electric field inside it. In dual phase mode, the gas pocket created thanks to a bubbler has a 7 ± 1 mm thickness. A 3 mm hole constrains it. Two SiPMs arrays are disposed at the top and bottom of the TPC [124] [125] [123].

Finally, scattered neutrons are tagged thanks to a neutron spectrometer. It is composed of an array of nine liquid scintillator based detectors (LSci) coupled with ETL 9821 photo multipliers. Each LSci uses an organic scintillator mixture EJ-309 from Eljen Technology. They are disposed in a semi-circle structure centred on the centre of the TPC with an opening angle of 36.8°, so equal to the neutron scattering angle. Eight of them are disposed at 80 cm of the TPC. The remaining one, used for low recoil energy measurements, is outside the semi-circle, at 97 cm from the TPC and 3° angle from its axe. This structure allows measuring different scattering azimuth angles at fixed recoil energies and their time of flight with nanosecond precision and 30% quantum efficiency [124] [125].

II.4.2.3 Electronics and Data Acquisition

The ReD experiment uses 11.7 × 7.9 mm^2 rectangular NUV-HD SiPMs (cf. Section II.3.2) with a maximum photon detection efficiency at around 420 nm. They have 10 MΩ quenching resistance, 25 μm cell pitch and triple doping concentration. They are powered by CAEN SY 5527 power supply modules. They are divided between two different tiles, each one coupled to a different Front-End Board, one at the top and the other at the bottom of the TPC. In the bottom tile, SiPMs are separated into four groups of six, coupled in series and summed in parallel, on a 6 × 4 array. Each SiPM corresponds to a single channel. Each of the 24 channels is amplified by an independent low-noise transimpedance amplifier based on the LMH6629SD. The top tile has a single readout to improve xy resolution of s_2 and 4 channels [124] [125].

ReD data acquisition system is composed of three 14-bit CAEN V1730 Flash ADC boards, each one with 16 channels. However, only 42 are used, 28 for the SiPMs, 9 for the LSci and 5 for the Si-detectors. All subsystems are remotely monitored by a Slow Control system, which allows graphical display and storage of all the parameters of the experiment. The data acquisition rate is limited to 40 MB/s, the limit of the hard disk of the data acquisition system. The associated software is an adapted version of the PADME experiment code.
The acquisition window is changing depending on the use of the TPC as a single phase or dual phase. For single-phase, the window is 20 μs long with a 6 μs pre-trigger; for a

dual phase, it is around 100 μs with 10 μs pre-trigger. The trigger used for directionality measurements is a triple coincidence between the Si-telescope, the TPC and the LSci, which should correspond to a nuclear recoil event [124] [125].

II.4.2.4 Calibration

TPC single electron response. Single-electron response in ReD is studied the same way as in DarkSide-50 (cf. Section II.2) with a pulsed diode laser through optical fibres. The laser has a wavelength of 403 nm and pulses 50 ps long. Charge and amplitude spectra are produced for each channel of each SiPM. In these spectra, each peak, corresponding to 1, 2, 3 ..., N number of photo-electrons are fitted by a Gaussian distribution. The fit allows to retrieve the mean value for each peak and to determine a calibration equation linking in a linear way the number of photo-electrons and the mean charge or mean amplitude depending on studied spectra. The variance is determined the same way. This procedure is described in detail in Chapter IV.

S1 light yield and resolution. Scintillation signal characterization is performed with an ^{241}Am source. This isotope emits 59.5 keV γ-rays by α decay. A fit of this γ peak in the TPC allows retrieving a light yield that is estimated at 8.3858 photo-electron per keV when the correlated noise from optical readouts is accounted for. Associated resolution (standard deviation over the mean value of the peak) is estimated at around 6.6%. The use of the same procedure with ^{83m}Kr, as for DarkSide-50, allowed to confirm the value of the light yield [124] [125].

Silicon detectors. Energy calibration of the three silicon detectors was performed using the beam with two different targets. The first target was ^{197}Au which allows elastic scattering with ^{7}Li beam. ^{197}Au was exposed to different beam energies. The second target was a triple γ-source with ^{239}Pu, ^{244}Cm and ^{241}Am which displays emission lines between 5.1 and 5.8 MeV. Measurements were performed at these energies. In the end, both sources allowed plotting a linear calibration curve between the measured signal amplitude and the energy [124].

Chapter III

DarkSide-50 Lowmass Analysis

> Essentially, all models are wrong, but some are useful.
>
> George Box and Norman Draper (1987)

DarkSide-50 was designed to operate in an WIMP mass range from 100 GeV to several TeV. At recoil energies of the order of the keV, the scintillation component, which has a low efficiency (g_1=0.16), is too faint to be measurable anymore. However, the ionisation component has a 100% extraction efficiency and a high ionisation yield (g_2=22). Hence, in what is called the low mass regime, below 10 GeV/c^2, it is still possible to search for dark matter signals by dropping the scintillation component and using only the ionisation one. Nevertheless, we do not have anymore a background free analysis as we loose the pulse shape discrimination and the s_2/s_1 ratio. It is however possible to fiducialize in XY, apply multiple scatter event rejection and model the background.

Low-mass limits for DarkSide-50 were already derived in 2018 [101]. However, since then an effort was made to refine retrieved limits and test new dark matter candidates. Refinements are possible mainly through:

- Improving the calibration of nuclear recoil and electronic recoil scales, *i.e.* translation of respectively nuclear recoil and electronic recoil energies into photo-electrons,
- Refining the background model and particularly ^{39}Ar and ^{85}Kr contributions,
- Extending the data set (from 16660 kg day in 2018 to 24786.88 kg day).

In this chapter, we will first go through the low-mass analysis framework, its structure and how it allows retrieving limits for DarkSide-50 (Section III.1). Section III.2 will detail the response model. Then, we will go through the background model in Section III.3. Data selection will be presented in Section III.4.
We will then display the new limits for WIMPs nuclear recoils without (Section III.6) and with Migdal effect (Section III.7) that these improvements have allowed. We will continue this chapter by detailing inferred limits for ALPs (Section III.8) and sterile neutrinos (Section III.9), two dark matter candidate models that we have implemented in the framework. Finally, we will go through an analysis of the annual modulation hypothesis using DarkSide-50 low-mass data.

III.1 Low-mass Analysis Framework

The low-mass analysis framework consists of a python framework designed to study the sensitivity of DarkSide-50 using a profile likelihood approach.

The low-mass framework is composed of different classes and macros which follows the logic of Figure III.1. This framework was first developed for WIMPs searches and was extended for extracting limits for other models such as ALPs and sterile neutrinos.

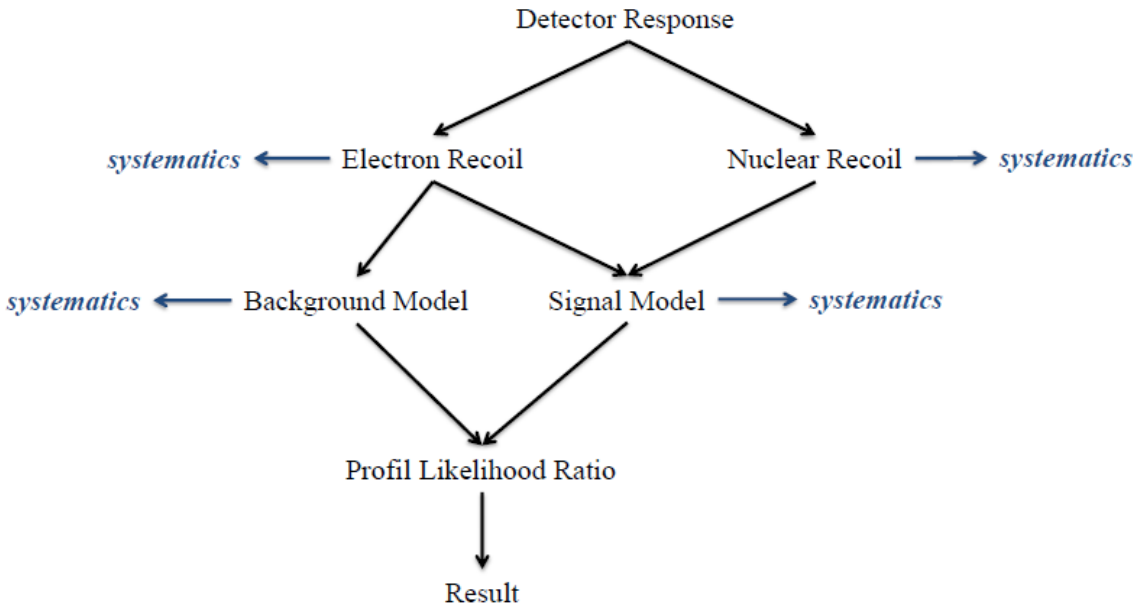

Figure III.1 – Logical structure of the low-mass framework

The first step is the computation of the detector LAr ionization response to both nuclear and electronic recoils (cf. Section III.2) from which ionisation yields are computed with their associated systematics.

Then, knowing the response we compute the background model (Section III.3) and its associated systematics. In parallel, we compute theoretical models for each dark matter candidate under study (*i.e.* WIMPs nuclear recoil with or without Migdal effect, ALPs and sterile neutrinos here) and their associated systematics. Quantities of interest are their cross-section and flux that allow deriving their rate. Mathematical expressions of these quantities are developed in the following Sections - respectively III.6 for WIMPs nuclear recoil, III.7 for WIMPs nuclear recoil with Migdal effect, III.8 for ALPs and III.9 for sterile neutrinos. Their respective signal spectra are computed by convolving the rate with the detector response. Several corrections mostly due to the electron-lifetime and geometry of the detector are applied.

The last step consists of computing limits by comparing the data to the signal plus background spectra using the profile likelihood ratio approach. This likelihood is built using the RooFit package including multiple systematics. These systematics impact both the signal and background spectral shape and normalization. They are listed in Table III.1

along with correlations across components.

Table III.1 – Systematics included in the analysis.

Name	Type	Source	Components
exposure	Amplitude	1.5% uncertainty on the active mass	WIMP, ^{39}Ar, ^{85}Kr, PMT, Cryo
qy_nr	Shape	uncertainty on the Q_y^{NR} energy scale	WIMP
qy_er	Shape	uncertainty on the Q_y^{ER} energy scale	^{39}Ar, ^{85}Kr, PMT, Cryo
norm_39ar	Amplitude	14% (high energy background fit)	^{39}Ar
norm_85kr	Amplitude	8.2% (^{85m}Rb fast-coincidence analysis)	^{85}Kr
norm_pmt	Amplitude	12.6 (7.7% from material screening, 10% from source location)	PMT
norm_cryo	Amplitude	6.6% (material screening)	Cryo
39ar_shape	Shape	1% uncertainty on the Q-value	^{39}Ar
85kr_shape	Shape	0.4% uncertainty on the Q-value	^{85}Kr
39ar_screen	Shape	up to 25% uncertainty on the screening function (<200 eV)	^{39}Ar
85kr_screen	Shape	up to 25% uncertainty on the screening function (<200 eV)	^{85}Kr

Background spectra contain backgrounds from cryostat, photo-multipliers, ^{39}Ar, and ^{85}Kr. We loop over the mass range of the chosen candidate which should be contained in the mass range for which spectra were computed.

III.2 Response Model

To perform low mass analyses, the calibration of the LAr ionization response to both electronic and nuclear recoils in the keV region is needed. Unlike xenon, very few studies have been performed for argon. Hence, a complete procedure was developed inside DarkSide-50 at an electric field of 200 V/cm [96].

In this section, we will describe the detector response model (Section III.2.1) and the computation of electronic recoil (Section III.2.2) and nuclear recoil (III.2.3) ionisation yields.
The response model is based on measurements performed using intrinsic β-decay sources, namely ^{37}Ar and ^{39}Ar as well as neutron sources outside the TPC (^{241}Am-^{13}C and ^{241}Am-^{11}Be) and external datasets to better constrain nuclear recoil ionization response. The precise procedure is presented in [96]. We will summarize here only the main steps as well as the validation of the detector response model using ^{37}Ar, to which I contributed.

III.2.1 Detector Response

The detector response model takes into account several distortions due to instrumental effects. Its resolution is affected by 1) the gas phase electro-luminescence and PMT response, 2) electrons that can be captured during their drift introducing a distortion on the drift distance due to the electron lifetime of a few percents with respect to the maximal drift time (376 μs) and, 3) the dependency of s_2 response on the XY radial position [96]. To account for all these effects and improve the measurement of the ionization response, a full Monte-Carlo simulation is implemented.

To validate the detector response model, we use samples of ^{37}Ar, and more particularly the subtraction between the first 100 days and the latest 500 days of the UAr campaign,

where ^{37}Ar have almost entirely decayed, both normalized by their lifetime [96]. This distribution shows both K and L1 shells peaks (Figure III.3). With the detector response model, we retrieve the precise position of both peaks (hereby called P1 and P2, respectively) in terms of the number of electrons (Ne_1 and Ne_2, respectively) and then calculate the branching ratio between both modes.

For that, we create a Monte-Carlo simulation with the mean number of electron as free parameter that we apply to the ^{37}Ar data spectra. For each simulation, we apply a χ^2 to perform the minimization. We treat both peaks independently. P1 is fitted between 6 and 20 electrons and P2 between 34 and 60 electrons. We loop on these ranges, first with a step between two numbers of electrons of 1, and then of 0.1, in the area of interest highlighted by the first step.

To recreate the data at a given number of electrons inside the Monte-Carlo simulation we generate a random radial position uniformly distributed in the TPC and for each one of them:

- extract the channel associated to the radial position,
- reject events outside the TPC core,
- add intrinsic electronic recoil fluctuations,
- apply radial efficiency,
- apply single-electron response smearing,
- correct by the channel-by-channel efficiency in the data

The applied χ^2 is such as Equation III.1:

$$\chi^2 = \sum_i \frac{(O_i - E_i)^2}{\sigma_i^2} \tag{III.1}$$

with i the bin in number of electrons, O_i values from the data, E_i values from the Monte-Carlo simulation and σ_i^2 the error on the data squared times the error on the Monte-Carlo simulation squared.

Following this procedure, we get the χ^2 maps for P1 and P2 (Figure III.2) giving the best fit:

$$Ne_1 = 11.7 \pm 0.1 \tag{III.2}$$

$$Ne_2 = 48.1 \pm 0.2 \tag{III.3}$$

The Monte-Carlo fits for these two best-fits are shown in Figure III.3. This is a preliminary study meant to set up the tools, and we hence observe a very small deviation on the final result compared to the published study [96].

From theses measurements of both ^{37}Ar peaks, we compute the branching ratio such as Equation III.4. The inferred value is in good agreement with the theoretical value of $\sim$ 0.11. We consider here as a branching ratio the fraction of particles decaying into a mode in regards to those decaying in the other mode.

$$BR = BR_{Ne_1}/BR_{Ne_2} = 0.10 \pm 0.01 \tag{III.4}$$

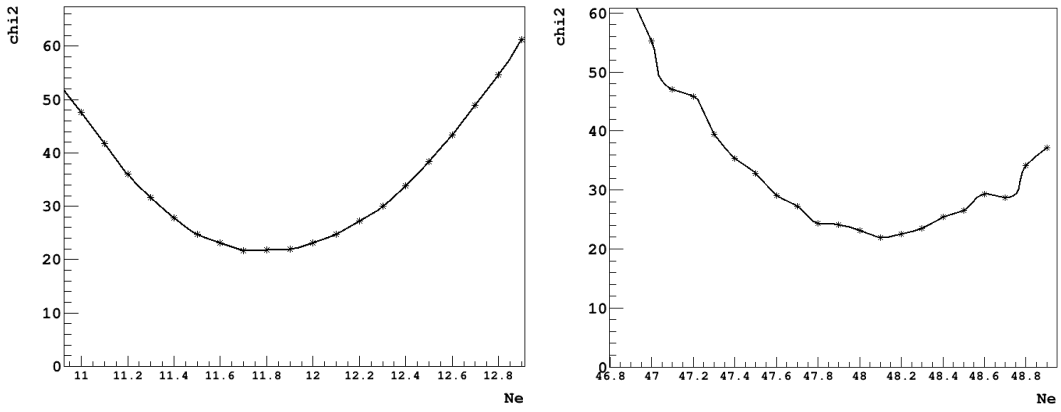

(a) (b)

Figure III.2 – χ^2 maps for the P1 on the left and for the P2 on the right.

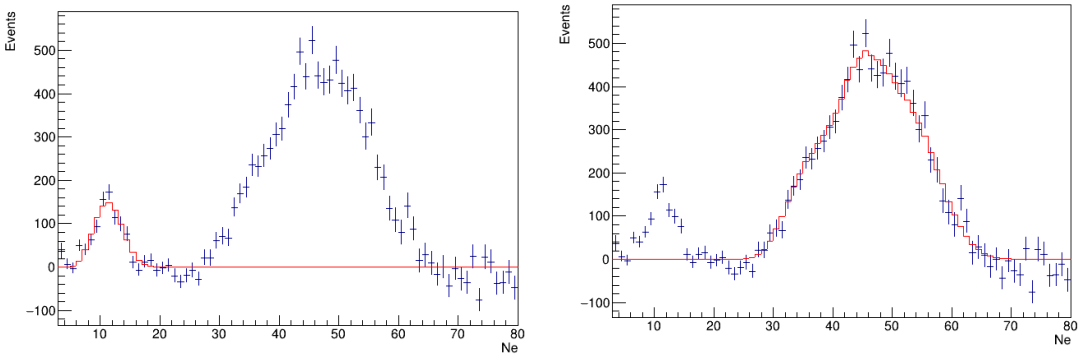

(a) P1 fit with $Ne_1 = 11.7$ (b) P2 fit with $Ne_2 = 48.1$

Figure III.3 – ^{37}Ar data spectra (blue) with fits of the Monte-Carlo simulation on the first and the second peak (P1 and P2) with the number of electrons for each one of them corresponding to the best fits found with χ^2 maps

with the error calculated taking into account both statistical and bin error.
This branching ratio is compatible with what can be already found in literature [126], [127], [128]. In addition, for the K shell (P2), we see a bump that account for the none uniformity of the radial detector response. This bump is perfectly fitted by the detector response model. All of these tend to validate this model.

III.2.2 Electronic Recoil Ionization Yield

In Section III.2.1, we extracted the number of electrons of both ^{37}Ar K and L1 shell peaks. We will consider here the final values from [96] of 12.0±0.1 electrons for the L1 shell and 48.2±0.2 electrons for the K shell. To compute the ionisation yield from these two measurements, we estimate the number of ionisation electrons from the extracted number by subtracting the contribution from the primaries, which are the emitted cascades from atomic relaxation spectra of UV photons, X-rays and Auger electrons [96]. The evaluation of theses emitted cascades is performed using the RELAX software [129] (EADL2017 library of atomic transition data) [130] and the BetaShape code [131] [96]. It gives on average 3.9 and 2.8 primaries for the K and L1 shell, respectively. Details of the

calculation are available in [96].

For the L1 shell, subtracting the number of primaries from the extracted number of electrons gives 8.2±1.3 ionization electrons at 179 eV, which is the energy of the Auger electron which interacts instead of the L1 shell [96]. For the K shell however, the event topology being more complex, there is no accurate model to estimate the overall recombination effect. Consequently, we exclude the K shell for the computation of electronic recoil ionization yields [96].

In addition to the electronic recoil ionization yield from the L1 shell, and to compute more electronic recoil ionization yields, we use atmospheric argon runs (enriched in ^{39}Ar) on which we apply cuts on the drift time (tdrift $\in$ [76,300] μs) and on the radius (r $<$ 2 cm). For that, above 2 keV where both s_1 and s_2 are reconstructed, we build the rotated energy which corresponds to the reconstructed recoil energy deposited in the detector, as defined by:

$$E_{rot} = w\left(\frac{s_1}{g_1} + \frac{s_2}{g_2}\right) \tag{III.5}$$

w = 19.5 eV is the work function, $g_1 = 0.16 \pm 0.01$ is the s_1 collection efficiency and $g_2 = 23 \pm 1$ photo-electrons per electron, is the s_2 amplification factor.

The electronic recoil ionization yield, Q_y^{ER} is defined per unit of electronic recoil energy E_{er} as [96]:

$$Q_y^{ER} = \frac{(1-r)N_i}{E_{er}} \tag{III.6}$$

with N_i the number of produced electron-ion pairs and r the electron recombination probability. This last is predicted using the Thomas-Imel box model [132]. It allows to parametrize Equation III.6 with $\rho = N_i/E_{er}$ and γ a free parameter describing electron-ion pairs recombination as:

$$Q_y^{ER} = \frac{1}{\gamma}\frac{\ln\left(1+\gamma\rho E_{er}\right)}{E_{er}} \tag{III.7}$$

The ^{37}Ar calibration line (L1 shell) and ^{39}Ar data are fitted using Equation III.7 up to 3 keV$_{ee}$. The model is then extended thanks to Doke-Birks parametrization [133] which is in agreement with data from ARIS experiment above around 40 keV$_{ee}$ [110]. The Thomas-Imel model works for short tracks inside the detector. However, above 3 keV, the electronic recoil tracks are too long for the Thomas-Imel model. To recover the incompatibilities with ^{39}Ar data a custom term, with two free parameters p_0 and p_1, was added (Equation III.8). Fitting this new expression allows having a coherent yield for the whole energy spectra (Figure III.4).

$$Q_y^{ER} = \left(\frac{1}{\gamma} + p_0(E_{er}/keV_{ee})^{p_1}\right)\frac{\ln\left(1+\gamma\rho E_{er}\right)}{E_{er}} \tag{III.8}$$

III.2.3 Nuclear Recoil Ionization Yield

The nuclear recoil ionization yield is formalized similarly to the one for electronic recoils with the recombination probability r still defined by the Thomas-Imel box model

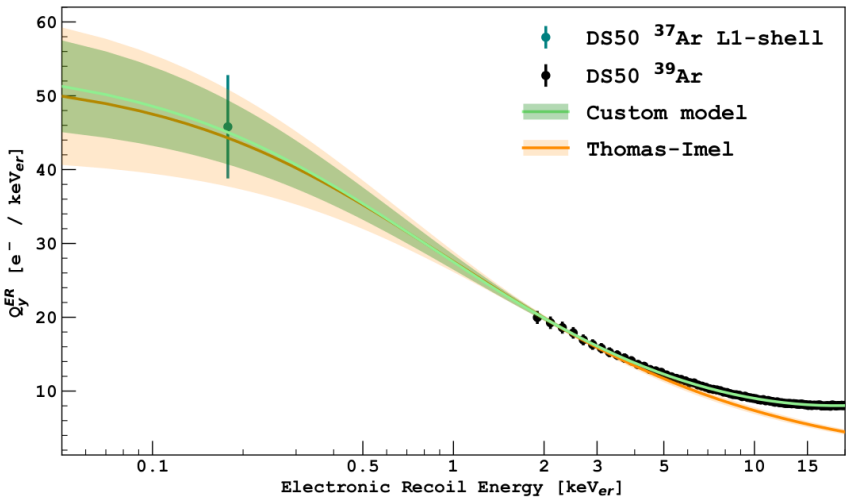

Figure III.4 – Fit of the electronic recoil ionization yield with Thomas-Imel box model up to 3 keV$_{ee}$ and the additional term up to 20 keV$_{ee}$. Fitted data are from ^{39}Ar (black) and ^{37}Ar (teal). The bands on the model are accounting for the 1σ uncertainties [96]

(Equation III.9) [132] [96]. There are always short tracks for nuclear recoils.

$$Q_y^{NR} = \frac{(1-r)N_i}{E_{nr}} \tag{III.9}$$

The excitation-to-ionization ratio is supposed constant and N_i can consequently be expressed as [134]:

$$N_i = \beta \frac{\epsilon s_e(\epsilon)}{s_n(\epsilon) + s_e(\epsilon)} \tag{III.10}$$

with the normalization constant β, the reduced energy $\epsilon = \frac{a}{2e^2Z^2} E_{nr}/\text{keV} \sim 0.0135 E_{nr}/\text{keV}$ with a the Thomas-Fermi screening length, s_n the nuclear stopping power and s_e the electronic stopping power. In other words, s_e is the rate at which electrons are excited in inelastic collision and s_n the rate of energy transferred to recoiling nuclei by elastic collisions. Both s_n and s_e can be further parametrized thanks to [135] and [134], respectively.

This model is fitted on calibration datasets, ^{241}Am-^{13}C and ^{241}Am-^{11}Be neutron sources and from external datasets. First, ^{241}Am decaying α induces via spallation on ^{13}C a neutron without γ-emission. The activity of ^{241}Am is around 3.6 MBq inducing pile-up X-rays and a high rate of low energy γ's that can contaminate the active volumne. Actually, those at 59.5 keV, with a branching ratio of 35.9, are absorbed by the shield and the liquid argon buffer. However, those above 99 keV, with a lower branching ratio of 10^{-9} are not. Consequently, they are simulated using Monte-Carlo simulations, and to reduce their contamination, only signals of the four central PMTs the farther away from the source are taken into account. This reduces down to 5.2% the contamination from γ's according to Monte-Carlo simulation. In the end, looking at the number of reconstructed electrons (Figure III.5), we can remove the contamination coming from ^{241}Am and UAr to find the excess of events from neutron scattering. No loss of efficiency is observed as it does not rely on s_1 coincidence [96].

This is not the case for the ^{241}Am-^{11}Be source. This time the ^{241}Am α produces a neutron via spallation on ^{11}Be, with the emission of a γ. Consequently, nuclear recoil events are

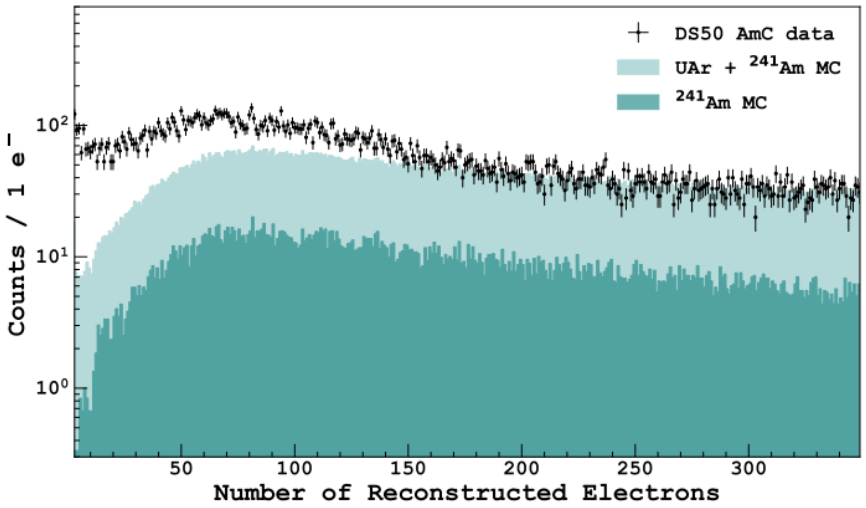

Figure III.5 – Spectrum of events from the ^{241}Am-^{13}C source (black) and contamination from intrinsic events in the TPC and γ's from ^{241}Am [96].

selected by triple coincidence: a prompt γ at 4.4 MeV in the liquid scintillation veto, an s_1 event in the TPC and an α (1.47 MeV) and γ (4.4 MeV) capture at the TPC exit in the liquid scintillation veto. The necessary coincidence with the s_1 implies that we loose sensitivity at low energy, when s_1 signals are not longer measurable. The electronic recoil background is assessed using a control region where no nuclear recoil events are expected. The spectra is then normalized and retrieved from the ^{241}Am-^{11}Be one (Figure III.5) to retrieve events from neutron scattering [96].

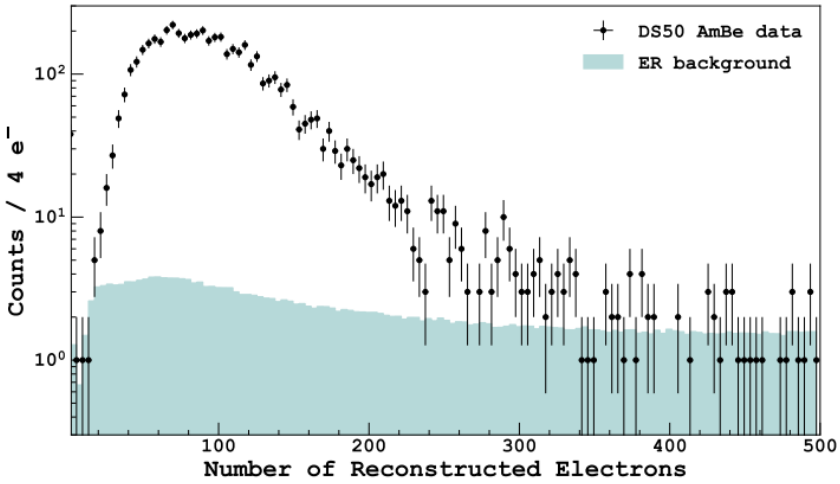

Figure III.6 – Spectrum of events from the ^{241}Am-^{11}Be source selected in triple coincidence (black) along with normalized electronic recoil background [96].

External datasets are also used. Four calibration lines are measured with SCENE apparatus [112]. They are re-normalized to DarkSide-50 response by the g_2 ratio between both experiments. ARIS experiment only characterized the scintillation response for eight different energies [110]. Consequently, for ARIS data the scintillation response is normalized

to DarkSide-50 by the ratio between field-off s_1 yields and s_2 by the nuclear recoil s_2/s_1 ratio within the ^{241}Am-^{11}Be dataset (MC simulations). Joshi et al. [136] ionization yield is only compared to the final fit due to a correction posterior to the publication [96].

A simultaneous fit of ^{241}Am-^{13}C, ^{241}Am-^{11}Be, ARIS and SCENE is performed giving the combined fit shown on Figure III.7. The ionization yield by Joshi et al. [136] is compatible with it. The response is measured down to 3 ionization electrons (around 500 eV$_{nr}$) which is the lowest performed for LAr. Comparisons between the model at the best fit and the data for AmC and AmBe are showed in Figure III.8.

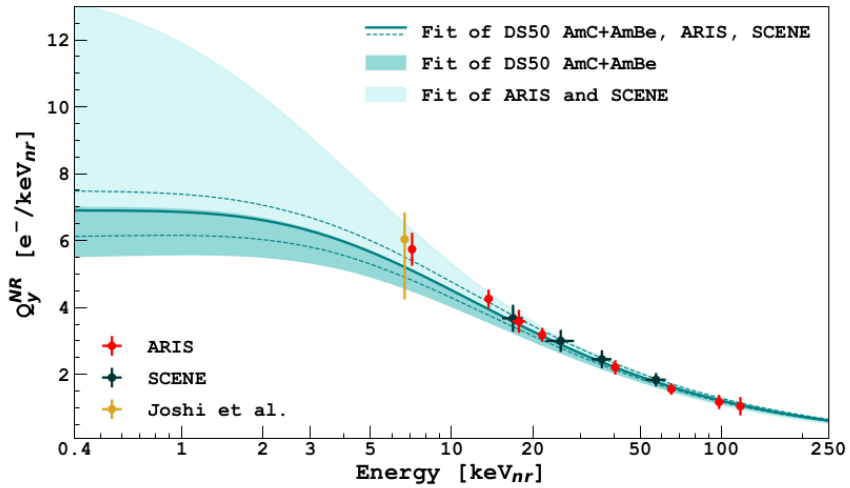

Figure III.7 – The fit of the nuclear recoil ionization yield based on combined data from calibration (AmC and AmBe) and external datasets: SCENE [112], ARIS [110] and [136]. Bands on the model are accounting for the 1σ uncertainties [96]

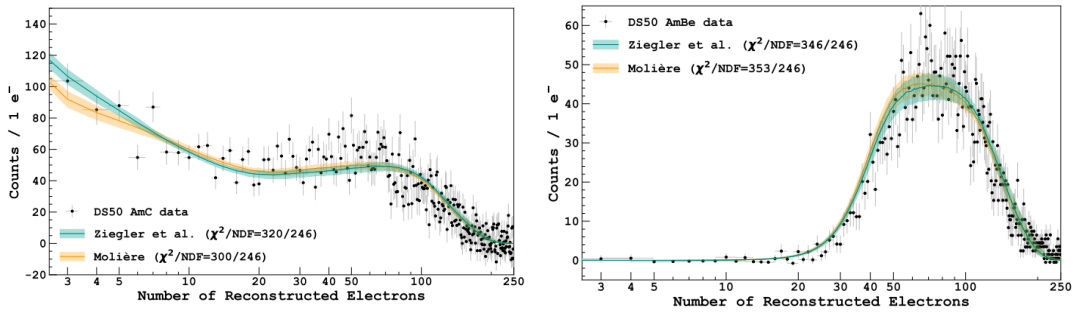

(a) (b)

Figure III.8 – Best fit on (a) AmC and (b) AmBe data using two different screening functions (Ziegler et al. and Molière) [96]. The Ziegler screening function was used in the final analysis as it is the most conservative one: it yields the lowest ionization yield in the WIMP region of interest (cf. [96]). The bands corresponds to the 1σ uncertainty.

III.3 Background Model

Another improvement that was made with respect to previous low-mass analysis [101] is a more accurate background model. The background model describes spectra and expected rates induced by natural radioactivity originating in the LAr bulk, dominated by intrinsic ^{39}Ar and ^{85}Kr contamination, and in PMTs and cryostat, the two most relevant TPC components in terms of contamination. ^{39}Ar is a β-emitter with a q-value of 565 keV while ^{85}Kr is a β-emitter with a q-value of 685 keV.

We will present in this section the activities of ^{39}Ar and ^{85}Kr including an independent measurement of the ^{85}Kr activity to which I participated (Section III.3.1). Then we will report new spectral shapes of ^{39}Ar and ^{85}Kr for which I contributed to the conversion to number of electrons (Section III.3.2). Finally, we will present the PMTs and cryostat contributions to the background model in Section III.3.3.

III.3.1 Activities of ^{39}Ar and ^{85}Kr

^{39}Ar specific activity was measured at 0.73 ± 0.10 mBq/kg, by fitting the s_1 spectrum above 50 photo-electrons [98]. From the same fit we obtained 2.05 ± 0.13 mBq/kg for the ^{85}Kr specific activity, which is however relative to the first 70 days only of the UAr campaign. An alternative method for estimating the ^{85}Kr contamination is based on the identification of the short β+γ delayed coincidence when ^{85}Kr β-decays to ^{85m}Rb (0.43% BR, endpoint 173 keV), which subsequently transitions to the ground state via emission of a 514 keV γ-ray, with half-life of 1.015 μs. The signature consists of two s_1 pulses delayed by up to a few μs. Full simulations of the detector and the reconstruction chain have been performed to estimate the probability for the γ-ray to escape the active volume without interacting and the acceptance of the selection criteria. The resulting efficiency, 65.9$\pm$3.5%, is lower than the one reported in [98] due to the simulation of 514 keV γ at the center of the TPC instead of uniformly distributed. The new result, 1.85$\pm$0.15 mBq/kg, is evaluated on the same dataset used for this report, and differs from the published one because of the fixed bug and because of the ^{85}Kr decay during the data taking.

This result is cross checked with an independent approach, by fitting the ^{85}Kr decay time (10.76 yr half-life) in the low-energy region ($50 < \mathrm{Ne} < 200$), that we will describe here.

For this approach, we take into account other radioactive elements present in the detector: ^{60}Co and ^{37}Ar. For each one of them, as their decay constants are known, it is possible to compute their respective activity at time zero as well as the mean activity by fitting the data over time. Inside the dataset we select the event distribution corresponding to the event selection (in terms of numbers of electrons and drift time). Then, we perform a first estimation of ^{85}Kr activity at t = 0 by fitting the time series by an addition of decay laws for each one of the radioactive elements present in the detector: ^{85}Kr, ^{60}Co and ^{37}Ar (Figure III.9).

For retrieving the activity at the time of each run, we correct the activity at t = 0 as expressed in Equation III.11.

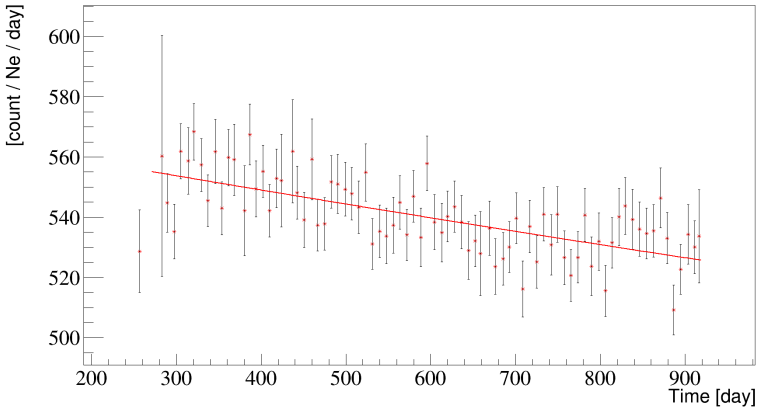

Figure III.9 – Decay laws fit on time series

$$A_{Kr_{corr}} = \frac{A_{Kr}}{M\epsilon_{tdrift}\epsilon_{iscore}\epsilon_{energy}} \times \frac{\tau}{L_T}\sum_{run}(e^{-t_{min}/\tau} - e^{-t_{max}/\tau}) \tag{III.11}$$

with $M = 46.4$ kg the detector mass, $\epsilon_{tdrift} = \frac{376-tdrift}{376}$ the correction of the tdrift selection on the maximum tdrift 376 μs, $\epsilon_{iscore} = 0.415$ the core fraction of the detector, ϵ_{energy} the normalisation factor on the krypton energy, L_T the lifetime of the run, $\tau = t_{1/2}/ln(2) = 5,667.814$ day the decay constant, t_{min} = day[run] and t_{max} = day[run]+ L_T.
From the data selection, we find a mean activity for ^{85}Kr of 1.75 ± 0.23 mBq/kg. This value is in agreement with the one from the delayed coincidence.
In the end, we keep as a final result the weighted mean between the different ^{85}Kr activity measurements.

III.3.2 Spectral shapes of ^{39}Ar and ^{85}Kr

A major improvement in this analysis with respect to the one published in 2018 lies in the new spectral shapes of ^{39}Ar and ^{85}Kr, accounting for the contribution of additional atomic orbitals thanks to an extension of atomic exchange effect to forbidden unique transitions which impact the spectra below 100 keV (Figure III.10). The new corrections were validated on measured ^{63}Ni and ^{241}Pu spectra with a 200 eV threshold [137].

To assess the number of electrons detected due to both of these contaminants, we convert these energy spectra into the number of electrons in DarkSide using the response model.

Values from the energy spectra are given in keV with a value every 5 eV up to 200 eV and then 0.1 keV up to 560 keV. Both energy spectra are shown in Figure III.11. From these spectra, we first compute the probability density function. For that, we extrapolate each point of the energy spectra on the whole energy range with a 2 eV step. We then normalize this distribution by its sum. This probability density function is then used to make a random distribution of energies with 10^7 entries following this distribution. We discard events outside the core of the TPC. Hence, the number of events is reduced by the fiducial mass. We then convert the energy into a number of electrons following the energy scale of the detector. We apply fluctuations and corrections on the electron lifetime, radius and channel inside the TPC. We are also taking into account the effect of the PMT response. By making an histogram of these energies translated in numbers of

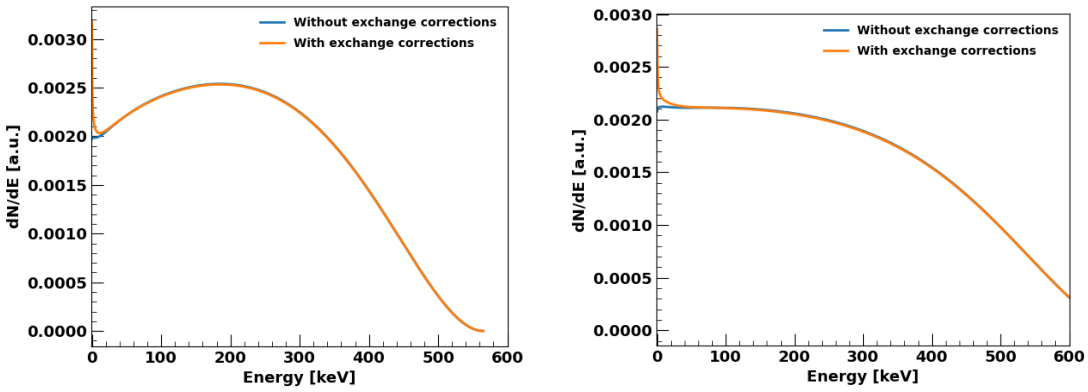

Figure III.10 – ^{39}Ar (left) and ^{85}Kr (right) differential number of events depending on the energy before and after the addition of the atomic exchange effect to forbidden unique transitions.

electrons we retrieve the expected spectra.

Concerning the systematic uncertainties, from the upper and lower bounds for both ^{39}Ar and ^{85}Kr we retrieve their shape in numbers of electrons by applying the same procedure. However, due to the statistical treatment and the very close proximity of the bounds performing this procedure once is not enough: we retrieve entangled shapes. Consequently, to increase the statistics, we perform the procedure a hundred times for the main value and its bounds and then retrieved for each one of them their mean values. This way, the algorithm had time to converge and we retrieve correct shapes (cf. Figure III.12).

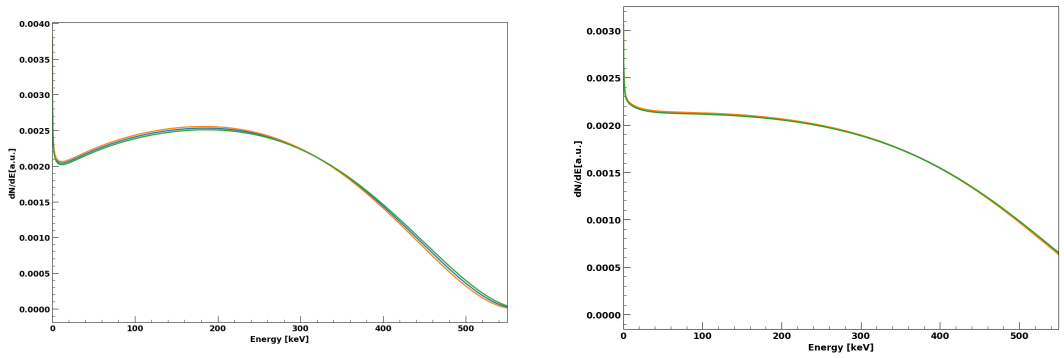

Figure III.11 – ^{39}Ar (left) and ^{85}Kr (right) differential number of events depending on the energy from Xavier Mougeot. The blue line is the main value, orange and green lines are upper and lower bounds, respectively.

Finally, on the spectra below 200 eV we add the 25% exchange correction which is a correction computed on β-decay spectra accounting for effects of exchanges of virtual photons or emission of undetected final state photons [138]. Computation with lower and upper bounds display a 40% band of uncertainty on the ^{39}Ar and ^{85}Kr values. If we have a 25% exchange correction of this 40% band of uncertainty, then we have a 10% systematic below 200 eV. Figure III.13 shows a zoom on the main value with this 10% uncertainty added below 200 eV.

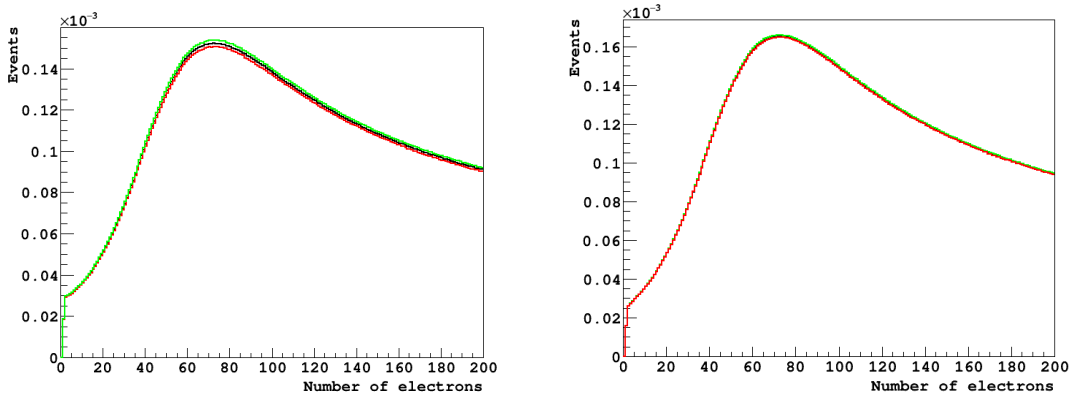

Figure III.12 – ^{39}Ar (left) and ^{85}Kr (right) spectra in number of events depending on the number of electrons. The black line is the main value, green and red lines are upper and lower bounds, respectively.

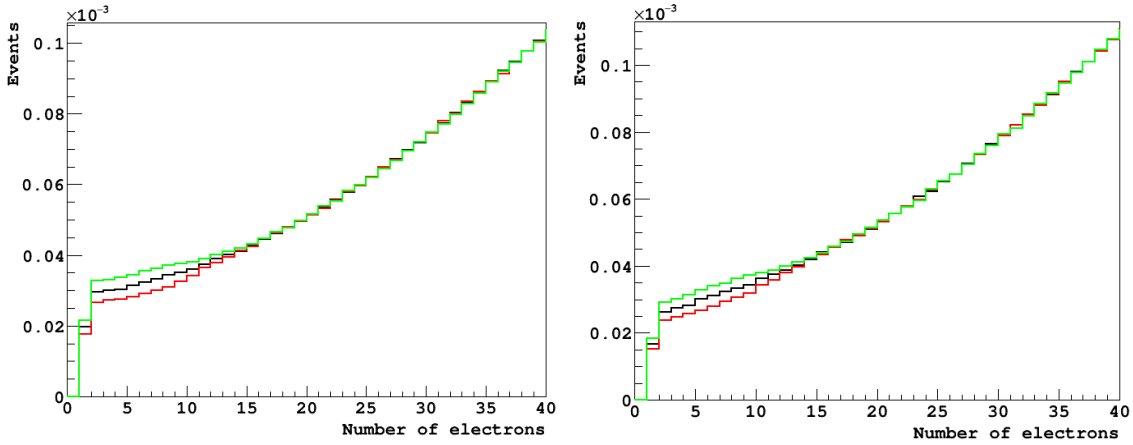

Figure III.13 – ^{39}Ar (left) and ^{85}Kr (right) spectra in number of events depending on the number of electrons zoomed on the 0 - 40 electron range. The black line is the main value, green and red lines are a 10% systematic upper and lower bound, respectively.

The estimation of further uncertainties was then performed inside the collaboration. In addition to the exchange correction mentioned above, uncertainties arise from errors on the β Q-value (1% for ^{39}Ar and 0.4% for ^{85}Kr), on the extrapolation of the material screening errors and on g_2 errors coming from calibration uncertainties. The exchange correction is hence negligible with respect to the other sources. Previous decay spectra with these additional errors are shown in Figure III.14 depending on the number of electrons and on energy (keV$_{ee}$).

III.3.3 PMTs and cryostat contributions

Additional sources of background due to radioactivity from the PMTs and from the cryostat are evaluated. Their contributing activities are assumed from the material assays measurements. The dominant components are ^{60}Co, ^{40}K and ^{54}Mn isotopes and by ^{238}U, ^{235}U and ^{232}Th decay-chains. The associated energy spectra are simulated by generating

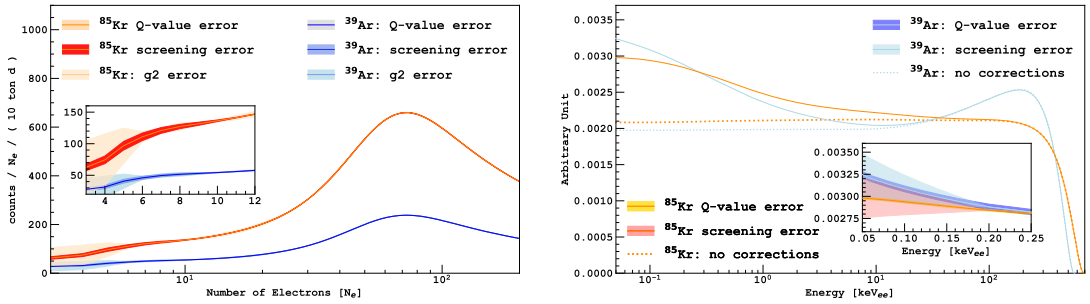

Figure III.14 – ^{39}Ar and ^{85}Kr spectra depending on (left) the number of electrons and (right) the energy with their associated uncertainties.

isotopes in the cryostat and in PMTs. For the latter, applying the prescription of those who participated in the material screening campaign, we assume two different contaminant locations, partitioned as: the stems in the back of the PMT, and kovar and ceramic in the PMT body. The different locations do not impact the spectral shapes, but have a large impact on the associated event rate. As an example, 100% of the activity in the stems result in about half the event rate compared to the 100% assumption in the PMT body. Thus, in addition to the uncertainties of material screening measurements, we must consider for the PMT contribution an additional error associated with the uncertainty of the contamination partitioning between stems and body. Very high-statistics samples of cryostat and PMT events are generated with G4DS[1] for each isotope and fully tracked through the detector geometry. The amount of deposited energy and the location of each interaction in the active LAr volume are then recorded. Multiple scattering events are identified by looking at energy deposits farther than at least 2 mm along the vertical axis, and then discarded. As for the bulk case, energy spectra are converted in number of electrons by applying the electronic recoil response model. We neglect the spill-in/spill-out effect for the PMT and cryostat background.

Table III.2 reports the input activities, the probabilities to induce a signal and the induced event rate in the fiducial volume and in the energy range of interest (4 to 200 electrons). Figure III.15 reports the different background model components and the fit of the data with this model.

The good quality of the background model is demonstrated by Figure III.16. It indeed shows that the data pulls from the fit in the number of electrons range studied (4-170 electrons) are normally distributed. In addition, even before the fit, the residual value is centered near zero.

[1]G4DS is the version of the Geant4 software [139] for DarkSide experiment.

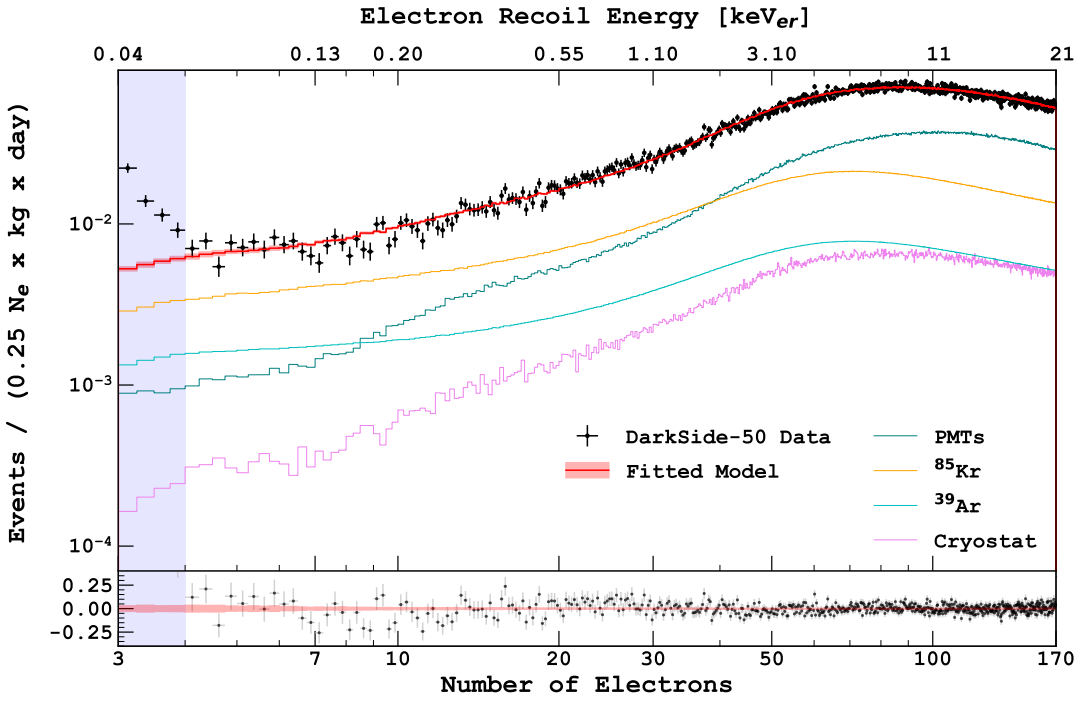

Figure III.15 – Fit of the selected data sample with the background model only. The pulls quoted in the plot are expressed in terms of $(v_i - v_i^0)/\sigma_i$, where v_i is the fitted value, and v_i^0 and σ_i are the input value and associated systematics, respectively.

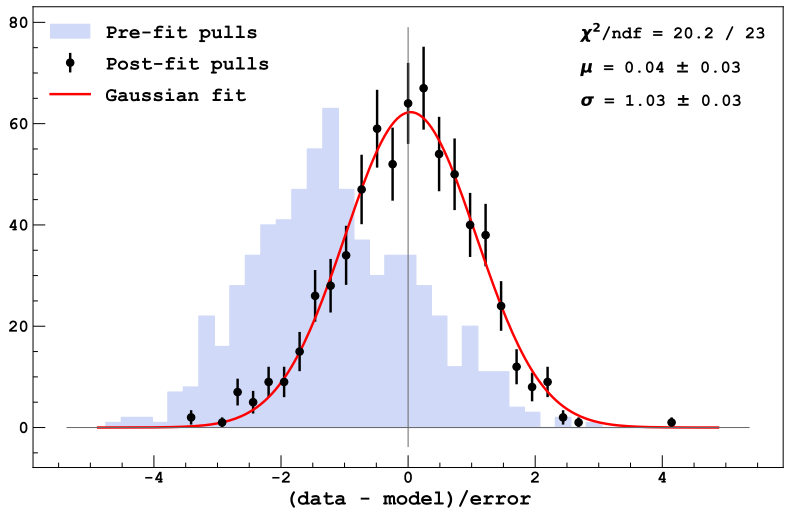

Figure III.16 – Pulls from the background-only fit (black points) are normally distributed, as highlighted by the Gaussian fit (red line). The shaded blue histogram corresponds to pre-fit distribution.

Table III.2 – Background activities from the bulk, PMTs, and cryostat; associated probability to make a single scatter in ROI and fiducial volume; and final event rate in ROI and fiducial volume with error. The event rates of decay chains are provided for full chains, while the activity measurements are given for progenitors only. Accounting for the uncertainty on the PMT contamination distribution between stems and body, an additional 10% systematic error is included in the all PMT errors. [137].

Location and source		Activity [Bq]	Single-scatter events in the RoI	
			Event rate [Hz]	Total rate [Hz]
LAr	^{39}Ar	0.034 ±0.005	$(8.4 \pm 1.2) \times 10^{-4}$	$(8.4 \pm 1.2) \times 10^{-4}$
	^{85}Kr	0.084 ±0.004	$(2.0 \pm 0.1) \times 10^{-3}$	$(2.0 \pm 0.1) \times 10^{-3}$
PMT Stems	^{232}Th	0.16 ± 0.03	$(3.2 \pm 0.6) \times 10^{-4}$	$(3.5 \pm 0.4) \times 10^{-3}$
	^{238}U up	1.06 ± 0.22	$(4.7 \pm 1) \times 10^{-5}$	
	^{238}U low	0.34 ± 0.03	$(3.2 \pm 0.2) \times 10^{-4}$	
	^{235}U	0.05 ± 0.01	$(1.2 \pm 0.2) \times 10^{-4}$	
	^{40}K	2.39 ± 0.32	$(1.8 \pm 0.2) \times 10^{-4}$	
	^{54}Mn	0.05 ± 0.02	$(3.5 \pm 0) \times 10^{-5}$	
PMT Ceramic	^{232}Th	0.07 ± 0.01	$(2.4 \pm 0.4) \times 10^{-4}$	
	^{238}U up	4.22 ± 0.88	$(4.1 \pm 0.8) \times 10^{-4}$	
	^{238}U low	0.34 ± 0.03	$(5.3 \pm 0.4) \times 10^{-4}$	
	^{235}U	0.21 ± 0.03	$(9.6 \pm 1.4) \times 10^{-4}$	
	^{40}K	$(0.61 \pm 0.08$	$8.1) \pm 1.1 \times 10^{-5}$	
PMT Body	^{60}Co	0.17 ± 0.02	$(2.5 \pm 0.3) \times 10^{-4}$	
Cryostat	^{232}Th	0.19 ± 0.04	$(8.0 \pm 1.7) \times 10^{-5}$	$(6.1 \pm 0.4) \times 10^{-4}$
	^{238}U up	$1.30^{+0.2}_{-0.2}$	$(1.5 \pm 0.2) \times 10^{-5}$	
	^{238}U low	$0.38^{+0.04}_{-0.19}$	$(5.4 \pm 0.6) \times 10^{-6}$	
	^{235}U	$0.045^{+0.01}_{-0.02}$	$(9.7 \pm 1.5) \times 10^{-6}$	
	^{60}Co	1.38 ± 0.1	$(4.9 \pm 0.4) \times 10^{-4}$	
	^{40}K	$0.16^{+0.02}_{-0.05}$	$(3.5 \pm 0.4) \times 10^{-6}$	

III.4 Data Selection

With respect to the previous DarkSide publication [101], this analysis was performed on an extended data set and the data selection was refined.
The total detector lifetime is 534.2 days with a LAr mass of 46.4±0.7 kg [100]. The selection is then based on the identification of single scatter low energy events. Single scatters can be either an s_1+s_2 signal or only an s_2 depending if s_1 is detected. Variables used during the analysis are reported in Table III.3.

Several cuts are then applied on single scatters (Table III.4). Some are specific to either s_1+s_2 (Table III.5) or s_2 only (Table III.6). In each table are summarized the cuts, their explanation and their efficiency. The total efficiency over all the cuts is equal to 0.396.

Table III.3 – Variables used during the analysis

Variable	Meaning
s1	Number of s_1 photoelectrons
s2	Number of s_2 photoelectrons
ne_corr	Number of s_2 electrons, defined as s_2/g_2, where g_2 is the mean number of pe/e$^-$ observed by each top array PMT
s1_f90	f_{90} applied to s_1 pulses
s2_f90	f_{90} applied to s_2 pulses
s2_tba	s_2 top/bottom asymmetry
npulses	Number of identified pulses
s2_max_frac	Fraction of s_2 light observed by the top PMT seeing most of the light
s2_max_chan	Top array PMT observing the maximum fraction of s_2 light
deltaT	Time difference from the previous event [s]
sX_start_time	Start time of pulse X, with X=1 to 4
sX_end_time	End time of pulse X, with X=1 to 4
s2_peak_time	Time of the s_2 pulse peak, identified with a moving average over a 64 ns gate, with respect to the pulse start time
s2_gate	s2_end_time - s2_start_time
s2_fwhm	FWHM of the s_2 peak, evaluated on the moving average of the waveform with a 64 ns gate

The fiducial volume cut is designed to store events inside the fiducial volume to avoid background from lateral walls. The XY position algorithm is based on the maximal fraction of light observed by one of the top PMTs. Simulation and DarkArt, DarkSide-50 reconstruction tool, are used to determine the efficiency of this cut. In addition:

- A minimum time difference of 20 ms with the preceding event is defined to discard correlated events.
- s_2 pulse length has to be below 150 μs to avoid unresolved multiple pulses.
- Peak times should be greater than 0.2 μs and smaller than 5 μs to avoid α's and spurious s_2's (expected value is 1-2 μs).
- s_2 fraction of photons in the first 90 ns of the pulse should be greater than 0.1.
- s_2 top-bottom asymmetry has to be between 0.1 and 0.95.
- It is required that photons are not present at more than 75% in a single top PMT or entirely in a top or bottom array.

In addition to these general cuts, for the case of a s_1+s_2, kept events have only either two pulses or three if the third is an s_1 or an s_2 echo. An echo is a low energy signal following the scintillation pulse by the maximum drift time due to the electron emission of photo-ionization from the cathode. The s_1 start time should be between -6.10 and -6.00 (to be close to the trigger offset of -6.04). To remove Cerenkov effects, s_1 fraction of photon in the first 90 ns of the pulse has to be below 0.85. High energy events (mostly α's) are removed by selecting s_1 energy below 500 photo-electrons and α's by an s_2/s_1 cut based on calibration.

Table III.4 – Global cuts

Cut	Comment	Efficiency
s2_max_chan in [24, 25, 26, 29, 30, 31, 35]	Fiducial volume cut	0.412
deltaT > 20	Remove events if within 20 ms from the preceding one, to avoid correlated events.	0.97
s2_gate < 100	s_2 pulse length < 100 μs: long gates are associated to unresolved multiple pulses.	1.00
0.1<s2_tba < 0.95	Top/bottom asymmetry for s_2 pulses in the [0.1, 0.95] range.	1.00
s2_f90 < 0.1	f_{90} of s_2 pulses < 0.1	1.00
s2_max_frac < 0.75	Remove events with more than 75% of s_2 seen by a single top PMT.	1.00
s2_peak_time > 0.2	Remove events with a peak time within 200 ns from the start time. These events are likely related to alpha s_1 + random s_2 pulses.	1.00
s2_peak_time < 6	Remove events with peak time s_2 larger than 6 μs, likely corresponding to unresolved s_2+s_2 pulses. The efficiency is estimated on the ^{83m}Kr sample.	1.00
s2_fwhm > 0.1	Remove events with s_2 FWHM lower than 100 ns	1.00

Table III.5 – s_1 + s_2 cuts

Cut	Comment	Efficiency
npulses = 2 or (npulses = 3 and s_1 echo) or (npulses = 3 and s_2 echo)	Either 2 pulse events or two pulses plus an s_1 or s_2 echo.	1.00
-6.1 < s1_start_time < -6.0	s_1 start time close to the trigger time offset (6.04 μs)	1.00
s1_f90 < 0.85	Remove Cerenkov events.	1.00
rotated energy < 25 keV$_{er}$	Remove high energy s_1 events (mostly alphas).	1.00
alpha_cut	s_2/s_1 vs s_1 cut, build on AmBe calibration events, to remove alpha events close to the walls, with low s_2, since most of electrons are absorbed by the TPC surface. See description in the text.	0.99

Finally, for the case with only an s_2, we discard events that have more than one pulse unless there are two and the second is an s_2 echo. In addition, the s_2 start time is cut depending on the pulse start time to avoid unresolved multiple pulses.

Table III.6 – s_2 only cuts

Cut	Comment	Efficiency
npulses = 1 or (npulses = 2 and s_2 echo)	Either 1 pulse event or two pulses where the second is an s_2 delayed by more than 375 μs.	1.00
s2_start_time_cut	This cut is defined as a function of ne_corr using Monte Carlo and full DarkArt reconstruction, in order to remove unresolved multiple pulses. The main criterion is based on the pulse start time: if it is too early compared to the trigger time, it cannot be associated with a physical event. The cut is constructed to obtain a flat efficiency as a function of ne_corr.	0.99

The resulting data selection is shown in Figure III.17. When comparing to the 2018 analysis (Figure III.18), the main difference in event rate is at low N_e. It is due to the improvement of a set of cuts and not to only one of them. The additional improvement between 40 to 50 N_e is due to a bias (over-estimation) of the old s_2/s_1 cut.

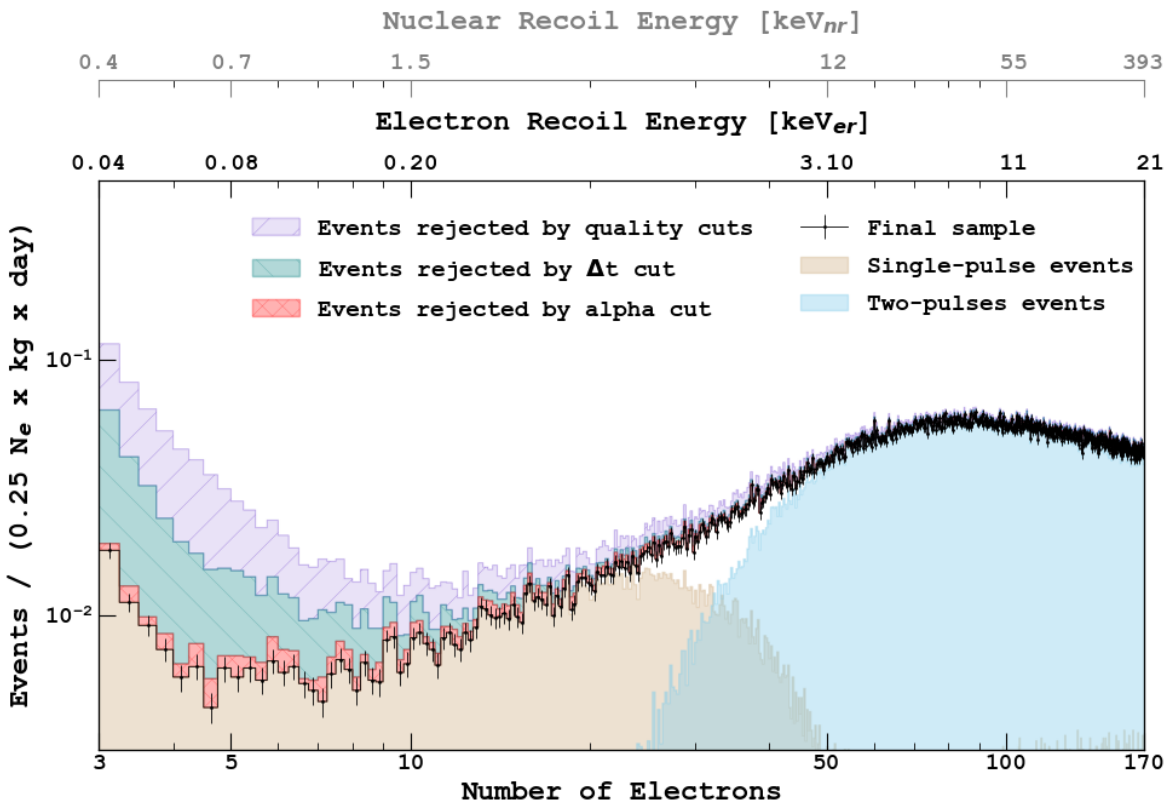

Figure III.17 – Data sample after applying the different selection cuts.

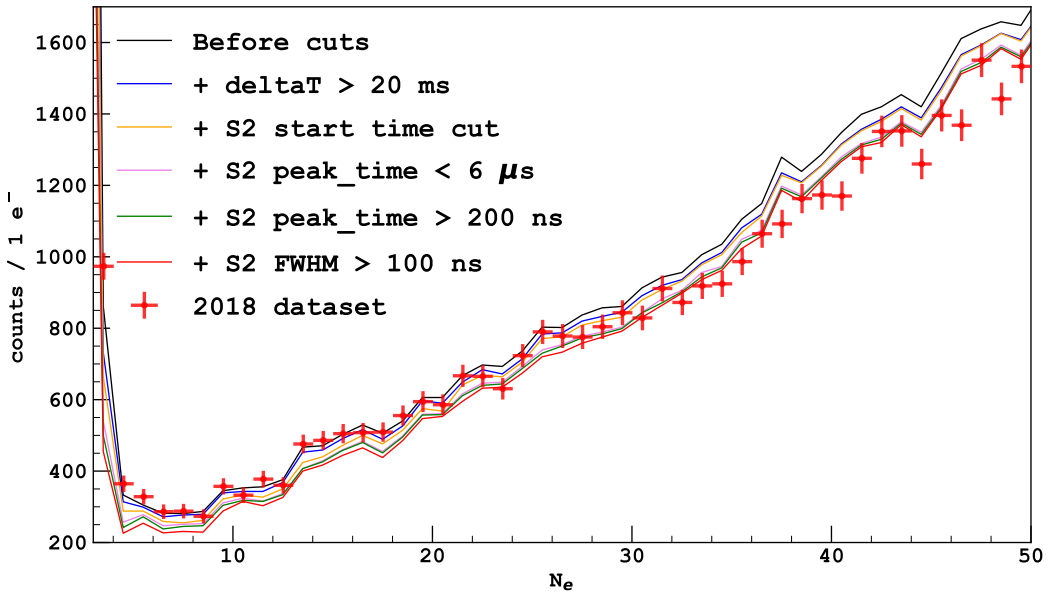

Figure III.18 – Comparison of the spectra from the 2018 dataset versus the new one after selection cuts. The 2018 spectra are normalized to the new dataset lifetime.

III.5 Standard Halo Model

The Standard Halo Model (SHM) describes cold dark matter velocity distribution at the galactic scale and more particularly in the Solar System where detection experiments are taking place. As discussed in Section I.2, dark matter is collisionless and hence the halo is considered static in an isothermal and isotropic sphere of gravitational bound dark matter [140]. Its density follows a $1/r^2$ law [141].

Following the SHM, the velocity distribution $f(\vec{v})$ in the lab frame is taken accordingly to a Maxwell Boltzmann distribution (Equation III.12) [142] [88]. This distribution is only valid for $|\vec{v}| < v_{esc}$, with $v_{esc} = 544$ km/s the galactic escape velocity. Above this value, particles are not gravitationally bounded anymore, hence the velocity distribution is equal to zero.

$$f(\vec{v}) = \frac{k\,|\vec{v}|}{\sqrt{\pi} v_0 v_{Earth}(t)} e^{-((|\vec{v}|-v_{Earth}(t))/v_0)^2} - e^{-(|\vec{v}|^2+v_{Earth}^2(t)+2\alpha|\vec{v}|v_{Earth}(t))/v_0^2} \tag{III.12}$$

and

$$k = erf(v_{esc}/v_0) - \frac{2(v_{esc}/v_0)}{\sqrt{\pi}} e^{-(v_{esc}/v_0)^2} \tag{III.13}$$

Other parameters of the model are α the maximum angle for the velocity, v_{Earth} the velocity of earth relative to galactic rest frame, $v_0 = 220$ km/s the most probable velocity of dark matter in the halo regarding to the galactic center.

This velocity distribution is shown in Figure III.19 depending on the dark matter particle speed.

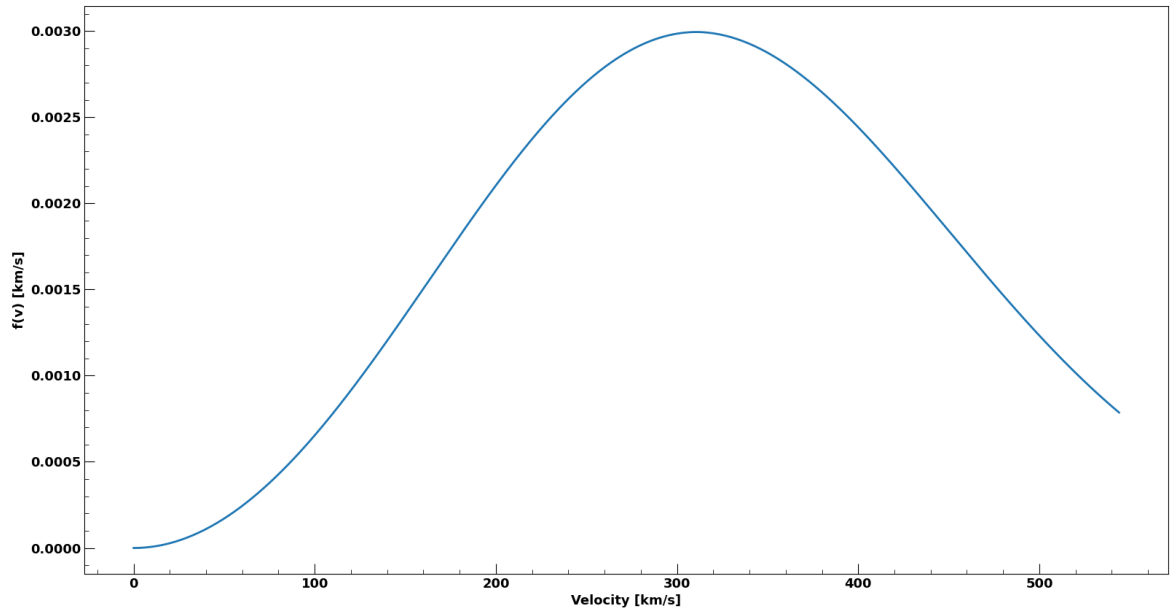

Figure III.19 – Velocity distribution following the Standard Halo Model

The SHM is used in the derivation of all the signal models.

III.6 Nuclear Recoil WIMPs Low-mass Limits

Nuclear recoil WIMPs are the main candidates probed with the DarkSide experiment. We will introduce their model before presenting their improved limits.

III.6.1 WIMP-nucleon Signal Model

The model was implemented for low-mass WIMPs, *i.e.* WIMPs below 10 GeV/c^2 and we are only considering in this section scattering off nuclei. As the subject of quenching fluctuations, *i.e.* fluctuations for nuclear recoil energy quenching is still unsolved we will consider two cases, the one where we will suppress all fluctuations (NQ) and the other where we will consider binomial fluctuations (QF). Fluctuations of ionization and recombination processes are however determined and considered binomial.
We will briefly describe the WIMPs nuclear recoil rate and spectra computation already implemented in the low-mass framework.

We first compute the differential elastic WIMP-nucleus $d\sigma_{\chi-N}/dE_R$ cross-section (Equation III.14). It depends on the WIMP-nucleon cross-section $\sigma_{\chi-n}$, which is the parameter on which we will compute the limits. $d\sigma_{\chi-N}/dE_R$ is also function of the electronic recoil energy E_R, of the WIMP mass m_χ and velocity v_χ and finally on the mass of the mediator M_{med}. These quantities allow computing the maximum kinematic nuclear recoil energy E_{max} as well as the reduced mass between nuclei and WIMPs $\mu_{\chi-N}$. Finally, F^2_{Helm} stands for the squared Helm form factor [143].

$$\frac{d\sigma_{\chi-N}}{dE_R} = \sigma_{\chi-n}\frac{\mu^2_{\chi-N}M_{med}F^2_{Helm}(E_R)}{E_{max}(m_\chi, v_\chi)} \tag{III.14}$$

From this differential cross-section, we can infer the differential WIMPs rate following Equation III.15 with ρ_0 being the local dark matter density of 0.3 GeV/(c^2 cm^3), f the velocity distribution following the Standard Halo Model (cf. Equation III.12) and m_N the nucleus mass. The velocity integration is performed between v_{min} the minimum velocity achievable for a given E_R and v_{esc} the escape velocity of 544 km/s. We assume a local standard of rest velocity of 232 km/s.

$$\frac{dR}{dE_R} = \frac{\rho_0}{m_\chi m_N}\int_{v_{min}}^{v_{esc}}\frac{d\sigma_{\chi-N}}{dE_R}v_\chi f(v_\chi)dv_\chi \tag{III.15}$$

For each given WIMP mass, the differential rate is then multiplied by the exposure of the detector in ton-years and integrated over energy. These energy spectra is then normalized to retrieve a probability distribution from which we will be able to sample energies in the energy range we consider. We then apply detector distortions contained in the response model. We apply channel, radial and electron lifetime corrections to the spectra. Finally, thanks to the nuclear recoil energy scale we convert the energy in numbers of photo-electrons. These final spectra in photo-electrons (Figure III.20) will be used as the input signal for further limit computation. As we can see, the expected signal is at a few electrons - few tens of electrons and hence, the importance of both a precise liquid argon response calibration and an accurate background modeling in that range.

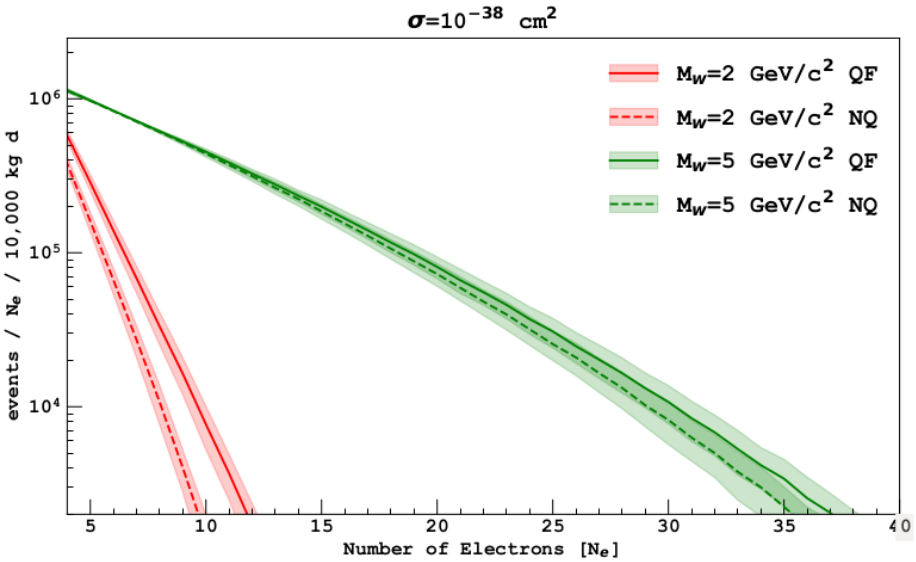

Figure III.20 – Spectra of WIMPs nuclear recoil at two different masses, taking into account either quenching fluctuations (QF) or no quenching fluctuations (NQ), depending on the number of electrons. Error bands are associated to the uncertainties on the calibration of electronic and nuclear recoil energy scales.

III.6.2 Observed limits

We apply the procedure of the low-mass framework described in Section III.1 to retrieve limits, with and without quenching fluctuations. The number of electrons in which limits are computed is between 4 and 170 as the background is not modelled below 4 electrons and above 170 electrons the energy scale of the liquid argon ionization response is no more calibrated. Observed and expected upper limit of 90%C.L. with and without quenching fluctuations are shown in Figure III.21. We can see the compatibility between both expected and observed limits within 1σ. In addition, the impact of quenching fluctuations becomes negligible for WIMPs masses above 5 GeV/c^2. Exclusion limits with and without quenching fluctuations are plotted in Figure III.22 alongside with limits from other experiments. These exclusion limits are a factor 10 better than the ones from the 2018 analysis and are giving the best limits in the 1.2 to 3.6 GeV/c^2 WIMP mass range.

Finally, data and background model compared to expected WIMP spectra is shown in Figure III.23 for several WIMP masses with quenching fluctuations at the cross-section of 10^{-41} cm^2.

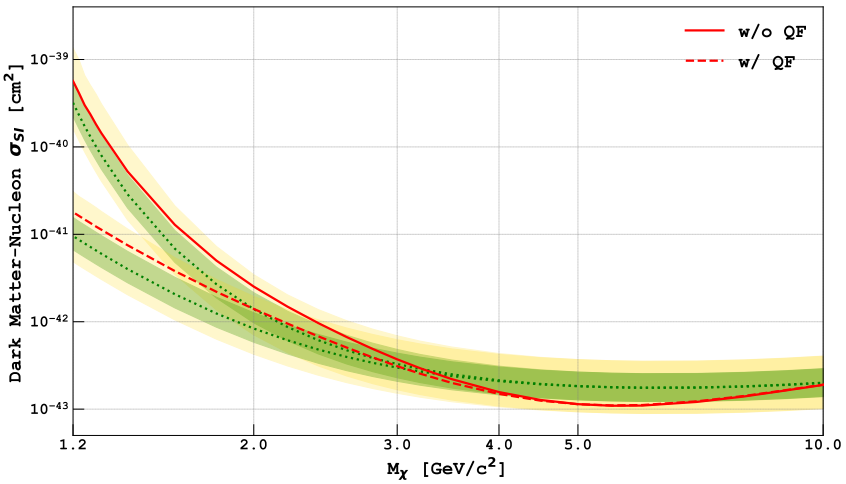

Figure III.21 – Observed (red lines) and expected limits (green dotted lines) with the ± 1-σ (green shaded area) and ± 2-σ (yellow shaded area) bands for 90% upper limits on spin independent WIMP-nucleon cross-section for both non-quenching (NQ, solid red line) and quenching (QF, dashed red line) fluctuations models.

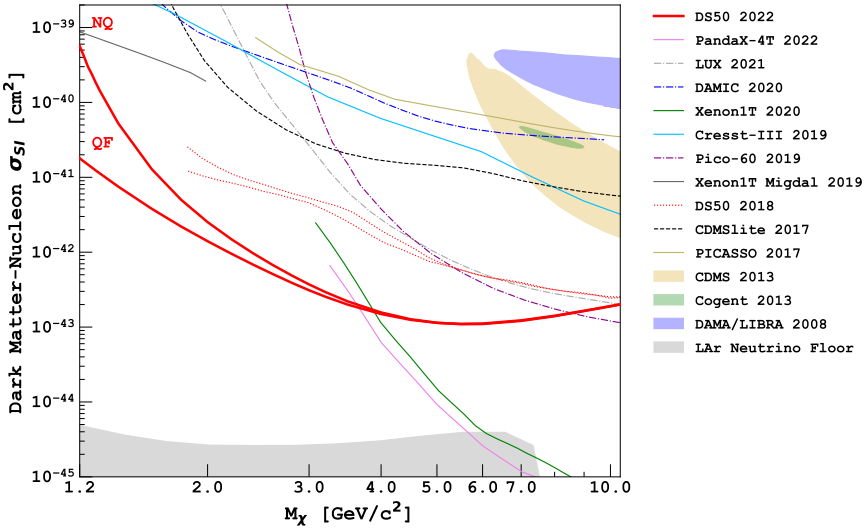

Figure III.22 – Exclusion limits at 90% CL on spin independent WIMP-nucleon cross-section depending on the WIMP mass from DarkSide-50 between 4 and 170 electrons. Limits from other experiments are also reported XENON-100 [144], DarkSide-50 2018 [101], CDMS [145], CDEX [146], PandaX II [147], CDMSlite [148] PICASSO [149], LUX [150], NewsG [151], DAMIC [152], CRESST III [153], Pico-60 [154], XENON 1T [155] [156] [27], CRESST II [157], CoGeNT [158], DAMA/LIBRA [159] and the LAr neutrino floor [160].

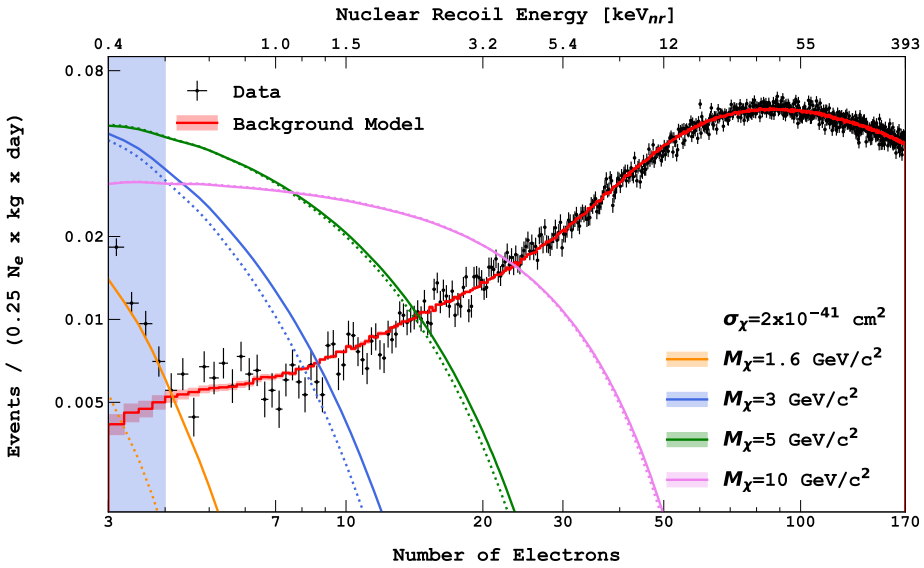

Figure III.23 – Data and background model compared to expected WIMP spectra with WIMP-nucleon scattering cross section equal to 2×10^{-41} cm^2 and quenching fluctuations.

III.7 Migdal Low-mass Limits

When incoming particles scatter elastically off nuclei at rest they excite and ionize atoms. In a fraction of cases, the inner shell ionization can be followed by X-rays or Auger electron emission. This process is called the Migdal effect [161].

The energy released by electronic recoil events up to a few keV when undergoing this process increases visible energy. This process is relevant in the low-mass range as it allows to enhance the detection of otherwise too low signals [162].

The differential rate of ionization events in case of Migdal effect is the product between the differential recoil rate $d^2R_{\chi T}/dE_r dv$ and the ionization rate: [163]

$$\frac{d^3R}{dE_r dE_{em} dv} = \frac{d^2R_{\chi T}}{dE_r dv}\frac{1}{2\pi}\sum_{n,l}\frac{d}{dE_e}p^c_{q_e}(nl \to E_e) \tag{III.16}$$

where v is the dark-matter velocity. E_e represents for the outgoing unbounded electron energy and E_{nl} its de-excitation energy, equal to the binding energy at a given (n, l) state. E_{em} is the total electromagnetic energy, equivalent to the sum of E_e and E_{nl} [163]. Finally, $p^c_{q_e}$ is the ionization probability at an average electron in the target momentum transfer at a given (n, l) state transition [163]. For argon, this probability lies between $\sim 10^{-2}$ and $\sim 10^{-5}$ from the most external shells (with a binding energy around 10 - 30 eV) to the most internal shells (with a binding energy of 3.2 keV).

In this analysis, the contributions of nuclear and electronic recoils are both considered and summed up in the signal model. For what concerns the response model, electronic recoil and nuclear recoil contributions are independently treated. The whole electronic recoil energy is described as a single deposit.

After computing the argon atomic wave function, Equation III.16 is integrated and multiplied by the exposure of the detector. As done for WIMPs without the Migdal effect, energy spectra are normalized to retrieve a probability distribution for sampling energies in the toy Monte-Carlo. Then, detector corrections are applied on an event-by-event basis: channel, radial, electron lifetime to obtain the final spectra first in energy and then in photo-electrons (Figure III.24).

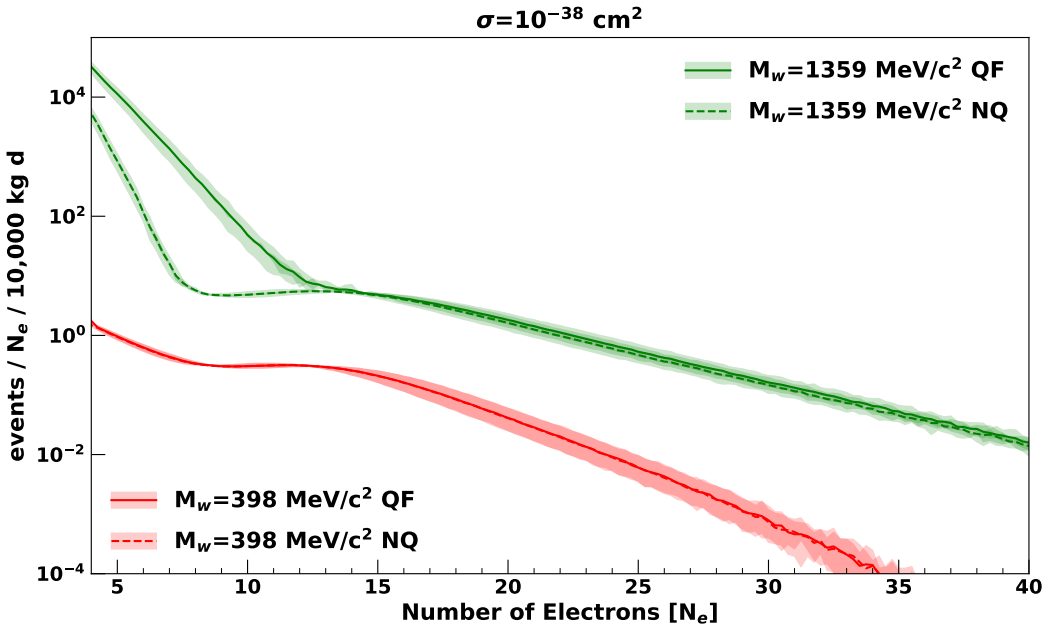

Figure III.24 – Spectra of WIMPs nuclear recoil with Migdal effect at two different masses, taking into account either quenching fluctuations (QF) or no quenching fluctuations (NQ), depending on the number of electrons. Error bands are associated to the uncertainties on the calibration of electronic and nuclear recoil energy scales.

Observed and expected upper limit of 90%C.L. for WIMPs nuclear recoil without Migdal effect are shown in Figure III.25 where we can see that they are compatible at 1-σ. Exclusion limits at 90% CL on WIMP-nucleon cross-section with Migdal effect are shown on Figure III.26). DarkSide-50 sets the best limits from 40 MeV/c^2 to 3.6 GeV/c^2.

Finally, data and background model compared to expected WIMP spectra is shown in Figure III.27 for several WIMP masses at the cross-section of 10^{-35} cm^2.

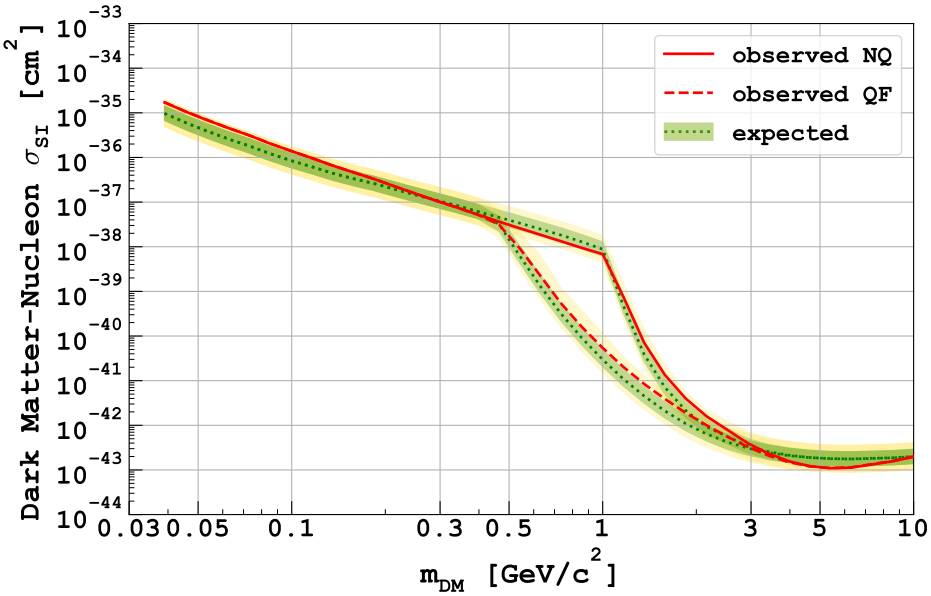

Figure III.25 – Observed (red lines) and expected limits (green dotted lines) with the ± 1-σ (green shaded area) and ± 2-σ (yellow shaded area) bands for 90% upper limits on spin independent WIMP-nucleon cross-section with Migdal effect for both non-quenching (NQ, solid red line) and quenching (QF, dashed red line) fluctuations models.

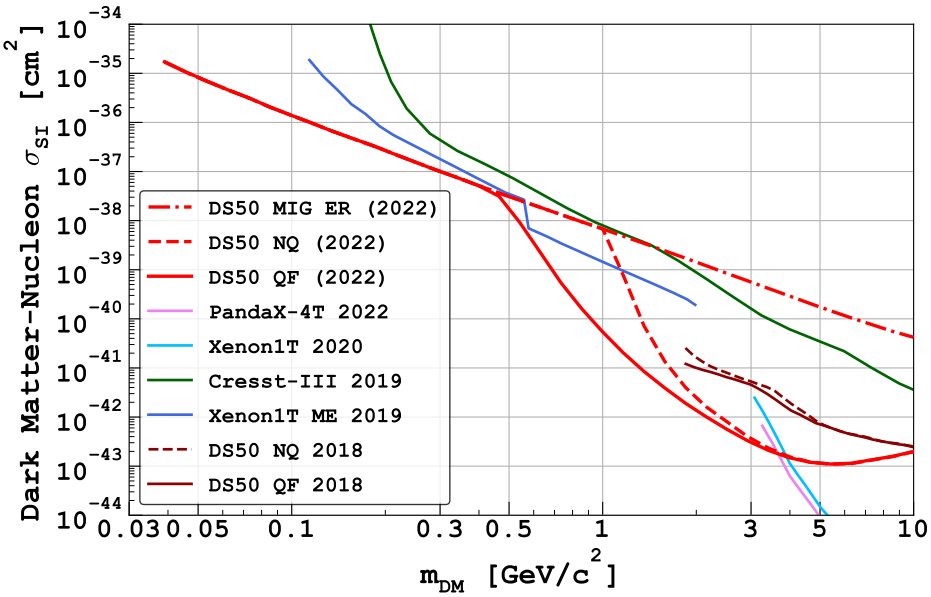

Figure III.26 – Upper limits at 90% CL on WIMP-nucleon cross-section with Migdal effect depending on the WIMP mass from DarkSide-50. Limits from other experiments are also reported SuperCDMS [164], PandaX-4T [165], CRESST III [153], XENON 1T [27] [156] and DarkSide-50 2018 [101].

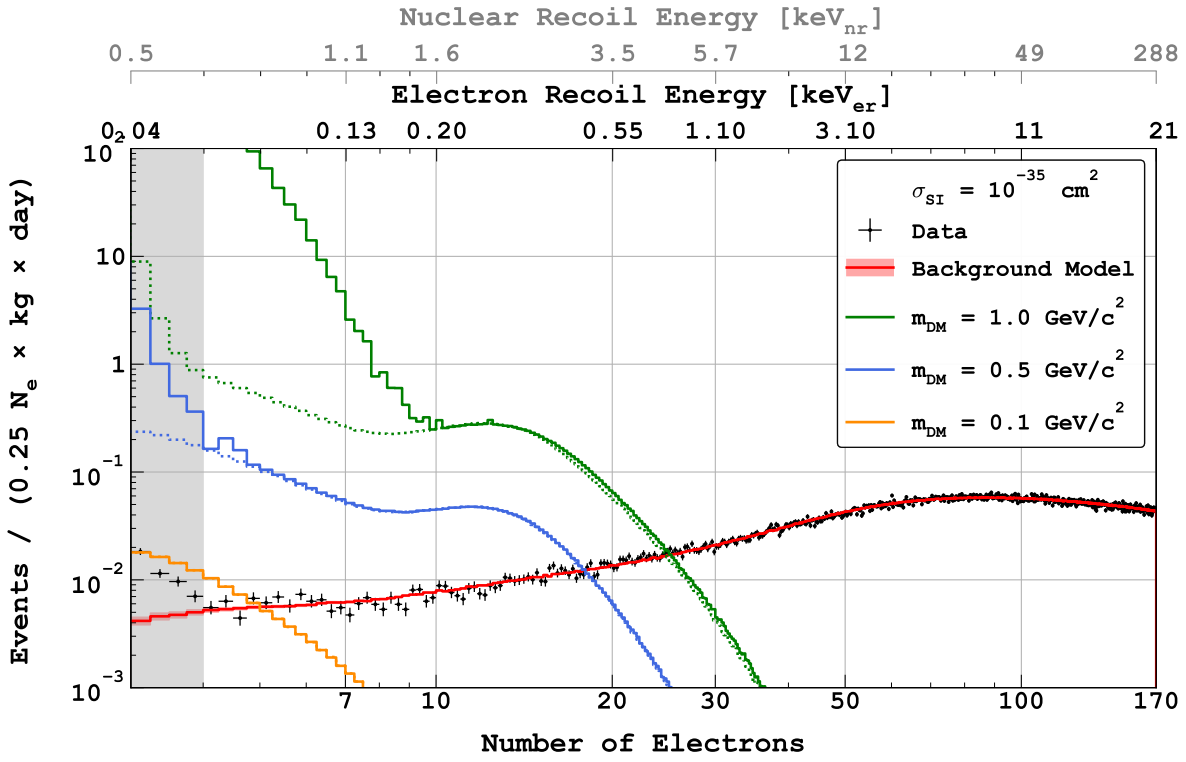

Figure III.27 – Data and background model compared to expected WIMP spectra with the Migdal effect with a WIMP-nucleon scattering cross section equal to 10^{-35} cm^2.

III.8 ALPs Low-mass Limits

Axion-like particles (ALPs) are a class of well motivated candidates, as discussed in Section I.3. We consider first solar ALPs, produced and emitted by the Sun and then galactic ALPs, which are primordial from the early Universe.
Both types of ALPs can be detected via axio-electric effect, similarly to the photoelectric effect where ALP's absorption leads to electron emission. The axio-electric cross-section is expressed as Equation III.17 [166]:

$$\sigma_{Ae} = \sigma_{pe}(E_A)\frac{|g_{ae}|^2}{\beta_A}\frac{3E_A^2}{16\pi\alpha_{em}m_e^2}(1-\frac{\beta_A^{2/3}}{3}) \tag{III.17}$$

with σ_{pe} the photoelectric cross-section between ALPs and the target material, g_{ae} the axio-electric coupling, α_{em} the fine-structure constant, m_e the electron mass, β_A the ALP velocity divided by light speed and E_A the ALP's energy. The photoelectric cross-section used (cf. Figure III.28) was retrieved from NIST database [167] for argon.

Galactic ALPs are considered at rest within the galaxy. Consequently, we expect a kinetic energy for their electronic recoil equal to their mass giving a monoenergetic spectrum depending on each ALP mass [166].

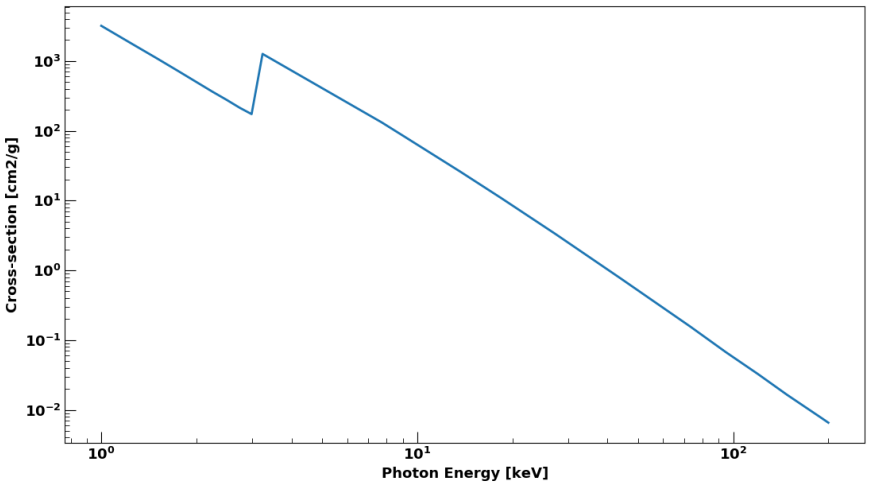

Figure III.28 – Photo-electric cross-section on argon atoms [167]

III.8.1 Solar ALPs Flux, Rate and Spectra

Solar ALP fluxes have three production mechanisms. The main one is called ABC and contains **A**tomic recombination and de-excitation, **B**remsstrahlung and **C**ompton scattering. ABC axions are coupled to electrons via $|g_{ae}|$, the axio-electric coupling constant [168]. The second one is from Primakoff thermal conversion of two photons into an axion in the electric and magnetic field of Sun plasma [169] [170]. Its axion-photon coupling constant will be written $|g_{a\gamma}|$. The last one arises from a mono-energetic 14.4 keV M1 nuclear transition of ^{57}Fe in the Sun [170]. This would be a thermal de-excitation process of ^{57}Fe nuclei [171] [170]. Its effective axion-nucleon coupling constant is referred to $\left|g_{an}^{eff}\right|$.

ABC differential flux is distributed as shown in Figure III.29 [172] for energies ranging from 0 to 12 keV, although it is only relevant in the 0 to 1 keV/c^2 range here. Indeed, this model is only valid when the total energy is dominated by kinetic energy, so for massless ALPs or ALPs with masses up to 1 keV/c^2 [166]. This also implies that β, the ALP velocity divided by the light speed, is equal to one in this approximation.

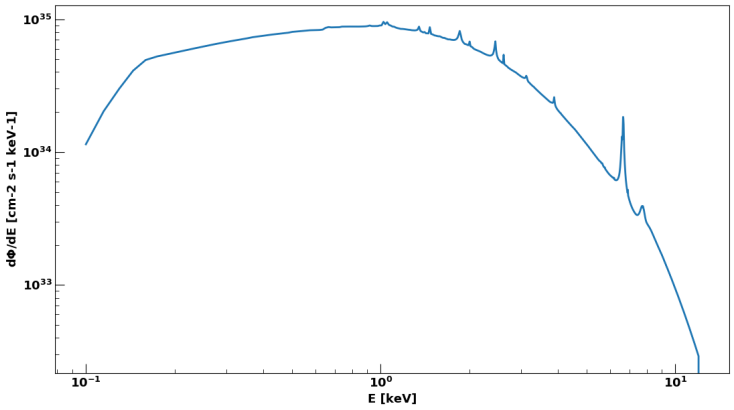

Figure III.29 – Solar ABC ALP flux depending on energy, plotted from [172]

The differential Primakoff flux is expressed as [170]:

$$\frac{d\Phi_a^{Prim}}{dE} = |g_{a\gamma}|^2 E^{2.481} e^{-E/1.205} \times 6 \times 10^{30} [cm^{-2} s^{-1} keV^{-1}] \quad \text{(III.18)}$$

with $|g_{a\gamma}|$ the axion-photon coupling expressed in GeV^{-1} and E the energy expressed in keV.
The flux from ^{57}Fe is expressed as [170]:

$$\phi^{^{57}\text{Fe}} = \left(\frac{k_a}{k_\gamma}\right)^3 \times \left|g_{an}^{eff}\right|^2 \times 4.56 \times 10^{23} [cm^{-2} s^{-1}] \quad \text{(III.19)}$$

with the ratio of axion and photon momenta (respectively k_a and k_γ) equal to one.

In addition to these three production processes, there are two possible detection processes: axio-electric effect and inverse Primakoff effect.
The cross-section associated with the axio-electric effect is already expressed in Equation III.17 and the one for inverse Primakoff effect is expressed as:

$$\sigma_{inversePrim} = \frac{\alpha Z^2 \hbar^2 c^2 |g_{a\gamma}|^2}{8\pi} \left[\frac{2\eta^2 + 1}{4\eta^2} \ln(1 + 4\eta^2) - 1\right] \quad \text{(III.20)}$$

with Z the atomic number of the target material, α the structure fine constant, $\hbar$ the reduced Planck constant, c the light speed, and $\eta = r_0 k/\hbar$ a dimensionless number depending on k, the ALP momentum and r_0 the atomic radius of the target material. For argon $r_0 \approx 71$ pm.

The differential rate is then derived as the product of the flux, the cross-section and the number of target atoms:

$$\frac{dR}{dE}[keV^{-1} kg^{-1} day^{-1}] = \frac{d\Phi}{dE} \times \frac{N_A}{A} \times \sigma \quad \text{(III.21)}$$

where Φ the flux and σ the cross-section depending on the chosen production and detection processes. N_A is the Avogadro constant and A the atomic mass number.

Differential rates for the three production processes are shown in Figure III.30 for axio-electric detection process and Figure III.31 for inverse Primakoff detection.

After multiplying the rate by the detector exposure and integrating different correction terms (cf. Section III.1), we compute the spectrum for mass less solar ALPs for axio-electric and inverse Primakoff detection processes, extrapolated up to 1 keV (Figure III.32). DarkSide-50 time exposure is of $T = 515$ days and its effective mass is $M = 19.56$ kg.

III.8.2 Galactic ALPs Flux, Rate and Spectra

Galactic ALP flux Φ_{ALPgal} is inversely proportional to the ALP mass m_A [168] (Figure III.33):

$$\Phi_{ALPgal}[/cm^2/s] = \frac{9 \times 10^{15}}{m_A} \beta_m \quad \text{(III.22)}$$

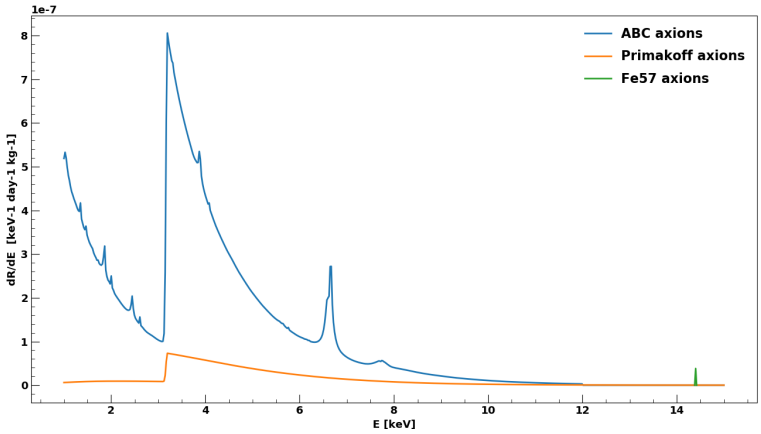

Figure III.30 – ABC, Primakoff and ^{57}Fe solar ALP differential rate by axio-electric detection process depending on energy, $|g_{ae}| = 10^{-12}$, $|g_{a\gamma}| = 2\times10^{-11}$ GeV^{-1} and $\left|g_{an}^{eff}\right| = 10^{-7}$

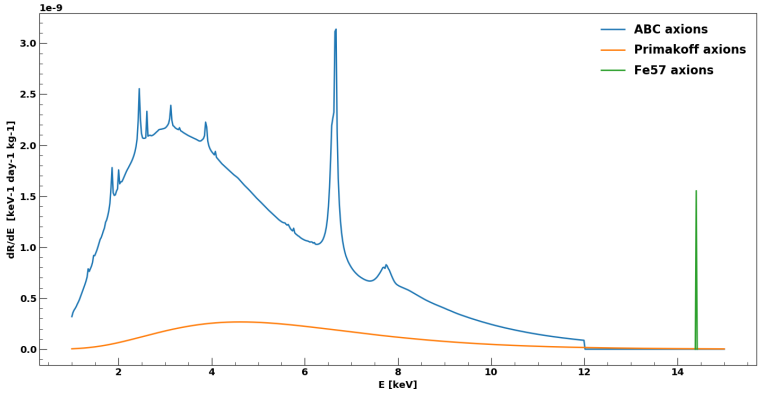

Figure III.31 – ABC, Primakoff and ^{57}Fe solar ALP differential rate by inverse Primakoff detection process depending on energy, $|g_{ae}| = 10^{-12}$, $|g_{a\gamma}| = 2\times10^{-11}$ GeV^{-1} and $\left|g_{an}^{eff}\right| = 10^{-7}$

with β_m ALP mean velocity in the unit of light speed with respect to the Earth equal to 10^{-3} [168].

Considering the flux definition from Equation (III.22), the rate R_{ALPgal} for galactic ALPs is [173]:

$$R_{ALPgal}[/kg/day] \simeq |g_{ae}|^2 \frac{1.2\times10^{19}}{A} m_A[keV/c^2]\sigma_{pe}[barn] \quad \text{(III.23)}$$

where A the atomic number of the target.

For cold dark matter, we are only considering non-relativistic ALPs. Hence, their rate is independent on the ALP velocity since the flux depends on β and the cross-section on $1/\beta$.
From the signal rate (Equation III.22, shown on Figure III.34), we derive the spectrum for different galactic ALP masses, between 1 and 20 keV (for instance for 1 keV, $|g_{ae}|$ input 10^{-12}, Figure III.35) using DarkSide-50 exposure (cf. Section III.8.1).
.

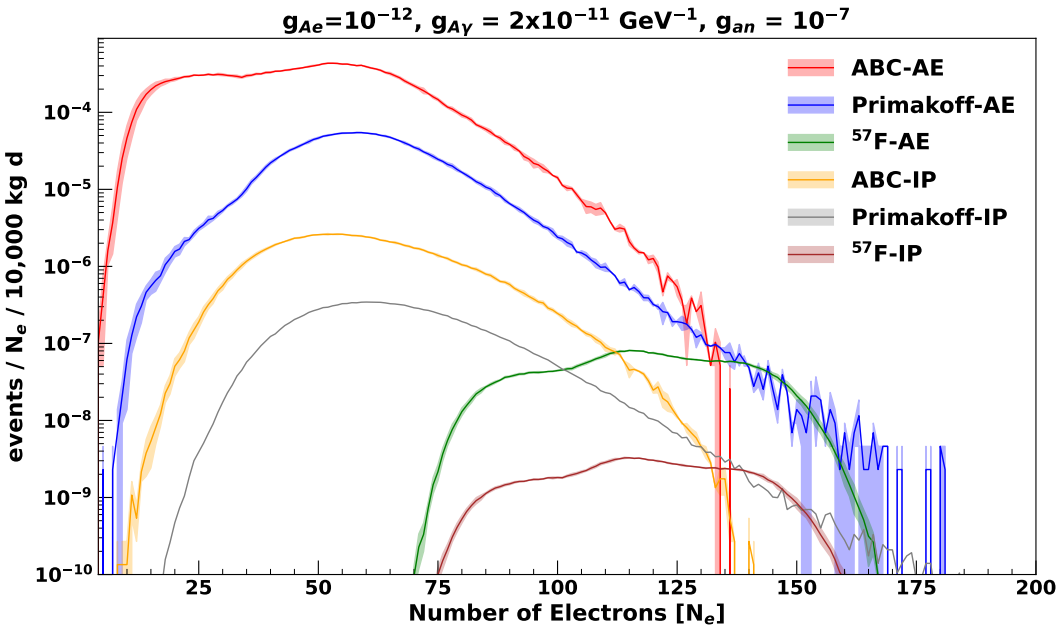

Figure III.32 – ABC, Primakoff and ^{57}Fe solar ALP number of events by either axio-electric (AE) or inverse Primakoff detection process (IP) depending on the number of electrons. Error bands are associated to the uncertainties on the calibration of electronic and nuclear recoil energy scales.

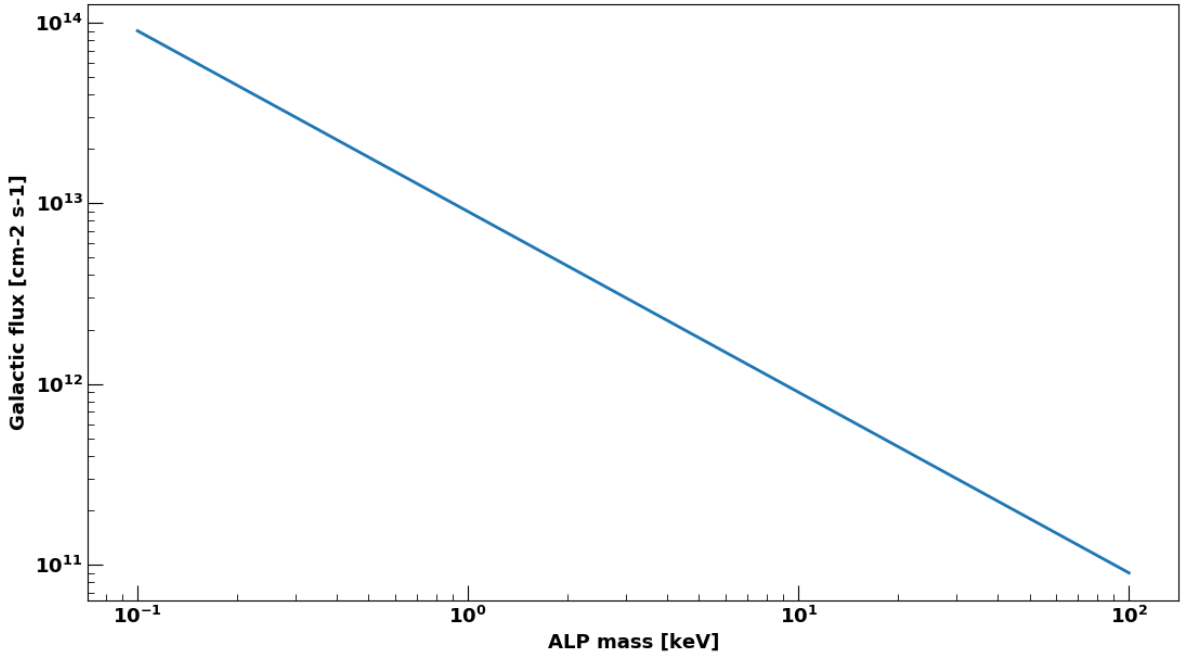

Figure III.33 – Galactic ALP flux depending on energy

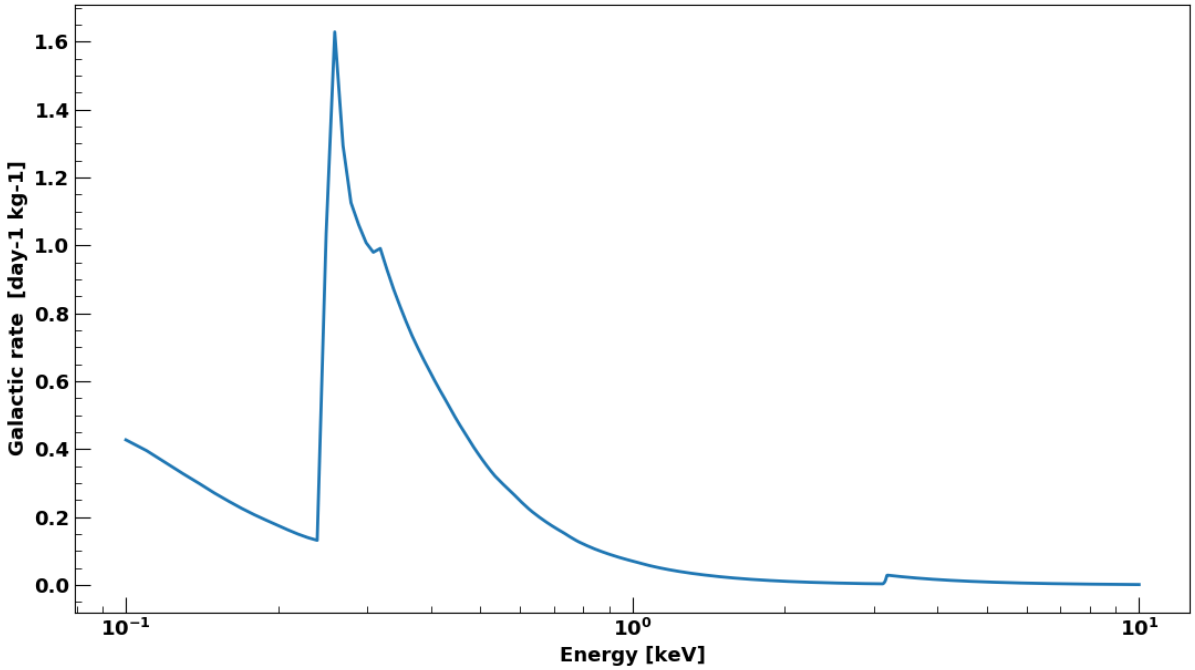

Figure III.34 – Galactic 1keV-ALP rate depending on energy, $|g_{ae}| = 10^{-12}$

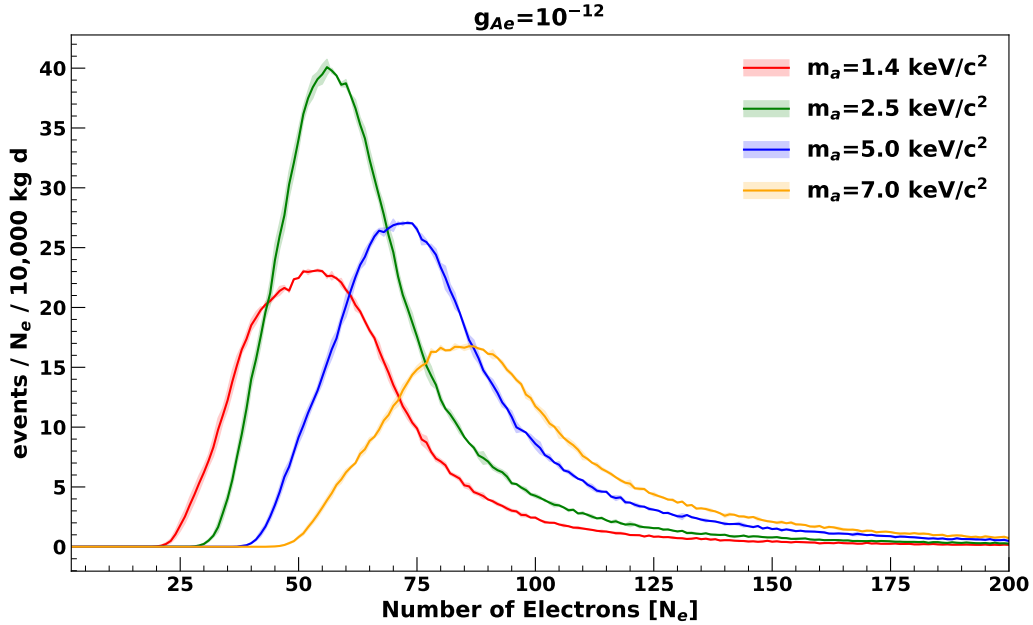

Figure III.35 – Galactic ALP spectra depending on the number of electrons at a mass of 1keV, $|g_{ae}|$ input= 10^{-12}. Error bands are associated to the uncertainties on the calibration of electronic and nuclear recoil energy scales.

III.8.3 Observed Limits

Observed limits on coupling constants depending on the process for solar ALPs are quoted in Table III.7. They are not competitive with limits set by other experiments [174] [175] [166] [176] [177] and by the most stringent limits set by astrophysical measurements: $|g_{a\gamma}| < 6$ - 8×10^{-13} GeV^{-1} (depending on the magnetic field model) [178], $|g_{ae}| < 1.3 \times 10^{-13}$ [179]. Figure III.36 shows the current best limits of both coupling constants depending on each other [180]. Concerning, mono-energetic 14.4 keV M1 nuclear transition of ^{57}Fe, limits were set on the product of coupling constant $\left|g_{an}^{eff} g_{a\gamma}\right| < 1.36\times 10^{-16}$ GeV^{-1} by CAST [170] and only on $\left|g_{an}^{eff}\right| < 3.0\times 10^{-6}$ by a Si(Li) detector [181]. It is however the best limits obtained with an argon target.

Table III.7 – DarkSide-50 limits for coupling constant of the different production (line) and detection (column) mechanisms of solar ALPs, *i.e.* respectively for the solar ALP flux ABC, Primakoff or ^{57}Fe and for either a axio-electric or an inverse Primakoff cross-section.

	axio-electric	inverse Primakoff
ABC	$\|g_{ae}\| <2.45\times10^{-8}$	$\|g_{ae}g_{a\gamma}\| <4.59\times10^{-6}$ GeV^{-1}
Primakoff	$\|g_{a\gamma}g_{ae}\| <2.27\times10^{-7}$ GeV^{-1}	$\|g_{a\gamma}\| <3.73\times10^{-5}$ GeV^{-1}
^{57}Fe	$\left\|g_{an}^{eff} g_{ae}\right\| <8.68\times10^{-5}$	$\left\|g_{an}^{eff} g_{a\gamma}\right\| <2.14\times10^{-3}$ GeV^{-1}

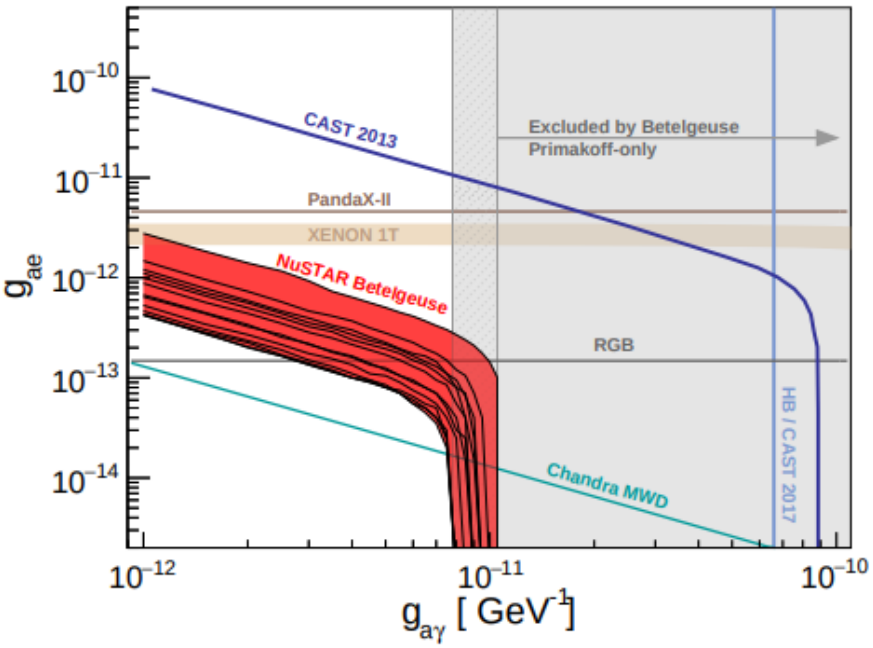

Figure III.36 – $|g_{ae}|$ as a function of $|g_{a\gamma}|$ 95% C.L. upper limit for a solar ALP mass below 3.5×10^{-11}eV/c^2 [180].

In the case of galactic ALPs, and within an extended mass range below 1 keV/c^2 thanks to M. Poelhmann, observed and expected upper limit at 90% C.L. are shown in Figure III.37. The solid red line shows the observed limit set by this approach and the associated dashed line is the expected limit at -1σ which highlights regions where under-fluctuations of data can drive observed limits. When comparing with limits by other experiments (Figure III.38), we can see that DarkSide-50 limits are improving existing best limits around

0.26 keV/c^2.

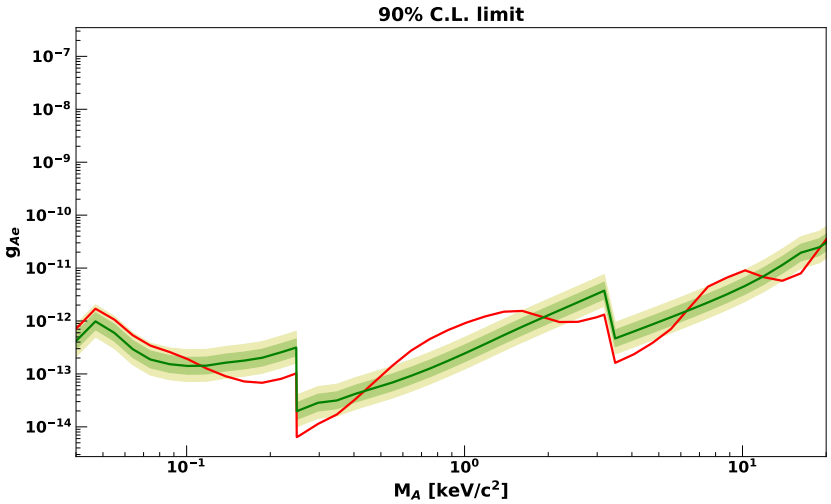

Figure III.37 – Observed (red lines) and expected limits (green dotted lines) with the ± 1-σ (green shaded area) and ± 2-σ (yellow shaded area) bands for 90% upper limits on galactic ALPs-axio-electric coupling constant g_{Ae}.

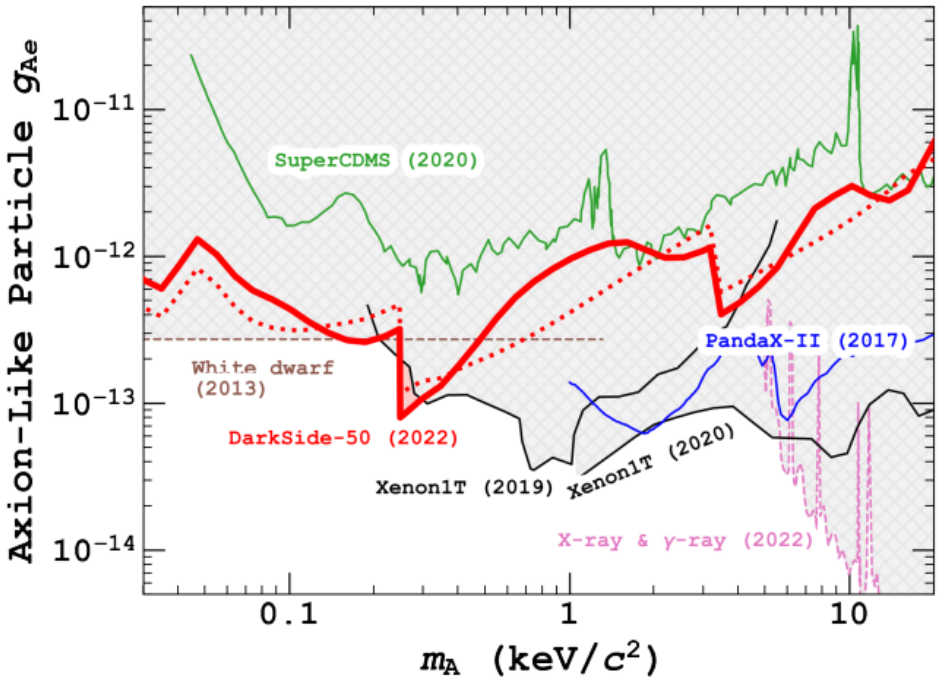

Figure III.38 – Exclusion limits on galactic ALP interaction with DarkSide-50 along with limits from PandaX-II [177], XENON-1T [27] [182], SuperCDMS [183], white dwarfs [184] and X-rays γ-rays [185].

Finally, data and background model compared to expected spectra of leptophilic candidates, including galactic ALPs, are shown in Figure III.39.

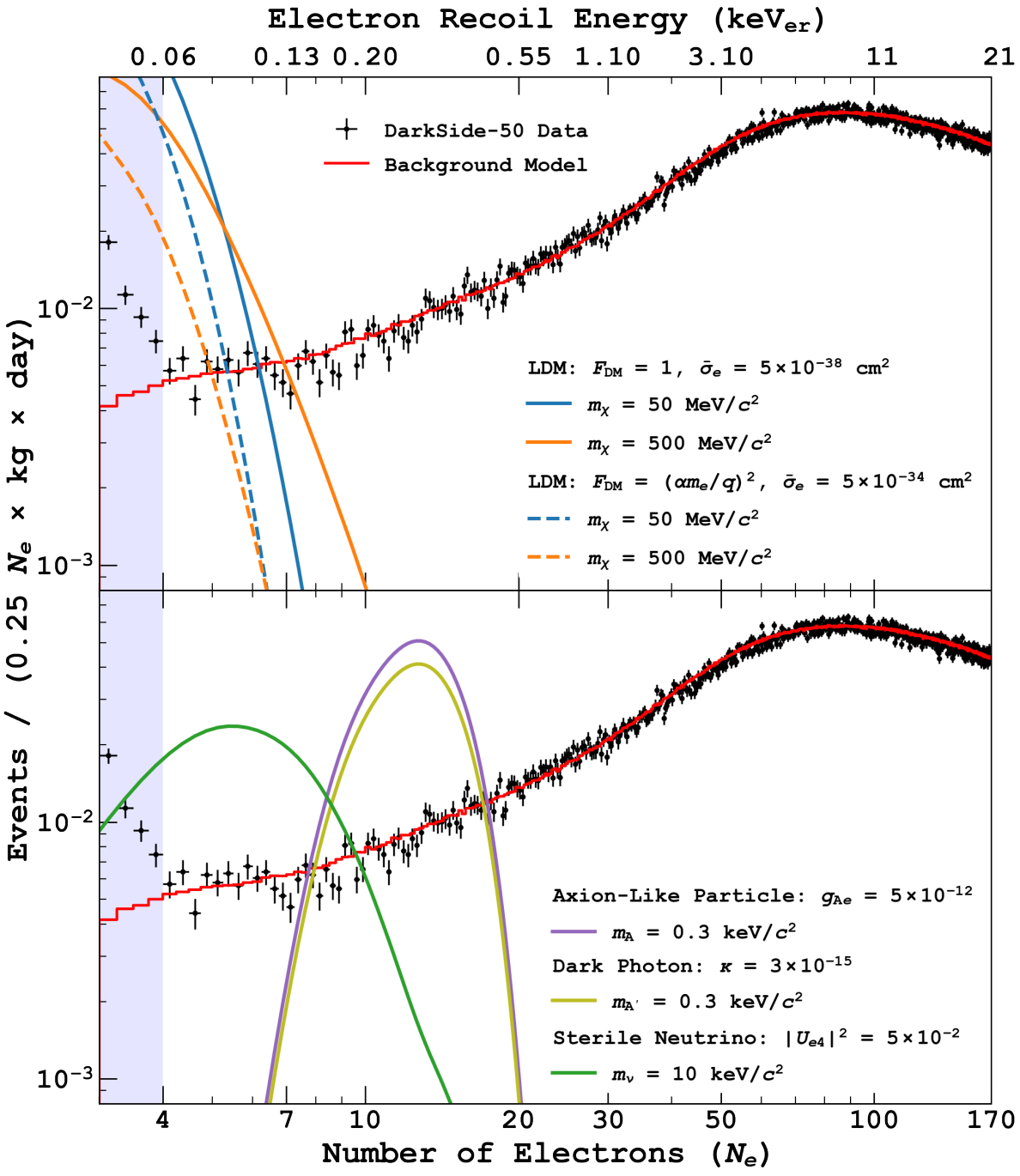

Figure III.39 – Data and background model compared to expected ionization spectra for several dark matter candidates: LDM (heavy and light mediator), ALPs, dark photons, and sterile neutrinos

III.9 keV Sterile Neutrino Low-mass Limits

Another possible dark matter candidate would be sterile neutrinos (cf. Section I.3). More specifically, we are looking for a specific range of sterile neutrino masses compatible with dark matter: between 7 and 36 keV [68]. Sterile neutrinos with masses larger than around 5 keV can be considered as behaving like CDM [69] [68], so we will be using the Standard Halo Model [142] [88] developed for CDM for computing their velocity profile. In this mass range, sterile neutrino associated wavelengths are comprised in the 10^{-8}-10^{-9} cm range [186] [187], which means that they scatter incoherently with argon atoms (radius: 1.88×10^{-8} cm).

Search for sterile neutrino dark matter is based on a two steps process: the mixing of a sterile neutrino into its active state, parameterized by its mixing angle $|U_{e4}|^2$, and then its inelastic scattering with a bound electron from an argon atom such as

$$\nu_s(p_{\nu_s})e(p_B) \rightarrow \nu_e(p_{\nu_e})e(p_e) \tag{III.24}$$

and

$$\bar{\nu_s}(p_{\nu_s})e(p_B) \rightarrow \bar{\nu_e}(p_{\nu_e})e(p_e) \tag{III.25}$$

To match the actual observed dark matter density, the mixing angle between keV-sterile neutrinos and active neutrinos has to be very tiny, $|U_{e4}|^2 \ll 10^{-7}$ [188] [189] [190].

The associated Feynman diagrams of the process are shown in Figure III.40.

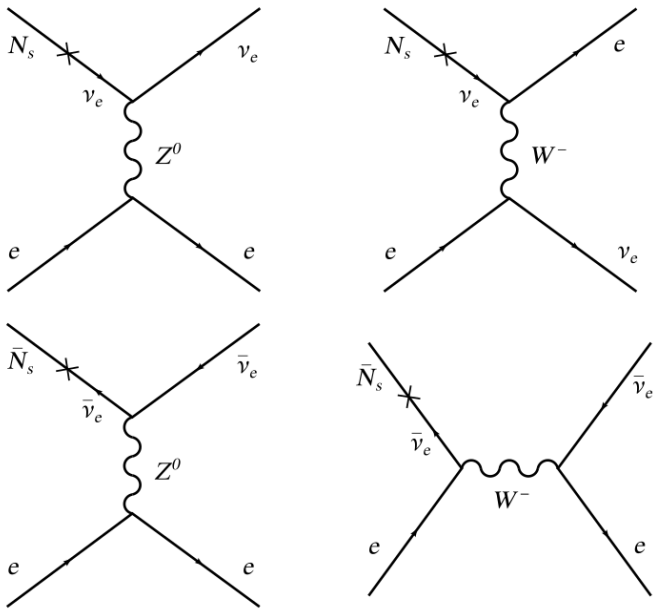

Figure III.40 – Feynman diagram of the interaction between sterile neutrinos and electrons [187]

The interaction is described by the Lagrangian

$$\mathcal{L} = -\frac{G_F}{\sqrt{2}}[\bar{\nu}_e\gamma^\mu(1-\gamma^5)\nu_e][\bar{e}\gamma_\mu(g'_V - g'_A\gamma^5)e] \tag{III.26}$$

with $g'_V = 1 + g_V$, $g'_A = 1 + g_A$ and

$$\begin{aligned} g_V &= -\frac{1}{2} + 2sin^2(\theta_W) \\ g_A &= -\frac{1}{2} \end{aligned} \tag{III.27}$$

As sterile neutrinos are interacting by incoherent electronic recoils [70], to correctly evaluate the event rate and hence the spectra (cf. Section III.9.3), the ionization cross-section between sterile neutrinos and electrons must be taken into account (cf. Section III.9.2). For this calculation, the first step is to compute the atomic form factor for argon developed in Section III.9.1.
In order to set up the model in the low mass framework, we will follow the procedure used for a similar study with xenon data described in [70], itself following the more general procedure of [191].

III.9.1 Argon Radial Momentum Waveform

As atomic orbitals are time independent, the orbital wave-function Ψ_{nlm} can be expressed as a product of a radial waveform $R_{nl}(r)$ and an angular one $Y_{lm}(\theta, \phi)$ such as:

$$\Psi_{nlm}(r, \theta, \phi) = (-1)^l R_{nl}(r) Y_{lm}(\theta, \phi) \tag{III.28}$$

with n the principal quantum number, l the angular quantum number and m the magnetic quantum number.

The argon spin dependence in the waveform is considered negligible [191].
In the case of noble atoms such as argon, electronic shells are full, hence the orbital wave-function only depends on the radial part and not on the angular one [191]:

$$\sum_{m=-l}^{l} |Y_{lm}|^2 = \frac{2l+1}{4\pi} \tag{III.29}$$

The radial waveform is computed for each argon shell to derive the atomic form factor. For that we use the Roothan-Hartree-Fock method [192]:

$$\widetilde{R}_{nl}(k) = \sum_j \widetilde{S}_{jl}(k) C_{jln} \tag{III.30}$$

in which k is the momentum, $\widetilde{S}_{jl}$ are primitive radial functions taken as a Slater-type orbital depending notably on Z_{jl} the orbital exponent in $m_e\alpha = 3.73$ keV/c^2 units, C_{jln} the orbital expansion coefficients, n and l the usual quantum numbers and j is enumerating orbitals as shown in Figure III.41. The radial momentum waveform is expressed in energy $\mathrm{E}^{-3/2}$.

The expression of S_{jl}'s for several electronic shell configurations can be found in Appendix A.2 of [191]. In our case, we consider the following ones:

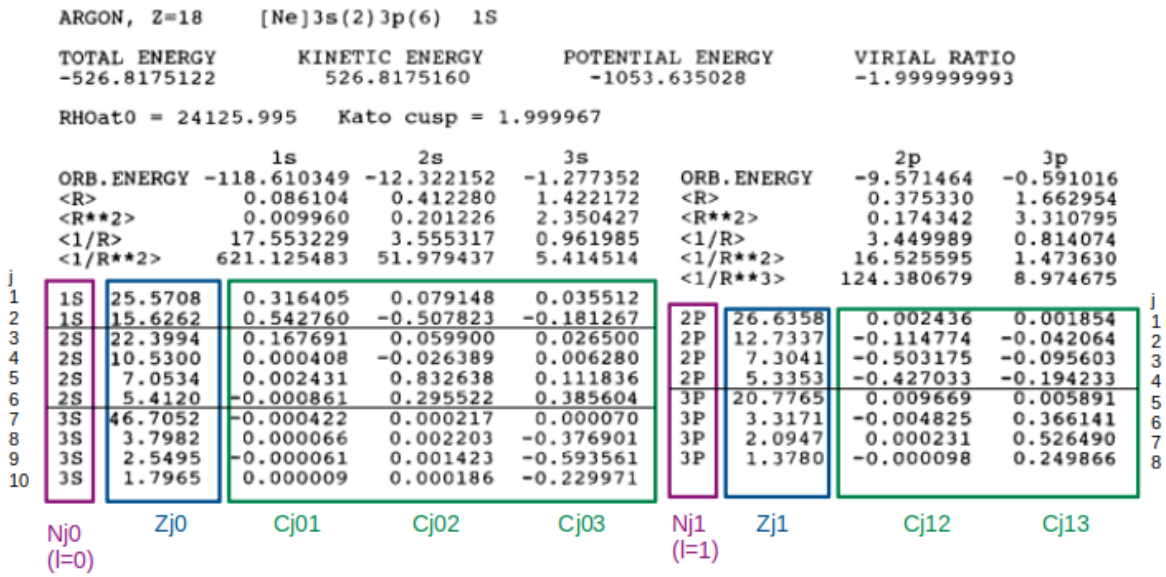

Figure III.41 – Roothaan-Hartree-Fock ground state atomic wave function for argon from [192]

$$
\begin{aligned}
l = 0, N_{j0} = 1 \rightarrow S_{j0}(k) &= \frac{16\pi Z_{j0}^{5/2}}{(Z_{j0}^2 + k^2)^2} \\
l = 0, N_{j0} = 2 \rightarrow S_{j0}(k) &= \frac{16\pi Z_{j0}^{5/2}(3Z_{j0}^2 - k^2)}{\sqrt{3}(Z_{j0}^2 + k^2)^3} \\
l = 0, N_{j0} = 3 \rightarrow S_{j0}(k) &= \frac{64\sqrt{10}\pi Z_{j0}^{9/2}(Z_{j0}^2 - k^2)}{5(Z_{j0}^2 + k^2)^4} \\
l = 1, N_{j1} = 2 \rightarrow S_{j1}(k) &= \frac{64\pi k Z_{j1}^{7/2}}{\sqrt{3}(Z_{j1}^2 + k^2)^3} \\
l = 1, N_{j1} = 3 \rightarrow S_{j1}(k) &= \frac{64\sqrt{10}\pi k Z_{j1}^{7/2}(5Z_{j1}^2 - k^2)}{15(Z_{j1}^2 + k^2)^4}
\end{aligned}
\tag{III.31}
$$

The expression for the 1s shell is hence such as

$$
\begin{aligned}
\widetilde{R}_{10}(k) = c_{101}\frac{16\pi Z_{10}^{5/2}}{(Z_{10}^2 + k^2)^2} + c_{201}\frac{16\pi Z_{20}^{5/2}}{(Z_{20}^2 + k^2)^2} + c_{301}\frac{16\pi Z_{30}^{5/2}(3Z_{30}^2 - k^2)}{\sqrt{3}(Z_{30}^2 + k^2)^3} + c_{401}\frac{16\pi Z_{40}^{5/2}(3Z_{40}^2 - k^2)}{\sqrt{3}(Z_{40}^2 + k^2)^3} \\
+ c_{501}\frac{16\pi Z_{50}^{5/2}(3Z_{50}^2 - k^2)}{\sqrt{3}(Z_{50}^2 + k^2)^3} + c_{601}\frac{16\pi Z_{60}^{5/2}(3Z_{60}^2 - k^2)}{\sqrt{3}(Z_{60}^2 + k^2)^3} + c_{701}\frac{64\sqrt{10}\pi Z_{70}^{9/2}(Z_{70}^2 - k^2)}{5(Z_{70}^2 + k^2)^4} \\
+ c_{801}\frac{64\sqrt{10}\pi Z_{80}^{9/2}(Z_{80}^2 - k^2)}{5(Z_{80}^2 + k^2)^4} + c_{901}\frac{64\sqrt{10}\pi Z_{90}^{9/2}(Z_{90}^2 - k^2)}{5(Z_{90}^2 + k^2)^4} + c_{1001}\frac{64\sqrt{10}\pi Z_{100}^{9/2}(Z_{100}^2 - k^2)}{5(Z_{100}^2 + k^2)^4}
\end{aligned}
\tag{III.32}
$$

Expressions for 2s and 3s, respectively $\widetilde{R}_{20}$ and $\widetilde{R}_{30}$, are similar to Equation III.32 at the exception of the coefficients which should be taken in the appropriate column in Figure III.41 (respectively, Cj02 for 2s and Cj03 for 3s).

Concerning p shells, the radial wave-form for the 2p shell can be express as $\widetilde{R}_{21}$:

$$\begin{aligned}\widetilde{R}_{21}(k) = c_{112}\frac{64\pi k Z_{11}^{7/2}}{\sqrt{3}(Z_{11}^2+k^2)^3} + c_{212}\frac{64\pi k Z_{21}^{7/2}}{\sqrt{3}(Z_{21}^2+k^2)^3} + c_{312}\frac{64\pi k Z_{31}^{7/2}}{\sqrt{3}(Z_{31}^2+k^2)^3} \\ + c_{412}\frac{64\pi k Z_{41}^{7/2}}{\sqrt{3}(Z_{41}^2+k^2)^3} + c_{512}\frac{64\sqrt{10}\pi k Z_{51}^{7/2}(5Z_{51}^2-k^2)}{15(Z_{51}^2+k^2)^4} + c_{612}\frac{64\sqrt{10}\pi k Z_{61}^{7/2}(5Z_{61}^2-k^2)}{15(Z_{61}^2+k^2)^4} \\ + c_{712}\frac{64\sqrt{10}\pi k Z_{71}^{7/2}(5Z_{71}^2-k^2)}{15(Z_{71}^2+k^2)^4} + c_{812}\frac{64\sqrt{10}\pi k Z_{81}^{7/2}(5Z_{81}^2-k^2)}{15(Z_{81}^2+k^2)^4}\end{aligned} \tag{III.33}$$

The expression for 3p, $\widetilde{R}_{31}$ is similar to Equation III.33 at the exception of the coefficients which should be taken in the 3p / Cj13 column in Figure III.41.

III.9.2 Cross-section

To calculate the cross-section, we start by computing the free cross-section before taking into account bound electrons as they lead to larger recoils [70]. This last will then be used for inferring the rate and spectra as it is a more realistic description.

Free Cross-section. We consider the case where the initial electron is free. This electron is supposed at rest, so its energy is equal to its inertial mass: $E_e = m_e$. As the sterile neutrino velocity in the standard halo model gives $\beta \simeq 10^{-3}$, its behavior is considered none-relativistic. In addition, we can consider $E_{\nu_s} \simeq m_{\nu_s} + \frac{1}{2}m_{\nu_s}\beta^2$ with m_{ν_s} the sterile neutrino mass and β its velocity divided by the light speed.
It gives the differential free cross-section as developed in Equation III.34 [70].

$$\frac{d\sigma^{free}}{dE_k} = \frac{2G_F^2 m_e}{\pi\left|\vec{p}_{\nu_s}\right|^2}\left|U_{e4}\right|^2\left[g_1^2 E_{\nu_s}(E_{\nu_s}+\frac{m_{\nu_s}^2}{2m_e}) + g_2^2(E_{\nu_s}-E_k)(E_{\nu_s}-E_k+\frac{m_{\nu_s}^2}{2m_e}) - gg_1gg_2(m_eE_k+\frac{1}{2}m_{\nu_s}^2)\right] \tag{III.34}$$

$$\begin{aligned} gg_1 &= 1+\frac{1}{2}(g_V+g_A) \\ gg_2 &= \frac{1}{2}(g_V-g_A)\end{aligned} \tag{III.35}$$

G_F stands for the Fermi coupling constant expressed in distance per energy units as 1.45×10^{-24} cm/GeV, E_k the recoil energy, gg_1, gg_2 as Equation III.35, $\left|U_{e4}\right|^2$ the mixing angle between the sterile neutrino and the electronic active neutrino and $|\vec{p}_{\nu_s}|$ the sterile neutrino momentum equal to $|\vec{p}_{\nu_s}| = m_{\nu_s}\beta$.
We only consider the electronic coupling as we are measuring interactions between sterile neutrinos and electrons via: $\nu_s e^- \to \nu_e e^-$ and $\bar{\nu}_s e^- \to \bar{\nu}_e e^-$. The free cross-section shown for a 40 keV sterile neutrino, assuming $\left|U_{e4}\right|^2 = 5\times10^{-4}$ at $\beta = 10^{-3}$ is showed in Figure III.42. The results we obtain are the same as the one in [70] since Equation III.34 do not depends on the target nuclei.

Ionisation Cross-section. To correctly evaluate the scattering cross-section we have to consider bound electrons. Hence, we consider a bound electron (p_B, θ_B, ϕ_B) in a shell

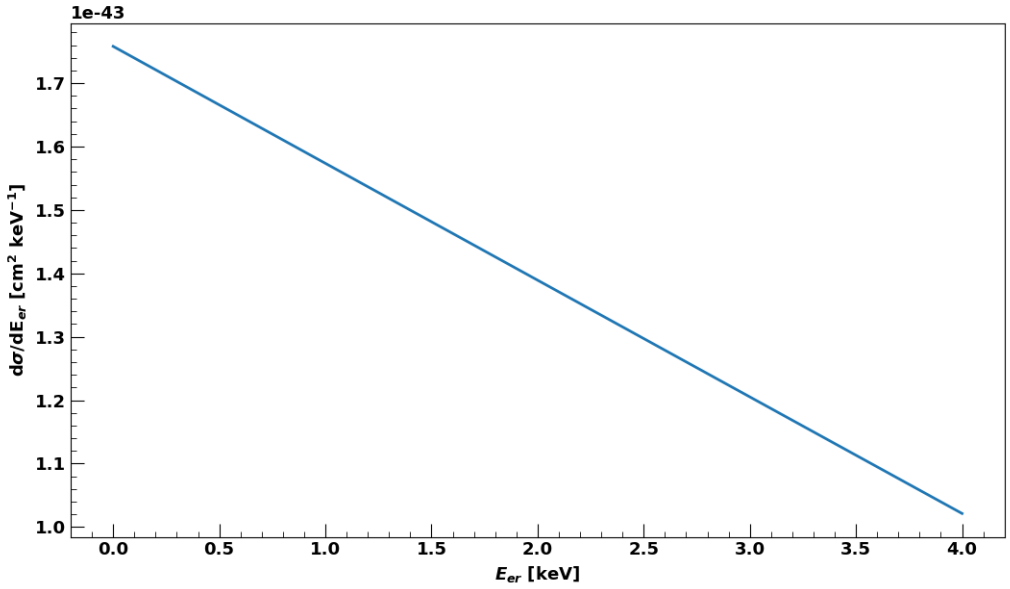

Figure III.42 – Free differential cross-section of 40 keV sterile neutrinos with $|U_{e4}|^2 = 5 \times 10^{-4}$ for a recoil energy between 0 and 4 keV

t (t being either 1s, 2s, 2p, 3s or 3p). We consider its effective mass $\widetilde{m}$ such as Equation III.36 with $E_B = m_e - \epsilon$ its energy and p_B its momentum [191] [70][2]. ϵ is the binding energy of the bound electron and depends on its shell.

$$\widetilde{m}^2 = E_B^2 - |\vec{p}_B|^2 \tag{III.36}$$

From the Lagrangian of Equation III.26, we derive the averaged square amplitude $|\mathcal{M}|^2$ as:

$$|\mathcal{M}|^2 = 16G_F^2 |U_{e4}|^2 [gg_1^2(s-m_e^2)(s-\widetilde{m}^2-m_{\nu_s}^2)+gg_2^2(u-\widetilde{m}^2)(u-m_e^2-m_{\nu_s}^2)+2gg_1gg_2m_e\widetilde{m}(t-m_{\nu_s}^2)] \tag{III.37}$$

Its cross-section is then expressed as Equation III.38 [70]. This expression considers neither spin effects nor relativistic effects.

$$\frac{d\sigma_t}{dE_k} = \int \frac{p_B^2 dp_B d(cos(\theta_B) d\phi_B}{(2\pi)^3} \frac{|R_t(\vec{p_B})|^2}{4\pi} \frac{|\mathcal{M}|^2}{4E_{\nu_s}E_B|\beta - p_B/\widetilde{m}|} \frac{1}{8\pi\lambda^{1/2}(s, m_{\nu_s}^2, \widetilde{m}^2)} \left|\frac{du}{dE_k}\right| \tag{III.38}$$

with $\lambda(a,b,c) = a^2+b^2+c^2-2ab-2bc-2ac$ the Kallen function. As usual, $\beta = v_{\nu_s}/c$ with v_{ν_s} the sterile neutrino velocity and c the light speed. The radial momentum waveform $|R_t(\vec{p_B})|^2$ is calculated following Section III.9.1.
The kinematic variables used are:

- for the sterile neutrino:

$$p_{\nu_s} = (E_{\nu_s}, 0, 0, |\vec{p}_{\nu_s}|) \tag{III.39}$$

$$E_{\nu_s} = m_{\nu_s} + \frac{1}{2} m_{\nu_s} \beta^2 \tag{III.40}$$

[2]There is a dimension mistake in [70], page 2, on the effective mass that should be squared as shown in Equation III.36.

$$|\vec{p}_{\nu_s}| = m_{\nu_s}\beta \tag{III.41}$$

- for the bound electron:

$$p_B = (E_B, |\vec{p}_B|\sin\theta_B\cos\phi_B, |\vec{p}_B|\sin\theta_B\sin\phi_B, |\vec{p}_B|\cos\theta_B) \tag{III.42}$$

$$E_B = m_e - \epsilon \tag{III.43}$$

$\theta_B \in [0,\pi]$ is integrated in the ionisation cross section integral. $\phi_B \in [0, 2\pi]$ is integrated in the ionisation cross section integral
$|\vec{p}_B|$ is integrated in the ionisation cross section integral between 0 and $p_{B_{max}}$, $p_{B_{max}} = |\vec{p}_{\nu_s}| + \sqrt{(E_{\nu_s} + m_e - \epsilon)^2 - m_e^2}$ for $E_{\nu_s} > \epsilon$.

- for the outgoing electron:

$$p_e = (E_e, |\vec{p}_e|\sin\theta_R, 0, |\vec{p}_e|\cos\theta_R) \tag{III.44}$$

$$E_e = m_e + E_k \tag{III.45}$$

$$|\vec{p}_e| = \sqrt{E_e^2 - m_e^2} \tag{III.46}$$

$$\theta_R = 2\arctan\left(\frac{\zeta_1 \pm \sqrt{\zeta_1^2 - \zeta_2}}{2\zeta_3}\right) \in [0,\pi] \tag{III.47}$$

with $\zeta_1 = 2|\vec{p}_B||\vec{p}_e|\sin\theta_B\cos\phi_B$
$\zeta_2 = 4[(E_e(E_{\nu_s} + E_B) - \xi)^2 - |\vec{p}_e|^2(|\vec{p}_{\nu_s}| + |\vec{p}_B|\cos\theta_B)^2]$
$\zeta_3 = E_e(E_{\nu_s} + E_B) - \xi + |\vec{p}_e|(|\vec{p}_{\nu_s}| + |\vec{p}_B|\cos\theta_B)$
$\xi = (1/2)(m_{\nu_s}^2 + \widetilde{m}^2 + m_e^2) + E_{\nu_s}E_B - |\vec{p}_{\nu_s}||\vec{p}_B|\cos\theta_B$
θ_R angle is obtained by using the conservation of momentum and neglecting the electronic neutrino mass, $p_{\nu_e}^2 = (p_{\nu_s} + p_B - p_e)^2 = 0$.

- for the electronic neutrino:
$m_{\nu_e} = 0$
$p_{\nu_e}^2 = 0$

Usual Mandelstam variables s, t, u are defined and developed in Equation III.48 [70] [187].

$$\begin{aligned} s &= (p_{\nu_s} + p_B)^2 = m_{\nu_s}^2 + \widetilde{m}^2 + 2(E_{\nu_s}E_B - |\vec{p}_B||\vec{p}_{\nu_s}|cos(\theta_B)) \\ t &= (p_{\nu_s} - p_e)^2 = -m_{\nu_s}^2 + 2E_{\nu_s}(E_e - E_B) + 2|\vec{p}_{\nu_s}|(|\vec{p}_B|cos(\theta_B) - |\vec{p}_e|cos(\theta_R)) \\ u &= (p_e - p_B)^2 = m_{\nu_s}^2 + m_e^2 - 2(E_{\nu_s}E_e - |\vec{p}_{\nu_s}||\vec{p}_e|cos(\theta_e)) \end{aligned} \tag{III.48}$$

A derivative of u by the recoil energy is also present in the cross-section. As $E_e = m_e + E_k$, $\frac{du}{dE_k} = \frac{du}{dE_e}$ whose expression is such as [191] [187]:

$$\left|\frac{du}{dE_e}\right| = -2\left(E_{\nu_s} - |\vec{p}_{\nu_s}|\frac{E_e}{|\vec{p}_e|}\cos\theta_R + |\vec{p}_{\nu_s}||\vec{p}_e|\sin\theta_R\frac{d\theta_R}{dE_e}\right) \tag{III.49}$$

with

$$\left|\frac{d\theta_R}{dE_e}\right| = \frac{E_e(|\vec{p}_{\nu_s}|\cos\theta_R + |\vec{p}_B|(\cos\theta_B\cos\theta_R + \sin\theta_B\cos\phi_B\sin\theta_R)) - |\vec{p}_e|(E_{\nu_s} + E_B)}{|\vec{p}_e|^2[|\vec{p}_{\nu_s}|\sin\theta_R + |\vec{p}_B|(\cos\theta_B\sin\theta_R - \sin\theta_B\cos\phi_B\cos\theta_R))]} \tag{III.50}$$

Finally, the energy of the outgoing electron E_e is bound by the condition in Equation III.47 that $\zeta_1^2 \geq \zeta_2$ to ensure a positive value inside the square root. This leads to

$$E_{e_{min}} = \frac{\xi(E_{\nu_s} + E_B) - \Xi\sqrt{\xi^2 - m_e^2((E_{\nu_s} + E_B)^2 - \Xi^2)}}{(E_{\nu_s} + E_B)^2 - \Xi^2} \tag{III.51}$$

$$E_{e_{max}} = \frac{\xi(E_{\nu_s} + E_B) + \Xi\sqrt{\xi^2 - m_e^2((E_{\nu_s} + E_B)^2 - \Xi^2)}}{(E_{\nu_s} + E_B)^2 - \Xi^2} \tag{III.52}$$

with

$$\Xi^2 = (|\vec{p}_{\nu_s}| + |\vec{p}_B|\cos\theta_B)^2 + (|\vec{p}_B|\sin\theta_B\cos\phi_B)^2 \tag{III.53}$$

Differential ionisation cross-sections for various sterile neutrino masses are shown in Figure III.43. As expected, the cross-section is mainly increasing with sterile neutrino masses.

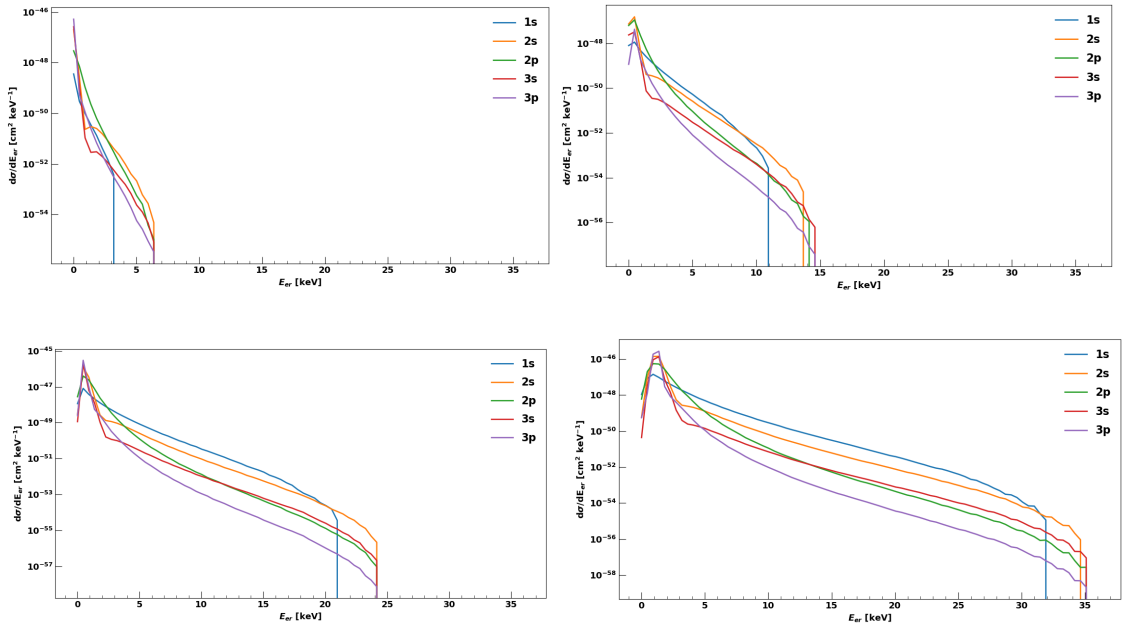

Figure III.43 – Differential ionisation cross-section with $|U_{e4}|^2 = 5 \times 10^{-4}$ from the low mass framework for each of the argon shell for respectively from top to bottom and left to right, 7, 15 and 25 and 36 keV sterile neutrinos.

III.9.3 Rate and Spectra

The differential event rate for each shell t is:

$$\frac{dR_t}{dE_k} = \frac{\rho_0 n_e}{m_{\nu_s}} \int \frac{d\sigma_t}{dE_k} f(v) v dv \tag{III.54}$$

with $\rho_0 = 3 \times 10^5$ keV/cm^3 the dark matter local density [193], m_{ν_s} the sterile neutrino mass, $n_e = \frac{1[kg]}{M_{Ar}} \times N_A = 2.7 \times 10^{26}$ kg^{-1} the number of electrons per kilogram, N_A Avogadro constant and M_{Ar} the argon molar mass.

We integrate the sterile neutrino rate between $v_{esc}/10,000$ and v_{esc}. Then, by multiplying the differential event rate summed on all shells by M_{det} the detector mass and T its exposure time, we can draw the differential number of events (Equation III.55). In DarkSide-50, $M_{det} = 46.7$ kg and $T = 515.21$ days.

$$\frac{dN}{dE_k} = M_{det} T \sum_t n_t \frac{dR_t}{dE_k} \tag{III.55}$$

with n_t the number of electrons per orbital.

Finally, for each mass, we integrate between 0 and the rest mass this differential number of events depending on E_{er}, the recoil energy retrieving a global keV-spectrum (cf. Figure III.44). Then, we convert the keV scale into a number of electrons using the electronic recoil energy scale that has been calibrated for DarkSide-50 and take into account the detector's corrections (Figure III.45). The spectra obtained in this way is used for inferring the limits in the next section.
The minimum recoil energy taken for integration is not model dependent and is assumed equal to 0 [67] [68].

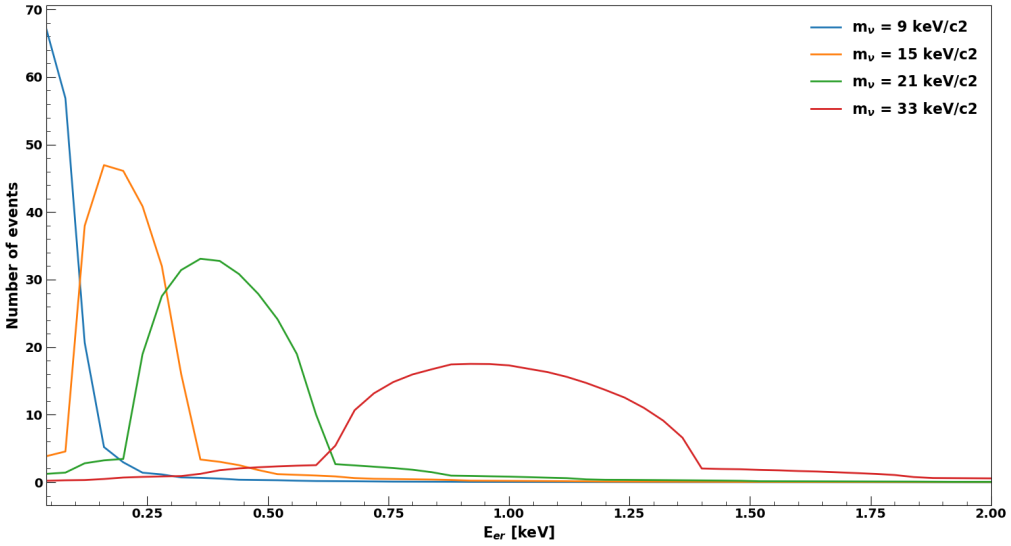

Figure III.44 – Number of events for bound electrons with $|U_{e4}|^2 = 5 \times 10^{-4}$ for 9, 15, 21 and 33-keV sterile neutrino masses on a 0 - 36 keV electronic recoil range

III.9.4 Observed Limits

For inferring the limits, we compute which minimal numbers of electrons can be detected by the detector and apply the corresponding threshold. In XENON100, the cut was taken at 1 keV [70]. However, with DarkSide-50 we can have a lower threshold as its minimum threshold is at 4 electrons (the background is not evaluated below). This corresponds to recoil energy of 55 eV. The maximum number of electrons taken is 170 which contains the whole sterile neutrino spectra. In addition, it is enough to have a good estimation of the background and within the range of the liquid argon ionization response calibration.

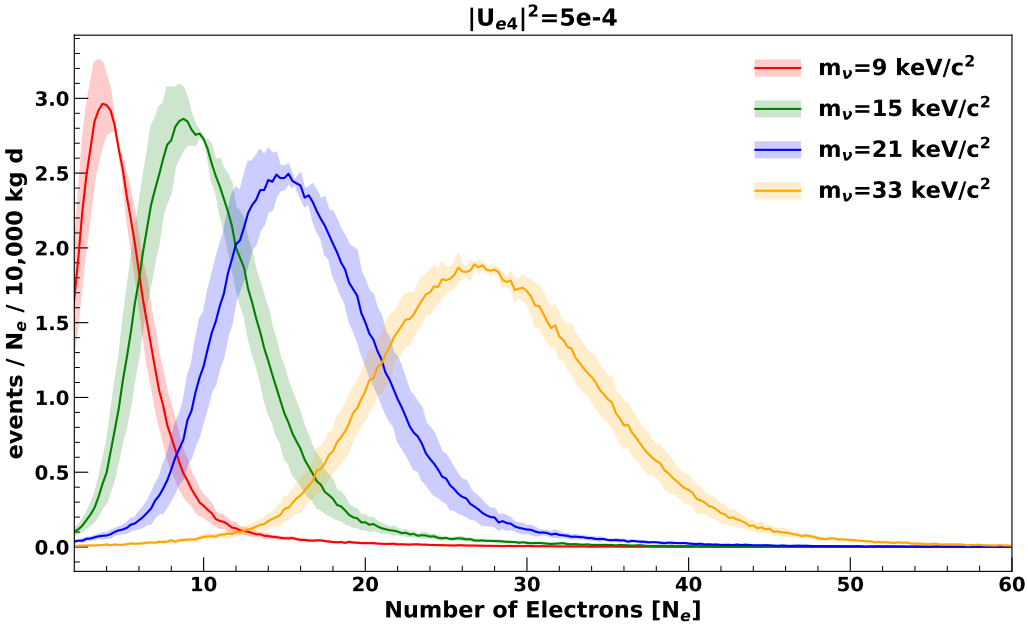

Figure III.45 – 9, 15, 21 and 33-keV sterile neutrino spectra depending on number of electrons, $|U_{e4}|^2 = 5 \times 10^{-4}$. Error bands are associated to the uncertainties on the calibration of electronic and nuclear recoil energy scales.

It is worth noting that, as mentioned previously, between 0.08 and around 1 keV (the precise value depends on the sterile neutrino mass), the rate is higher for low sterile neutrino masses (cf. Figure III.44) which will cause an inversion on the limit slope along with the masses when taking into account the whole recoil energy range.

Observed and expected upper limit of 90%C.L. are shown in Figure III.46. When comparing with the expected mixing angle range ($\ll 10^{-7}$) [188] [189] [190] and with limits from astrophysical measurements [74] and β-decay neutrino detection [194] (Figure III.47), the DarkSide limit is not competitive.

Finally, data and background model compared to expected spectra of leptophilic candidates, including sterile neutrinos, are shown in Figure III.39.

III.10 Annual Modulation

As presented in Section I.4, the annual modulation is one of the expected signature for dark matter. While DAMA/LIBRA has claimed to have observed such modulation at 8.9σ [89], other experiments tend to discard such observation. Using DarkSide-50 data, we construct time series along the whole data taking allowing to test both the DAMA/LIBRA and the no-modulation hypotheses.

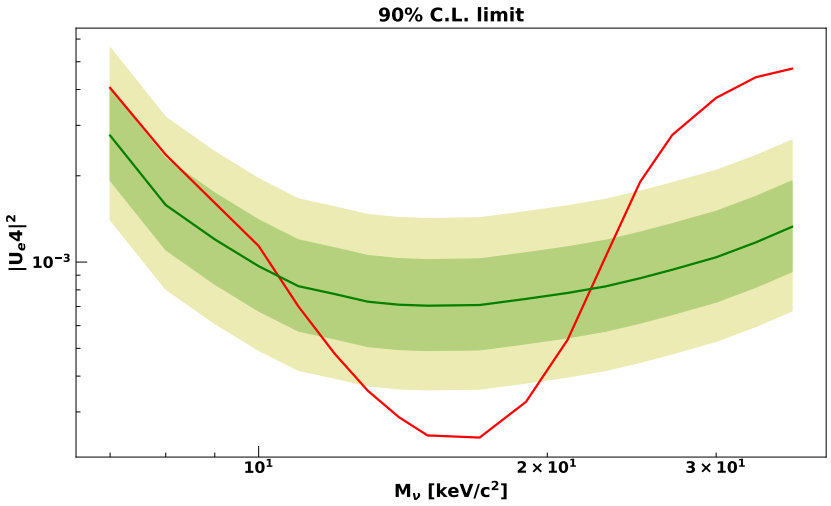

Figure III.46 – Observed (red lines) and expected limits (green dotted lines) with the ± 1-σ (green shaded area) and ± 2-σ (yellow shaded area) bands for 90% upper limits on sterile neutrino-electron mixing element $|U_{e4}|^2$.

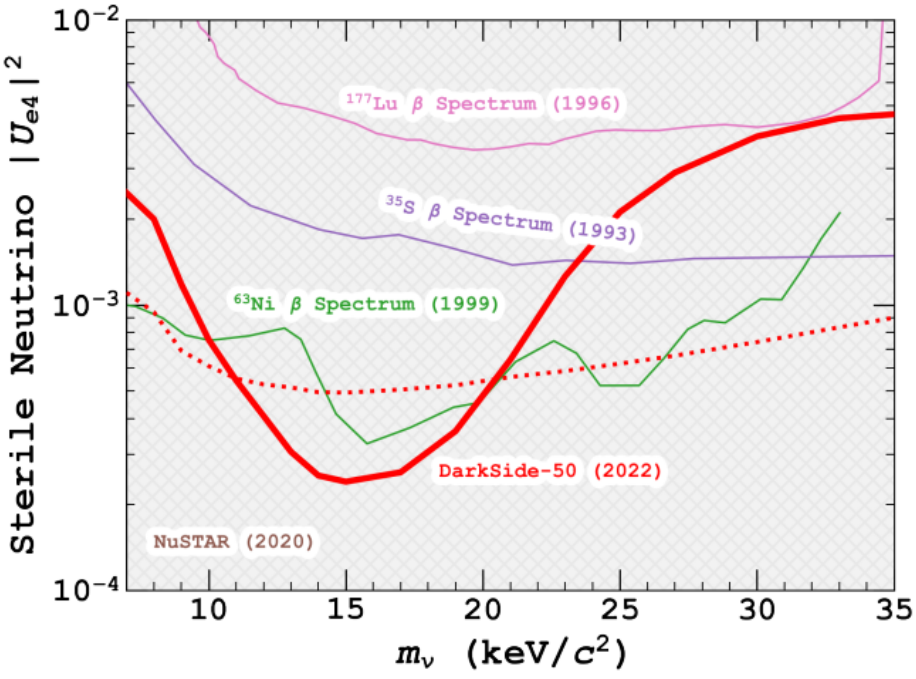

Figure III.47 – Exclusion limits at 90% CL on $|U_{e4}|^2$ for sterile neutrinos depending on their mass from DarkSide-50 between 0.08 - 36 keV (4e- cut). The observed limit is shown as a solid red lines while the expected limit at -1σ is shown as a dashed red line. Limits from Nickel [194], Sulfur [195] and Lutetium [196] β-decays are also reported. The strongest limit set by NuSTAR experiment [74] goes to $|U_{e4}|^2 = 10^{-13}$ at 20 keV/c^2.

III.10.1 Time series preparation

We use DarkSide-50 low-mass data selection as presented already in Section III.4. The dataset consists of $\sim 7.5\times10^5$ single scatter events. It includes runs from January 26th, 2016 (run 14698) to October 23th, 2017 (run 19698). Dates of each run are extracted and converted to calendar date considering the origin date (April 20th, 2015).

We then apply a cut on the number of electrons. DAMA/LIBRA claims to observe an annual modulation below 6 keVee and has a minimum threshold of 2 keVee [89]. XENON-100 uses the same energy cut [197] while XMASS-1 [198] uses a lower threshold of 1 keVee, still stopping at 6 keVee. In DarkSide-50 we are able to reach a minimum threshold of 4 electrons which means an energy of 0.06 keVee. Hence, it seems natural to test the modulation hypothesis in the 0.06-6 keVee range, so between 4 and 68 electrons.

Once we performed the selection on the energy range, we group events by run, and for each we count the number of events. Grouping runs in 14 days bins, we compute in each bin the total number of events divided by the lifetime within that time bin. The number of days associated to each bin is taken as the mean of the time value of each bin. The resulting time series is shown in Figure III.48.

III.10.2 Fit of the time series

As described in Section I.4, the theoretical model for annual modulation is composed of a time average rate and a cosine modulation term (Equation I.5). In the case of an experiment, additional background due to long-live radioactivity should also be taken into account. In the case of DarkSide-50, we take into account both ^{60}Co ($\tau_{Co} = 2777.59$ days) and ^{85}Kr ($\tau_{Kr} = 5667.814$ days) decays. We fix ϕ, T to their expected values.

$$f(t) \simeq A_{flat} + B_{sig}\cos\left(\frac{2\pi(t-\phi)}{T}\right) + C_{kr}\exp\left(-t/\tau_{Kr}\right) + D_{co}\exp\left(-t/\tau_{Co}\right) \quad \text{(III.56)}$$

The fit is also shown in Figure III.48.
The amplitude of modulation (B) is expressed in cpd (count per day) and is compatible with zero. To compare it with results from other experiments, we convert it in cpg/kg/keV by dividing it by the mass of the core area of the detector (46.233 kg) and the energy range in keV based on the electron energy scale of DarkSide-50 [96]. It gives $2.5\times10^{-3}\pm2.4\times10^{-3}$ cpg/kg/keV.

III.10.3 Statistical tests

We consider two different null hypothesis. First, the no modulation scenario where the modulation amplitude B in the model equals zero. Then, the DAMA/LIBRA scenario with a modulation amplitude of (0.0116 ± 0.0013) cpd/kg/keV, a phase of (146 ± 7) days and a period of (0.999 ± 0.002) years [89]. All other parameters of the model are set to the fit values. The models for the different scenarios are shown in Figure III.49.

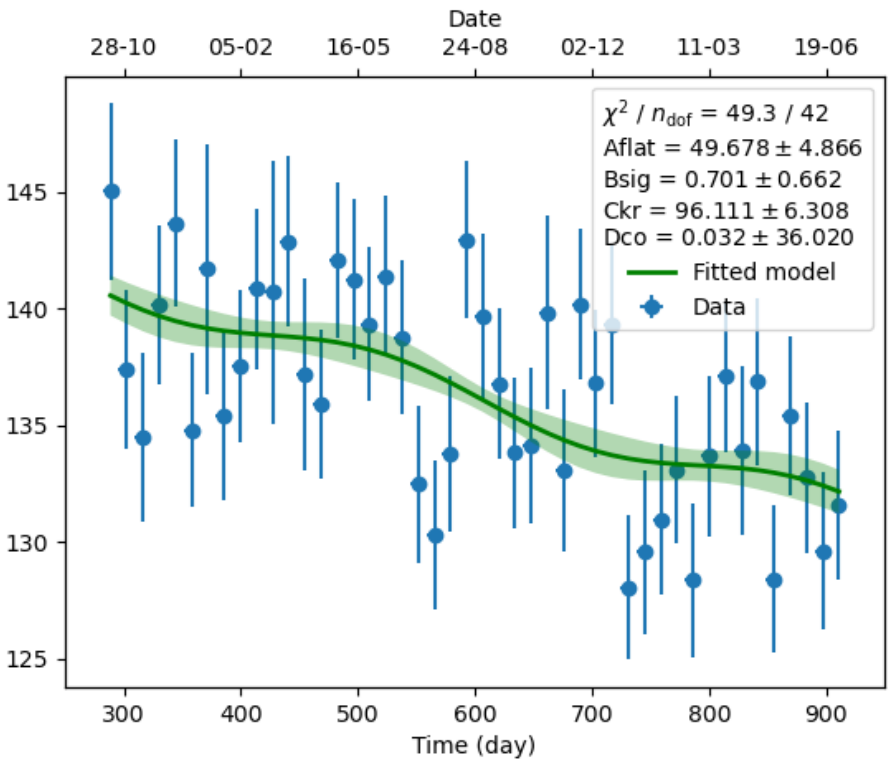

Figure III.48 – Fit of the time series between 0.06 and 6 keVee using the model described by Equation III.56.

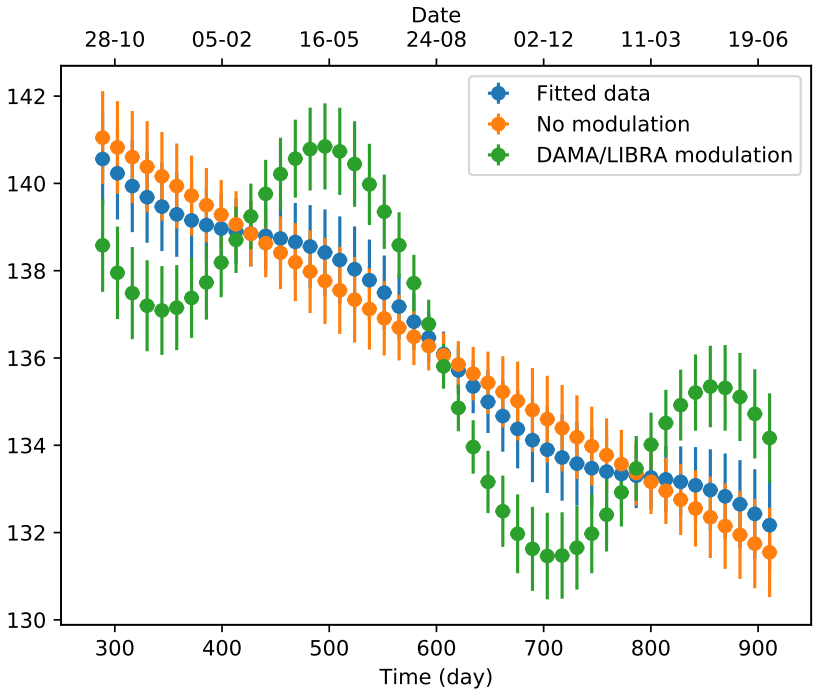

Figure III.49 – Models of the different modulation scenarios between 0.06 and 6 keVee using model III.56. Details of the parameters in the text.

We compare the parameter value of the fitted modulation amplitude to the one for both

null hypotheses. To do this, for each null hypothesis, we use a statistical test (t-test) following a t-distribution, with the number of degrees of freedom as the number of values of the data set (n) subtracted to the number of variable parameters d, defined such as [199]:

$$t_{stat} = (\beta_{fit} - \beta_{nh})/\sigma \tag{III.57}$$

with β_{fit} the value of the parameter given by the fit, β_{nh} the value of the parameter from the null hypothesis and σ the error of the parameter given by the fit.

The associated p-value for this test is [199]:

$$p = 2(1 - \mathbb{P}(T_{n-d} \leq |t_{stat}|)) \tag{III.58}$$

with $\mathbb{P}(T_{n-d} \leq |t_{stat}|)$ the probability for a random variable T with n - d degrees of freedom to be below or equal to $|t_{stat}|$.

When performing multiple tests (two null hypotheses in this case), we have to control the family-wise error rate which is the probability of having false positives or type one error in multiple tests. To do this, we use Holm-Bonferroni method [200] which allows to compute the associated correction of the p-value.

For the no-modulation hypothesis, we find a p-value of 0.295, so the no-modulation is not rejected, only slightly disfavored at 1σ.
However, for the DAMA/LIBRA hypothesis, we find a p-value of 0.001, so this scenario is rejected at 3.29σ.

This is a preliminary study and we did not take into account the different systematics.

Chapter IV

Low-level Data Reconstruction

Big things have small beginnings sir.

Lawrence of Arabia (Movie: 1962)

In order to reconstruct events in DarkSide-20k, we apply a strategy aiming at identifying each photo-electron in the acquired waveforms. To do this, we developed a procedure based on a custom algorithm with the following steps:

- The raw waveform is filtered using matched filtering. This filtering is implemented to maximize the signal-to-noise ratio. The filter is the convolution between the waveform and the SiPM time-reversed response. An example is shown on Figure IV.1 in which we can see the cusp produced after the application of the filter.

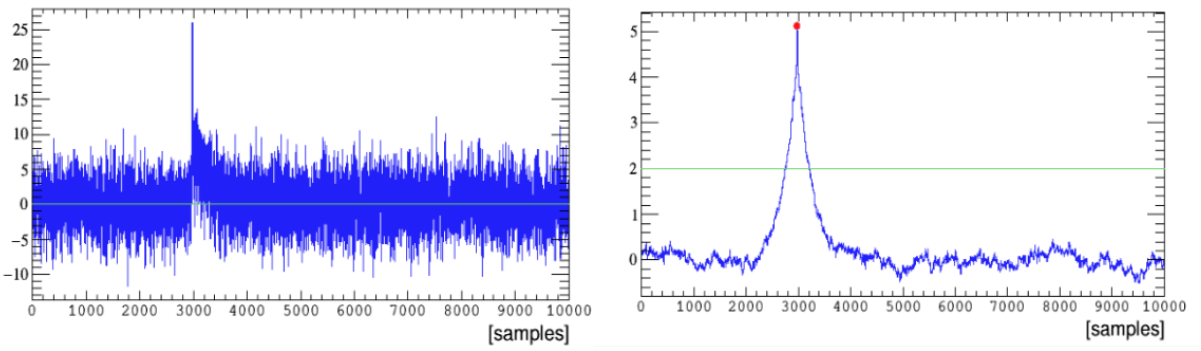

Figure IV.1 – Raw waveform (left) and resulting waveform after filtering (right).

- The moving average of the filtered waveform is then subtracted from the filtered waveform itself (Figure IV.2).
- The RMS of the resulting shape is calculated on the first n samples.
- All samples with values below 3×RMS are set to zero and slices of non-empty waveforms ("segments") are identified (Figure IV.3 - left).
- For each one of these segments, the time and height of the maximal hit ("prominence") and the integral of the segment (Figure IV.3 - right) are stored.
- Last, hits with an integral-to-prominence ratio smaller than a given threshold (which account for fluctuations) are rejected.

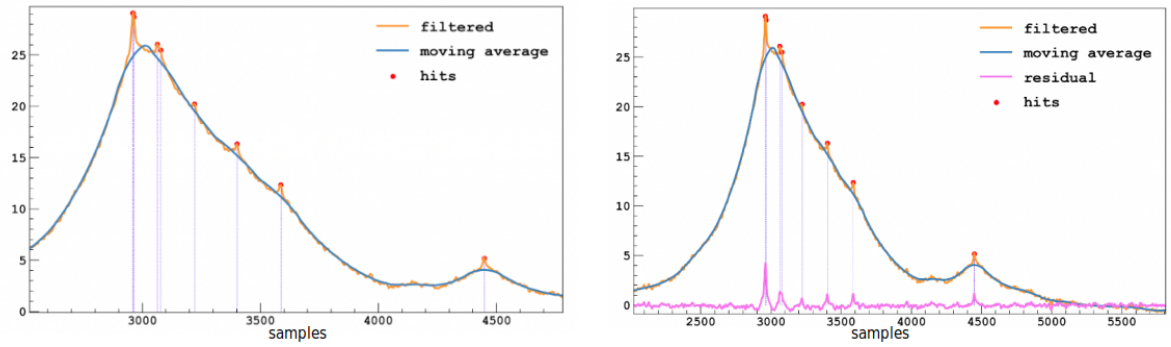

Figure IV.2 – Hit finder algorithm description: (left) Moving average computed from the filtered waveform and (right) residuals computed from the difference between the filtered waveform and its moving average.

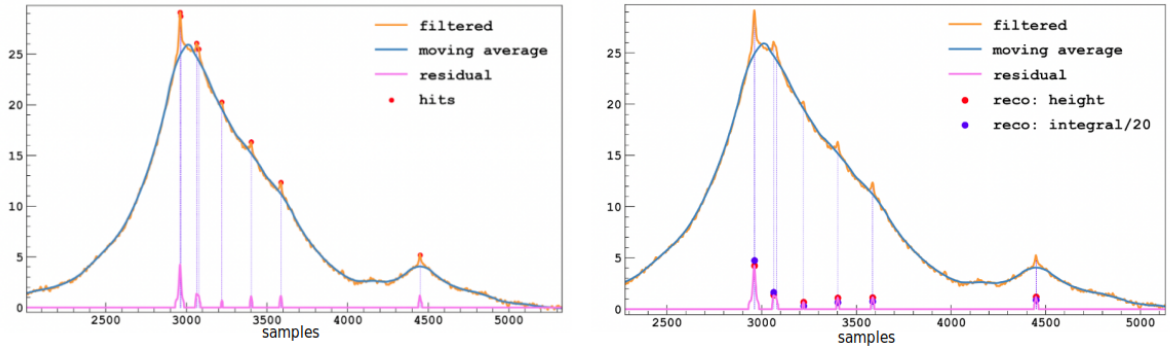

Figure IV.3 – Hit finder algorithm description: (left) residuals with values below 3×RMS are set to zero, (right) the height and integral of residuals hits are computed.

It is implemented with the Numba python libraries for optimizing the computing resources.
From this algorithm, we define the prominence (or pk_p) as the maximal height of the filtered waveform after the moving average subtraction and the hit integral (or pk_k) as the integral of the positive segment of the filtered waveform after the moving average subtraction.

IV.1 Hit Finder Optimisation

In order to optimize the hit finding, the hit finder algorithm must be fine tuned. Its parameters are:

- **The window length used for calculating the moving average (MA-gate).** A gate too short approximates too much the cusp lowering prominence and hence the detection efficiency. However, a gate too large induces a large number of hits due to waveform fluctuations. We expected this value to be around 150 samples, a sample being 4 ns.
- **The size of the window (SW) to compute the RMS**.
- **The discrimination threshold** between real hits and fluctuations. To tune this threshold we tested several options such as using a cut on the prominence, on the

hit integral or on the hit integral divided by the prominence. The second option, setting a cut on the hit integral, gives the best performance. To be noted that the hit integral and prominence are strongly depending on the MA-gate, and hence this parameter is dependant on both others.

In order to optimise these three parameters we test them on laser runs. We start by fixing the first two parameters at their nominal values (respectively 150 and 550 samples) and test different discrimination thresholds. When a range of working thresholds is determined we optimize values for the other parameters to improve results. Then, we do the full laser reconstruction by looking at the prominence and the hit integral in each channel. For that, we look for correlation between the prominence and the hit integral. Examples of laser events are shown in Figure IV.4.

We test different thresholds by applying cuts on the integral. We achieve a good hit identification with a cut ranging from 5 to 23 samples.

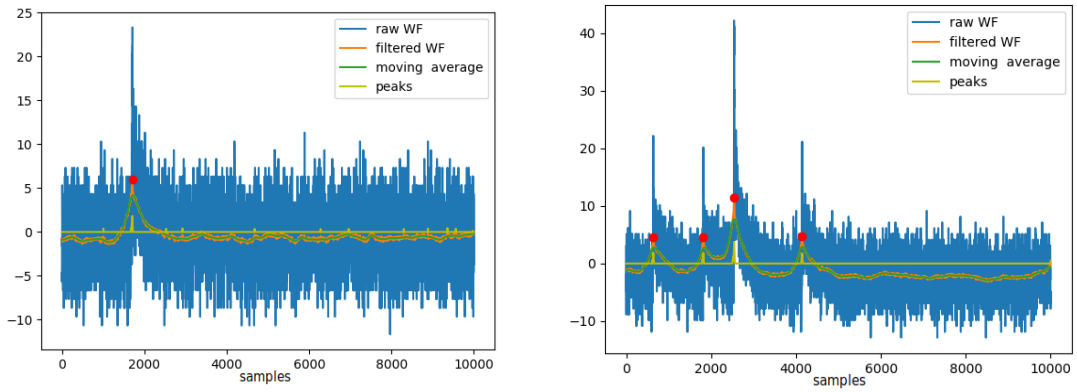

Figure IV.4 – Examples of hit detection on laser runs (run 1650) with MA-gate = 150 samples, SW = 550 samples and an hit integral threshold between 5 and 23 samples. Kept peaks are highlighted by a red point at their top.

To retrieve more precise and robust values for these adjustment parameters, further tests have been performed inside the collaboration on simulation and physics runs. The results of these tests have been implemented inside reconstruction frameworks using this hit finder.

IV.2 Laser Calibration

SiPM response needs to be calibrated to retrieve for each hit of the signal the associated number of single photo-electrons. Thanks to the calibration, we also monitor the occupancy and stability of the detector over the runs.
The calibration procedure relies on a 405 nm laser diode that emits light pulses at 1 kHz rate with a power higher than 200 mW. Laser pulses are brought inside the detector by optical fibers.

We perform this calibration on two different data sets. First on Proto-0 laser runs taken during November 2019 and then on laser runs of ReD taken between December 2019 and

February 2020. In this chapter we report the procedure and results on Proto-0 data. No significant differences are observed when looking at ReD data.

We will first go through the different steps of the calibration procedure before examining the laser occupancy and the monitoring of calibration outputs.

IV.2.1 Calibration Procedure

Each channel of each run is calibrated individually. To perform this calibration, we use two different variables: the charge roi, which is the integral of the raw waveform within a 2 μs gate starting slightly before the beginning of the signal, and the prominence as defined using the hit finder custom algorithm defined in this chapter. Both variables are correlated, but do not provide the same information.

The charge roi response allows to count the number of zero which is necessary for computing the occupancy. However, it has a poorer resolution than the prominence which has a very good resolution and keeps the temporal information, but do not keep track of the zeros (shapes Figures IV.5a and IV.6a, respectively). In addition, the charge roi should theoretically be a Poisson distribution, but the shape is lost because of cross-talks and after-pulses.
The procedure is then twofold: first we fit the prominence (temporal information and good resolution) to secondly select the right charge roi peak which keeps the information concerning zeros. With the prominence step, fits are more accurate.

Calibration Curve. The first step consists on generating the histogram (or finger plot) of the prominence (Figure IV.5a). For that, we select the prominence based on the trigger time and identify peaks that are corresponding to 1, 2, 3, etc, photo-electrons. To have a proper calibration curve we identify at least three prominence peaks. Each one of them is independently fitted by a Gaussian. The fit parameters, namely the centre of the Gaussian (peak position), its sigma and amplitude, are stored.
The calibration curve (Figure IV.5b) is then retrieved by fitting the number of photo-electrons as a function of their associated peak position. A linear fit is performed giving the relation (Equation IV.1) between the prominence position ($prom$) and the number of photo-electrons (npe) with a and b the fit parameters:

$$prom = a \times npe + b \tag{IV.1}$$

Charge roi Gain and σ^2. We then look at charge roi distributions. Using the calibration curve, we identify charge roi peaks associated with a prominence peak, so that they could be associated to the number of photo-electrons thanks to the calibration discussed above. To find the mean charge roi and its width for each number of photo-electrons, each identified charge roi peak is fitted independently with a Gaussian fit (Figure IV.6a). Retrieved fit parameters are the peak position and its sigma.
Each one of these charge roi gains is then associated with its corresponding number of photo-electrons (npe) giving a linear relation (Equation IV.2, Figure IV.6b) between both.

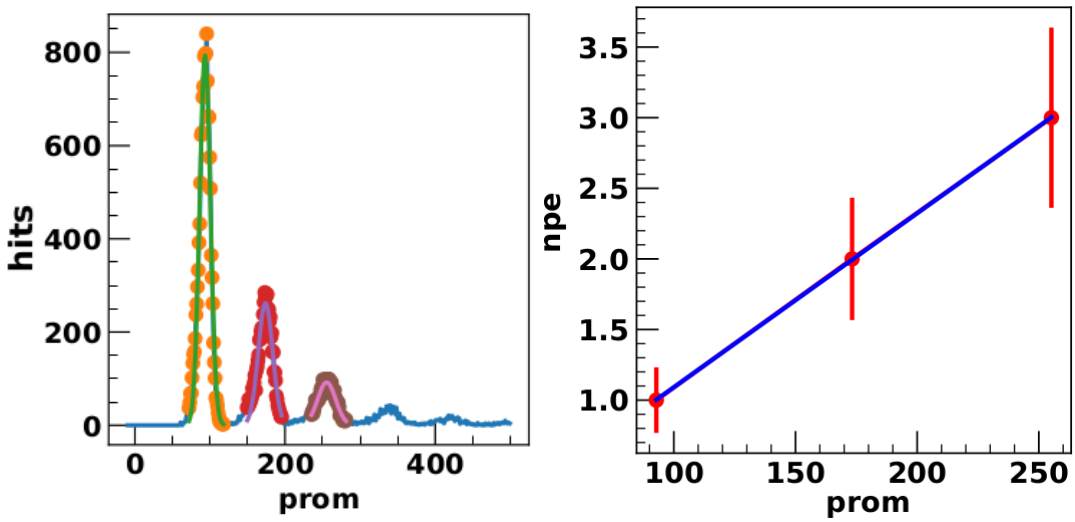

(a) (b)

Figure IV.5 – (a) Independent Gaussian fits on prominence distribution and (b) calibration curve between prominence and number of photo-electrons using results of the fits - Proto-0 run 888, channel 56.

Their parameters c and d are retrieved thanks to a linear fit.

$$gain = c \times npe + d \tag{IV.2}$$

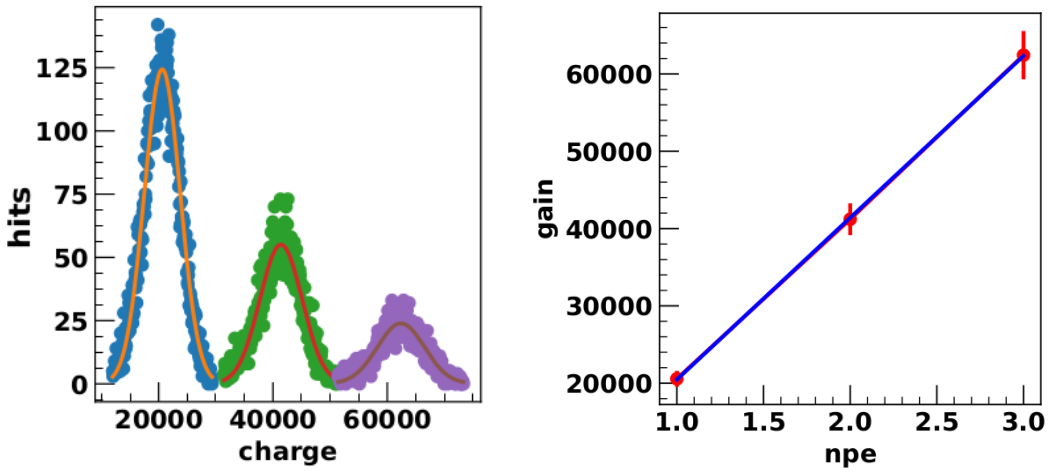

(a) (b)

Figure IV.6 – (a) Independent Gaussian fits on charge roi hits associated with prominence ones and (b) charge roi gain depending on the number of photo-electrons - Proto-0 run 888, channel 56.

The same procedure is applied to the sigma of the charge roi. The square of the sigma is expected to be linear with the number of photo-electrons. The fit parameters σ^2_{ped} and σ^2_{av} are associated to σ^2 of the pedestal and the avalanche, respectively,

$$\sigma^2 = \sigma^2_{ped} \times npe + \sigma^2_{av} \tag{IV.3}$$

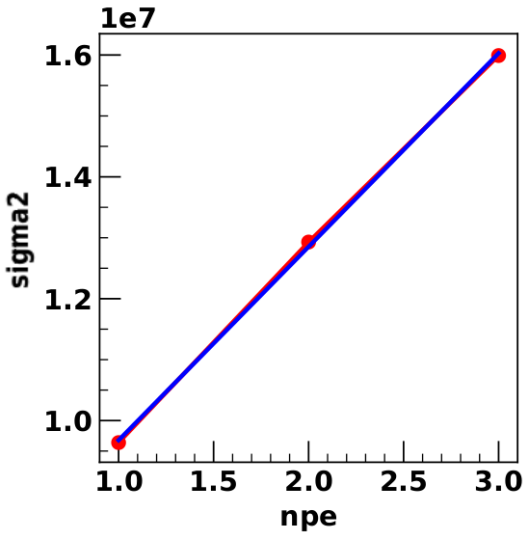

Figure IV.7 – σ^2 depending on the number of photo-electrons - Proto-0 run 888, channel 56. Error on the σ^2 are of the order of 10^4 and so not visible at this scale.

For ReD, we use the same procedure while tuning it and adding a new variable, the hit integral, as defined previously, when using the custom hit finding procedure developed in introduction of this chapter. An example channel 4 (C1) is showed in Figure IV.8.

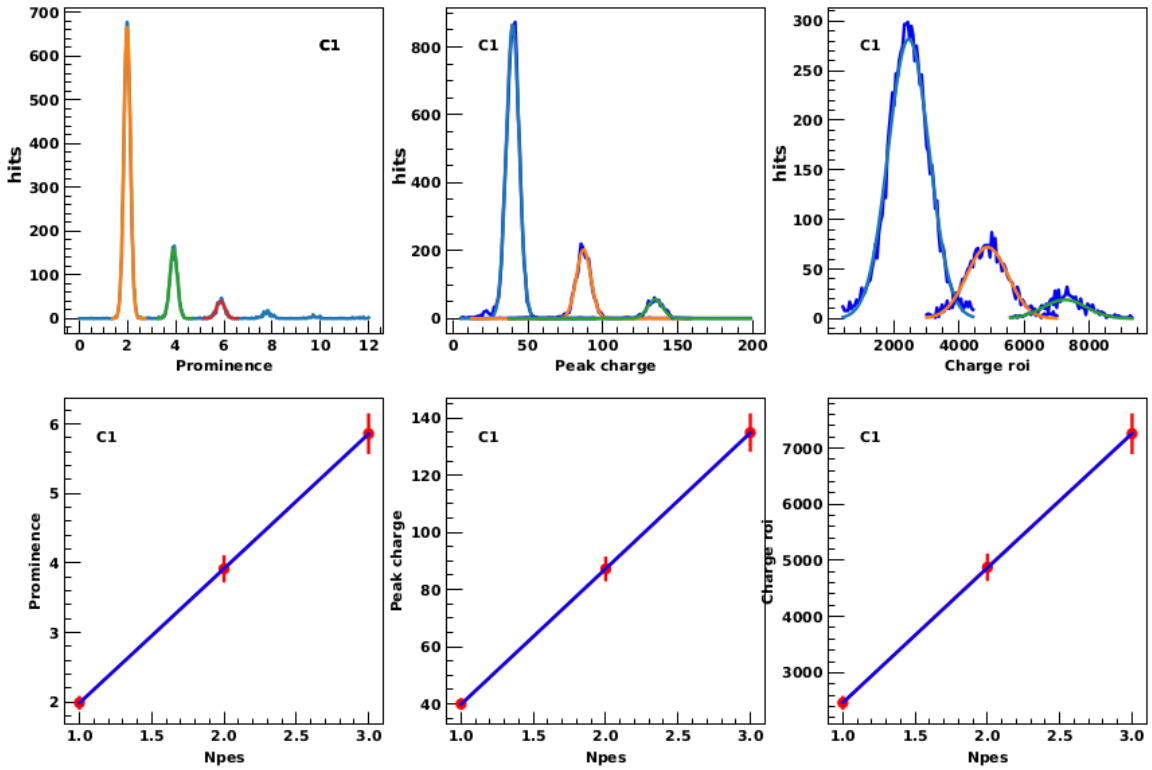

Figure IV.8 – Fits of the prominence, hit integral and charge roi for ReD channel 4 (C1) of laser run 1357 by independent Gaussian and associated linear relationships to the number of photo-electrons.

Output variables of the calibration are stored in a database along with the run, channel and PDM number. These variables are the following: charge roi slope, intercept and number of hits, occupancy; prominence slope, intercept and number of hits; charge roi sigma pedestal and avalanche.

IV.2.2 Laser Occupancy

Laser occupancy is a good parameter for monitoring the stability of the detector as we expect a larger occupancy in channels near the source as they are more exposed to the laser.
Laser occupancy O_{laser} is defined as

$$O_{laser} = log\left(\frac{N_{tot}}{N_0}\right) \tag{IV.4}$$

with N_{tot} the total number of hits in a given channel and N_0 the number of hits present in the same channel in the pedestal only. The pedestal consists of the amount of hits with a charge roi compatible to zero, so without any photo-electrons. To retrieve N_0, we perform a Gaussian fit of the pedestal peak of the charge roi (Figure IV.9).

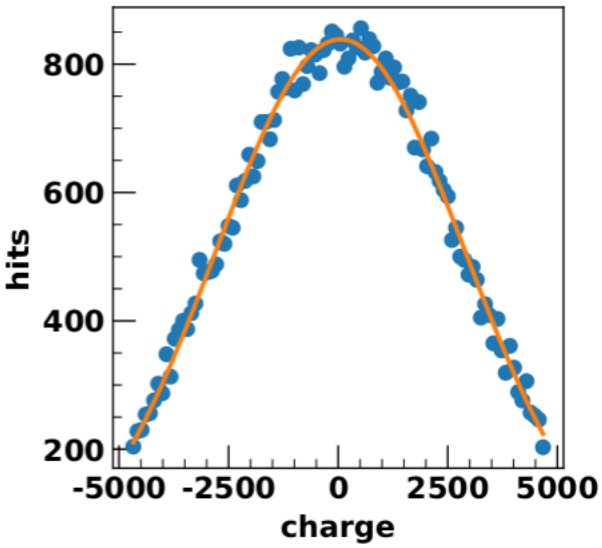

Figure IV.9 – Gaussian fit of the charge roi pedestal peak - Proto-0 run 888, channel 56.

Laser occupancy for all channels of Proto-0 is shown in Figure IV.10. The occupancy is higher on the top right corner (near the source) and then it decreases towards the bottom left corner. It was expected as the laser source was placed on the top right corner. A notable exception can however be spotted. It is due to PDM 10 and 11 (channels 20 and 22 - cf. Section II.4.1) whose channels were inverted by mistake during the data taking. This mismatch was highlighted by the laser occupancy and corrected for further analyses.

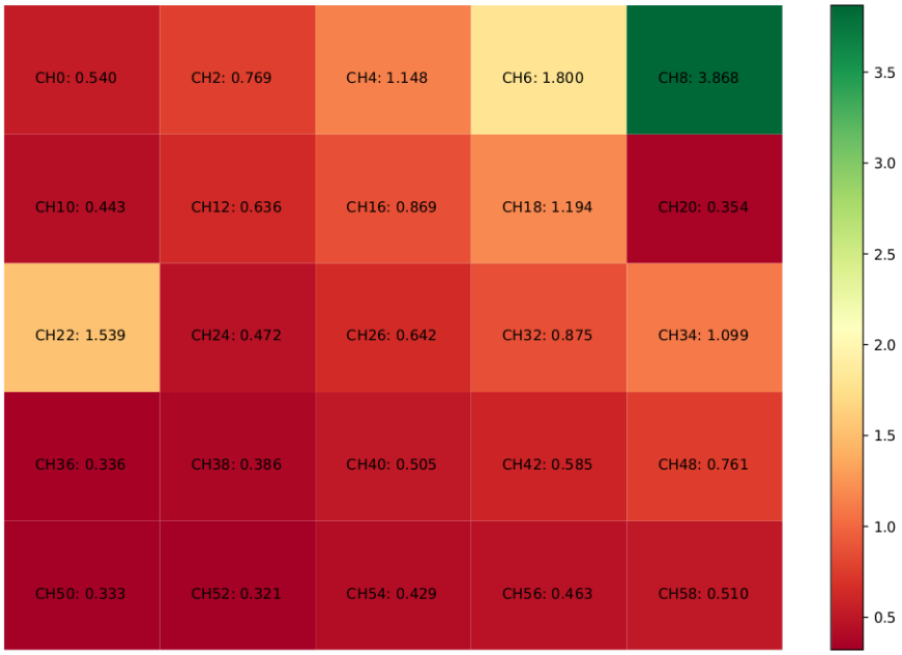

Figure IV.10 – Spatial display of the laser occupancy in Proto-0 detector - run 888

IV.2.3 Monitoring of Calibration Outputs

Once laser calibration is done and its output stored in the database, it is possible to monitor the behaviour of each channel during the different runs to look for instabilities during data taking.
Figures IV.11 and IV.12 show for several channels of Proto-0 charge roi gain and prominence offset, respectively, through 15 days of runs.

- Laser occupancy was stable along with the runs.
- Charge roi gain and prominence gain were mainly stable except for runs 889 and 894, and for both last runs only for channels 4 and 56. Runs 889 and 894 had a different bias voltage, thus the shift. There is no explanation for the other discrepancy, however.
- Charge roi offset was stable except for channels 52, 38 and 34 (both last in a smaller way). Some channels were quite noisy.
- Prominence offset was stable except for one run in channel 20 and channel 58 which seems to be noisy channels over the runs.
- Charge roi sigma pedestal was stable, but channels 38 and 52 were very noisy and 34, 20, 8 and 50 noisy.
- Charge roi sigma avalanche was stable, but channels 38, 20, 42 were noisy.

So, in conclusion, the detector seemed mostly stable. The noise inside some channels is the main concern in the results for this data set.

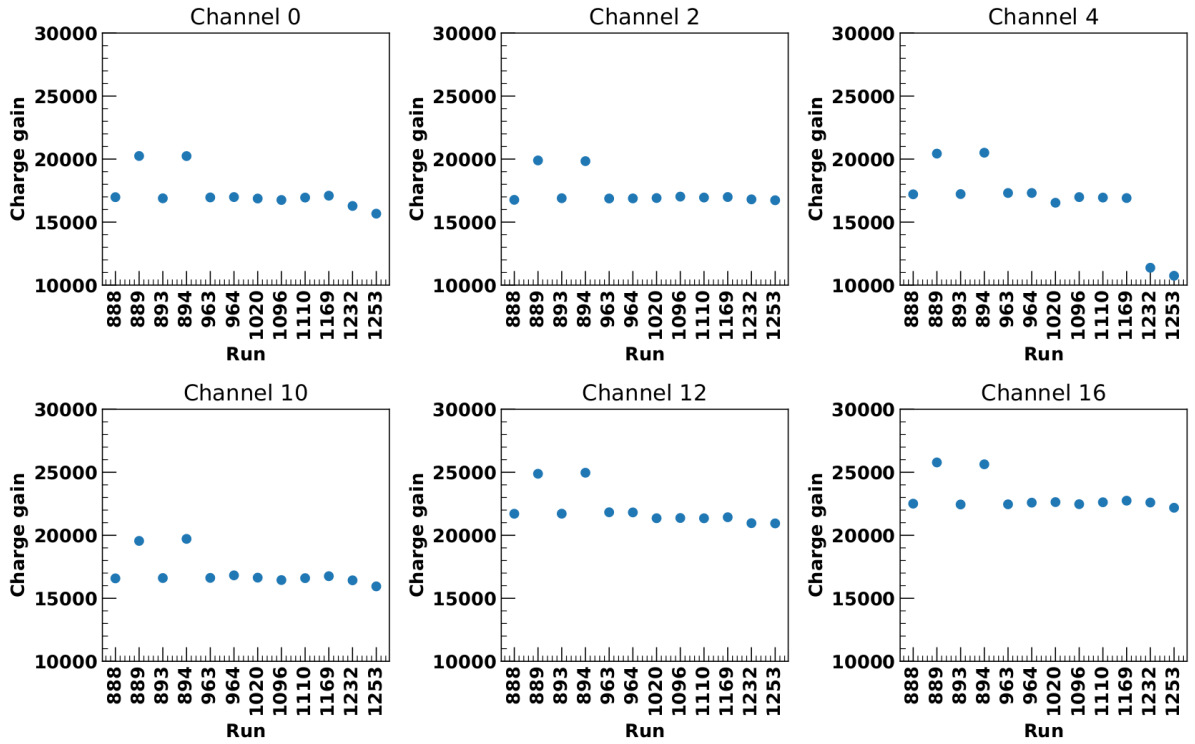

Figure IV.11 – Charge roi gain depending on the run number of Proto-0 November 2019 data taking for channels 0, 2, 4, 10, 12 and 16. A different bias voltage is applied for runs 889 and 894, thus the discrepancy compared to other values. Both last values of channel 4 are also showing a large discrepancy. This is still unsolved.

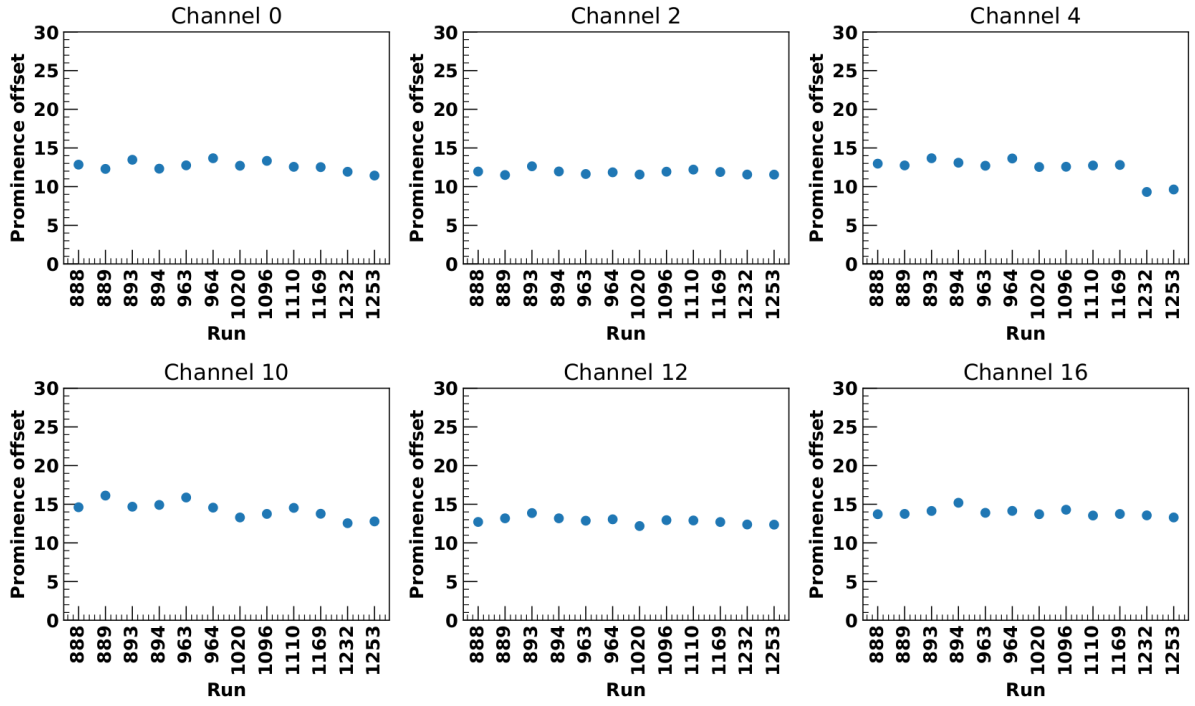

Figure IV.12 – Prominence offset depending on run number of Proto-0 November 2019 data taking for channels 0, 2, 4, 10, 12 and 16.

IV.3 Pulse Finding Procedure

The next step in the reconstruction procedure is focused on the identification and classification of pulses, or clusters of hits. The developed procedure is applied to ReD physics runs taken between December 2019 and February 2020.

The algorithm is based on the computation for each event of the number of hits per channel, the associated hit histogram and the number of photo-electrons per channel. Figure IV.13 shows an example of event with s_1 pulses highlighted in red while s_2 pulses in green. All the different variables are plotted with respect to the number of samples (one sample is equal to 2 ns). We will use the event shown in Figure IV.13 as a running example.

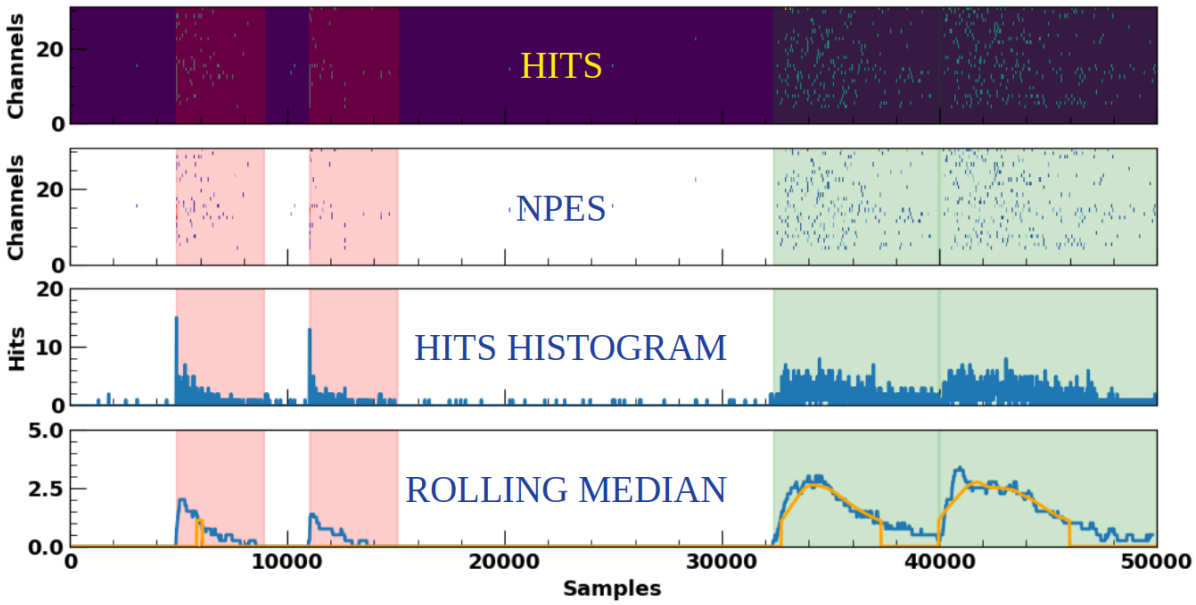

Figure IV.13 – Pulse viewer description. The showed event is run 1359, event 1463. Red areas are highlighting s_1 pulses and green areas s_2. The orange curve in the lower part of the plot is the median of the rolling median.

The algorithm has the following steps:

1. We first apply the rolling median (40 samples window) to the sequence of hits as shown in the example of Figure IV.13.

2. We identify segments of non-zero samples in the rolling median histogram.

3. To search for possible sub-segments, we apply the running mean to each of the identified segments (in orange on the rolling median plot of Figure IV.13). We then apply a hit finder algorithm (from scipy [201]) to divide into sub-segments if necessary.

4. If the hits in the highest 20-ns bin of a sub-segment are observed by at least 45% of the channels, we classify it as an s_1 pulse. This criterion is motivated by the isotropy of the s_1 light distribution with respect to s_2 for which the interaction

occurs near the top optical plane and hence, the light distribution is more localized. The window for s_1 events is fixed at 8 μs (400 samples) to contain the whole pulse.

5. We classify residual pulses based on s_1 and s_2 physical properties. S_1 pulses have a large number of hits in the very beginning and then a sharp slope. This is caused by the nuclear recoil which has a fast component - the singlet state (7 ns) - and then a slow component - the triplet state (1.6 μs) respectively causing a large and narrow peak followed by a small and wider one. S_2's shape is quite different from s_1's, it has an elongated shape because the light emission is continuous while ionization electrons drift in the gaseous region. Hence, we also classify as s_1 candidates for which at least 7 channels had received hits and with an f_p (fraction of photo-electrons received in the first 2 samples divided by the total number) greater than 0.013.

6. The residual clusters are then identified as s_2's.

7. The classified pulses undergo a check of the gate length to avoid overlapping, typically a s_1 and either another s_1 or an s_2. If the total time of the rolling median pulse is more than 2 times larger than an s_1 (so 8 μs), we apply a peak finder to separate them and follow again the previous determination based on the number of hits per channel and f_p. Candidates for the example event are highlighted in Figure IV.14.

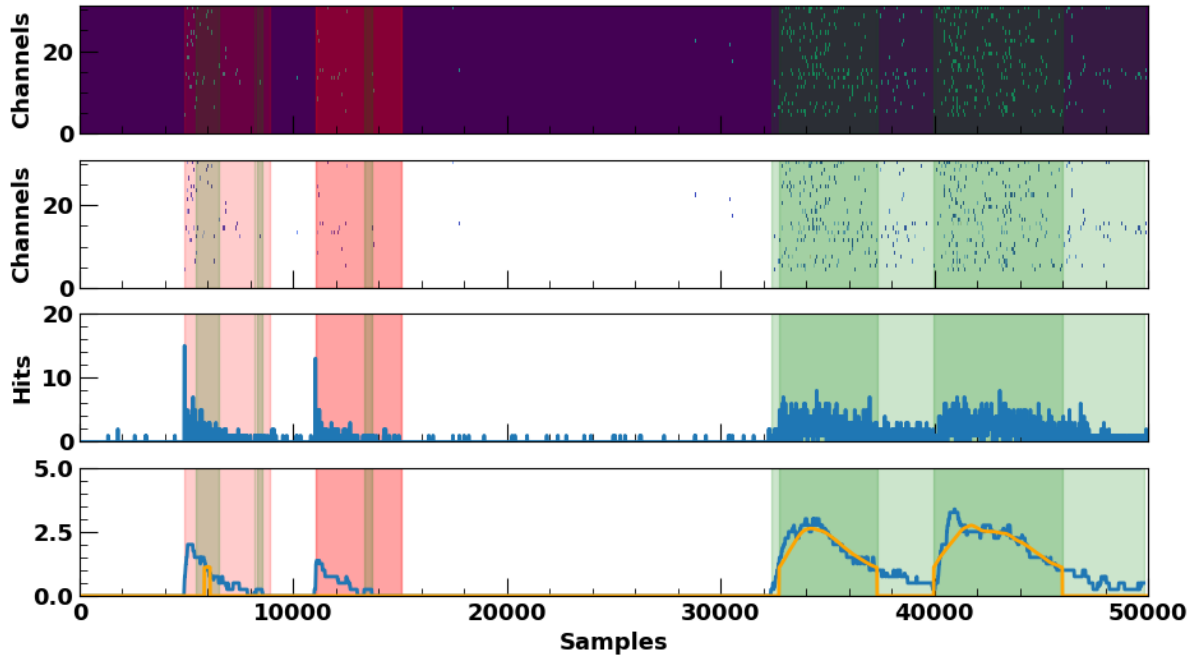

Figure IV.14 – Selection of s_1 and s_2 candidates with the pulse finding algorithm - ReD run 1353, event 7296. Light red areas are highlighting s_1 candidates and light green areas s_2 candidates. At this stage, all hits can be selected inside several s_1 or s_2 clusters. Hence, there are overlaps of colors creating darker colors or a mix between red and green.

8. We then remove wrong classifications. For that we apply the following cuts:

   - Pulses with length zero or infinite,
   - s_2 with gate $<$ 100 samples,

- s_2 with $f_{400} > 0.2$, f_{400} being the fraction of photons collected during the first 400 ns of the scintillation pulse,
- s_2 fully contained in a s_1 gate,
- s_1 below 8 μs unless another pulse is behind,
- very low hits not involved in any pattern.

9. Finally, overlapping pulses are merged or stopped 100 ns before the next one. In case they are not stopped in another way, s_2's are stopped after 20 μs.

In the end, we have a rather clean determination of s_1 and s_2 pulses (cf. Figure IV.15). Additional examples from run 1359 can be seen in Figure IV.16.

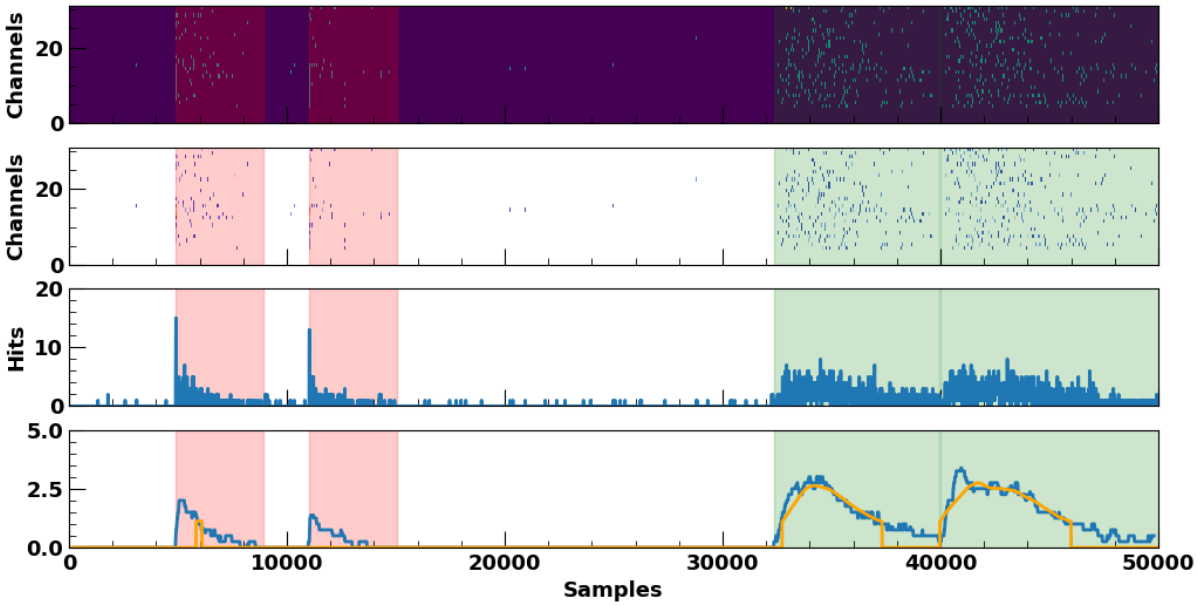

Figure IV.15 – Final selection of s_1 and s_2 candidates with the pulse finding algorithm - ReD run 1359, event 1463. Red areas are highlighting s_1 candidates and green areas s_2.

The procedure works well, but is not optimal. Indeed, the goal was to keep a rather simple approach based on physical shapes of either s_1 and s_2 and so it is a highly parameterised code subject to over-tuning. In addition, the fine-tuning of s_2 start time (due to the re-sampling of the histogram) can be improved. A machine learning approach was also developed inside the collaboration, but it did not improve much the results. Some other efforts to find alternative methods for pulse finding are in development inside the collaboration.
A detailed study of the performances using this method using ReD data will be shown in Section IV.5.

We define cluster prominence, cluster integral and cluster charge as the analogue variables to the prominence, hit integral and charge roi, but computed on the hit clusters (*i.e.* s_1 or s_2 pulses found by the pulse finder) rather than on single hits.

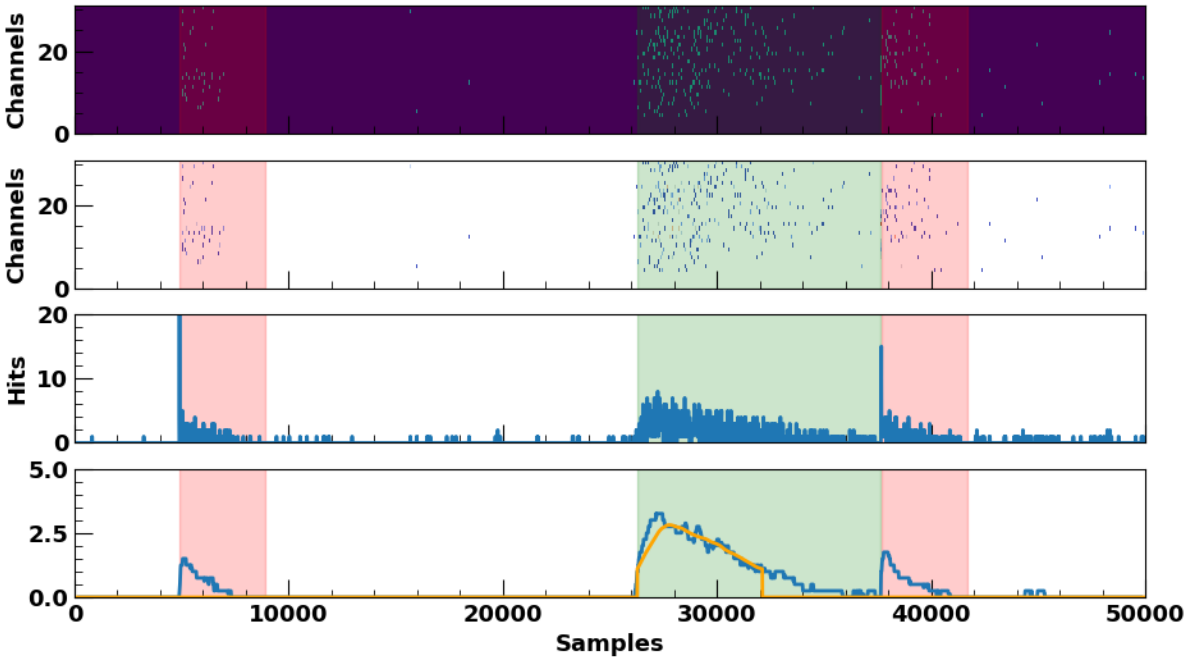

(a) Event 431

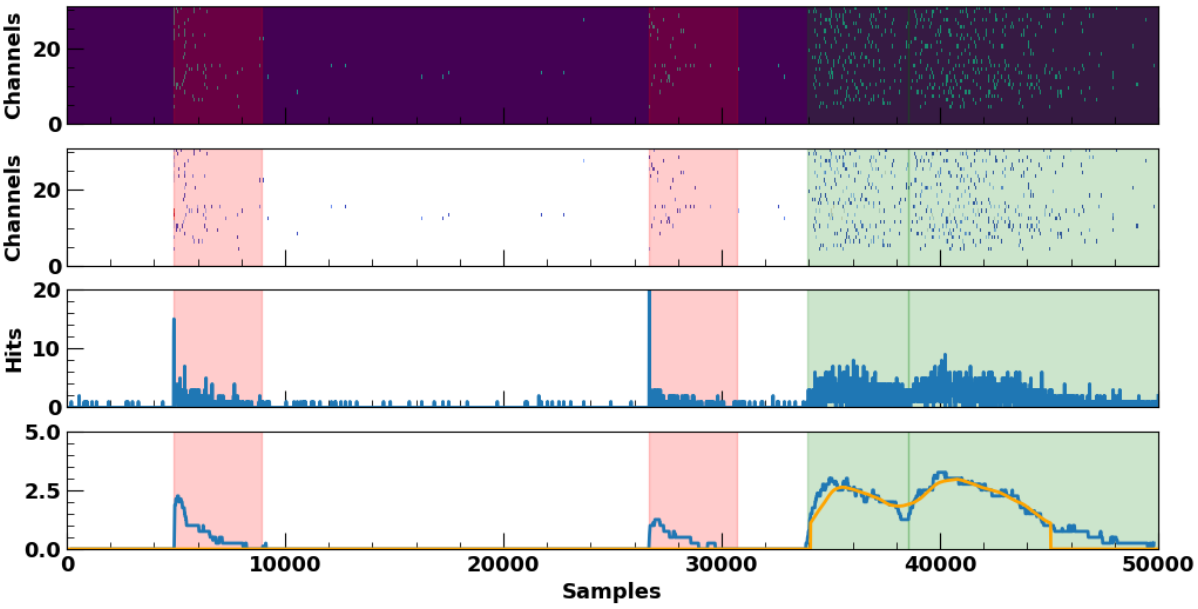

(b) Event 8393

Figure IV.16 – Final selection of s_1 and s_2 candidates with the pulse finding algorithm - ReD run 1359, events 431 and 8393, respectively. Red areas are highlighting s_1 pulses and green areas s_2. The orange curve is the median of the rolling median.

IV.4 Impact of the Hit Finding Method

The hit finder algorithm was developed for substituting the peak finder of the scipy library [201] which was originally implemented as it was too slow from the computing point of view.
We use calibration data from ReD acquired in dual-phase mode (presence of the gas pocket) with an external source of ^{241}Am emitting mono-energetic γ-rays at 59.5 keV irradiating the detector. It creates single scatters with liquid argon which allows to study s_1 and s_2 pulses.
Based on this data, we compare in this section the performance of the two hit finding approaches by comparing physical variables such as the light yield and the resolution.

We find a similar number of clusters using both reconstructions, with a time around 5 times faster with the hit finder algorithm with respect to scipy. In addition, we observe that the number of reconstructed hits has doubled for the reconstruction with the hit finder algorithm and that the hit time has a less distorted shape (Figure IV.17).

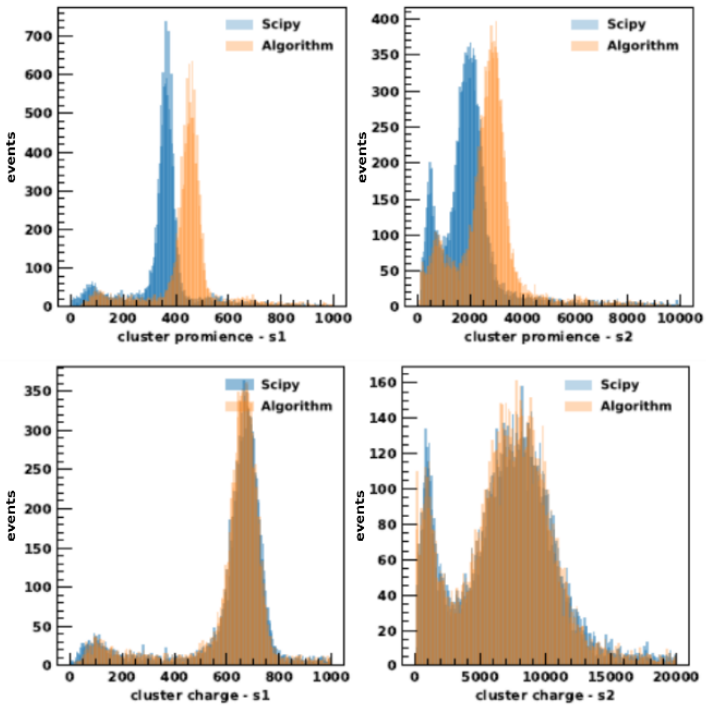

Figure IV.17 – Comparison of several quantities - namely the cluster prominence and cluster charge for s_1 and s_2 - between the scipy peak finder and the algorithm hit finder reconstructions for ReD run 1359.

The resolution is measured by fitting s_1 and s_2 pulses with a convolution between the Monte-Carlo spectra for ^{241}Am (the source used in the runs) and a Gaussian shape. Indeed, 80% of the interactions are due to the photoelectric effect inside argon and the residual from Compton scattering which is responsible for the asymmetric shape. The fit returns the light yield (L_y) and geometrical factor (F_f) of the pulse which are defined from the width of the Gaussian σ as $\sigma = \sqrt{F_f L_y E_{\gamma Am}}$ with $E_{\gamma Am} = 59.5$ keV the energy

of the Americium γ peak. The resolution (R) of the pulse is:

$$R = \frac{\sigma}{\mu} = \sqrt{\frac{F_f}{L_y E_{\gamma Am}}} \tag{IV.5}$$

We compare the resolution and light yield of the cluster charge, the cluster prominence and the cluster integral. Values for s_1 in run 1366 are showed in Table IV.1. Similar conclusion can be drawn for s_2's (Figure IV.17).
Resolution and light yields are similar when using the cluster charge. This is what we expect as we already saw that the cluster charge variable did not change much between both reconstructions (cf. Figure IV.17). For the cluster prominence, we find with the hit finder algorithm a higher light yield and a slightly better resolution as well.

Comparing the three cluster variables we find that the best light yields are found using the cluster charge ($\sim$ 11.3 pe/keV) and the worse using the cluster prominence ($\sim$ 7.7 pe/keV). The resolution variation between the different variables is small, up to 0.8%, with the best resolution obtained for the cluster integral which makes it a very promising variable for further analyses.

Table IV.1 – S_1 light yield in photo-electron per keV, geometrical factor (F_f) and resolution for both the custom hit finder and the scipy peak finder reconstructions computed on the cluster charge (cl_q), the cluster prominence (cl_p) and the cluster integral (cl_k) for run 1366.

	Light Yield [pe/keV]	F_f	Resolution [%]
Algorithm cl_q	11.282 ± 0.004	3.026 ± 0.030	6.714 ± 0.001
Algorithm cl_p	7.693 ± 0.003	1.909 ± 0.019	6.457 ± 0.001
Algorithm cl_k	8.264 ± 0.003	1.730 ± 0.017	5.932 ± 0.001
Scipy cl_q	11.334 ± 0.004	3.193 ± 0.33	6.881 ± 0.001
Scipy cl_p	6.139 ± 0.002	1.752 ± 0.003	6.925 ± 0.001

We also look at the light yield variation between a field on and a field off with different gas pockets (cf. Figure IV.18 for cluster charge). As expected, we find higher light yields for field off compared to field on. The same pattern is observed for cluster prominence and cluster integral shifted to their own light yield range. It is also worth noting that light yield values tend to decrease with time, maybe due to impurities in the TPC.

IV.5 Reconstruction Efficiency

To test the efficiency of the hit finding algorithm, we reconstruct three simulated samples generated by G4DS using DarkSide-20k geometry (Table IV.2). Samples A and E are composed of 300 keV nuclear recoils with s_1 only or s_2 only pulses, respectively. Sample B is composed of 700 keV electronic recoils with s_1 only. The baseline for this study is the hit finding algorithm which was validated in Section IV.4.

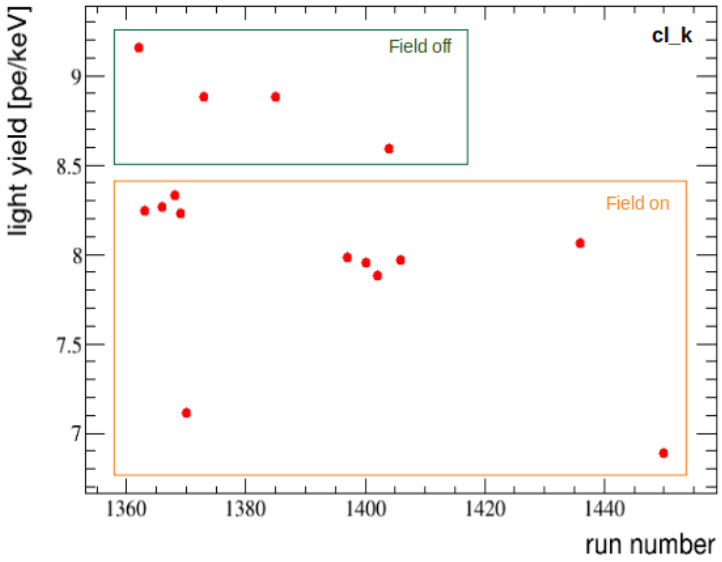

Figure IV.18 – S_1 light yield values for different runs with a field on (orange) and a field off (green). Different gas pockets were used.

Table IV.2 – Details of the different samples. PE stands for photo-electron, NR for nuclear recoil, ER for electronic recoil, Volume refers to the detector volume used for the G4DS simulation and g_2 to the detection efficiency for s_2 signals.

Sample	Energy [keV]	Recoil type	Signal	PE number	Volume	s_2/s_1	g_2 [PE/e-]
A	300	NR	s_1	10^3	full active	/	/
B	700	ER	s_1	4.7×10^3	fiducial	/	/
E	300	NR	s_2	3.5×10^3	full active	3	50

Reconstruction is performed with the following instrumental noise parameters: 10% after-pulses probability, 20% direct cross-talk probability, no external cross-talk, dark count rate of 200 Hz/s^{-1} and a signal-to-noise ratio of 5.

We first look at the number of photo-electrons per channel for each sample. The first 4899 are bottom channels, others are top channels. We observe an excess of reconstructed hits compared to the initial MC photo-electrons for samples A, B and bottom channels of sample E. For the latter, the number of reconstructed hits is slightly smaller than the MC ones. An example for sample A is shown on Figure IV.20.

When removing the noise - after-pulses, direct and external cross-talks - and setting to zero dark count rate - (Figure IV.19) we find that the reconstructed number of hits becomes slightly lower than the MC one. This highlights the presence of an inefficiency. An exception is raised for top channels of sample A where the reconstructed hits are still slightly larger, but this is due to fluctuations of the baseline that induce fake hits (cf Figure IV.20). Table IV.3 summarize inefficiencies for each sample by reporting the mean difference of the MC with the reconstructed number of photo-electrons over the channels. It shows that, except for top channels of sample E where the inefficiency is larger, the inefficiency of the reconstruction is less than 10%.

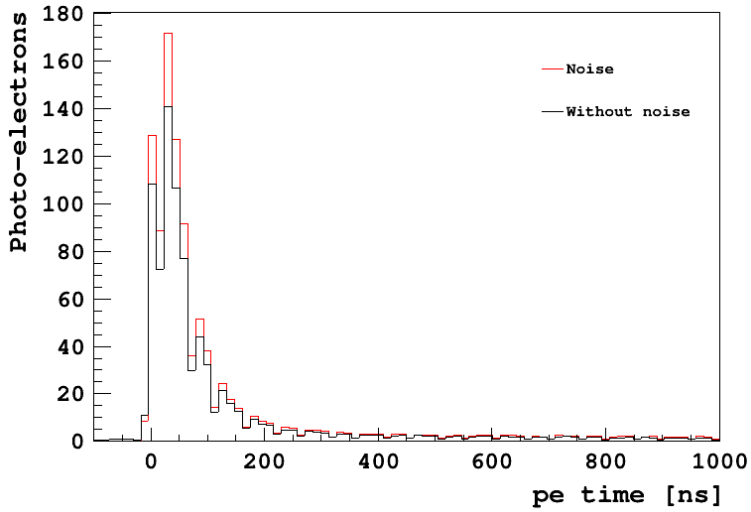

Figure IV.19 – Average number of photo-electrons reconstructed with and without noise depending on the photo-electron time (sample A).

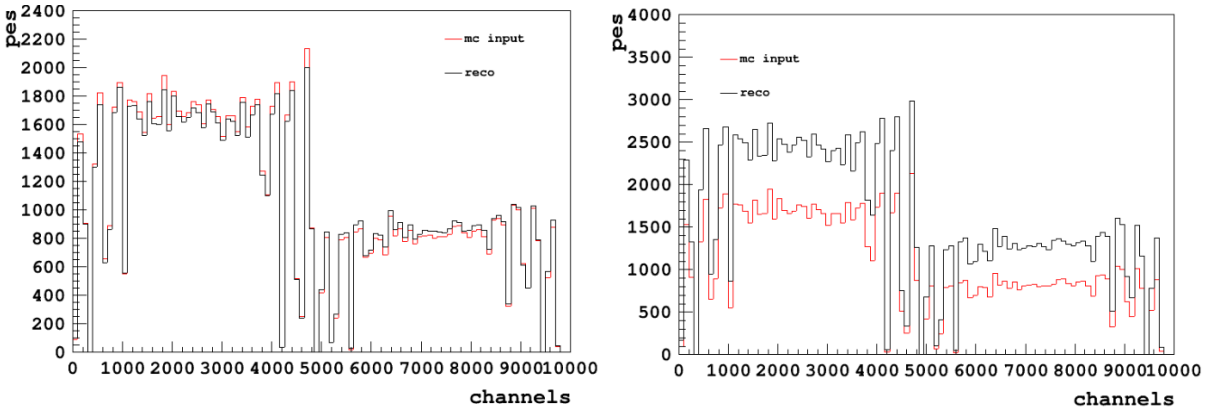

Figure IV.20 – Number of photo-electrons per channels for MC and reconstruction, either without noise (left) and with noise (right) for 300 keV s_1 nuclear recoils (sample A).

Table IV.3 – Inefficiency (cumulative of the absolute average percentage of the difference between the MC and reconstructed number of photo-electrons with respect to the MC number of photo-electrons over the channels) for the three different samples.

Sample	Top channels	Bottom Channels	All channels
A	2%	2%	4%
B	3%	6%	9%
E	16%	3%	19%

Then we look at the number of hits depending on the photo-electron time difference between the reconstruction and the MC. We do not find a significant distortion between both shapes (cf. Figure IV.21 for Sample A).

Finally we look at the finger plots, *i.e.* the hit distribution, to check the single-hit resolution. From the plot in Figure IV.22, we derive that the prominence provides higher

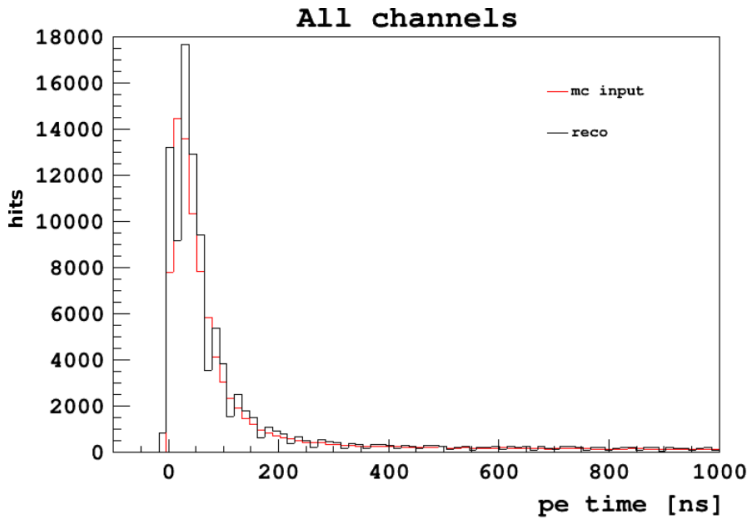

Figure IV.21 – Number of hits depending on the photo-electron time for MC and reconstruction (sample A).

resolution than the hit integral.

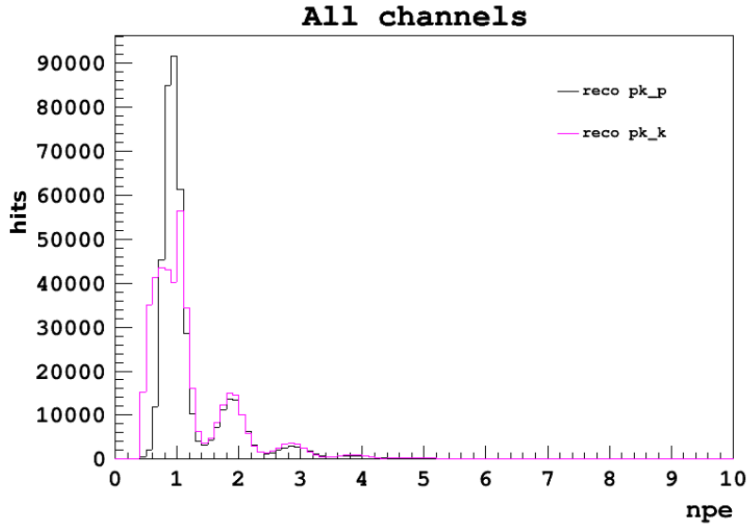

Figure IV.22 – Number of hits depending on the number of photo-electrons for reconstructed prominence (pk_p) and hit integral (pk_k) (sample A).

In the end, although some issues are still to improve, the reconstruction efficiency is validated allowing us to develop high-level analysis, as it will be seen in following chapters.

IV.6 Data Reduction

Due to computing limitations, the production of waveforms in DarkSide-20k will be too consequent (total volume estimated: around 20PB [113]) to allow their filtering. Consequently, the data acquisition is looking for relevant slices or segments of waveform to search for hits with the filtering approach defined in the beginning of this chapter.
For this reason, we test a time over threshold (ToT) algorithm. This quantity refers to

the width of the waveform at the level of the threshold. This distance is correlated to the energy channel by channel.

The algorithm to retrieve the ToT is made of two steps. The first one is a simulation of online data acquisition and the second is the offline treatment of acquired data. The first step is tested on a simulated raw waveform by:

- Subtracting the baseline
- Applying a rolling mean on a window of 1 μs (125 samples)
- Identifying segments of the waveforms above a given threshold (called ToT threshold) of around 8×RMS - the RMS computation is performed on the first 2.4 μs (300 samples) - Figure IV.23.
- Extending the segments before and after with a pre-window of 2 μs

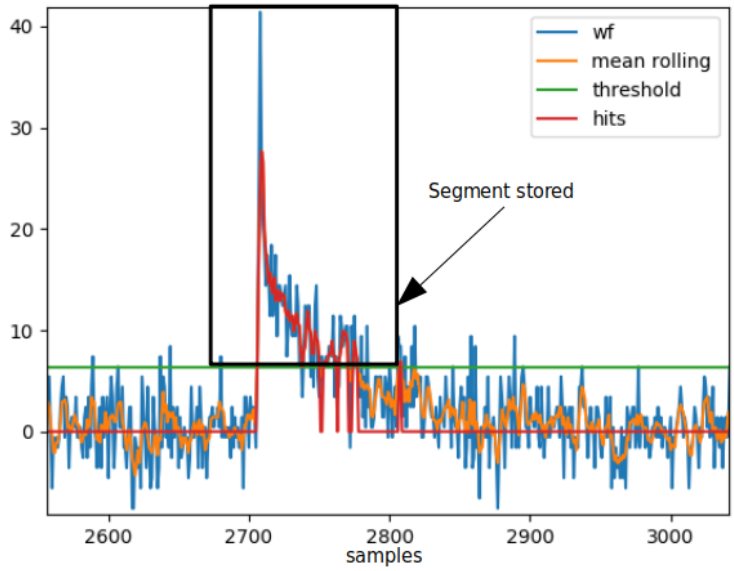

Figure IV.23 – Segment of waveform stored (black box) above the ToT threshold (green line) for a given waveform.

For each segment, we store its beginning, its end and its associated channels. Then, we filter each segment and store hits. To minimize the rate of fake hits, we apply a threshold on the hit finder, called hit finder threshold, based on the ratio between the the hit integral and the prominence (cf. Section IV.1).

Both the hit finder threshold and ToT threshold have to be tuned to optimise the reconstruction.
For that, we take into account two different factors, the efficiency of reconstruction and its impurity. The first is defined as the fraction of photo-electrons reconstructed at the trigger time with respect to the generated number of photo-electrons. The second refers to the rate of fake hits per channel (reconstructed hits not in coincidence with the trigger time).

To evaluate both the efficiency and the impurity we generate 2×10^5 events in one channel in laser mode. We start simulating events without correlated noise and without dark noise. On the generated waveforms we perform the usual reconstruction using the ToT

filter.

For each combination of thresholds from 6 to 11 RMS for the ToT threshold and 3 to 10 for the hit finder threshold, we look at the efficiency and impurity. For computing the efficiency, we count the hits reconstructed between ± 50 samples from the trigger time (as some jitters are present in the reconstruction). We then divide by the total number of hits generated (as we have one photo-electron by event, it corresponds to the number of events). For the impurity, we count the number of fake hits divided by the number of events (1×10^5) and the size of the gate (60 μs).

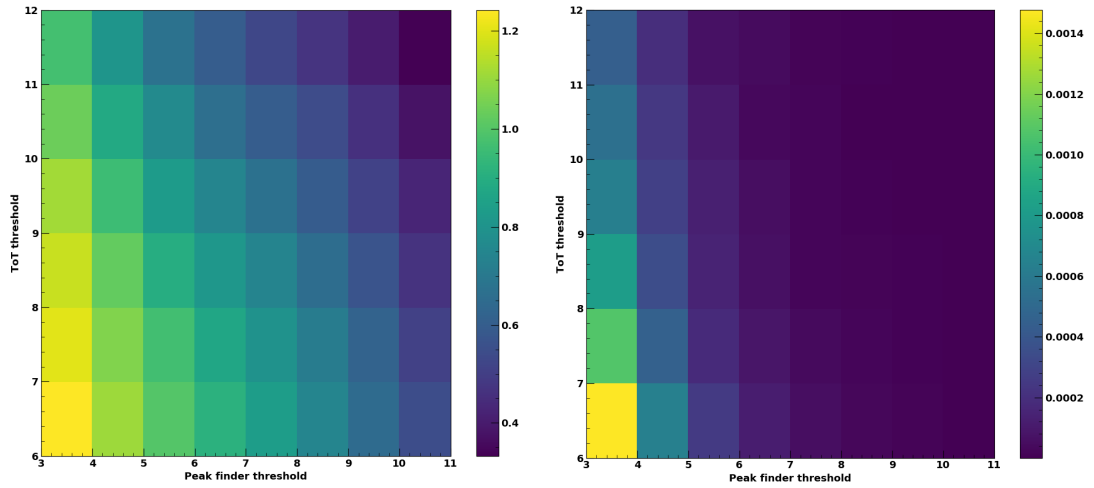

(a) (b)

Figure IV.24 – Simulation of (a) efficiency and (b) impurity reconstruction inside DarkSide-20k detector before any selection cuts and without any noise and an SNR of 5.

We only shot one photo-electron in each event, and consequently we should only have hits around one photo-electron. Consequently, we add a cut in prominence to remove hits that are not centered at one photo-electron (cf. Figure IV.25). The optimal cut is around 0.6 photo-electrons at SNR 5, decreasing to around 0.5 at SNR 10, getting closer to half a photo-electron. Optimized values of the cut in terms of gain and its conversion to photo-electrons are reported for an SNR of 5, 7 and 10 in Table IV.4.
Using this cut, we recover a good coherence in number of hits between the MC distribution and the reconstructed ones as it is shown in Figure IV.26.

Table IV.4 – Prominence cut in gain, and in the associated number of photo-electrons (npe) given by the calibration, depending on the SNR. These values are fluctuating depending on the chosen threshold's pair.

SNR	5	7	10
Gain cut	∼0.68	∼0.60	∼0.61
Npe cut	∼0.62	∼0.51	∼0.51

For an SNR of 5, the corresponding maps of efficiency and impurity depending on the thresholds are shown in Figure IV.27. The minimum ToT threshold is 6×RMS as below we catch the background noise in addition to fake hits.

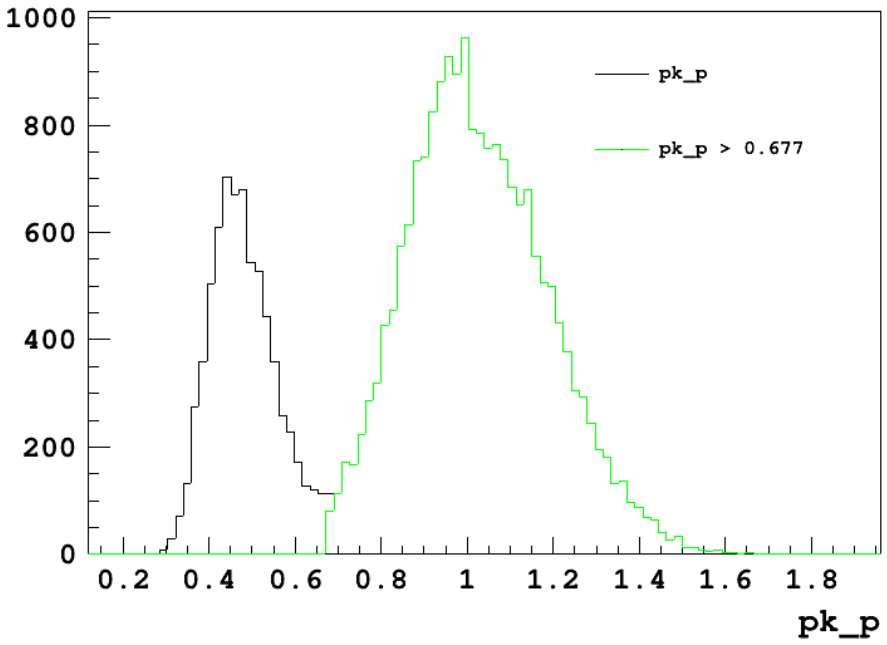

Figure IV.25 – Distribution of prominence for 2×10^5 events of one photo-electron laser shot in one channel at SNR 5, other noise variables are set to zero. The black distribution, which is below the green one on the right part, is the total prominence distribution. The green part is the prominence distribution above the optimal prominence cut for this configuration (0.677).

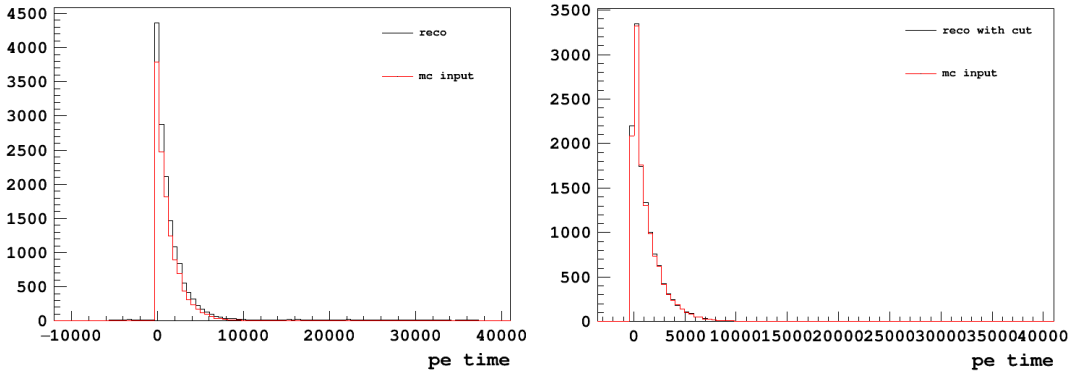

(a) (b)

Figure IV.26 – Comparison of photo-electron time reconstruction to the true Monte-Carlo (a) without any cut and (b) with the prominence cut for an s_1 30 keV nuclear recoil sample of 50 events.

In Figure IV.27, we observe that the efficiency is close to one and impurities are very low. We also test other values of SNR: 7 and 10 for which fake hits become negligible (cf. Figure IV.28 and IV.29). Concerning the efficiency, its value increases with the SNR, mostly at higher threshold pairs. As a consequence, the impact of the thresholds on the efficiency decreases with the SNR.

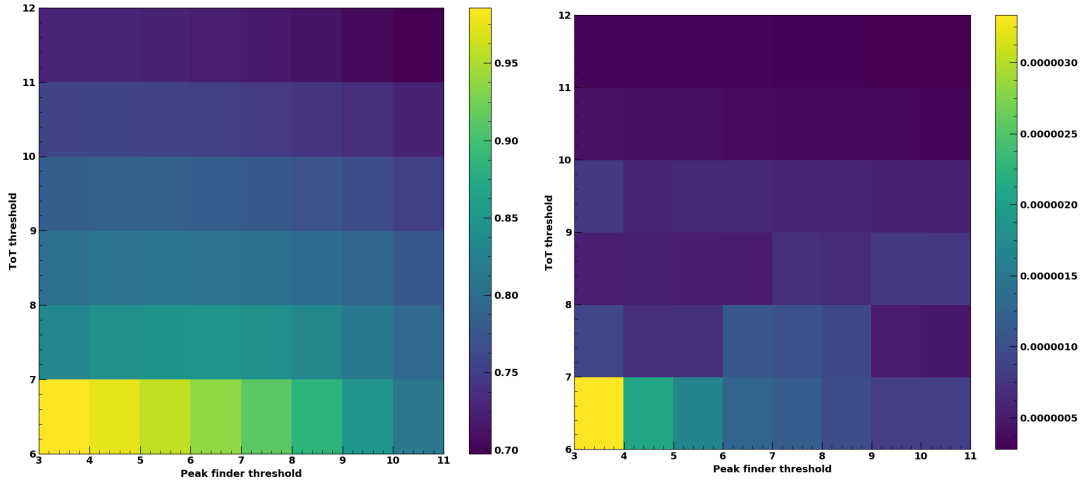

(a) (b)

Figure IV.27 – Simulation of (a) efficiency and (b) impurity reconstruction inside DarkSide-20k detector with a prominence selection cut and without any noise and an SNR of 5.

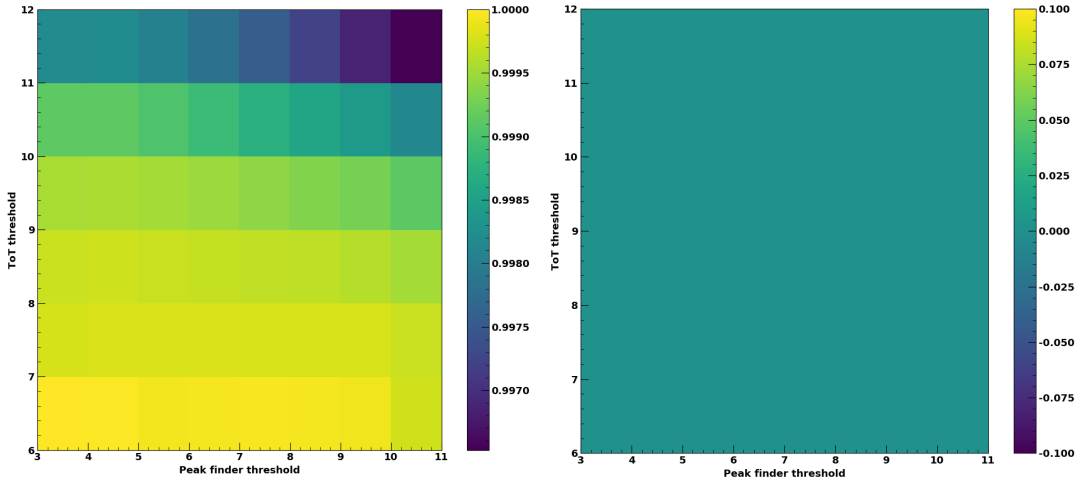

(a) (b)

Figure IV.28 – Simulation of (a) efficiency and (b) impurity reconstruction inside DarkSide-20k detector with a prominence selection cut and without any noise and an SNR of 7.

The optimisation of the threshold is consequently not dependent on the impurity but mostly on the efficiency. For each one of these three SNR cases (5, 7 and 10), the best pair is summarized in Table IV.5 along with the associated efficiency and impurity. For

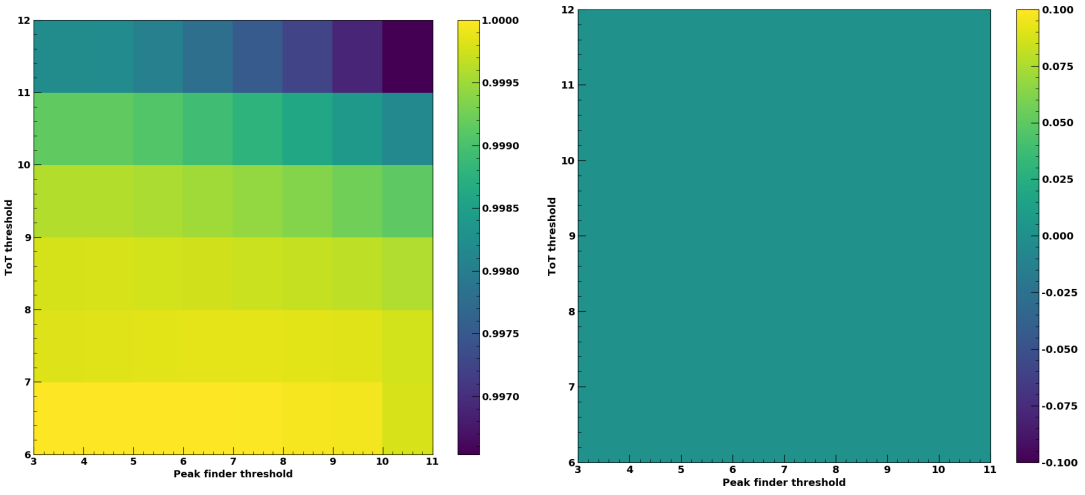

(a) (b)

Figure IV.29 – Simulation of (a) efficiency and (b) impurity reconstruction inside DarkSide-20k detector with a prominence selection cut and without any noise and an SNR of 10.

SNR 10, several threshold pairs provide 100% of efficiency: 6×RMS and 5, 6×RMS and 7, 7×RMS and 3, 7×RMS and 4 and 8×RMS and 3.

Table IV.5 – Summary of the best combination of ToT and hit finder thresholds based on their efficiency and impurity [in fake hits/channel/event/us] of reconstruction for several SNR values.

SNR	ToT thresold	Hit finder threshold	Efficiency	Impurity
5	6×RMS	3	98.58%	3.3×10^{-6}
7	6×RMS	3	100%	0
10	6×RMS	7	100%	0

We select the different possible pairs for SNR 10 and reconstruct nuclear recoil s_1 events at 30 keV from a sample of simulated G4DS data. We compare the Monte-Carlo photo-electron time to the reconstructed one weighted by the prominence gain. Based on these shapes, we select a 6×RMS and 5 threshold pair for SNR 10 as the best.

The impact of after-pulses on the efficiency is negligible. However, the impurity raises with after-pulses. At SNR 5 and 5% after-pulses probability, the impurity is of 5.5×10^{-4} fake hits/event/channel/μs. At 10% after-pulses, fake hits increase by around one order of magnitude (around 2.5×10^{-3}) as it can be seen on Figure IV.30.

IV.7 Conclusion

Data reconstruction is an important and necessary step before starting what is called high-level analysis, so analysis using reconstructed physical variables. The accuracy and performance of the reconstruction are crucial to have further relevant and precise analyses.

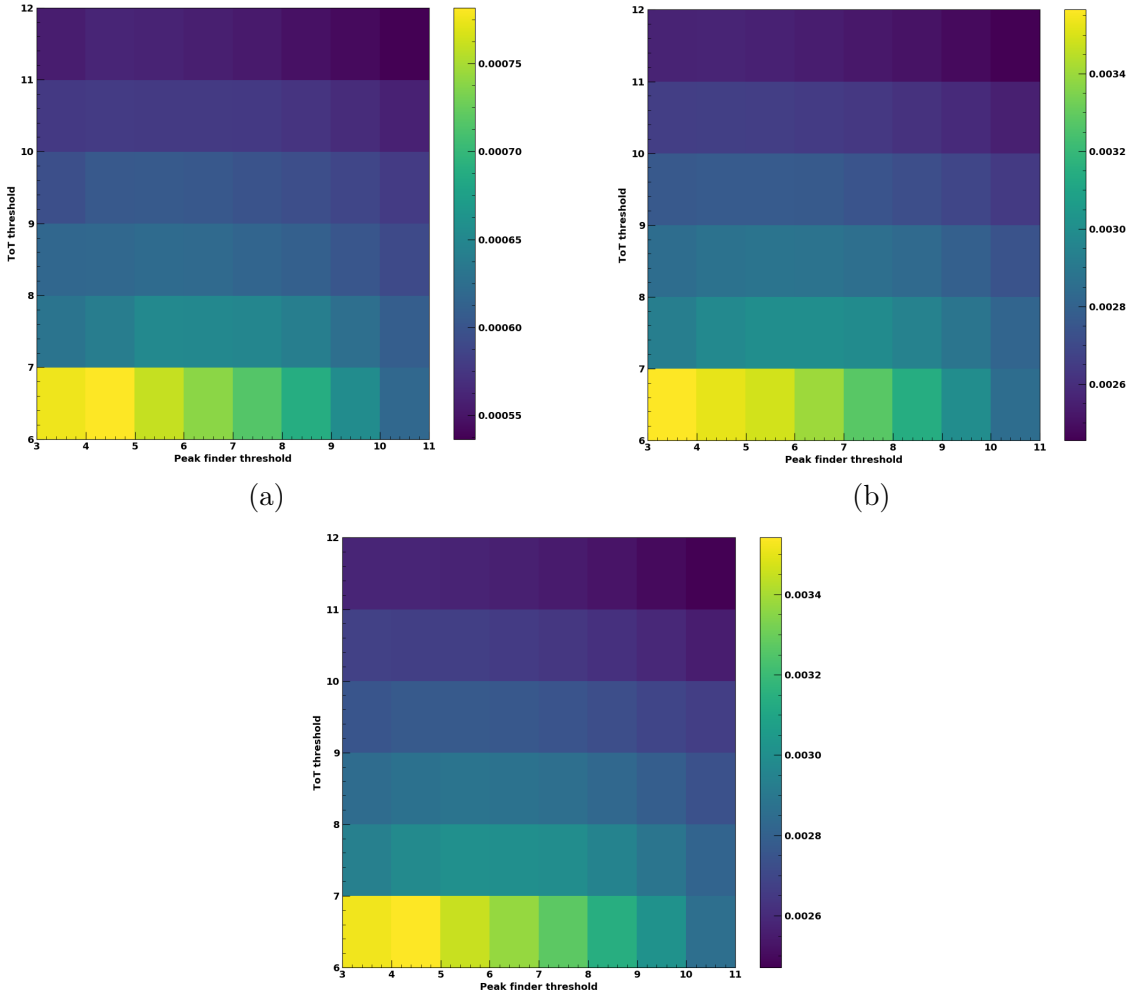

Figure IV.30 – Impurity reconstruction inside DarkSide-20k detector for (a) 5% after-pulses, (a) 10% after-pulses and (c) 20% after-pulses, with a prominence selection cut, without DCR and cross-talks and an SNR of 5.

The procedure developed in this chapter was demonstrated to be stable and effective. In addition, we showed that the hit finder algorithm is an improvement with regards to scipy one, mainly in terms of computing speed. The hit integral variable is also an improvement that can be of great value for further analyses. Finally, we showed that the ToT approach may be a way for the data reduction. Its reduction efficiency is however still to be established.

Chapter V

Gas Pocket Thickness

> La science, mon garçon, est faite d'erreurs, mais d'erreurs qu'il est bon de commettre, car elles mènent peu à peu à la vérité.
>
> Jules Verne (1864)

In a dual phase TPC, the so-called ionization signal s_2 (Section II.1.1) is induced by free electrons that are extracted into a gaseous region at the top of the TPC by the influence of an electric field. This region is called the gas pocket and the amount of s_2 light produced by one electron critically depends on its thickness. In order to ensure stable operations, the thickness of the gas pocket, whose typical size is around 1 cm, has to be uniform over the whole TPC surface and over time.

Changes in the thickness will induce biases in the reconstruction and so, have to be constantly monitored during the data taking. This can be done by monitoring tools based on the shape of the s_2 signal.

In this chapter we will describe the monitoring tool that we developed for the ReD experiment. This tool allows to measure the thickness of the gas pocket in different regions of the TPC and to monitor its changes over time. As we will show, a reduction of the gas pocket thickness was in fact observed during the data taking.
The method is based on the modelling of the s_2 pulse shape as described in [202]. Such a model depends on few parameters, including the drift time across the gas pocket that, knowing the drift velocity, gives a direct measurement of the gas pocket thickness.

We will introduce in Section V.1 the model that describes the s_2 pulse shape and the computation of the drift velocity in Section V.2. We will then describe the tests we made with simulated data to extract the gas pocket thickness in the ReD setup (Section V.3). Finally, we will present the results on the ReD data in Section V.4, its spatial distribution (Section V.5) and stability over data taking (Section V.6).

V.1 S_2 Pulse Shape Model

To fit the s_2 pulse shape, we use a model developed for DarkSide-50 [202] where an ideal s_2 pulse shape is convoluted with a Gaussian smearing accounting for the different extraction times of the ionization cloud.
The ideal shape is built by taking into account two different effects inside the gas pocket. When electrons reach the gas pocket, argon excimers are produced in a uniform way along the electron path. The de-excitation of these excimers produces light with two different decay times, τ_1 and τ_2. The emitted light is then observed by PMTs forming the s_2 signal. In the ideal case, the shape is given by [202]

$$y_{ideal}(t;\tau_1,\tau_2,p,T_d) = p \times y'_{ideal}(t;\tau_1,T_d) + (1-p)y'_{ideal}(t;\tau_2,T_d) \tag{V.1}$$

with

$$y'_{ideal}(t;\tau_j,T_d) = \begin{cases} 0, & \text{if t} < 0 \\ 1-e^{-t/\tau_j}, & \text{if } 0 \leq \text{t} \leq T_d \\ e^{-(t-T_d)/\tau_j} - e^{-t/\tau_j}, & \text{if t} > T_d \end{cases} \tag{V.2}$$

and j = {1, 2}. It depends on s_2 fast (τ_1) and slow (τ_2) decay times, on the s_2 fast component fraction (p) and on the drift time across the gas pocket (T_d).

In addition, effects induced by the diffusion in the electron clouds have to be included. This induces a smearing that is modelled as a convolution between the idealized shape and a Gaussian distribution of width σ occurring at the initial time. This gives the s_2 time profile given by [202]

$$y(t;\tau_1,\tau_2,p,T_d,\sigma) = p \times y'(t;\tau_1,T_d,\sigma) + (1-p)y'(t;\tau_2,T_d,\sigma) \tag{V.3}$$

with

$$y'(t;\tau,p,T_d,\sigma) = \frac{1}{2T_d}\left[y''(t;\tau,\sigma) - y''(t-T_d;\tau,\sigma)\right] \tag{V.4}$$

$$y''(t;\tau,p,\sigma) = \mathrm{erf}\left(\frac{t}{\sqrt{2}\sigma}\right) - e^{-t/\tau}e^{\sigma^2/2\tau^2}\mathrm{erfc}\left(\frac{\sigma^2-t\tau}{\sqrt{2}\sigma\tau}\right) \tag{V.5}$$

The quantity σ^2 is defined as the width of the longitudinal profile of the electron cloud divided by the electron drift velocity inside liquid argon v_d. So, σ^2 is equal to $(\sigma_0^2+2D_L t_d)/v_d^2$ with σ_0 a constant accounting for additional small smearing effects, D_L the longitudinal diffusion coefficient and t_d the electron drift time.

To fit the s_2 pulse three additional parameters must be included: a constant accounting for dark noise (y_0), a time offset (t_0) and a normalization factor (A). The form of the final fit is such as [202]:

$$y_{fit}(t;\tau_1,\tau_2,p,T_d,\sigma,A,t_0,y_0) = y_0 + A \times y(t-t_0;\tau_1,\tau_2,p,T_d,\sigma,A,t_0) \tag{V.6}$$

with the parameters summarized in Table V.1.

Table V.1 – Summary of the 8 parameters of the s_2 pulse shape model

Parameter	Definition
τ_1	Decay time of the s_2 fast component
τ_2	Decay time of the s_2 slow component
p	s_2 fast component fraction
T_d	Drift time inside the gas pocket
σ	Width of the initial Gaussian smearing
A	Normalization factor
t_0	Time offset
y_0	Constant accounting for dark noise

V.2 Drift Velocity inside the Gas Pocket

In order to measure the gas thickness it is necessary to know the electron drift velocity as a function of the electric field. This relationship was modelled in two different ways in [203] and [204]. In [203], the drift velocity in the gas is defined as the product of the electric field in kV/cm and the electron mobility. This latter depends on the electric field and the liquid argon temperature and is defined as [203]:

$$\mu = \frac{a_0 + a_1 E + a_2 E^{3/2} + a_3 E^{5/2}}{1 + (a_1/a_0)E + a_4 E^2 + a_5 E^3} \left(\frac{T}{T_0}\right)^{-3/2} \tag{V.7}$$

with a_0 the electron mobility at zero field (cm^2/s) and T_0 the temperature at which a_0 was measured. Values of each parameter are given in Table V.2.

Table V.2 – Parameter of the model of electron mobility from [203]

a_0	a_1	a_2	a_3	a_4	a_5	T_0
551.6	7953.7	4440.43	4.29	43.63	0.2053	89 K

In the other hand, in [204] the Boltzmann equation is solved to compute the drift velocity in gas depending on the electric field divided by the argon number density. The drift velocity as a function of the reduced electric field (*i.e.* the electric field divided by the argon number density) for the two approaches is given in Figure V.1.

Hence, to find the gaseous drift velocity we have to know the boiling temperature of argon at the pressure of the gas pocket, the electric field in the gas pocket in kV/cm and the argon number density.
The boiling temperature of argon at the pressure of the gas pocket for ReD was measured at 88 K. The electric field inside the gas pocket E_{el} is defined as [205]:

$$E_{el} = \frac{A}{H_g + H_l \epsilon_g / \epsilon_l} \tag{V.8}$$

where H_l is the distance from the extraction grid to the beginning of the gas pocket and H_g is the thickness of the gas pocket. ϵ_g and ϵ_l are the dielectric constants respectively for

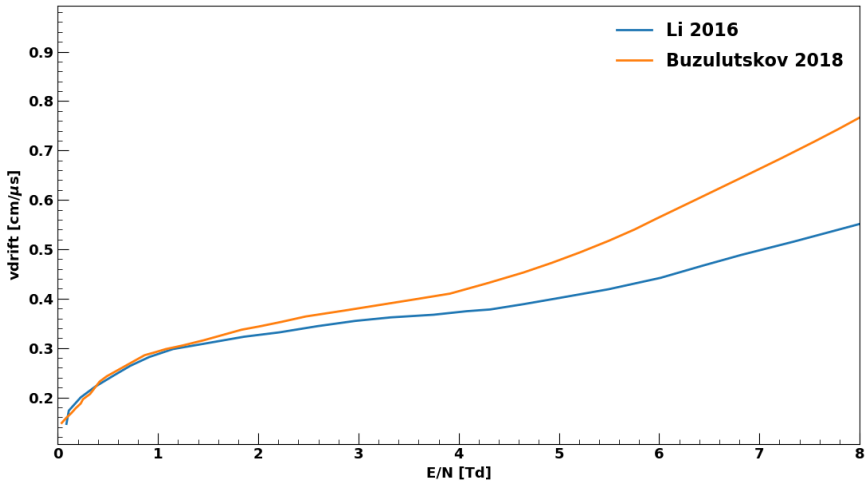

Figure V.1 – Electron drift velocity in gaseous argon depending on the reduced electric field. Two different calculations are proposed: by Li et al. [203] and by Buzulutskov et al. [204].

gaseous and liquid argon. A is the voltage applied between the grid and the anode window.

In the ReD experiment, the distance between the grid and the top window is 1 cm. A hole for the bubbler is present at 3 mm from the grid which mechanically creates a $\sim$ 7 mm gas pocket (H_g) and so the liquid part H_l is $\sim$ 3 mm [124]. The dielectric constant for gaseous and liquid argon are 1 and 1.5, respectively [124]. The applied voltage is A = 5211 V giving E_{el} = 5.79 kV/cm.

Finally, we derive the argon number density N, from the ideal gas law we have,

$$N = \frac{nN_A}{V} = \frac{P}{k_B T} \tag{V.9}$$

with n the amount of moles, V the gas volume, N_A Avogadro constant, P the pressure in the gas pocket [N/cm^2], T the temperature inside the gas pocket [K] and $k_B = 1.38\times10^{-21}$ N.cm/K the Boltzmann constant.
The pressure in ReD is 1.041 bar (so 10.41 N/cm^2) resulting in N = 8.572×10^{19}cm^{-3}.

The reduced field in ReD is then E/N = 6.75 Td, with 1 Td = 1×10^{-17} V/cm^{-2}, resulting in a drift velocity of inside gaseous argon of 0.48 cm/μs and 0.64 cm/μs based on [203] and [204], respectively.

V.3 Systematics Studies with Simulated Data

In order to test the model, we apply it to simulated waveforms. First, we probe the model in an ideal case using a Monte-Carlo approach and then with a full and realistic simulation including reconstruction effects.

V.3.1 Toy Monte-Carlo Approach

In the toy Monte-Carlo we do not assume diffusion ($\sigma = 0$). S_2 shapes are generated as follows. For each event a random time t_0 is generated between 0 and 1 μs and another random time t_1 from one of the two exponentials with decay times τ_1 = 10 ns^{-1} and τ_2 = 3.6 μs^{-1}. The choice between the two depends on the probability p. Then, hits are assigned a time $t_0 + t_1$.
To test the impact of after-pulses, we add them to the s_2 distribution with a probability p_{AP} at t_{AP} with a decay time τ_{AP} = 1 μs^{-1} which corresponds to one delayed photo-electron. t_{AP} is then added to the hit distribution.

Shapes with different configurations of after-pulses probabilities and decay times are simulated with the toy Monte-Carlo (cf. Figure V.2) and fitted with the s_2 pulse shape model. The parameters t_0 and y_0 are fixed to zero. Results are reported in Table V.3. This study shows that τ_1 value is too small to be sensitive and hence has to be fixed. The fitted values for τ_2 and p are close to their input value. The presence of after-pulses has a small impact on the determination of τ_1, τ_2 and p. Resulting T_d is rather stable regardless of the addition of after-pulses.

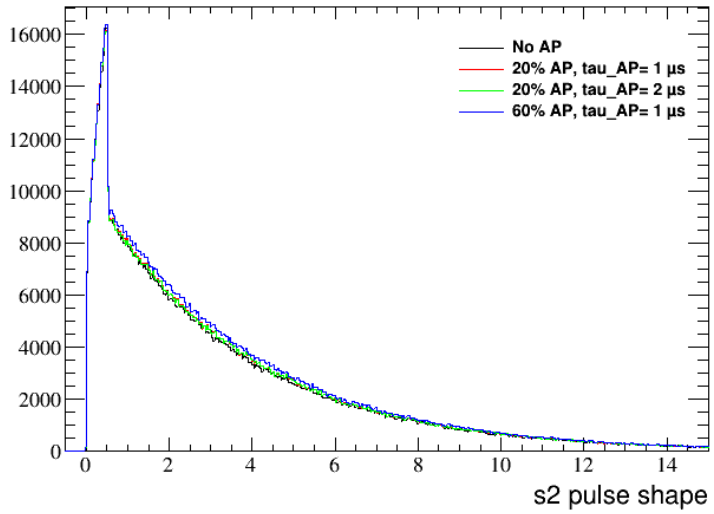

Figure V.2 – Impact of the presence of after-pulses on the s_2 pulse shape generated with a toy Monte-Carlo model.

Table V.3 – Results of the s_2 pulse shape model fit for different values of after-pulses (AP). Errors on these values are three orders of magnitude less than the given values. The only exception is τ_1 with an error of only one order of magnitude smaller. It is also the only parameter showing a discrepancy with theory.

	No AP	20% AP $\tau_{AP} = 1\ \mu s^{-1}$	20% AP $\tau_{AP} = 2\ \mu s^{-1}$	40% AP $\tau_{AP} = 1\ \mu s^{-1}$	60% AP $\tau_{AP} = 1\ \mu s^{-1}$
τ_1 $[\mu s^{-1}]$	0.0020	0.0018	0.0018	0.0025	0.0028
τ_2 $[\mu s^{-1}]$	3.591	3.595	3.595	3.597	3.601
p	0.101	0.100	0.100	0.101	0.102
T_d $[\mu s]$	0.508	0.503	0.503	0.505	0.505

Freeing the y_0 parameter, the best-fit value does not change significantly.

V.3.2 S_2 Generation with Full Monte-Carlo

For this second approach, we use the DarkSide electronic response simulation tool. This tool generates waveforms following argon electro-luminescence parameters using the singlet probability for s_2 (0.3) and the decay times of the fast (10 ns) and slow (3 μs) s_2 component.
The simulation tool is applied to the ReD setup composed by 28 channels, 24 in the top tile inside a 4×6 SiPM grid and 4 in the bottom tile, each the sum of 6 SiPMs [123]. Hence, in order to test this simulation for ReD, waveforms are simulated in 28 channels with a pre-determined occupancy, *i.e.* the mean number of photo-electrons per channel, that follows ReD setup: 24 channels with a small occupancy followed by 4 channels with a high occupancy (corresponding to bottom channels inside ReD).

We generate waveforms with an s_1 followed by an s_2 with a uniform drift time of 10 μs. The number of photo-electrons for s_1 is simulated each time by a Poisson's distribution with an expectation value of 20 primary photo-electrons. This last value is determined using ReD data. The associated number of photo-electrons for s_2 is computed as 10 times the number of photo-electrons for s_1. Three additional effects are taken into account in the computation of the s_2 number of photo-electrons.
First, the initial smearing, *i.e.* the time taken by the photo-electron to extract from the ionisation cloud (a Gaussian distribution of RMS 250 μs); Then the time taken by ionization electrons to reach the gas pocket (a uniform distribution with as maximal length the drift time); Finally the de-excitation time inside the gas pocket (an exponential distribution with a decay time either of the fast or slow components depending on the case). We simulate a drift time in the gas pocket of 1 μs, which gives a gas pocket in the range expected in ReD (between 4.8 and 6.4 mm depending on the velocity estimation (cf. Section V.2), so below 7 mm).

We also generate the instrumental noises expected in ReD: a 0.15 after-pulses probability with an associated $\tau_{AP} = 1\ \mu s^{-1}$; a 0.2 probability of cross-talk.

Once waveforms are simulated, we apply the hit finding algorithm of Chapter IV and then the pulse finding procedure described in Section IV.3. This reconstruction allows to have access to the quantities necessary to describe the s_2 pulse shape, namely the hit time, the hit integral, the number, type and start time of s_2 clusters. S_2 pulse shape is defined as the measured hit time subtracted by the start of s_2 pulses for events where a s_1 pulse is followed by an s_2 pulse.

We then apply the fit of the model described in the previous section for several configurations: a low occupancy channel, a high occupancy channel and a waveform simulated without noise in a low occupancy channel. The fit is not sensitive to τ_1 as already experienced in [202]. The best fits for these three cases are shown in Figure V.3. Different parameters in each case are summarized in Table V.4 with their discrepancies from input values.

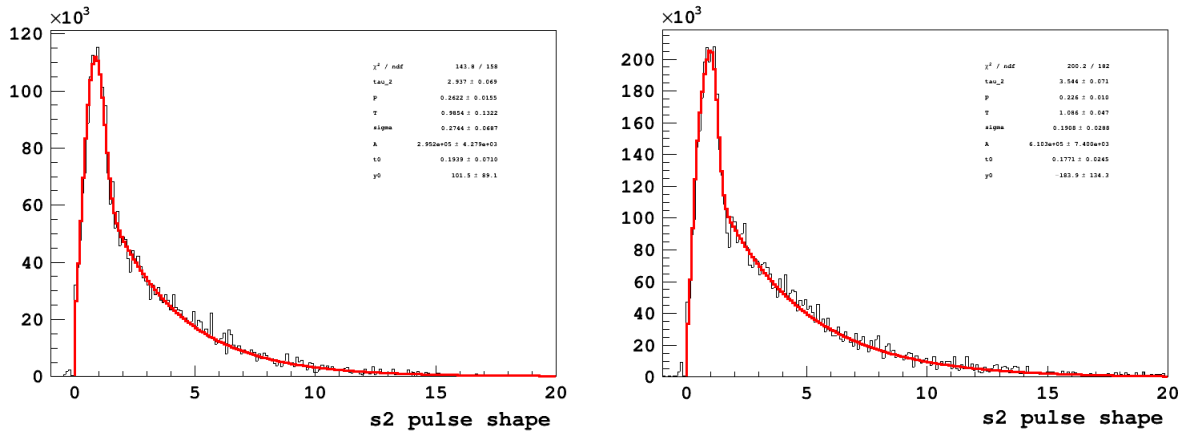

(a) (b)

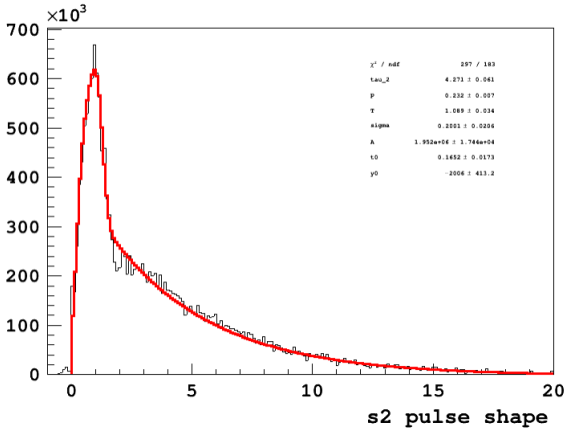

(c)

Figure V.3 – Best-fits for simulated waveforms with DarkSide electronic response simulation tool, (a) without noise and at low occupancy, (b) with noise at low occupancy and (c) with noise at high occupancy

Table V.4 – Fit parameter values τ_2, p, T_d and σ depending on three cases (without noise and low occupancy, with noise and low occupancy and with noise and high occupancy). The true value of σ is not known.

	Input value	Without noise	With noise	High occupancy
τ_2 $[\mu s^{-1}]$	3	2.94±0.07	3.54±0.07	4.27±0.06
p	0.3	0.26±0.02	0.23±0.01	0.23±0.01
T_d $[\mu s]$	1	0.98±0.13	1.09±0.05	1.09±0.03
σ	-	0.27±0.07	0.19±0.03	0.19±0.03

From Table V.4, we can see that the best results are obtained when noise is not included. Concerning p, it becomes smaller when adding noise as after-pulses tend to populate the slow component. When high occupancy is simulated, τ_2 tends to be over-estimated. This implies that we have to avoid high occupancy channels for the monitoring of the gas pocket.

We then look at correlation coefficients between the parameters, they are summarized

in Table V.5. We observe a strong anti-correlation between T_d and σ and a small one between p and σ in most cases and p and τ_2. This should be kept in mind for estimating systematics on the different fit values.

Table V.5 – Correlations coefficients between fit parameters depending on three cases (without noise and low occupancy, with noise and low occupancy and with noise and high occupancy)

	Without noise	With noise	High occupancy
T_d vs. σ	-0.88	-0.62	-0.53
T_d vs. τ_2	-0.13	0.05	0.07
p vs. σ	0.57	0.28	0.30
p vs. T_d	-0.34	0.12	0.16
p vs τ_2	- 0.13	0.36	0.26
τ_2 vs σ	0.23	0.11	0.11

V.3.3 Impact of the Occupancy

As shown in Table V.4, the channel occupancy has a strong impact on the fit. To look at this impact, we generate simulated waveforms with decreasing occupancies ranging from $\sim 7\%$ to $\sim 3\%$, mimicking the situation we have in ReD data. Retrieved occupancies are summarized in Table V.6.

Table V.6 – Percentage of occupancy inside each channel of the data simulated with a decreasing occupancy

Channel	0	1	2	3	4	5	6	7	8	9
Occupancy [%]	6.65	5.25	4.87	4.58	4.35	4.17	4.01	3.87	3.76	3.64
Channel	10	11	12	13	14	15	16	17	18	19
Occupancy [%]	3.53	3.46	3.39	3.33	3.24	3.18	3.13	3.08	3.04	2.99
Channel	20	21	22	23	24	25	26	27		
Occupancy [%]	2.94	2.89	2.86	2.83	2.78	2.75	2.71	2.67		

We perform a fit to extract the s_2 pulse shape parameters and we study their behavior as a function of occupancy (Figure V.4).

τ_2 increases with the occupancy, and for every fit, has a value between 2 to 4 times higher than the input one (3 μs^{-1}). T_d is decreasing with the occupancy, going away from its input value while p is raising from its input value with the increasing occupancy. Sigma is very slightly impacted by the occupancy: its value stays stable inside the interval 0.21 - 0.28. Finally, t_0 and y_0 values are not stable which would have been our first guess; they increase and decrease, respectively. In addition, y_0 is always negative and we would have expected it to be positive and around 0 as it should correspond to a shift of the baseline. The inverse behaviour of τ_2 and y_0 with the first one increasing and the other one decreasing might be linked and model-related.
So, we see here that the occupancy has a none negligible impact on the fitted values and hence on the final result.

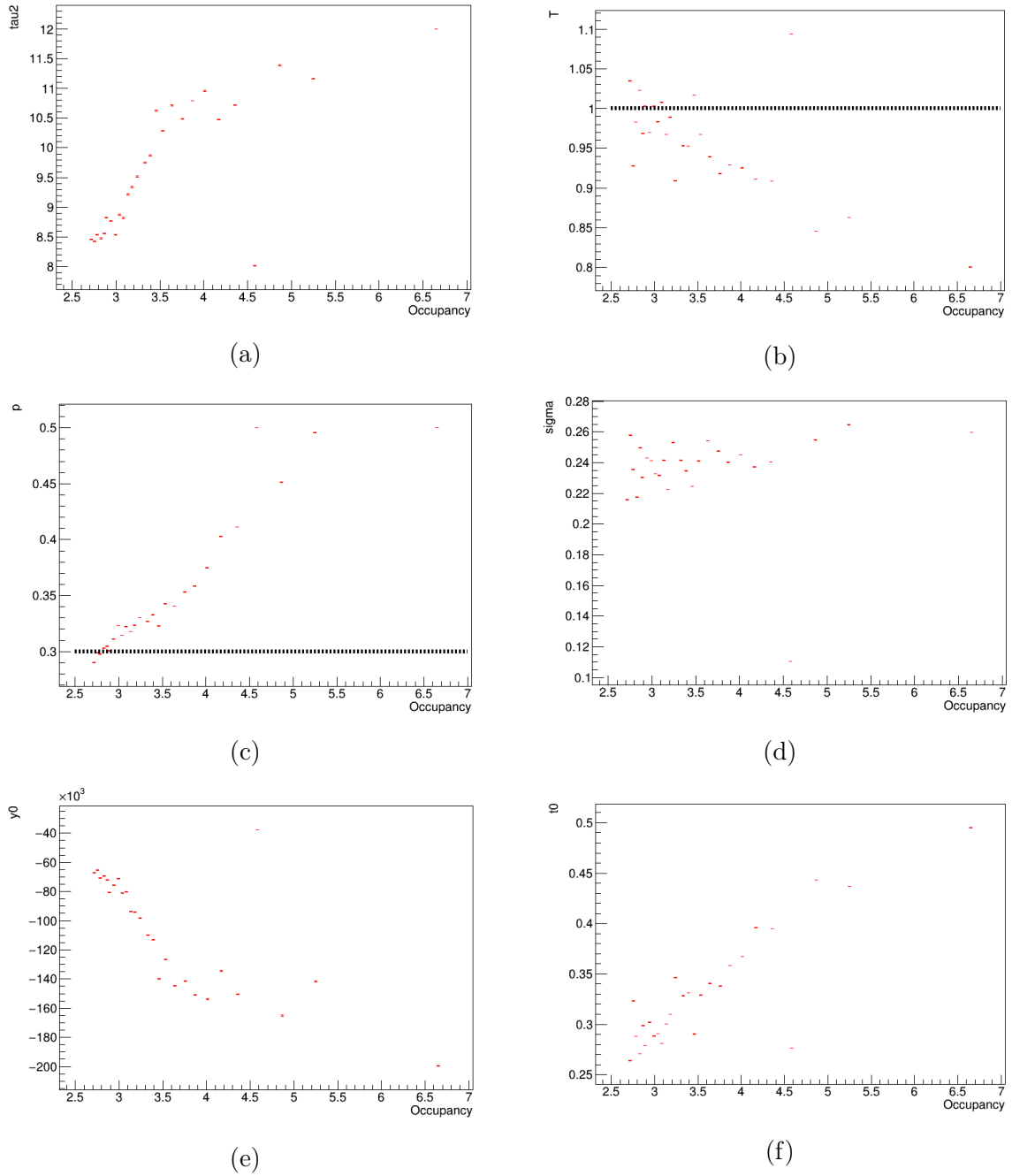

Figure V.4 – Fit values with their associated errors for (a) τ_2 and (b) T_d, (c) p, (d) σ, (e) y_0 and (f) t_0 depending on the occupancy for simulated data depending on the occupancy. The horizontal dotted line for τ_2, T_d and p correspond to their input values: 3 μs^{-1} (not shown on the plot as too small), 1 μs and 0.3 respectively

Concerning correlations coefficients we observe anti-correlation between T_d and sigma independently on the occupancy. This is coherent with what we observe in Table V.5.
The other anti-correlation that we observe is between p and τ_2 which is not observed at lower occupancies (again, Table V.5). Other variables can be considered as uncorrelated (values below $\pm$ 0.2) as observed before.

V.4 Measurement with ReD Data

For this analysis, we use runs taken by the ReD experiment when it was located at Catania during December 2019 and February 2020. We select runs taken with an ^{241}Am source at field on with an electric field of $\sim$ 200 V/cm and in presence of a gas pocket. Runs are reconstructed using the hit finder algorithm described in Chapter IV.

We select events having two pulses, an s_1 followed by an s_2 with a time difference between 10 and 20 μs. The peak time of s_2 pulses must be between 0.6 and 1.2 μs. Variables used during the analysis are summarized in Table V.7. The results shown in this section are given for channel 5, the channel with the smaller occupancy as occupancy induces a small distortion around the peak of the shape.
S_2 pulse shape is then built by subtracting measured hit times to the start of the s_2 pulses, all of that weighted by the prominence. An example for run 1363 is shown in Figure V.5.

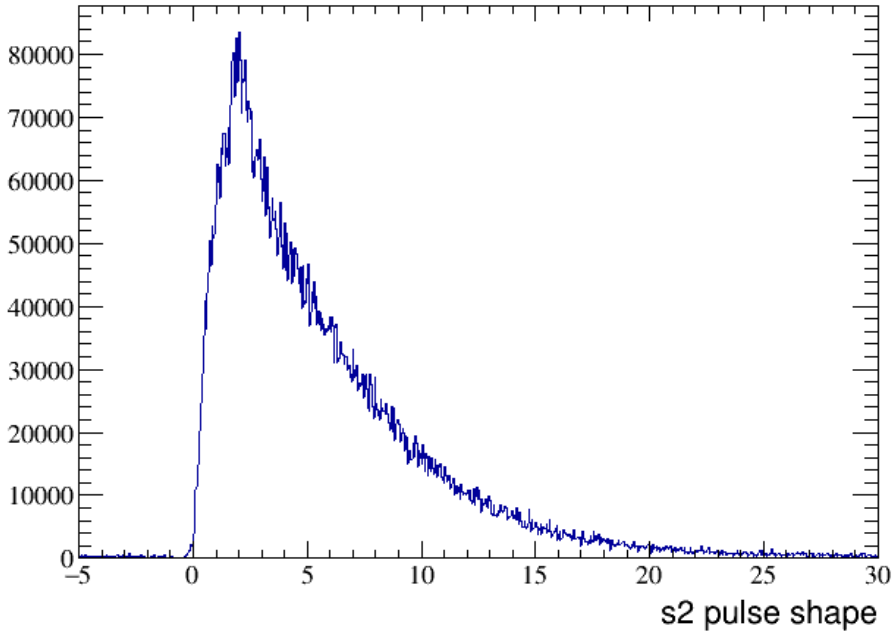

Figure V.5 – s_2 pulse shape for channel 5 of ReD run 1363

Table V.7 – Variables used in s_2 pulse shape computation

Variable	Meaning
pk_t	Time associated to each hit
pk_k	Hit integral for each hit
pk_p	Prominence for each hit
pk_ch	Channels associated to each hit
ncl	Number of clusters
cl_type	Type of each cluster, either 1 for s_1 or 2 for s_2
cl_p	Prominence for each cluster
cl_startt	Start time of each cluster

The fit of the s_2 shape for channel 5 with the model described in Section V.1 is shown in Figure V.6.

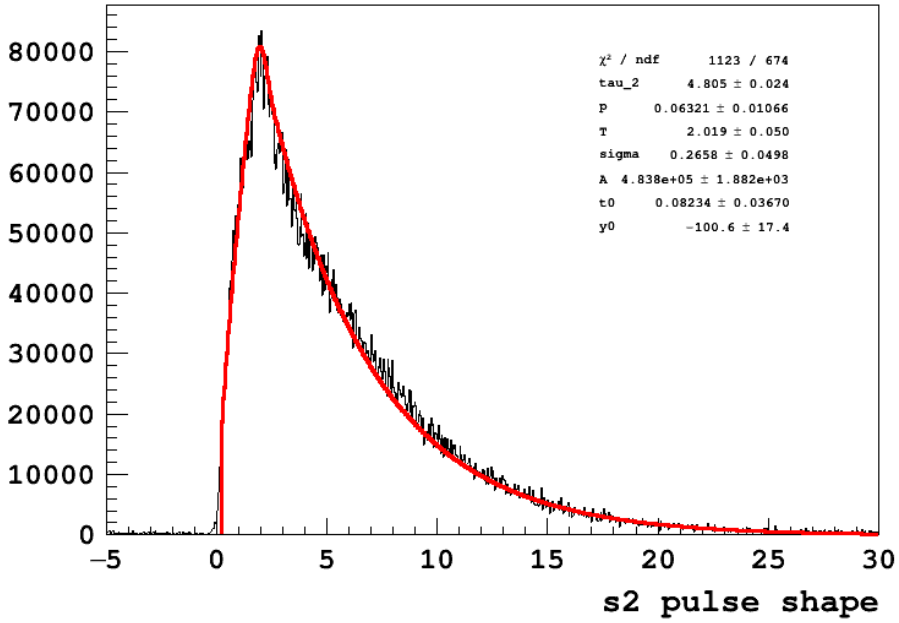

Figure V.6 – Fit with the model developed in Section V.1 of s_2 pulse shape for channel 5 of ReD run 1363

The fit returns a value of τ_2 around 4.80 ± 0.02 μs^{-1}, so higher than the expected one (around 3-3.5 μs^{-1}). Such a discrepancy was observed in the simulation Section V.3.3 for similar values of occupancy. Systematics are evaluated using a channel of similar occupancy in the Full Monte-Carlo study reported in Section V.3.2.

This gives:

$$\begin{aligned} T_d &= 2.02 \pm 0.05(stat.) \pm 0.07(syst.)\ \mu s \\ \tau_2 &= 4.80 \pm 0.02(stat.) \pm 1.83(syst.)\ \mu s^{-1} \\ p &= 0.06 \pm 0.01(stat.) \pm 0.03(syst.) \end{aligned} \tag{V.10}$$

The value of the drift time multiplied by the gas drift velocity (cf. Section V.2) gives a gas pocket thickness between 0.97 cm and 1.29 cm. The hole of the bubbler being at 3

mm from the grid the gas pocket should mechanically be at a maximum of 7 mm. The obtained value is hence physically incompatible. This should be due to some bias that is not yet understood and could require a remodeling of the s_2 pulse shape.

V.5 Spatial Uniformity

In Section V.3.3, we looked at the impact of the occupancy on fit results. To evaluate the spatial uniformity we do the same study over the different channels of the data as we know they have different occupancies due to the position of the ^{241}Am source. The occupancy map is shown in Figure V.7.

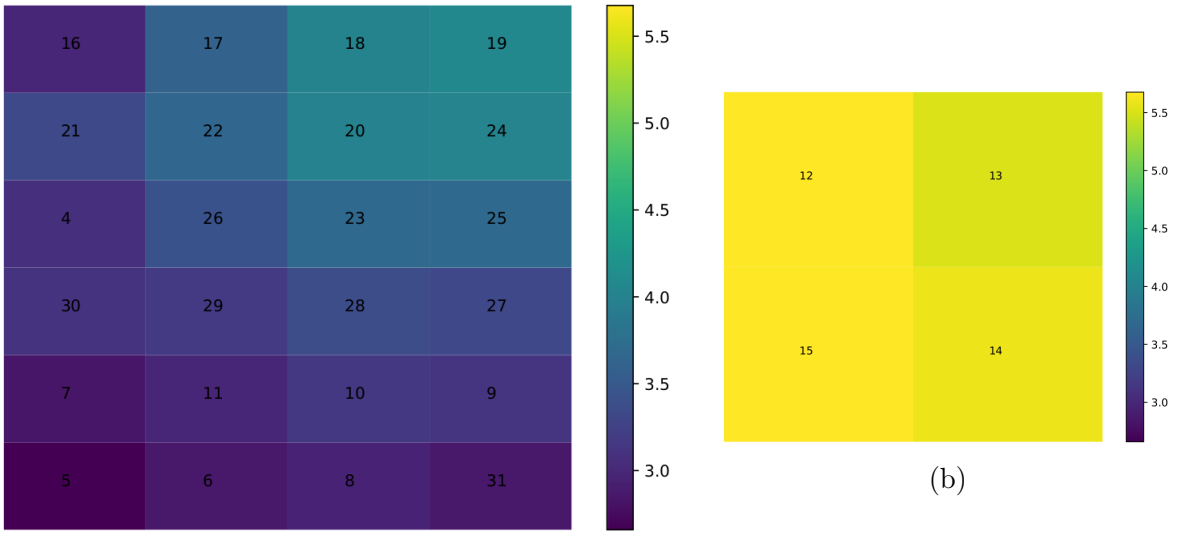

Figure V.7 – Map of the percentage of occupancy inside ReD TPC for (a) top and (b) bottom channels. The channel number is written in black for each one of them.

The best-fit values for T_d, τ_2 and p and their associated errors are plotted for each channel in Figure V.8. For p and τ_2 the values are uniform within the error bars over the detector. It is worth noting that bottom channels have higher values, but also larger errors bars, due to the high occupancy of these channels with respect to the top ones. For T_d, the effect of the occupancy among the channels is larger, with differences even between the different occupancies inside top channels. However, values are mainly contained in the range between 2 - 2.2 μs giving a rather uniform distribution over the detector within the error bars, so a difference of maximum 10% between the channels.

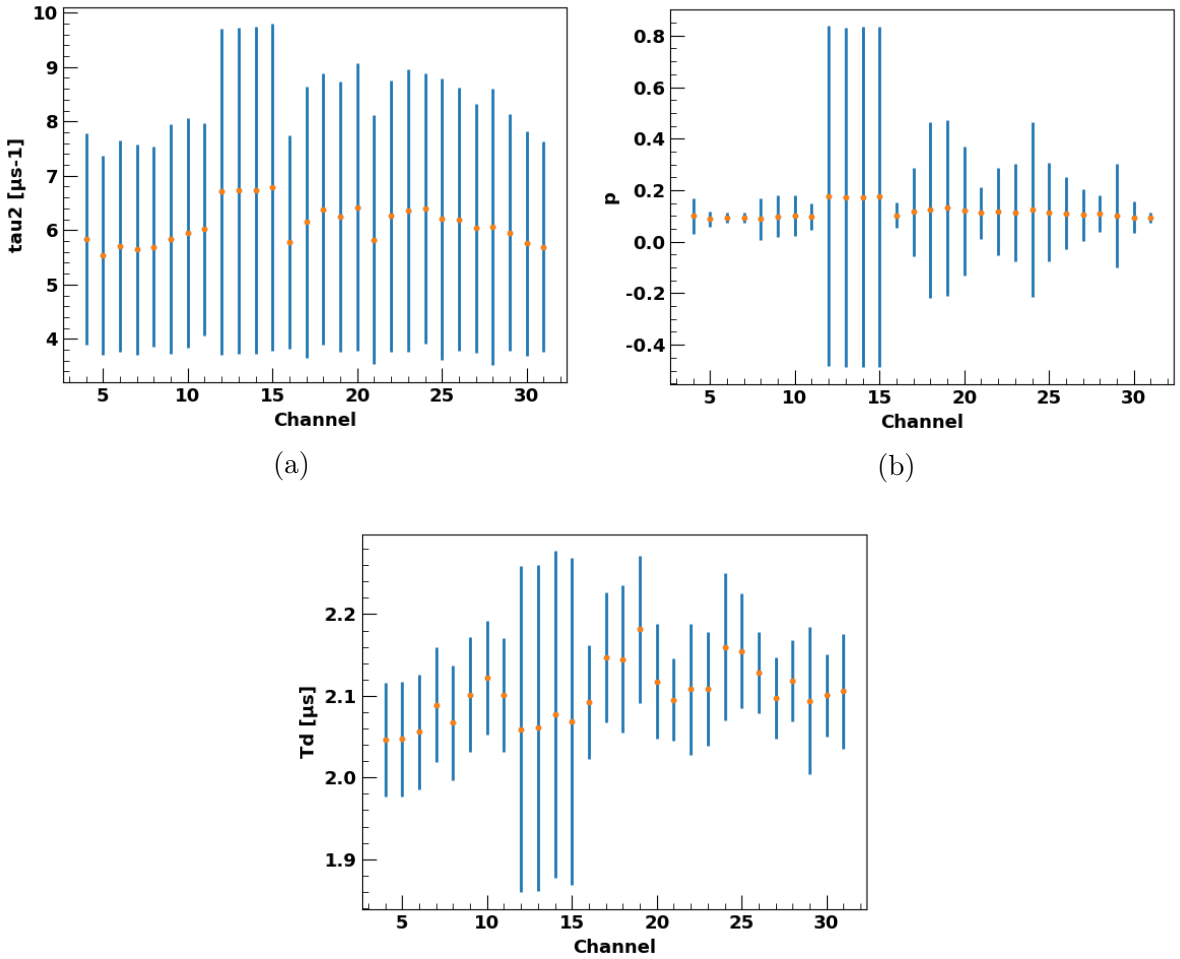

(a) (b)

(c)

Figure V.8 – τ_2, p and T_d values with their associated statistic (orange) and systematic (blue) errors depending on the channel inside ReD TPC. Channels 12 to 15 are bottom channels.

V.6 Stability over the Runs

We now look at the evolution of the gas pocket thickness along different runs. We use data from runs 1363, 1366, 1368, 1400, 1401, 1403, 1420 and 1436. As we already saw several times that the occupancy is impacting some of the variables, we are using for each run a channel with a low occupancy (around 2.7%, channel 5).

Values of τ_2 and p do not show any clear patterns over the runs, they are between 3 - 7 μs^{-1} and between 0 - 0.12, respectively (Figures V.9a and V.9b).
For T_d however, we observe a decrease of values over the runs (Figure V.9c). As maintaining the gas pocket was complicated during the data taking, the possibility of an instability of the gas pocket thickness is possible. Furthermore, this instability could also be due to an instability of the TPC electric field over time.

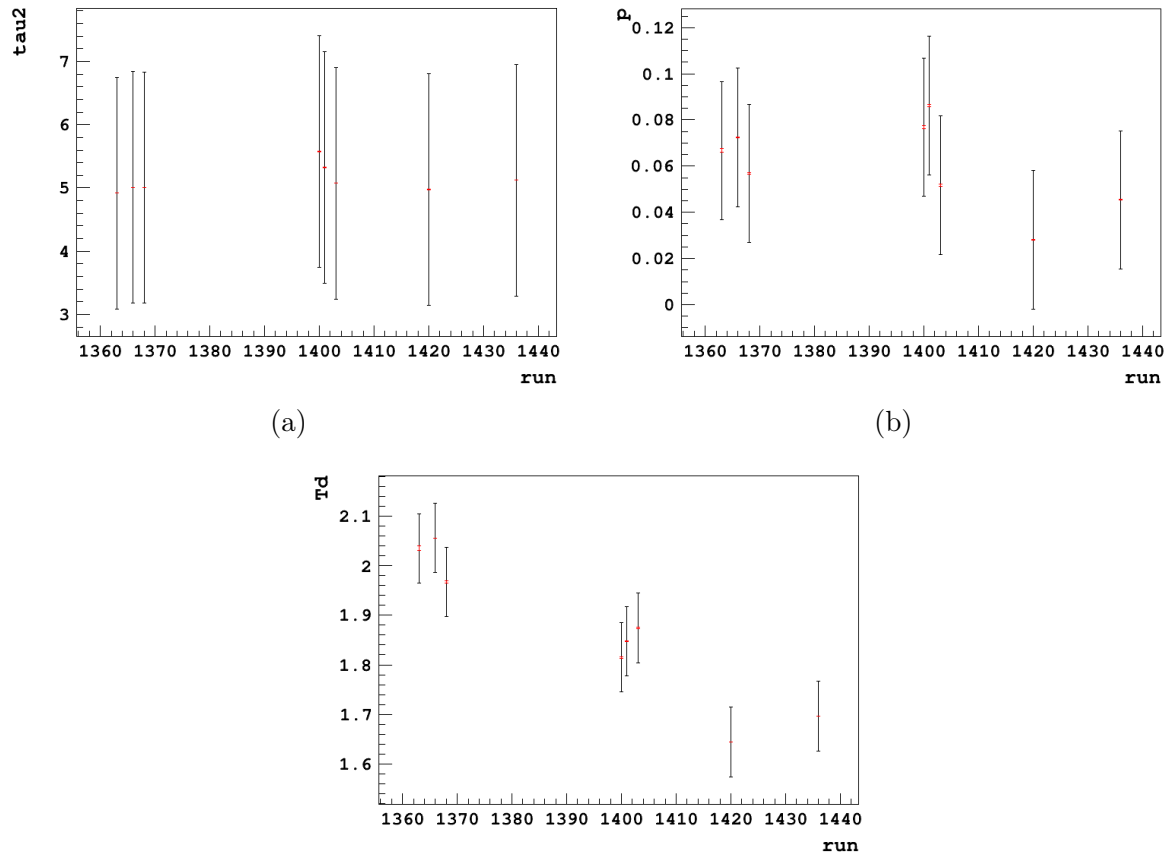

(a) (b)

(c)

Figure V.9 – Fit values and associated statistic (red) and systematic (black) errors for (a) τ_2 $[\mu s^{-1}]$, (b) p and (c) T_d $[\mu s]$ depending on the run number for channel 5.

V.7 Conclusion

We used the s_2 pulse shape model to fit the gas pocket thickness inside the ReD experiment. Simulations allowed us to compute errors on the model before applying it to the data. However, we found a gas pocket of 1 - 1.5 cm not compatible with mechanical constrains of the experiment (maximum of 7 mm). This indicates some biases in the model that would need further effort, possibly setting a new model describing better the diffusion, to fully understand the behavior of the s_2 pulse shape and to be able to use it for an absolute determination of the gas thickness.

However, this is still a valuable tool that has been used to monitor the gas pocket during ReD data taking. Indeed, looking at the drift time across the channels of the detector, we found that the dependence on the occupancy is small with a trend from the bottom/left to top/right of the detector as it was expected because of the position of the ^{241}Am source. This indicates a stable gas pocket over the TPC. Hence, this approach can still give a relative measurement of the gas pocket thickness over the channels and the data taking and allows to tackle changes during the run.

Chapter VI

Pulse Shape Discrimination

> Ce n'est pas la distance qui mesure l'éloignement.
>
> Antoine de Saint-Exupéry (1939)

As explained in Chapter II, one of the main advantages of liquid argon based TPC in the search of dark matter is the possibility of distinguishing between electronic and nuclear recoils thanks to the different pulse shapes of the scintillation signal. DarkSide-50 has demonstrated that the pulse shape discrimination (PSD) allows to reject electronic recoils with a discrimination factor above 10^8. This capability combined with the detector design, the shielding from the underground location and the use of underground argon allows to perform background-free searches of WIMPs for multi-ton exposures.

Differently, liquid xenon cannot rely on the PSD but on the ratio between ionisation and scintillation signals. Such technique, also available for liquid argon experiments, allows to reach a rejection power of $\sim 10^3$.

The PSD in liquid argon is based on different de-excitation times for singlet and triplet states (cf. Section II.1.2). The s_1 signals are exploited for PSD for recoil energies above 10 keV, where the photon statistics is large enough.
The variable f_p, representing the fraction of photo-electrons detected in the first p ns of the pulse, is used to distinguish electronic recoil from nuclear recoil. This variable allows to isolate the contribution of the s_1 signal induced by the de-excitation of singlet states that are produced in different fraction by nuclear and electronic recoils.
In the case of DarkSide-50 the optimal value was found at p = 90 ns and a background free search of WIMPs was performed over the whole exposure in the parameter space of (s_1, f_{90}) delimited by the boxed purple region in Figure VI.1.

To fully exploit the extraordinary discrimination power of the PSD a deep understanding of the processes leading to s_1 is required, and in particular, a careful treatment of the fluctuations of the electronic recoil distribution. Indeed, for example, a small amount of Cerenkov light can contribute to the prompt component of the s_1 signal which artificially increase f_p and shift it closer to the one expected for nuclear recoils. Additional instrumental effects, such as after-pulses, direct and external cross-talks, and dark count rate (cf. Section II.3.2), can also affect the time shape of s_1 and consequently the determina-

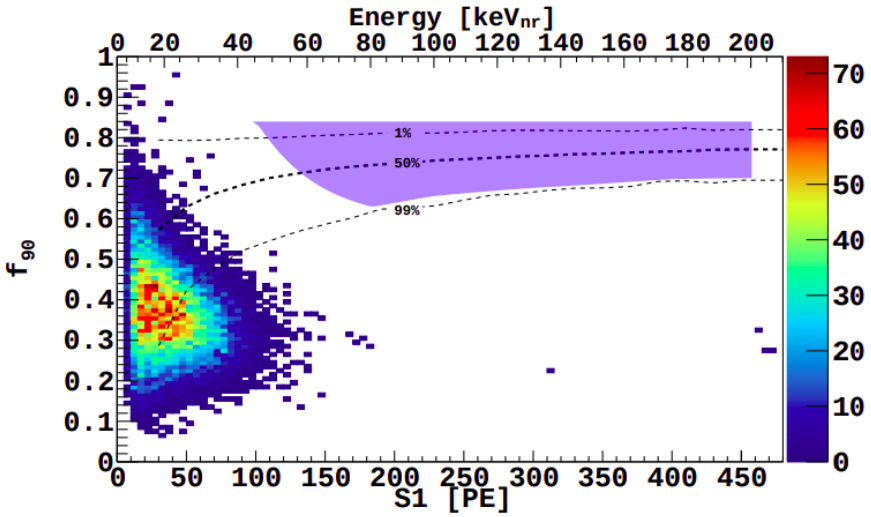

Figure VI.1 – Distribution of events in the (s_1, f_{90}) plane for DarkSide-50 after the data selection and the application of the different cuts [100]

tion of f_p.

In the case of DarkSide-20k, the use of SiPMs requires the development of new reconstruction tools, based on the determination of the hits, that were described in Chapter IV as well as a good understanding of the processes contributing to s_1.

In this chapter we will describe the work we did to optimize the PSD algorithm of DarkSide-20k that finally leads to the determination of DarkSide-20k sensitivity to WIMPs and contributed to provide its final design.
We will first describe the simulation package (Section VI.2) that generates the distribution of events inside the detector following key parameters that are easy to modify to run different scenarios. This tool also computes the acceptance region taking into account the description of the tails of the f_p distribution in the model (Section VI.1.2)). We will then show DarkSide-20k sensitivity to high mass WIMPs using the acceptance regions we computed (Section VI.3) and the impact on the sensitivity of different parameters and scenarios (Section VI.4).

VI.1 Statistical Approach Models

VI.1.1 The Hinkley Model

The approach to perform pulse shape discrimination traditionally used in DarkSide-50 is the Hinkley model [206]. This model is applied to the PSD where we consider as variables: the number of prompt photo-electrons n_p, the number of late photo-electrons n_l and the sum of both s_1, as

$$w = \frac{n_p}{n_p + n_l} = \frac{n_p}{s_1} \tag{VI.1}$$

If n_p and s_1 are normal distributions, the PSD can be written as a function of w:

$$f_h(w) = \frac{\mu_p w\sigma_l^2 + \mu_l(1-w)\sigma_p^2}{\sqrt{2\pi[w^2\sigma_l^2 + (1-w)^2\sigma_p^2]^3}} \exp \frac{-[\mu_l w - \mu_p(1-w)]^2}{2(w^2\sigma_l^2 + (1-w)^2\sigma_p^2)} \tag{VI.2}$$

with μ_p, μ_l, respectively the mean of the prompt and late part of the signal and σ_p and σ_l respectively the standard deviation of the prompt and late part of the signal. This provides a purely statistical description of the fluctuations of w and it is worth noting that fit variables are not associated to any physical effects.

However, this model does not take into account the procedure used in DarkSide-50 where s_1 is fixed to a given value, and hence is not a variable but a constraint (as $f_p < 1$, then $f_p \times s_1 < s_1$) and so s_1 cannot be considered as a random normal variable. In addition, this model overestimates the tails of distributions reducing the sensitivity of DarkSide and producing more conservative limits on WIMPs (cf. Figure VI.2).
A new model was developed to describe the pulse shape discrimination for DarkSide. This method is called the 'tail model'.

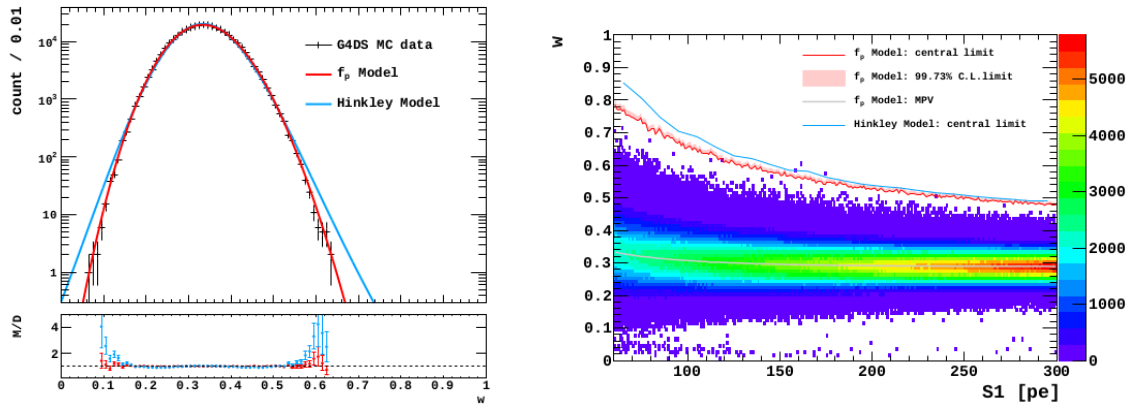

(a) (b)

Figure VI.2 – (a) w distribution at $s_1 = 60$ pe, with 3.1×10^5 statistics in 1-pe bin, from G4DS simulation of 8 keV electrons. Associated uncertainties are obtained by combining statistical errors and from the fit. (b) Comparison of the electron leakage acceptance between the Hinkley and the tail model on DarkSide-50 atmospheric argon data.

VI.1.2 The Tail Model

The pulse shape discrimination parameter w is defined as the fraction of light detected in the prompt component (corresponding to the first 90 ns in DarkSide-50). In contrary to the Hinkley model, and as mentioned above, we will only consider an infinitely small interval of 1 photo-electron in the neighbourhood of s_1 that we call s_{1_0}. With n_p the number of photo-electrons in the prompt component and n_l the number of photo-electrons in the late component, we then have :

$$n_p + n_l = s_{1_0} \tag{VI.3}$$

With $n_p \leq s_{1_0}$, the pulse shape discrimination parameter is consequently expressed as:

$$w = \frac{n_p}{s_{1_0}} \tag{VI.4}$$

We can define the variance of w as σ_w^2:

$$\sigma_w^2 = \left(\frac{\partial w}{\partial n_p}\right)^2 \sigma_p^2 + \left(\frac{\partial w}{\partial n_l}\right)^2 \sigma_l^2 - 2\frac{\partial w}{\partial n_p}\frac{\partial w}{\partial n_l}\sigma_p\sigma_l \tag{VI.5}$$

with σ_p the prompt component resolution and σ_l the late component resolution.

We assume that the following physical effects for n_p and n_l can be modelled either by a Poisson or a Binomial distribution:

- Photo-electrons emitted by the liquid argon scintillation: Poisson distribution [207]
- Effects related to photon emission, propagation and detection: Bernoulli process for prompt and late components leading to binomial distributions
- Correlated noise: Binomial contribution to prompt and late components

With large statistics both Poisson and Binomial distributions can be approximate by Gaussian distributions. Hence, we can use the standard deviation of Gaussian distributions to evaluate the prompt and late components:

$$\sigma_i = k_i\sqrt{s_{1_0}} \tag{VI.6}$$

with k_i a constant and i being either p or l.

In the end, the model that we can apply on the w distribution is such as:

$$f_p(w) = A\exp\left(-\frac{(w-w_0)^2}{2\sigma_w^2}\right) = A\exp\left(-\frac{s_{1_0}(w-w_0)^2}{2((1-w)k_p + wk_l)^2}\right) \tag{VI.7}$$

with w_0 the most probable value of w and A a normalisation factor. We obtain A, w_0, k_p and k_l by fitting w distribution by this $f_p(w)$ model for each s_{1_0}. We can also retrieve the electronic recoil leakage in the WIMPs acceptance band thanks to this model.

The uncertainty on the $f_p(w)$ model is obtained by analytically propagating the errors and is hence expressed as:

$$\sigma_{f_p}(w) = f_p(w)\left[\frac{\sigma_A^2}{A^2} + \left(\frac{w-w_0}{\sigma_w^2}\right)^2\left(\sigma_{w0}^2 + \left(\frac{w-w_0}{s_{1_0}\sigma_w}\right)^2(w^2\sigma_{kl}^2 + (1-w)^2\sigma_{kp}^2)\right)\right]^{1/2} \tag{VI.8}$$

with σ_A, σ_{w0}, σ_{kp} and σ_{kl} the uncertainties associated with respectively A, w_0, k_p and k_l. They are retrieved from the fitting procedure. In the end, a 99.73% C.L. belt is given by $f_p(w) \pm 3\sigma_{f_p}(w)$.
The fit of the w distribution for a given s_1 was shown in Figure VI.2 along with the resulting electron leakage acceptance.

In addition, the statistics governing w for electronic recoils and nuclear recoils are the same. Consequently the tail model can also be used to define the acceptance band of WIMPs. An example for data from an ^{241}Am^{9}Be neutron source inside DarkSide-50 is shown in Figure VI.3.

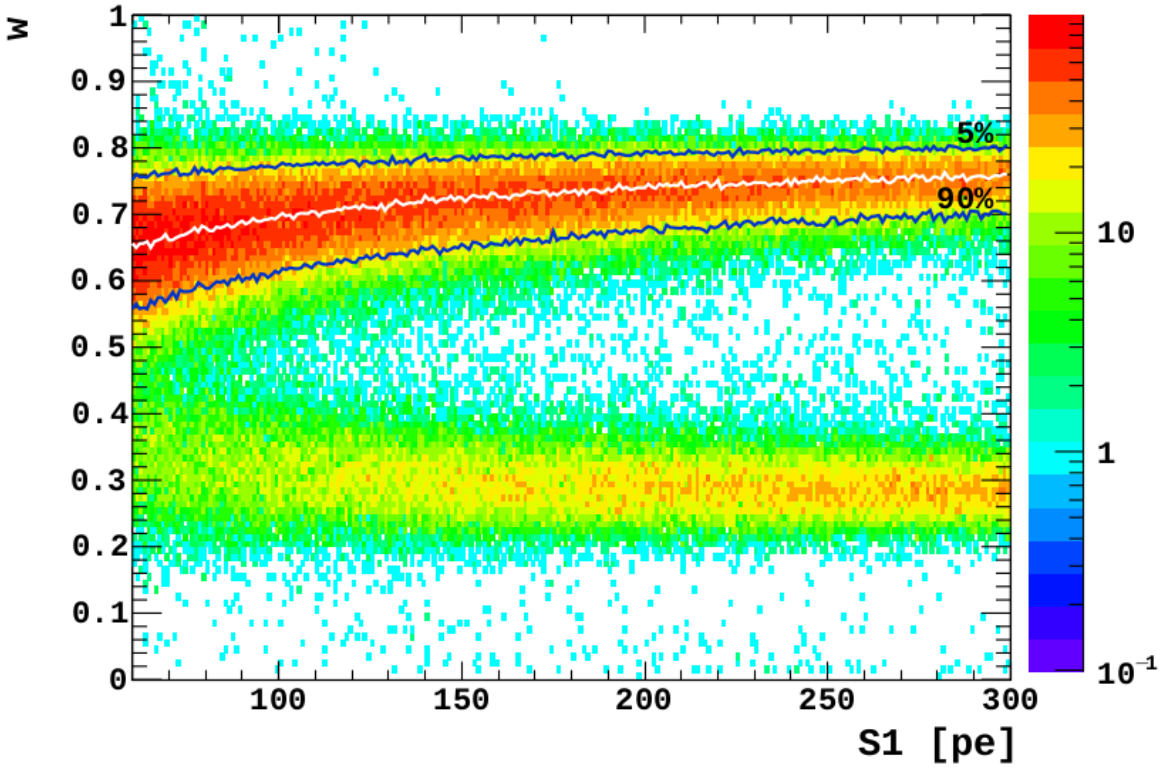

Figure VI.3 – (s_1, w) parameter space for ^{241}Am^{9}Be neutron source inside DarkSide-50 showing nuclear recoils from neutrons scatters and electronic recoils from the source and TPC background. Acceptance bands are displayed in blue and evaluated using the tail model. The white line shows the most probable value of the model nuclear recoil distribution following the tail model.

VI.2 A New Tool: the PSD package

To investigate the effects of instrumental parameters and design choices of the detector on the PSD and its impact on the final sensitivity of the detector, we set up a flexible toy model that can accurately simulate physical processes inside the detector.
The main difficulty of this approach is the statistics: more than 1.5×10^{8} events of electronic recoils are expected in a 100 year-ton exposure. Such a statistic cannot be simulated with the full DarkSide framework. The PSD tool is able to compute acceptance probabilities minimizing computing resources.

VI.2.1 Structure and Variables

In order to generate the spectra of electronic recoil and nuclear recoil events, the following steps are performed:

- **Spectra**: for electronic recoils we assume that all the backgrounds are coming from 39Ar with the corrections to the spectra described in Chapter III while for nuclear recoils we use a flat spectrum. As for low energy recoils electronic recoil and nuclear recoil distributions are not well separated and the PSD cannot be fully exploited,

we focus on the region of $s_1 > 70$ photo-electrons, so ∼25 keVnr. In addition, we include the range for WIMPs up to 10 TeV/c^2, so below 100 keVnr nuclear recoils (∼350 photo-electrons).

- **Scintillation**: for a given recoil, either electronic or nuclear, we include all the processes leading to the formation of the scintillation light presented in Section VI.2.2
- **Detector** effects are then simulated including the time of flight (cf. Section VI.2.3), the single photo-electron time resolution and reconstruction effects.
- **Noise**: Instrumental noises are added (after-pulses, direct and external cross-talks and dark count rate) as detailed in Section VI.2.4.

Different channel configurations can be used inside this model. We will further refer to them by referring to their grouping: 1x1 is usually the reference case without any grouping. 2x1 is the grouping of two channels (or PDMs) compared to the reference case. 2x2 is the grouping of four channels, making a square of four PDMs. Channel configurations will be described in more details in Section VI.4.4 where we will see their impact on the PSD.

Table VI.1 – List of variables used in the PSD package for the 1x1, 2x1 and 2x2 configurations. Variables are separated into their original classes in the following order: Scintillation, Spectra, Detector and Noise.

Physical meaning	1x1	2x1	2x2
Photon collection efficiency	0.20	0.21	0.225
Number of quanta produced by a deposit		19.5 eV	
Decay time of the fast component		6 ns	
Decay time of the slow component		1600 ns	
Scintillation efficiency distribution		ARIS paper	
Field quenching distribution		ARIS paper	
Ar39 spectra in UAr		from X.Mougeot	
Minimum ER energy		3 keVee	
Maximum ER energy		50 keVee	
Minimum NR energy		5 keVnr	
Maximum NR energy		100 keVnr	
Detection efficiency		0.97	
Acquisition gate for a pulse		8000 ns	
Single photo-electron time resolution	4 ns	7 ns	7 ns
Number of channels	8280	4140	2070
Time of flight distribution		from G4DS	
Minimum time to separate two hits		200 ns	
DCR rate [ns^{-1}]	2.07×10^{-5}	2.07×10^{-5}	5.17×10^{-5}
Direct cross-talk probability	0.25	0.30	0.45
After-pulses probability	0.05	0.06	0.10
Decay time of after-pulses		600 ns	
Smallest pe charge detected for after-pulses		0.5	
Volt over Voltage value	6	7	9
Time distribution of external-cross-talks		TF2 report	

VI.2.2 Scintillation Processes

Electronic recoils The main background in the TPC fiducial volume is due to β-decay of ^{39}Ar. We consider the same activity of ^{39}Ar than the one measured by DarkSide-50: 0.73 ± 0.11 mBq/kg [98]. We included only events producing recoils between 3 and 50 keVee. Assuming an exposure of 5-years 20 ton fiducial volume we expect around 1.5×10^8 electronic recoil events distributed following ^{39}Ar β-decay spectra. For keV electrons as the ones we consider, the track inside the detector is too short to disentangle the different deposits, so we consider it as a single scatter event.

The deposited energy can lead to excitation or ionization. All the energy from excitation contributes to s_1 while, in the ionization, some of the electrons can recombine exciting Ar molecules and contributing to the s_1 signal as well. Hence, to compute s_1, we take into account the probability of recombination.

The s_1 response is as [207] (Figure VI.4b):

$$s_1 = C_e \frac{E_{dep}}{w_i}(r(E_{kin}) + \alpha_{ER}) \tag{VI.9}$$

with C_e the photon collection efficiency, $w_i = w(1 + \alpha_{ER})$ the mean energy to create an electron-ion pair, w the mean energy to create a quanta, α_{ER} the electronic recoil excitation-to-ionisation ratio and E_{dep} the deposited energy. The recombination probability $r(E_{kin})$ can be written as:

$$r(E_{kin}) = erf(E_{kin}/p_1)(p_2 \times e^{-E_{kin}/p_3} + p_4) \tag{VI.10}$$

with p_i, i = 1, 2, 3, 4 free parameters taken from the fit of DarkSide-50 data at 200V/cm [207].

Figure VI.4 shows the recombination probability and the s_1 response as a function of the recoil energy.

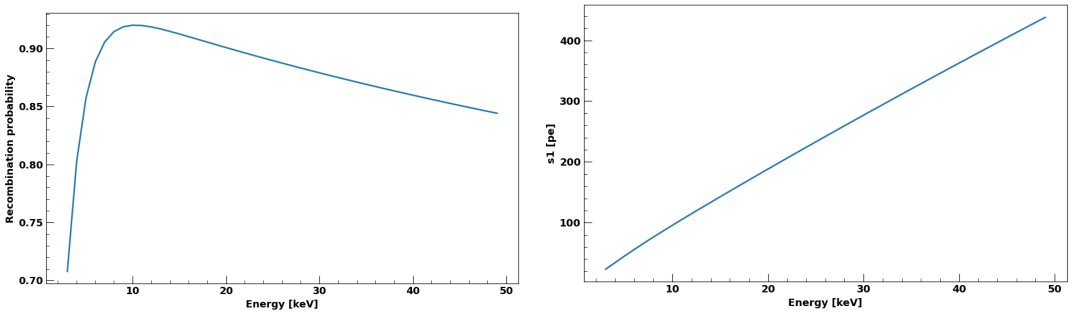

(a) (b)

Figure VI.4 – Electronic recoil (a) recombination probability depending on the kinetic energy and (b) energy scale depending on the deposited energy.

Nuclear recoils To investigate the efficiency of the PSD for nuclear recoils, we simulate a flat spectrum of nuclear recoils in the range 5 to 100 keVnr corresponding to the region of interest for WIMPs with masses up to 10 TeV/c^2.

The nuclear recoil energy E_{NR} [keV$_{NR}$] is translated in visible energy E_{vis} [keV$_{ee}$] by a scintillation efficiency factor depending on the nuclear recoil energy, also called quenching, as:

$$E_{vis} = L_{eff}(E_{NR}) \times E_{NR} \tag{VI.11}$$

This quenching reduces the amount of visible energy for a given nuclear recoil energy. Several quenching models exist for defining the quenching factor L_{eff}. For liquid argon, it was shown by the ARIS experiment that it is best described by a modified Mei model [110] (Figure VI.5a):

$$L_{eff} = f_n \times \frac{1}{1 + k_B \frac{dE}{dx} + k_B^*(\frac{dE}{dx})^2} \tag{VI.12}$$

Then, the conversion to s_1 is slightly different as we cannot analytically retrieve the electron-ion recombination term so we use an effective description. The electric field reduces the probability that electrons and ions recombine. This additional quenching consequently reduces s_1 and has to be taken into account:

$$s_{1_{nf}} = LY(E_{NR}) \times E_{vis} \tag{VI.13}$$

with LY the light yield depending on the nuclear recoil energy as computed in G4DS at 200V/cm [207] (Figure VI.5b).

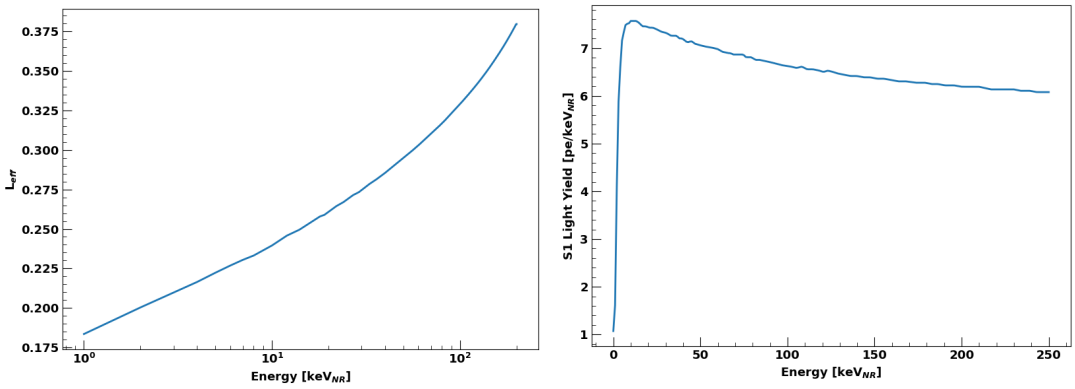

(a) (b)

Figure VI.5 – Nuclear recoil (a) scintillation efficiency depending on the nuclear recoil energy and (b) s_1 light yield depending on the nuclear recoil energy

Following [110], the dependence of s_1 on the electric field is modelled by the Thomas-Imel model f_{TI} [132] [110]:

$$s_1 = s_{1_{nf}} \times f_{TI}(E_{NR}) \tag{VI.14}$$

In the Thomas-Imel model the recombination probability is defined as:

$$R = 1 - \frac{\ln(1+\xi)}{\xi} \xi = C_{box} \frac{N_i}{F^\beta} \tag{VI.15}$$

From DarkSide-50 fit [110] at a field F=200V/cm, the constants have the values: C_{box}= 18.5±9.7 and β=1.07±0.09. N_i is the number of ions. For nuclear recoils, the number of ions is equal to the number of excitons ($\alpha_{NR} = 1$) consequently we have [207]:

$$N_{quanta} = 2N_i = L_{eff}(E_{NR}) \times \frac{E_{NR}}{w} \tag{VI.16}$$

Giving:

$$N_i = \frac{E_{vis}}{2w} \tag{VI.17}$$

In addition, we can also express s_1 as a function of the recombination probability and the number of ions:

$$s_1 = C_e \times (\alpha + R) \times N_i \tag{VI.18}$$

So, we can express this quenching as in ARIS [110] as the ratio of s_1 and $s_{1_{nf}}$ where there is full recombination (Figure VI.6):

$$\frac{s1}{s_{1_{nf}}} = \frac{\alpha_{NR} + R}{\alpha_{NR} + 1} = 1 - \frac{\ln 1 + \xi}{2\xi} = f_{TI}(E_{NR}) \tag{VI.19}$$

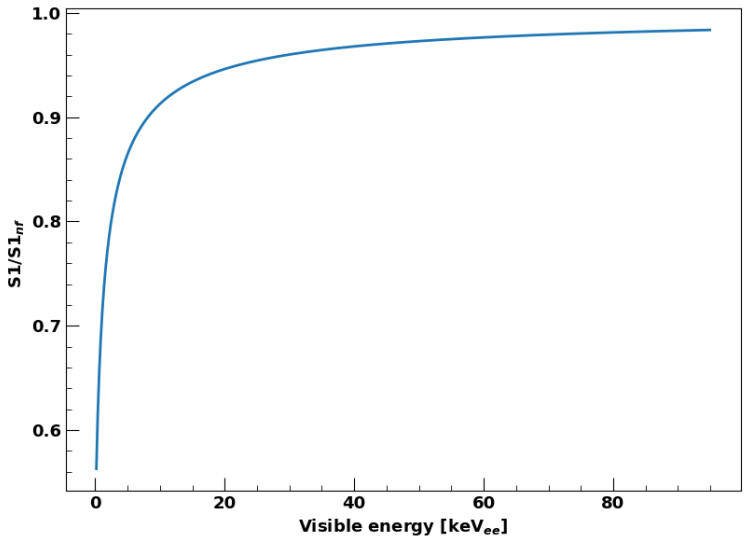

Figure VI.6 – Thomas-Imel model distribution depending on the visible energy at a 200V/cm electric field.

VI.2.3 Time of Flight Convolution

In DarkSide-50, due to the small size of the TPC, the propagation time inside the detector, also called the time of flight (ToF), was negligible. This is no longer the case for DarkSide-20k where we have to take it into account the time it will take for the photo-electrons to reach the SiPMs.

The time of flight inside the fiducial volume of the TPC is computed in the simulation. To do this, we simulate optical photons of 128 nm uniformly distributed inside the fiducial volume of the TPC and then simulate their propagation. We then are able to account for the ToF defined as the photo-electron times subtracted by the time of the first detected photo-electron. This distribution is shown in Figure VI.7. For each photo-electron, the time of flight is sampled from this distribution and added to the scintillation time.

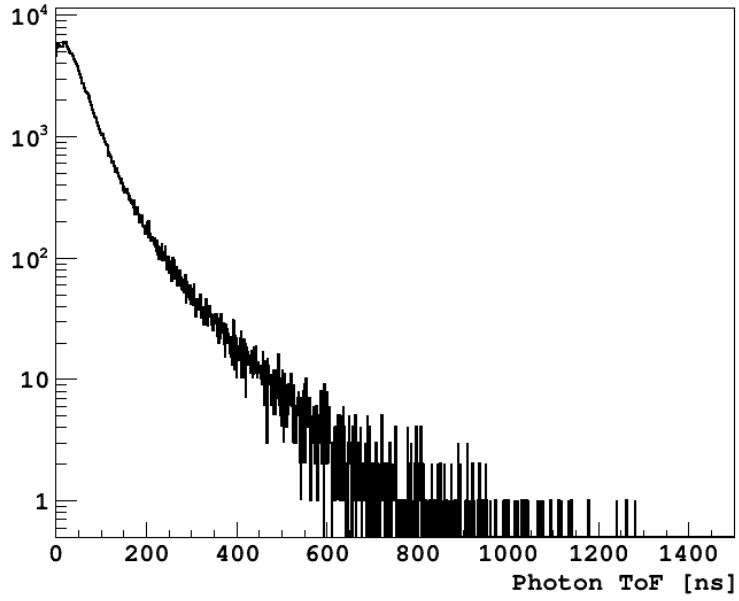

Figure VI.7 – Time of Flight distribution of optical photons inside DarkSide-20k from G4DS.

VI.2.4 Electronic and Detection Effects

Then, we add noises coming from electronics: correlated noises, external cross-talks and dark-count rate along with the detection efficiency.

Dark Count Rate. In DarkSide-20k, we expect a DCR frequency around 6×10^{-3} dark count/gate/m^2 for a 28m^2 SiPM coverage and a 8 μs gate. We compute additional photo-electrons due to this DCR as a Poisson distribution with a mean value corresponding to the DCR frequency multiplied by the SiPM coverage and the time length of each component.

Correlated noise. For each SiPM avalanche we create recursively cascades of cross-talks and after-pulses modelled by binomial probabilities. The delay time for after-pulses events is modelled by a random exponential with the characteristic decay time τ_{AP}= 600 ns.

External Cross-talks. We assume a production probability of 0.045×VoV and a detection probability of 11.9% on average on all the channels. Additional delay times are sampled from a pdf averaged over all the channels. Then delay times are added to primary times and these new photo-electrons are added to the total amount of photo-electrons in the prompt or late component depending on their final time.

Figure VI.8 shows slices at s_1 = 60 photo-electrons of a nuclear recoil distribution from the Monte-Carlo Toy Model with the addition of these three electronic noises. We see that the addition of correlated noise shift the f_{190} distribution to lower values while the external cross-talks and DCR impact the width of the distribution.

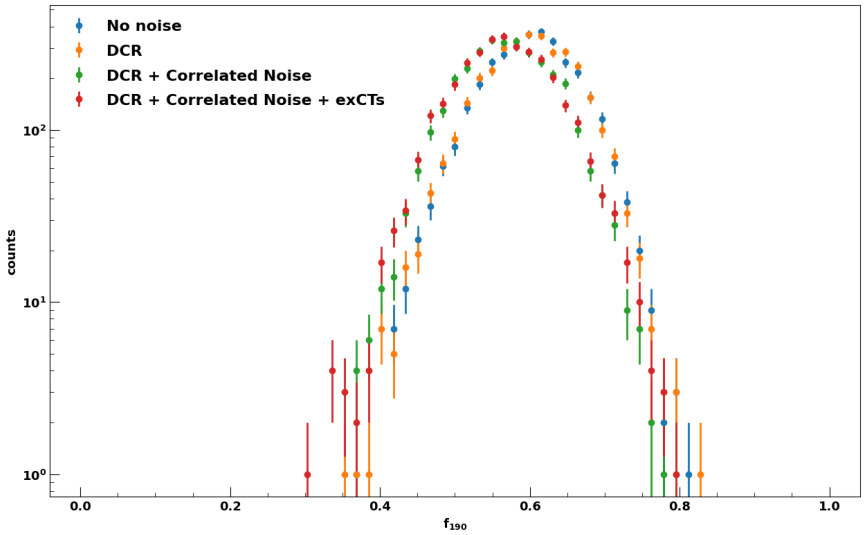

Figure VI.8 – Slice at $s_1 = 60$ photo-electrons for nuclear recoils for the f_{190} distribution from Monte-Carlo Toy Model without any electronic noise (blue), with only dark count rate (orange), with dark count rate and correlated noise (green) and with dark count rate, correlated noise and external cross-talks (red).

Detection efficiency. It is computed with the Time over Threshold method (Section IV.6) for an ideal detector. At SNR 5, the reconstruction efficiency is around 97%.

Photon pile-up. The observable is the number of hits and not single photo-electrons. So we count only one even when several photo-electrons are generated at the same time and channel. In addition, nearby photo-electrons in time cannot always be resolved by the hit finder. Hence, we consider that all hits within 200 ns in the same channel that are detected are a single hit. The number of channels of the detector is hence impacting the detection efficiency. We also add a time jitter due to the detection time distortion.

VI.2.5 f_p Distribution

We use the singlet probability distribution at 200 V/cm drift field coded in G4DS [207] for electronic recoils and nuclear recoils (Figure VI.9).

The cut on f_p is optimized to achieve the maximal separation between electronic and nuclear recoils. We are consequently looking at the cumulative of the photo-electron times for both distributions (Figure VI.10a). As expected for nuclear recoils the f_p distribution tends to ~ 0.7 while for electronic recoils it is ~ 0.3. The difference between both distributions is shown Figure VI.10b. We find that the maximal separation is around 190 ns. This will be the value we will be using unless otherwise stated. This value is larger than for DarkSide-50 (90 ns) as the time of flight is longer due to the larger size of DarkSide-20k.

The prompt component (first 190 ns) is computed with a binomial distribution. Then the late component is given by the difference between s_1 and the prompt component.
f_{190} is the prompt component divided by s_1. Once all the effects are taken into account,

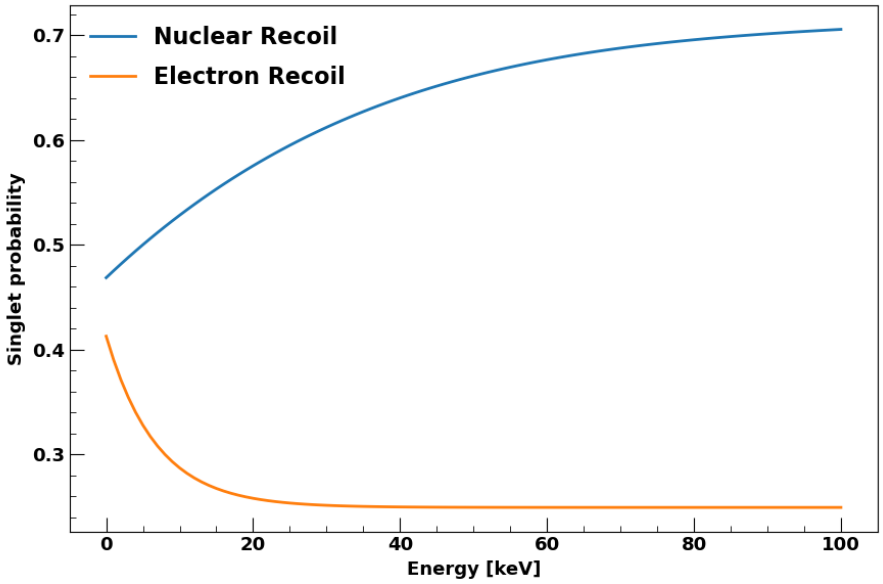

Figure VI.9 – Singlet probability depending on the energy for nuclear recoils (blue line) and electronic recoils (orange).

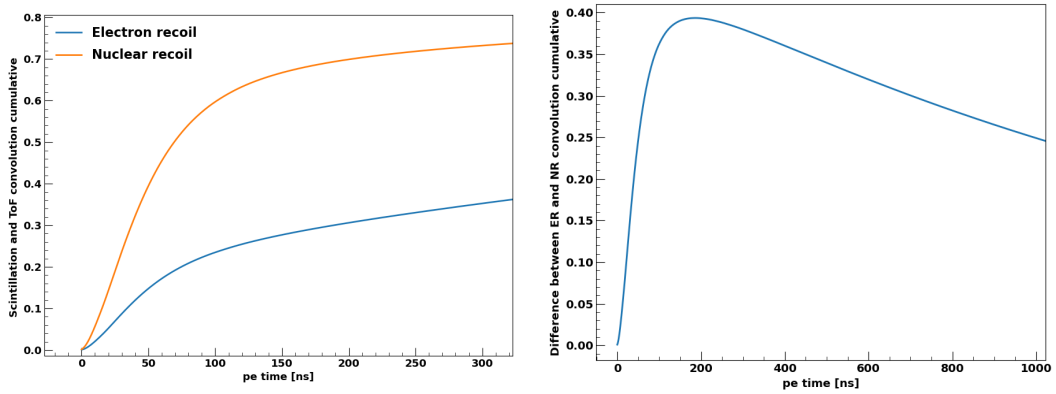

(a) (b)

Figure VI.10 – (a) Scintillation and Time of Flight convolution cumulative for electronic and nuclear recoils and (b) their difference (f_p). The maximum of their difference is around 190 ns.

the s_1 vs f_{190} distribution for nuclear and electronic recoils shows a distribution such as Figure VI.11.

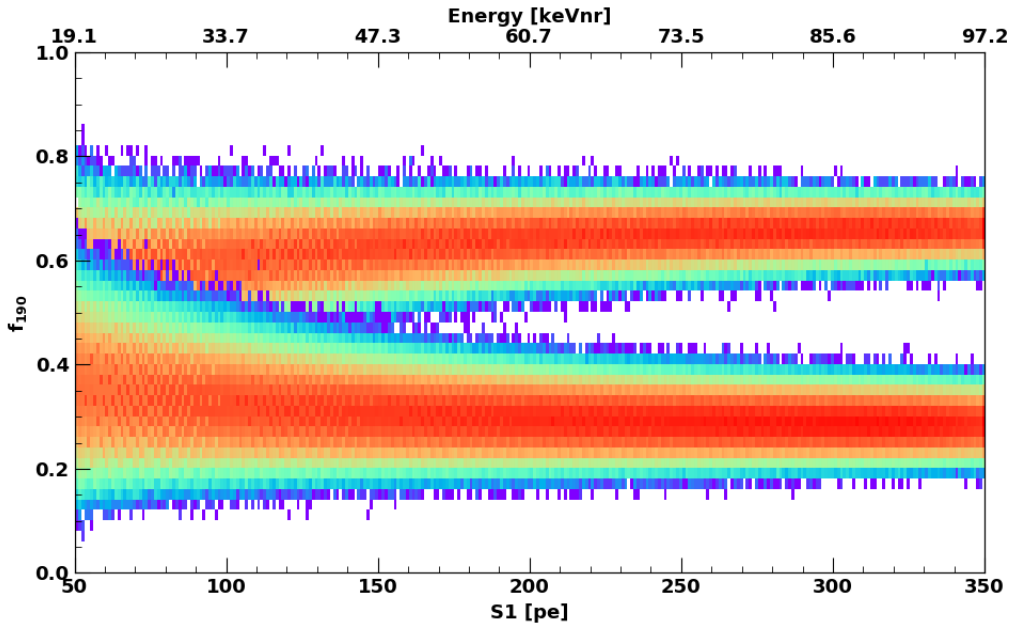

Figure VI.11 – f_{190} depending on s_1 for 10^6 events of nuclear recoils (upper band) and $2{\times}10^7$ events of electronic recoils (lower band) from a Monte-Carlo Toy Model neglecting detector effects with configuration 2x1 and 7 VoV.

VI.2.6 Acceptance Region

The acceptance region is defined as a region in the (s_1, f_p) space in which signals will be attributed to WIMPs induced scattering. Both the nuclear recoil efficiency and the electron leakage are optimized in order to maximize the sensitivity to WIMPs.
We define the acceptance region in order to have less than 0.1 electronic recoil events in the whole s_1 range for the full DarkSide-20k exposure.
We will go through the definition of nuclear recoil acceptance and electronic recoil leakage. Based on them, we will detail the computation of the acceptance region and its associated probability.

The Nuclear Recoil Acceptance is defined by the efficiency in selecting nuclear recoils as a function of s_1. For each s_1 value, we take the f_{190} distribution for nuclear recoil and we fit it with the model presented in Section VI.1.2 as it can be seen in Figure VI.12.

Then we compute acceptance curves for different values of efficiency as a function of s_1 and build the map in the (s_1, f_p) plane shown in Figure VI.13. In that plot the region in yellow corresponds to 100% efficiency for nuclear recoil and the region in purple to 0% efficiency.

The Electronic Recoil Leakage defines the maximum acceptable amount of electronic recoils we can except above this threshold. It is defined at 0.1 events on the whole s_1 range. As we will see we can define this leakage value, further called l_v in different

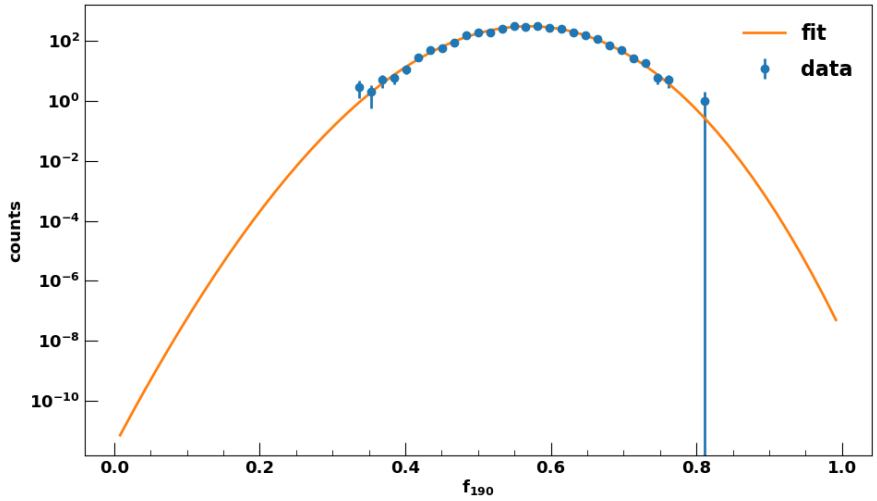

Figure VI.12 – Slice at $s_1 = 60$ photo-electrons of a 10^6 events nuclear recoils f_{190} distribution simulated from Monte-Carlo Toy Model fitted by the tail model (orange line).

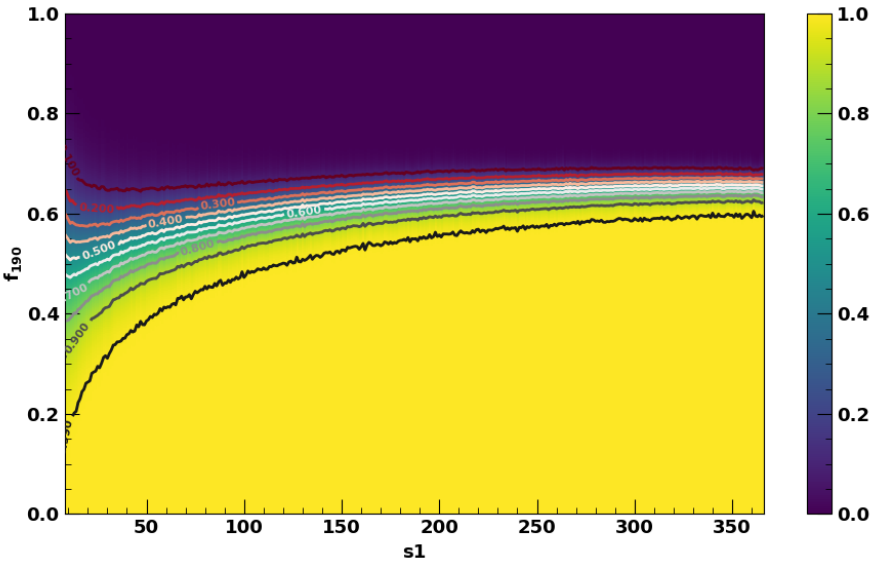

Figure VI.13 – Mapping of nuclear recoil acceptance in the (s_1, f_{190}) space from a Monte-Carlo Toy Model simulating 10^6 events with a 2x1 configuration at 7 VoV. Acceptance contours with their values written on them are displayed.

ways for each bin resulting in these 0.1 events in the whole range.
To retrieve the leakage curve, we apply the tail model to each slice of s_1 in the electronic recoil distribution of Figure VI.11. The bounding condition in each 1-photo-electron s_1 is such as:

$$\int_{w_{th}}^{1} (f_p(w) + 3\sigma_{f_p})dw = l_v \tag{VI.20}$$

Figure VI.14 shows the fitted electronic recoil slice at s_1= 100 photo-electrons with a flat electron leakage cut. The target total leakage over the whole s_1 range is 0.1 events. The flat electron leakage cut allows the same fraction of leakage to all the bins inside the whole range.

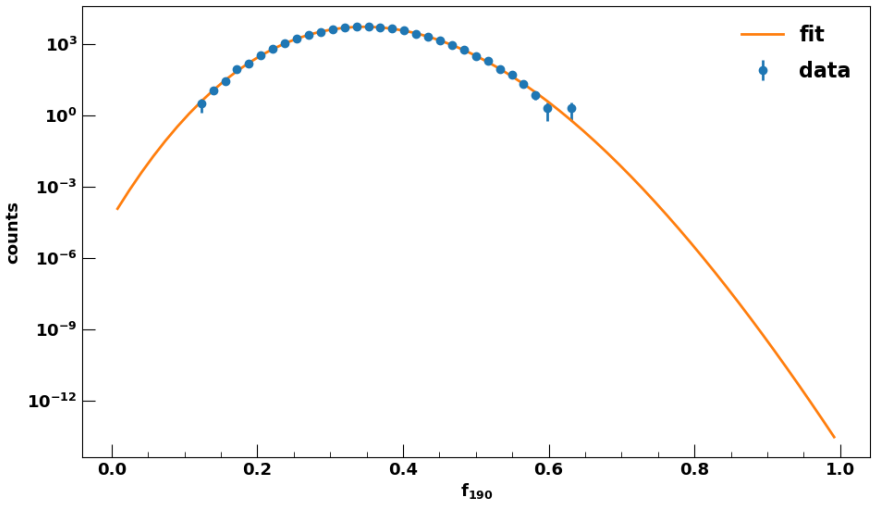

Figure VI.14 – Slice at s_1 = 100 photo-electrons for $2{\times}10^7$ events of electronic recoils of the f_{190} distribution simulated from Monte-Carlo Toy Model fitted by the tail model (orange line).

From the fit in each slice, we produce a map of the number of events depending on f_{190}. So, in the end, we retrieve a 2D grid of events in the (s_1, f_{190}) space that we can interpolate to have a 2D map from which we can select the s_1 region in which we can apply the leakage condition chosen (cf. Figure VI.15).

The choice of l_v in each bin can be done in several ways. Either in a flat way as used before, either in a weighted way. The second case allows to accept more leakage events in the bins where both nuclear and electronic recoil distributions are near one to another, and less where they are far from one to another. We look at several possible weighted distributions such as one following the electron singlet probability f_p distribution or distribution in $1/\eta$ with η the distance between both distributions such as:

$$\eta = \frac{|\mu_{NR} - \mu_{ER}|}{\sqrt{\sigma_{NR}^2 + \sigma_{ER}^2}} \tag{VI.21}$$

We also test distributions following $1/\ln(s_1)$, $1/s_1$ and disintegration laws with f_p or $1/\eta$ as argument. In each case, distributions are normalized to have a total leakage over the

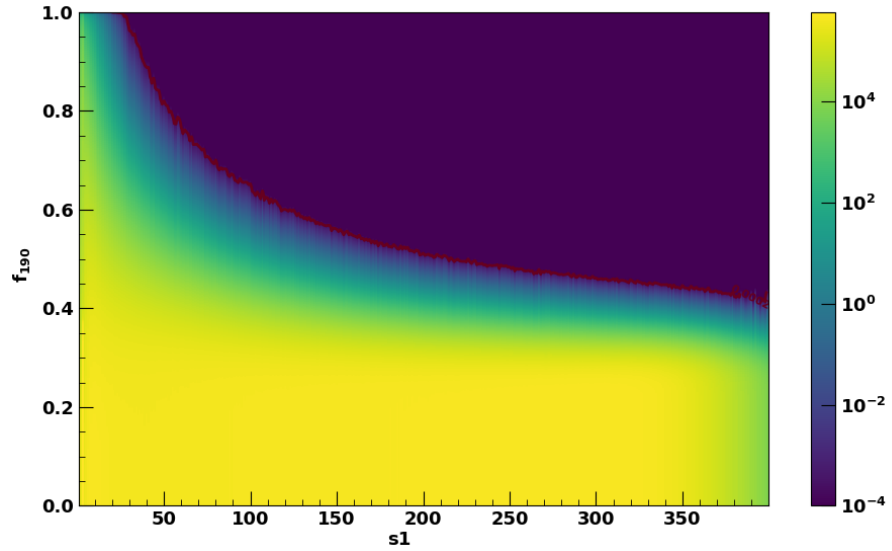

Figure VI.15 – Mapping of electronic recoil leakage in the (s_1, f_{190}) space from a Monte-Carlo Toy Model simulating 2×10^7 events. A flat leakage contour is displayed.

whole s_1 spectra of 0.1 events. Figure VI.16 shows the different distributions tested.

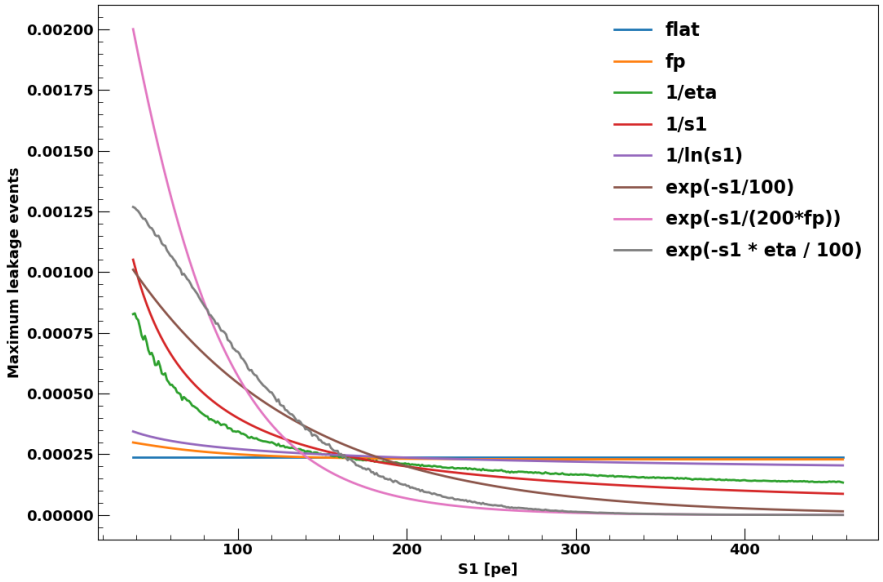

Figure VI.16 – Test distribution of maximum leakage accepted depending on the s_1 value with a total leakage value on the whole range of 0.1 events. The f_p is the electron singlet probability distribution depending on s_1 and η is the distance between nuclear and electronic recoil distributions as defined in Equation VI.21.

In Figure VI.16 we observe that a distribution following the electron singlet probability f_p or $1/\ln s_1$ does not change significantly with regards to the flat distribution. The $1/s_1$ and $1/\eta$ are close one to the other. The most different distribution with respect to the flat is $\exp(-s_1/(200 f_p))$. We will keep this one for further tests to compare it to the flat one.

The Acceptance Region is the region above the nuclear recoil acceptance curve and the electronic recoil leakage curve (cf. Figure VI.17). From this region in the (s_1, f_{190}) space we can evaluate an acceptance probability for each s_1 value. For large s_1 values, the electron leakage curve is well below the nuclear recoil acceptance region and we can maximize the sensitivity to WIMPs by increasing the nuclear recoil acceptance up to 90% or 99%. For smaller values of s_1 instead, we account for the electronic recoil leakage curve at the cost of reducing the nuclear recoil efficiency.

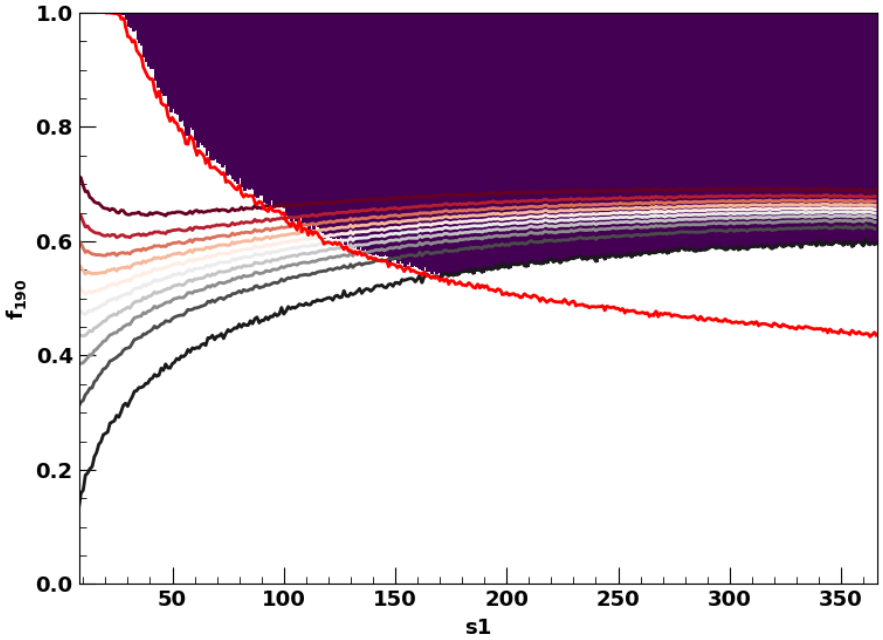

Figure VI.17 – The acceptance region in the (s_1, f_{190}) space from a Monte-Carlo Toy Model simulating $2{\times}10^7$ events electronic recoils and 10^6 events of nuclear recoils with a 2x1 configuration at 7 VoV, is highlighted in deep purple. The red contour is the electronic leakage curve. All the others are the nuclear recoil acceptances contours with their values written on it.

To find the probability in this part, we use the nuclear recoil acceptance map to determine acceptance values along the leakage curve. Indeed, we know the (s_1, f_{190}) coordinates of each point of the leakage curve, so we can retrieve the acceptance value using the nuclear recoil map up to the acceptance probability we choose. Then we fit with an error function as:

$$y = p_0 \times erf(\frac{x - p_1}{p_2}) + p_3 \tag{VI.22}$$

In order to study the sensitivity of WIMPs we convert the s_1 value into energy in keV_{NR}. Both values and the fit curve are shown in Figure VI.18.

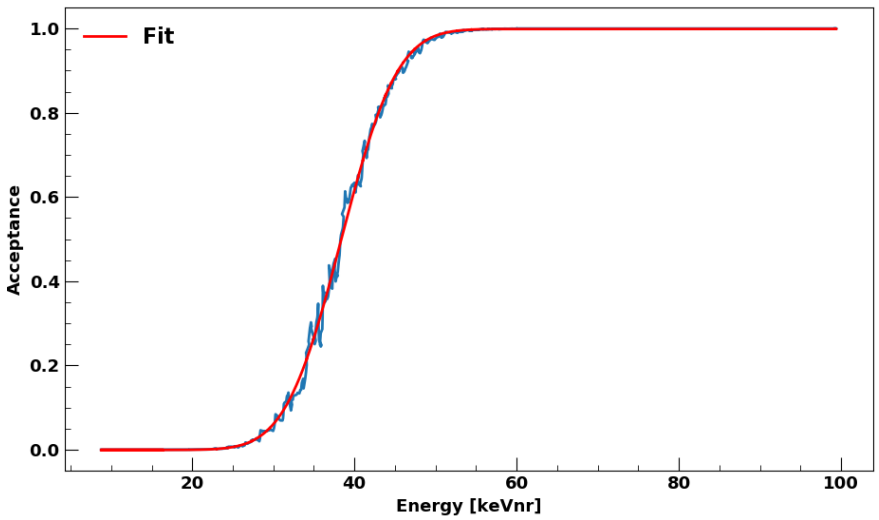

Figure VI.18 – Acceptance probability fit depending on the energy for 10^6 events nuclear recoils and 2×10^7 events of electronic recoils from a Monte-Carlo Toy Model simulation with a 2x1 configuration at 7 VoV. 100% nuclear recoil acceptance and a flat electron leakage are used.

VI.3 Sensitivity Computation

The DarkSide-20k sensitivity is obtained with the standard framework used by DarkSide to compute exclusion limits and discovery potential. The code is divided into two steps. The first generates samples of particles interacting in the detector: WIMPs at different masses from 15 GeV/c^2 to 10 TeV/c^2, solar, atmospheric and supernovae neutrinos, and neutrons from SiPMs and the cryostat. Neutrons are simulated with G4DS while WIMPs and neutrinos are computed from analytical distributions.

The second step consists of computing either exclusion limits or the discovery potential. It relies on a profile likelihood ratio approach. We set the parameters of the exposure to 5 years and 20 ton fiducial volume. An important parameter of this sensitivity computation is the acceptance probability as it defines the background-free region where we can search for WIMPs events. The acceptance probability retrieved with the PSD package depends on the energy in keVnr as we saw in previous sections. We go back to photo-electrons by converting this energy into keVee and multiplying it by the detection light yield that is assumed to be equal to 10 photo-electrons per keVee.

VI.4 Impacts on Sensitivities

Using this package we can test how different configurations and parameters can impact the acceptance and hence the sensitivity of DarkSide-20k. We test the possibility of using different leakage methods. In addition, we study the impact on the sensitivity of the following effects: photo-detection efficiency (PDE), instrumental noises, single photo-electron (SPE) time resolution, channel grouping, group velocity and pile-up.

VI.4.1 Definition of the Electronic Recoil Background Leakage Goal

We saw in Section VI.2.6 that we could use either a flat or a weighted electron leakage curve. Several ways of weighting the distribution were shown. We will compare only the flat distribution with the one giving the largest deviation ($\exp(-s_1/(200 f_p))$) to see the impact of the leakage method. In the weighted distribution expression, f_p refers to the electronic recoil singlet emission probability. This quantity is dependant on the kinetic energy, and consequently, this dependence is translated into a dependence on s_1 using the energy scale. Figure VI.19 shows the electron leakage curve and the acceptance probability inferred for both cases: flat and weighted. We observe that using the weighted distribution allows gaining a little acceptance at low energy while it reduces the acceptance at higher energy. However, at high energy we expect fewer events to be leaking as the f_{190} is quite different for both nuclear and electronic recoils.

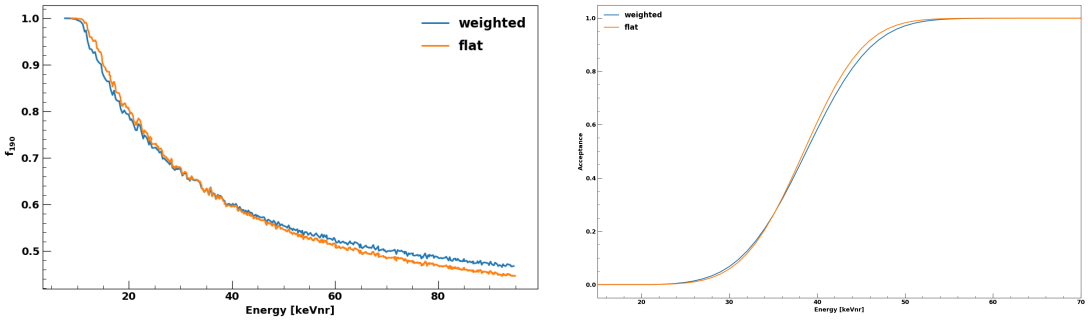

(a) (b)

Figure VI.19 – Comparison of flat and weighted electron leakages, (a) in the (s_1, f_{190}) parameter space and (b) acceptance probability fit depending on the nuclear recoil energy for 10^6 events nuclear recoils and $2{\times}10^7$ electronic recoils events from a Monte-Carlo Toy Model simulation at 7 VoV with channel configuration 2x1. 100% nuclear recoil acceptance is used for computing the acceptance.

We compute sensitivities to conclude on the relevance of using the weighted versus the flat leakage method. This is shown in Figure VI.20. The overall difference in acceptance (cf. Figure VI.19) has negligible effects on the sensitivity. Consequently, we will use a flat distribution in the following sections.

VI.4.2 PDE and Instrumental Noises

Until now, we used a photon detection efficiency of 21% and instrumental noises values of 6% after-pulses probability, 30% direct cross-talks probability, 31.5% external cross-talks probability and $2.07{\times}10^{-5}$ ns^{-1} of dark count rate. We investigate the impact of a variation of these quantities on the acceptance region.

Photon detection efficiency. We investigate the impact of the photon detection efficiency in the detector. For that, we vary C_e, the photon collection efficiency which is deeply correlated with it, within a 2x1 configuration at 7 VoV with $2{\times}10^7$ events of

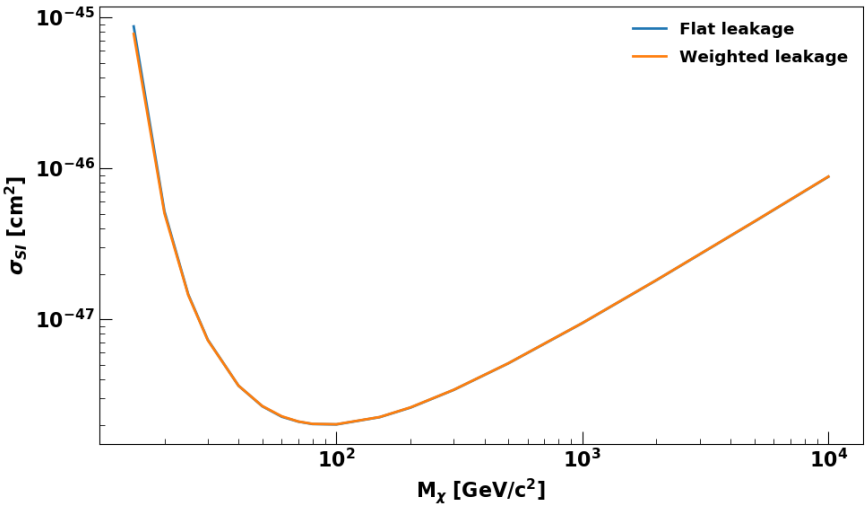

Figure VI.20 – Impact of leakage method on the sensitivity depending on the energy for 10^6 events of nuclear recoils and 2×10^7 events of electronic recoils from a Monte-Carlo Toy Model simulation with a 2x1 configuration at 7 VoV. 100% nuclear recoil acceptance is used.

electronic recoil and 10^6 events of nuclear recoil. We choose three values of C_e respectively belonging to 6, 7 and 9 VoV which correspond to a PDE of 40%, 42% and 45%. Figure VI.21a shows the acceptance for each case. As it is expected, when we raise the photon detection efficiency, the acceptance region increases. The effect on the sensitivity is shown in Figure VI.21b: as expected the higher photon collection efficiency the better the sensitivity.

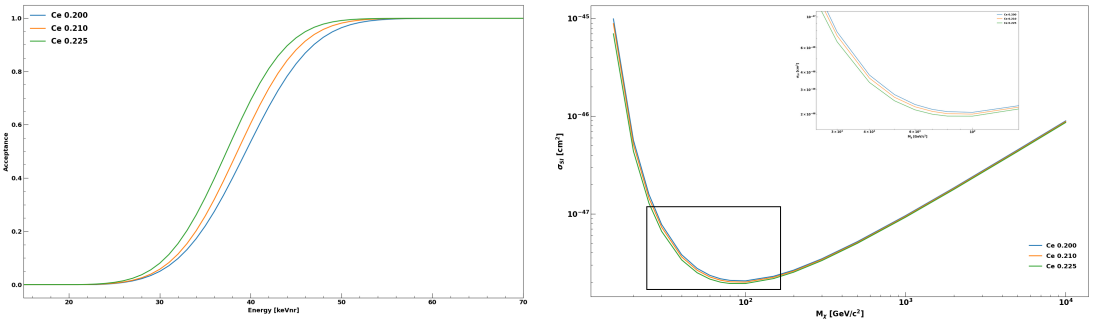

(a) (b)

Figure VI.21 – Impact of three different photon collection efficiencies C_e on the (a) acceptance probability fit and (b) sensitivity, depending on the energy for 10^6 events of nuclear recoils and 2×10^7 events of electronic recoils from a Monte-Carlo Toy Model simulation with a 2x1 configuration at 7 VoV. 100% nuclear recoil acceptance and a flat electron leakage are used. A zoom of the framed region of the sensitivity is given in the top right corner insert. It highlights the difference in sensitivities between the different scenarios.

Instrumental noises. Several instrumental noises are taken into account in the toy model as it was seen in Section VI.2.4: after-pulses (AP), direct cross-talks (DiCT), external cross-talk (exCT) and dark count rate (DCR). For each one of them, we take several

values in the range of what is expected for DarkSide-20k. We look at an AP probability of 5%, 10% and 15%, a DiCT probability of 25%, 35% and 45%, an exCT probability of 27% (6 VoV), 35% (8 VoV) and 45% (10 VoV), a DCR of 2×10^{-5} ns^{-1}, 4×10^{-5} ns^{-1} and 6×10^{-5} ns^{-1}.
Their impacts on the acceptance are variable as shown in Figure VI.22. APs and exCTs have significant effects on the acceptance, producing a non-negligible reduction of the acceptance region. On the contrary, an increase of DiCTs and DCR produces a very small impact on the acceptance region. Looking at the sensitivity, Figure VI.23 and Table VI.2, we observe a small impact from APs (2 to 5% discrepancy at 100 GeV/c^2), with as expected a loss of sensitivity for increasing APs. Same for exCTs, where the 45% case clearly implies a loss of sensitivity compared to the 27% case (6% difference at 100 GeV/c^2). As expected as the acceptance is similar, for the different cases of DCR and DiCTs we do not have significant impacts on the sensitivities (1 to 2% at 100 GeV/c^2). In conclusion, the most important instrumental noises to evaluate precisely are exCTs and APs to assess the acceptance, and hence the final sensitivity.

VI.4.3 SPE Time Resolution

Photo-electrons hitting on SiPMs are amplified and digitized. Typically front-end boards are used for this but such boards can increase noise due to the presence of radioactive elements. A solution could be to use ASICs, which have the advantage of being more radio-pure. However, their SPE time response is slower. This last is modelled by introducing an artificial jitter.

Consequently, we are looking at the impact of the SPE time response via the jitter configuration on the acceptance in order to decide on the feasibility of using ASICs. We fix at 2x1 at 7 VoV and set the jitter to 5 ns, 10 ns, 20 ns and 30 ns. 5 ns is the best time reachable by the front end board while 30 ns is an extreme value. ASICs response is estimated at 15-20 ns.

An important point to consider is that raising the SPE time resolution, so the jitter, is changing the timing of photo-electrons. Consequently, we have to optimise the f_p cut for each one of these cases. We use the same procedure as in Section VI.2.5 for each jitter (Figure VI.24). We found that increasing the jitter, the optimal value for f_p also increases. Results for each jitter are summarized in Table VI.3.

Table VI.3 – Optimized f_p cut for different values of jitters.

Jitter [ns]	5	10	20	30
f_p cut [ns]	190	200	230	260

With the optimized f_p cut for each jitter, we generate distributions and compute the acceptance and sensitivity (Figure VI.25). The difference for jitters 5 ns, 10 ns and 20 ns is none to negligible. This is confirmed by comparing them directly to their distribution at f_{190}. The main difference is for the 30 ns jitter where we have a small deterioration of the acceptance. It means that we could use ASICs in the experiment without losing too much in sensitivity.

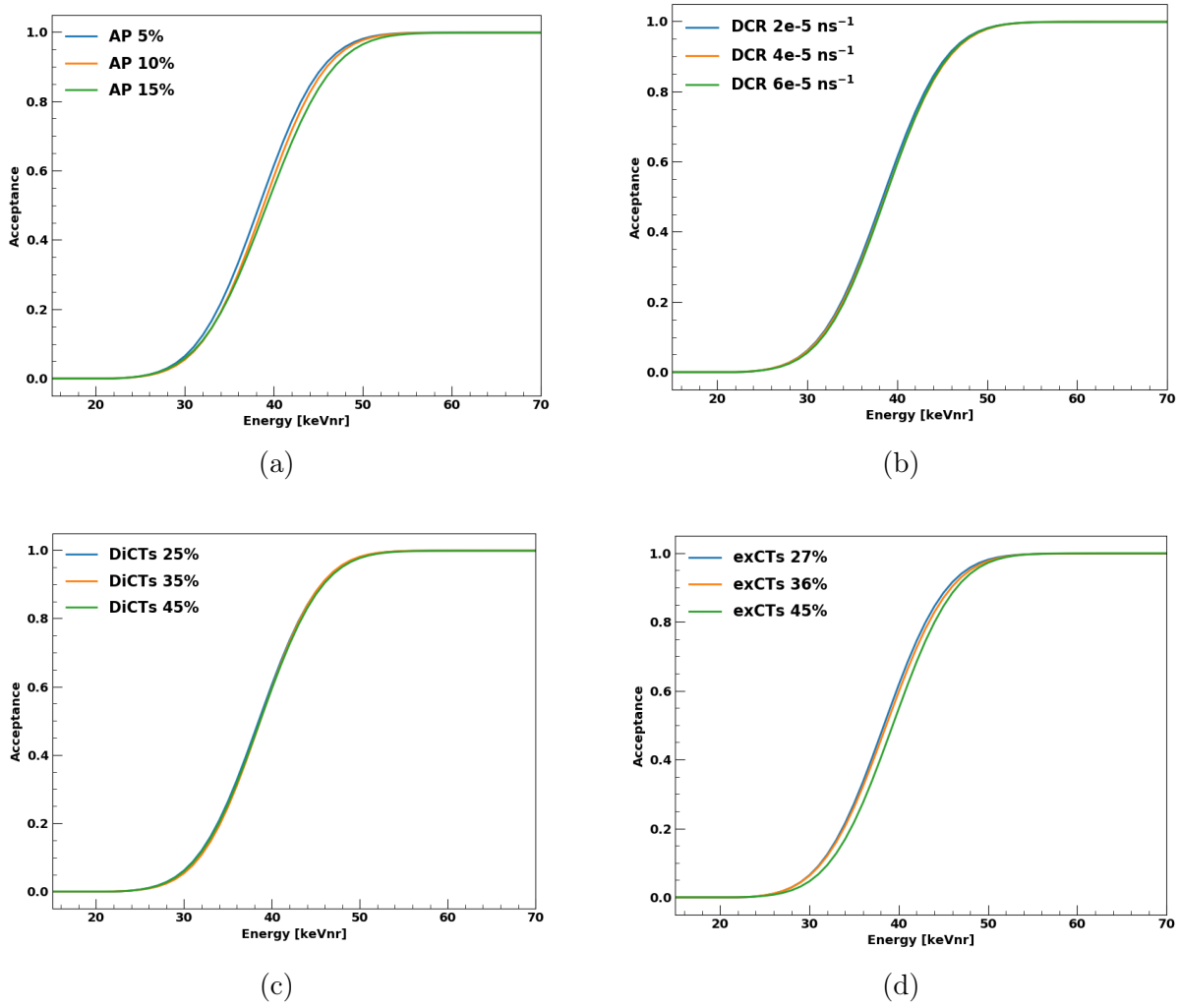

Figure VI.22 – Acceptance probability fit depending on the nuclear recoil energy for 10^6 events of nuclear recoils and 2×10^7 electronic recoils events from a Monte-Carlo Toy Model simulation at 7 VoV with channel configuration 2x1 and varying instrumental noises: (a) after-pulses, (b) dark count rate, (c) direct cross-talk and (d) external cross-talk. 100% nuclear recoil acceptance and a flat electron leakage are used.

VI.4.4 Channel Configurations

A possible reduction of the number of channels in DarkSide-20k is considered in order to reduce both the complexity and the cost. Hence, it is considered to sum the output of several PDMs. However, it increases the instrumental noise. To simulate this effect we test three different configurations. First, 1x1 grouping, which is the usual basic PDM of 5 x 5 cm^2. Then the 2x1, which is 10 x 5 cm^2, so two PDMs summed together and finally 2x2, which is 10 x 10 cm^2, so in fine 4 PDMs in a square summed together. Parameters for each configuration are gathered in Table VI.4. It can be noted that the collection efficiency is computed relative to the PDE.

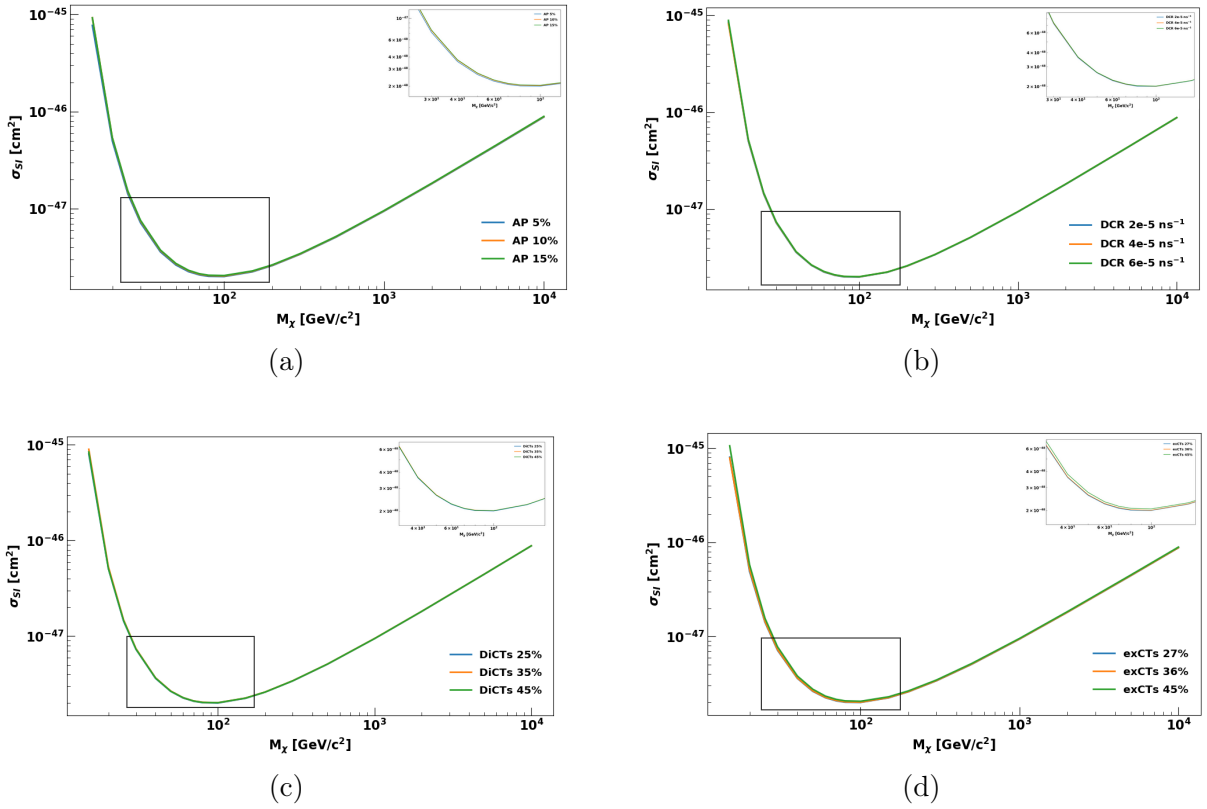

(a) (b)

(c) (d)

Figure VI.23 – Sensitivity depending on the nuclear recoil energy for 10^6 events of nuclear recoils and 2×10^7 electronic recoils events from a Monte-Carlo Toy Model simulation at 7 VoV with channel configuration 2x1 and varying instrumental noises: (a) after-pulses, (b) dark count rate, (c) direct cross-talk and (d) external cross-talk. 100% nuclear recoil acceptance and a flat electron leakage are used. A zoom of the framed region of the sensitivity is given in the top right corner insert. It highlights the difference in sensitivities between the different scenarios.

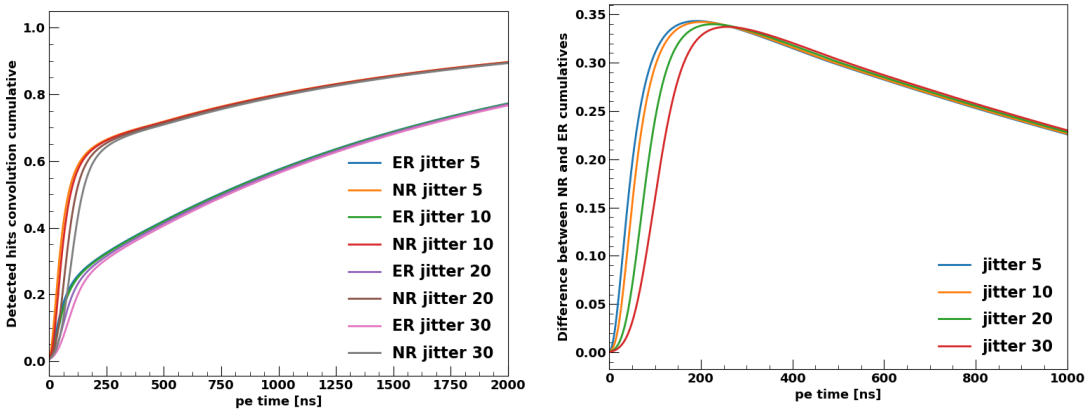

(a) (b)

Figure VI.24 – (a) Detected hits convolution cumulative for electronic and nuclear recoils and (b) their difference depending on different jitter values. The maximum of their difference depending on the jitter is summarized in Table VI.3.

Table VI.2 – Tested values for the different configurations and parameters.

Parameter	Value	Sensitivity at 100 GeV/c^2 [cm^2]
PDE	40% at 6 VoV (C_e=0.200)	2.06e-48
PDE	42% at 7 VoV (C_e=0.210)	2.00e-48
PDE	45% at 9 VoV (C_e=0.225)	1.94e-48
DCR	2×10^{-5} ns^{-1} at 6 VoV	2.00e-48
DCR	4×10^{-5} ns^{-1}	2.01e-48
DCR	6×10^{-5} ns^{-1}	2.01e-48
DiCT	25% at 6 VoV	2.00e-48
DiCT	35% at 8 VoV	2.02e-48
DiCT	45% NA	2.01e-48
AP	5% at 6 VoV	2.00e-48
AP	10% at 9 VoV	2.02e-48
AP	15% NA	2.05e-48
exCT	27% at 6 VoV	2.00e-48
exCT	36% at 8 VoV	2.01e-48
exCT	45% at 10 VoV	2.06e-48
jitter	5 ns with f190	2.00e-48
jitter	10 ns with f200	2.01e-48
jitter	20 ns with f230	2.03e-48
jitter	30 ns with f260	2.06e-48
grouping	1x1 at 7 VoV	2.00e-48
grouping	2x1 at 7 VoV	2.01e-48
grouping	2x2 at 7 VoV	2.01e-48
grouping	1x1 at 6 VoV	2.05e-48
grouping	2x1 at 7 VoV	2.01e-48
grouping	2x2 at 9 VoV	1.98e-48
pile-up gate	100 ns	2.00e-48
pile-up gate	200 ns	2.00e-48
pile-up gate	400 ns	2.01e-48

Table VI.4 – Parameters for channel configuration 1x1, 2x1 and 2x2 as determined by the TF2 internal report.

Parameters	1x1	2x1	2x2
Channel numbers	8280	4140	2070
Overvoltage	6 VoV	7 VoV	9 VoV
Hit finding efficiency	97%	97%	97%
Jitter (SPE time resolution)	4 ns	7 ns	7 ns
DiCT probability	25%	30%	45%
APs probability	5%	6%	10%
exCTs probability	20%	25%	40%
DCR [ns^{-1}]	2.07×10^{-5}	2.07×10^{-5}	5.17×10^{-5}
PDE	40%	42%	45%
Collection efficiency	0.2	0.21	0.225

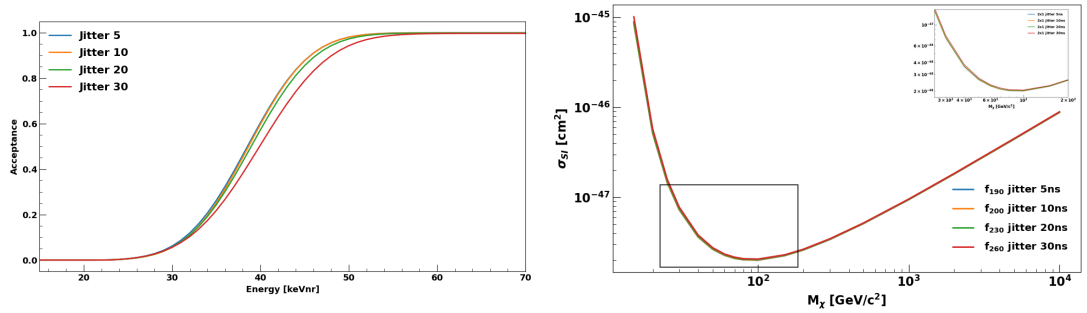

(a) (b)

Figure VI.25 – (a) Acceptance probability fit and (b) sensitivity, depending on the nuclear recoil energy for 10^6 events of nuclear recoils and 2×10^7 electronic recoils events from a Monte-Carlo Toy Model simulation at 7 VoV with channel configuration 2x1 and different jitter times [ns] with for each the optimized f_p cut summarized in Table VI.3. 100% nuclear recoil acceptance and a flat electron leakage are used. A zoom of the framed region of the sensitivity is given in the top right corner insert. It highlights the difference of sensitivities between the different scenarios.

Figure VI.26 shows the comparison of the three cases. The best acceptance is achieved for the 2x2 case, then 2x1 and finally the worst would be for the 1x1 case. The noise is increasing with the grouping which is due to the fact that the photo-detection efficiency is increasing with the VoV and that this effect is larger than the one due to the instrumental noise (Section VI.4.2).

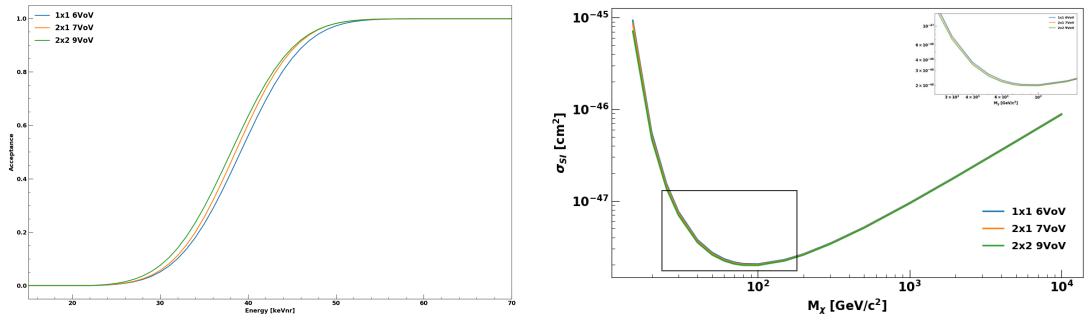

(a) (b)

Figure VI.26 – (a) Acceptance probability fit and (b) sensitivity, depending on the nuclear recoil energy for 10^6 events of nuclear recoils and 2×10^7 electronic recoils events from a Monte-Carlo Toy Model simulation for three different channel configurations and VoV. 100% nuclear recoil acceptance and a flat electron leakage are used. A zoom of the framed region of the sensitivity is given in the top right corner insert. It highlights the difference of sensitivities between the different scenarios.

Hence, we use the same VoV to check the impact of a given noise and PDE. At a given VoV, the difference is only the DCR and the number of channels and so, the pile-up which is increasing when the number of channels is decreasing. In Figure VI.27a displaying the three configurations at 7 VoV, we retrieve a similar acceptance and so the channelling itself does not impact the acceptance (as it was seen in a Section VI.4.2).

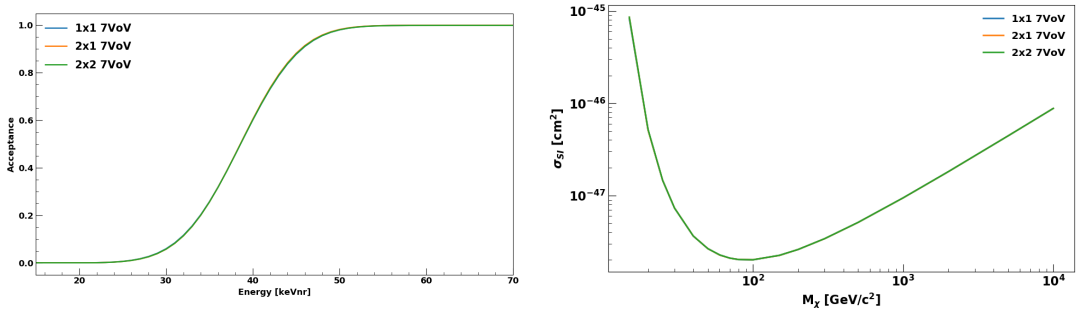

(a) (b)

Figure VI.27 – (a) Acceptance probability fit and (b) sensitivity, depending on the nuclear recoil energy for 10^6 events of nuclear recoils and 2×10^7 electronic recoils events from a Monte-Carlo Toy Model simulation for three different channel configurations at 7 VoV. 100% nuclear recoil acceptance and a flat electron leakage are used.

VI.4.5 Impact of the uncertainty on the group velocity

In the simulation, the time of flight distribution is computed using a group velocity inside the TPC v_g of 14.6 cm/ns (Figure VI.28, blue curve). It was however suggested that VUV light may propagate more slowly, around 10.6 cm/ns (Figure VI.28, red curve). Consequently, we test the impact of such a change in the final acceptance.

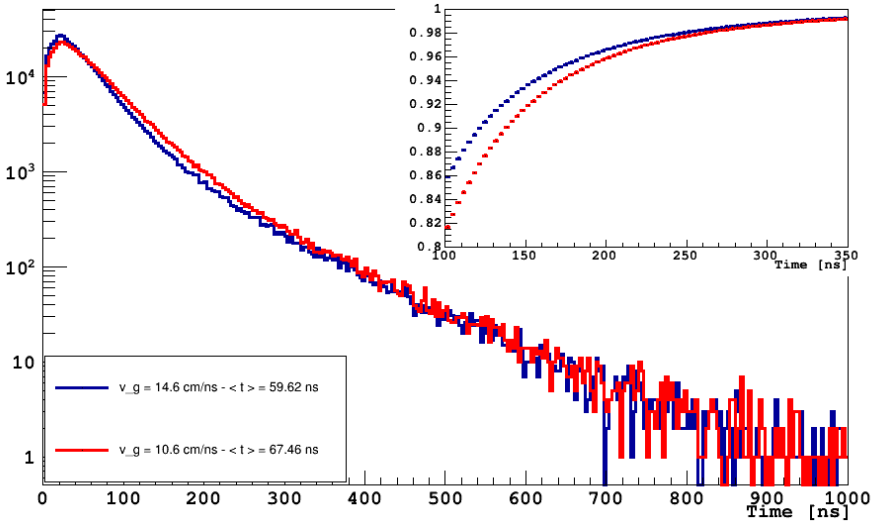

Figure VI.28 – Time of flight distribution for two different travel times. The insert shows the cumulative of each distribution.

For comparing both acceptances, we use the procedure described in Section VI.2.5 to optimize the f_p cut. For a v_g of 14.6 cm/ns, the best cut is at 190 ns, which is expected as we use the usual parameters of the previous analysis. For a v_g of 10.6 cm/ns, the best cut is slightly higher, at 210 ns.

Using the optimized f_p we compare both acceptances and associated limits (Figure VI.29). We notice that there is no significant difference between both distributions. Hence such

a small difference in travel time estimation, and so the precision of its evaluation, is not impacting the final result.

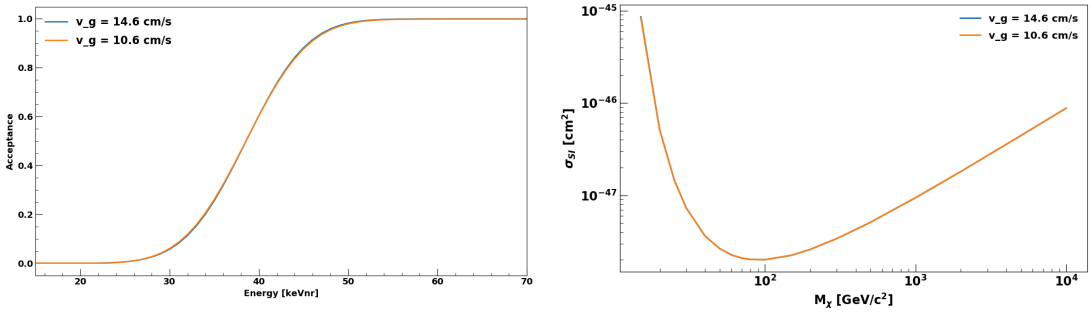

(a) (b)

Figure VI.29 – (a) Acceptance probability fit and (b) sensitivity, depending on the nuclear recoil energy for 10^6 events of nuclear recoils and 2×10^7 electronic recoils events from a Monte-Carlo Toy Model simulation for a 2x1 configuration at 7 VoV. 100% nuclear recoil acceptance and a flat electron leakage are used.

VI.4.6 Pile-up gate

The pile-up gate is the length of time in which two pulses arriving are considered as a single one. The impact of the gate on the acceptance and sensitivity is negligible as it can be seen on Figure VI.30 and Table VI.2.

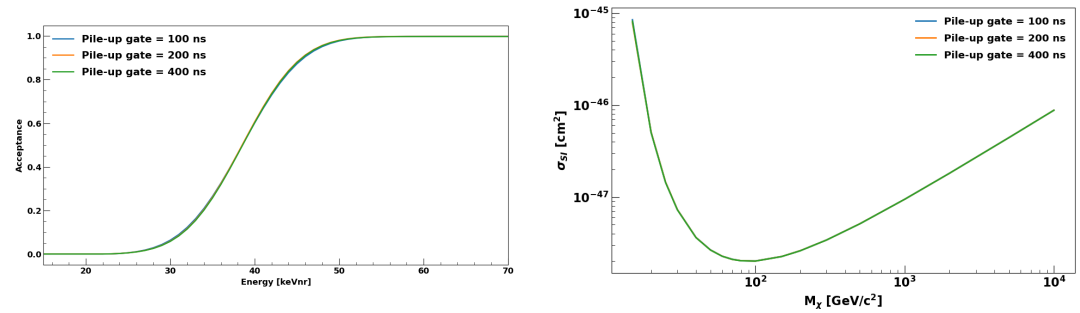

(a) (b)

Figure VI.30 – (a) Acceptance probability (b) and sensitivity as a function of the pile-up gate assuming 7 VoV with 2x1 channel configuration with 10^6 events of nuclear recoils and 2×10^7 electronic recoils events. 100% nuclear recoil acceptance and a flat electron leakage are used.

VI.5 Conclusion

We developed a new package to estimate the sensitivity of DarkSide-20k. This package has the advantage of being easy to use and flexible to account for different parameters. The preliminary studies that have been performed with this package allowed to show that in term of sensitivity, we could be able to use ASICs instead of front end boards as the

resulting loss of SPE time resolution is negligible. We also showed that channel grouping has a negligible impact on the final sensitivity. Instrumental noises, mostly APs and exCTs, are provoking sensitivity losses while raising the PDE is improving the sensitivity. The precision of the travel time estimation of the time of flight is not impacting the final sensitivity.

Chapter VII

S1 Position Reconstruction

> We are drowning in information and starving for knowledge.
>
> Rutherford D. Rogers (1985)

In DarkSide-20k the event rate is expected at around 120 Hz and the maximum drift time to 3.5 ms which would result in $\sim 42\%$ pile-up and hence in loss of lifetime.
A solution to avoid such loss would be to develop an algorithm to reconstruct the position of s_1 pulses. With respect to the s_2 XYZ reconstruction, the s_1 one is expected to have a much worse resolution. However, the s_1-based position can help in correctly associating s_1 and s_2 pulses, and so reducing the pile-up.

The s_1 XYZ position reconstruction is here based on the distribution of the channel occupancy, identified by means of two different machine learning techniques: 1/ unsupervised learning using barycentres and kernel density estimators (Section VII.1) and 2/ supervised learning, using convolution neutral networks (Section VII.2).

In both cases, and in order to make comparisons between their respective performances, we will compare true and reconstructed positions for events uniformly distributed in the TPC volume and for interactions in fixed positions.
Finally, we will describe in Section VII.3 a method to use calibration data in order to train the supervised algorithm. This will allow to use this algorithm based on measured data in the future.

VII.1 Unsupervised Reconstruction

We first develop a reconstruction for Z and (X, Y) positions based on unsupervised learning. Unsupervised learning algorithms learn patterns or data grouping from none labelled data.
We will consider uniformly distributed data sets as well as fixed extreme positions over the TPC (cf. Figure VII.1).

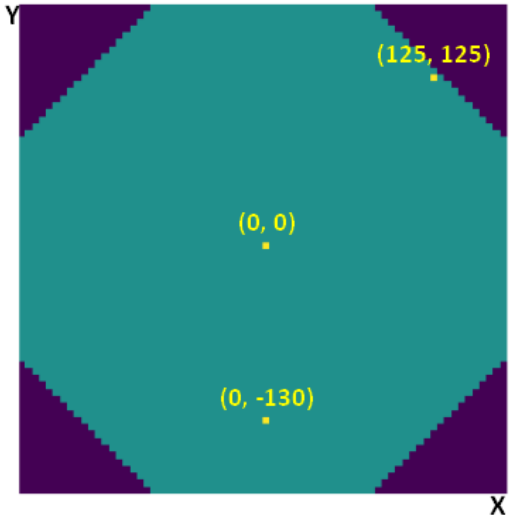

Figure VII.1 – Position (yellow) of the 3 XY positions of the 9 fixed configurations inside the detector (green area).

VII.1.1 Z reconstruction

Photo-electrons are distributed between the top and the bottom planes of the TPC in a non-uniform way depending on the s_1 position. The distribution is not symmetric with respect to Z=0 because of reflections in the gas pocket. Hence, we use the distribution of photo-electrons over the top and bottom channels to compute the top-bottom asymmetry (TBA) which is defined as the number of photo-electrons collected on the bottom plane over the total number of photo-electrons. Then, the relation between the TBA and the Z position is computed using a distribution of 10^4 events uniformly distributed over the TPC from which is extracted the mean and standard deviation (cf. Figures VII.2 and VII.3 for 50 keV and 8 keV, respectively). We then interpolate them on the whole range.

Using the TBA-Z relation, we determine the Z position within the standard deviation error. The obtained resolution is from around 20 cm to around 100 cm at 50 keV with a better standard deviation at the top of the detector. At 8 keV, the standard deviation on the Z position at each TBA is up to 200 cm, so too large to have a reliable reconstruction on the whole range.
At 50 keV, for each fixed position (cf. Figure VII.1), we compute 1/ the resolution using the RMS of the distribution to test the performance and 2/ the bias computed as the deviation from the true position (cf. Table VII.1).

We see that the input XY also has an impact on the Z resolution and bias. In addition, positions with large resolutions also have a significant reconstruction bias. We apply a cut on the arrival photo-electrons time (t_0) to check if it improves the results. After a systematic procedure testing the impact of t_0, so cutting every 10 ns from 10 ns to 3.8 μs, we find that it globally do not improved the RMS. We test this method with both 50 keV and 8 keV samples with the same outcome. The arrival photo-electrons time cut is the same for both cases.

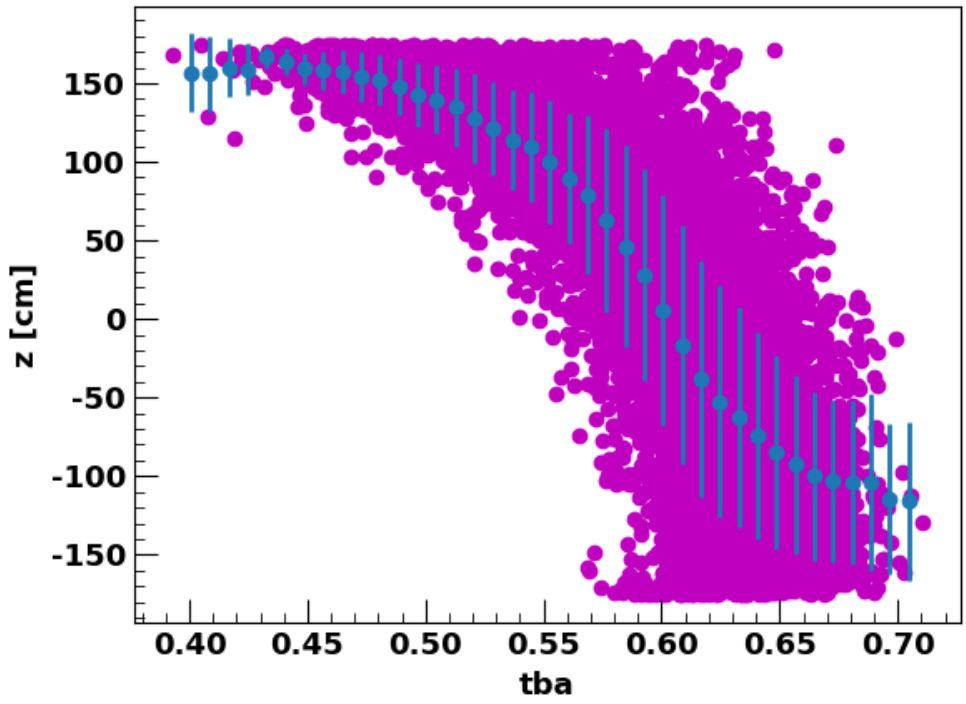

Figure VII.2 – TBA vs Z position in the TPC based on a 10^4 events of 50 keV uniformly distributed distribution from G4DS (purple points). The mean and standard deviation of the distribution are given in blue.

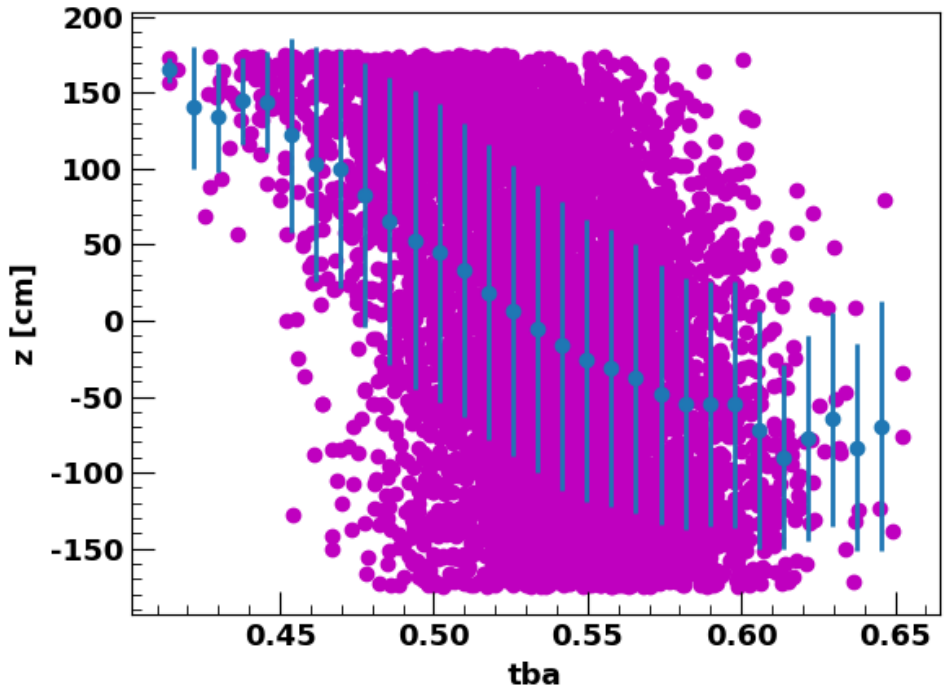

Figure VII.3 – TBA vs Z position in the TPC based on a 10^4 events of 8 keV uniformly distributed distribution from G4DS (purple points). The mean and standard deviation of the distribution are given in blue.

Table VII.1 – RMS of the s_1 reconstructed Z position at 50 keV using the top bottom asymmetry for several input positions.

Input XYZ [cm]	Z RMS [cm]	Z Bias [cm]
0 0 0	39	15
0 0 130	17	14
0 0 -130	81	66
0 -130 0	44	27
0 -130 130	69	12
0 -130 -130	141	60
125 125 0	56	52
125 125 130	109	130
125 125 -130	35	58

VII.1.2 Choice of the Optical Plane

In order to perform the XY learning, we have to choose the optical plane (top plane, bottom plane or both planes) that gives the best result depending on the input position. For that, we assess the difficulty of the task for each plane individually.
As expected, for events occurring at the top of the detector, the top plane gives the best results. Conversely for events occurring at the bottom of the detector, the bottom plane gives the best results. It is more delicate when events are occurring in the middle of the detector.
As we do not have access to the true position, we use the variance, computed as the average of the squared deviations from the mean in the XY 2D-plane. Figure VII.4 shows the variance for configurations 1 to 3 (respectively for XYZ at 0 0 0 cm, 0 0 130 cm and 0 0 -130 cm) in the top and the bottom plane for 50 keV electrons.

On the Z coordinate, the highest the variance, the easiest the determination as it means that we have in a given plane more photo-electrons due to an asymmetric dispersion of the photo-electrons between the top or bottom plane. As expected, in Figure VII.4, when the event occurs in Z near the top plane (configuration 2), its variance is larger on the top plane and smaller on the bottom. The opposite happens for configuration 3 when the true position of an input event is near the bottom plane.

It is however worth noting that if Z reconstruction had a good resolution (10 - 20 cm), it would work even better than the variance.

VII.1.3 XY reconstruction

Different metrics are tested to perform the XY reconstruction:

- The barycentre between all the photo-electrons (SB).
- The barycentre using only the channels where at least two photo-electrons are detected (MB).
- The barycentre of the channels with the highest number of photo-electrons (MOc).

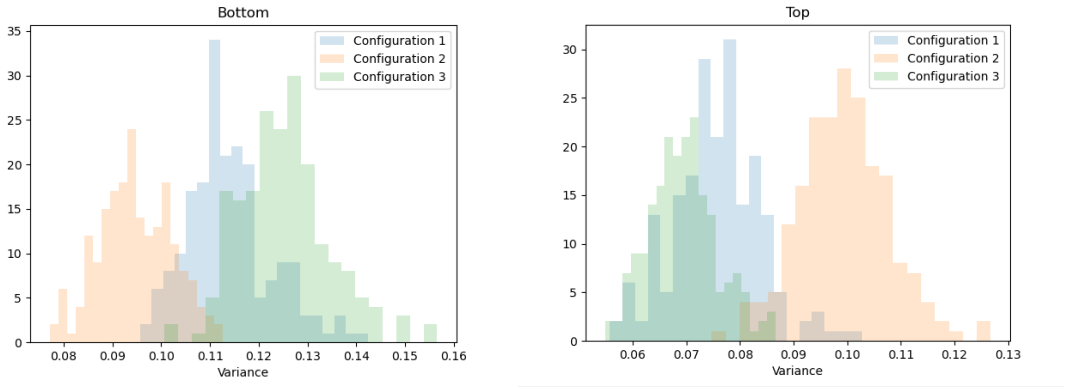

(a) (b)

Figure VII.4 – Comparison of 2D variance for 3 different configurations (respectively for XYZ at 0 0 0 cm, 0 0 130 cm and 0 0 -130 cm) of 50 keV electrons for (a) bottom and (b) top planes.

- A kernel density estimator based on the KDE which is an unsupervised learning technique putting more weight on large topological clusters. For this we use scikit learn package [208]. Let $\boldsymbol{a} = (\boldsymbol{x}, \boldsymbol{y})$ be a 2d-vector describing the set of points in XY. Density estimation with the KDE is performed on each $\boldsymbol{a_i}$, i ranging from 1 to N, following:

$$\rho(\boldsymbol{a}) = \sum_{i=1}^{N} K(\boldsymbol{a} - \boldsymbol{a_i}; h) \tag{VII.1}$$

  with a kernel K, which is a positive function whose shape will define the smoothness of the resulting distribution. This kernel depends on the parameter h, called bandwidth, which controls the trade-off between the bias and variance: a large bandwidth gives a biased distribution while a small one will have a high variance [208]. Kernel functions are for instance Gaussian ($\exp(-\boldsymbol{a}^2/(2h^2))$, exponential ($\exp(-\boldsymbol{a}/h)$) or linear ($1 - \boldsymbol{a}/h$ if $\boldsymbol{a} < h$).
  We optimize the best kernel, cuts and bandwidth. We also consider the arrival photo-electron time and apply a cut on it to improve the performance of the algorithm. The performance of the algorithm is evaluated based on the RMS of the reconstructed position. Hence, we find a best bandwidth around 4, an exponential kernel, a density cut at 50% and an arrival photo-electrons time (t_0) of 6500 ns. It is worth noting that the binning of the KDE does not change the results.
  Low photo-electron density clusters are rejected. A barycentre approach is finally used on the surviving clusters.

We test these algorithms using the 9 configurations of Table VII.1 using the SiPM plane following the variance defined in the previous section.
Figure VII.5 shows an example of reconstruction of a sample of events at a given XYZ input position. We see that the SB and MB methods are biased to the center: true events occurring in edges are reconstructed in the center. The MOc method returns almost flat distributions. The worst performances for KDE, in term of resolutions and biases, are observed for input position on the edge of the detector in XY and in the center in Z

(Tables VII.2 and VII.3).

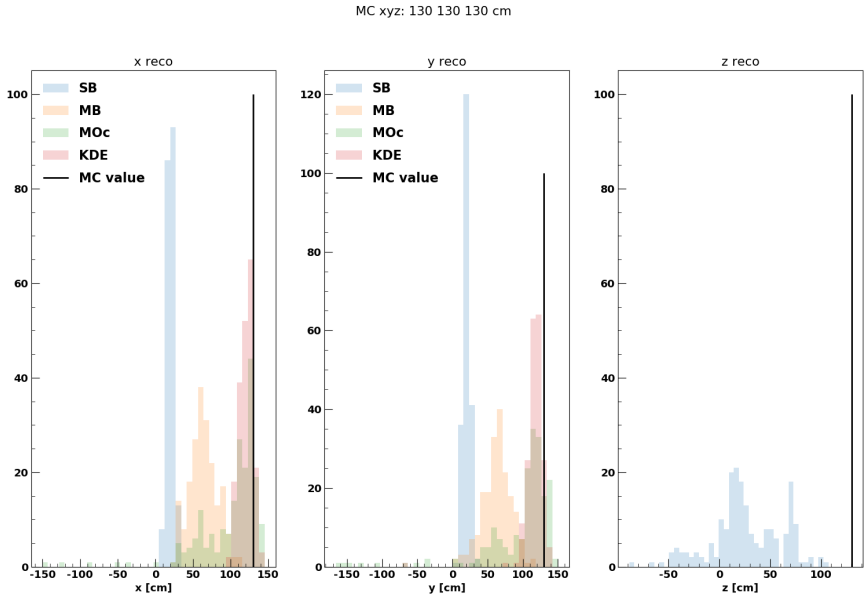

Figure VII.5 – Distributions of position reconstruction for XYZ of an input XYZ position of (125 125 130) cm at 50 keV using several methods developed in the text.

We also test the KDE at 8 keV for the 9 configurations used before. A re-optimization of the different parameters of the KDE (density cut, bandwidth, time cut) is performed. We do not change the time cut, but we raise the density cut and bandwidth. Indeed, at 8 keV signals are small and hence it is hard to find relevant structures. As expected, we get worse results than the one at higher energies (Table VII.2). Biases over the positions remain however similar at both energies (Table VII.3).

Table VII.2 – RMS of the s_1 reconstructed X and Y positions using KDE, with 50 keV and 8 keV input energy, for several input positions.

	50 keV		8 keV	
Input XYZ [cm]	X RMS [cm]	Y RMS [cm]	X RMS [cm]	Y RMS [cm]
0 0 0	29	27	51	49
0 0 130	19	19	40	40
0 0 -130	17	17	35	34
0 -130 0	27	111	48	111
0 -130 130	26	132	44	120
0 -130 -130	13	28	30	54
125 125 0	113	116	126	124
125 125 130	139	142	137	132
125 125 -130	25	26	54	46

Table VII.3 – Bias of the s_1 reconstructed X and Y positions using KDE, with 50 keV and 8 keV input energy, for several input positions.

	50 keV		8 keV	
Input XYZ [cm]	X Bias [cm]	Y Bias [cm]	X Bias [cm]	Y Bias [cm]
0 0 0	1	1	1	1
0 0 130	1	3	1	2
0 0 -130	4	1	2	1
0 -130 0	3	111	1	103
0 -130 130	1	122	1	122
0 -130 -130	2	30	1	9
125 125 0	113	116	111	110
125 125 130	135	138	137	140
125 125 -130	26	27	26	27

We also test the algorithms for uniformly distributed events at different energies: 8, 20, 30 and 50 keV. Figure VII.6 shows, as expected, that X and Y reconstruction performances are similar and that the performance improves with the energy. The Z resolution is better than the (X, Y) one, except at 8 keV. However, in the energy range of interest, the RMS of any position component is above 60 cm.

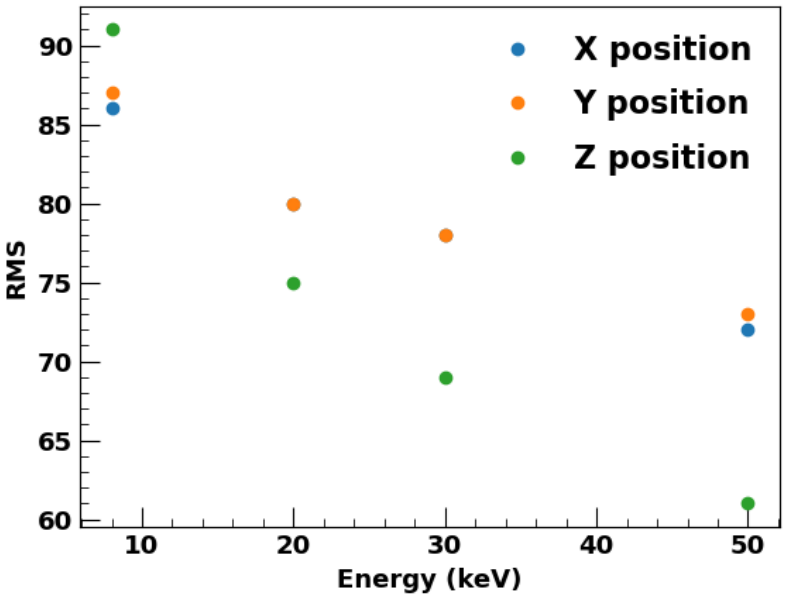

Figure VII.6 – Performance of the X, Y and Z position reconstruction in terms of RMS depending on the energy using the KDE algorithm on 10^4 uniformly distributed events at each energy.

VII.2 Supervised Reconstruction

Supervised learning is a category of algorithms aiming at learning a model to predict a result from labelled data. This task is known as statistical learning, a well-known field in

statistics (see [209] Chapter 2 for a complete introduction).

It relies on three kind of datasets:

- A training set: labelled data, uniformly distributed,
- A validation set: labelled data, uniformly distributed, different events than the training set,
- A prediction set: unlabelled data.

The objective is to make the algorithm learn the relation between the input (here the photo-electron distributions in the channels) and the output (here the position of the event) using the training dataset. For this task, we aim at minimizing a loss function, in our case the Mean Squared Error (MSE) between the prediction and the true position of the event. Computing the MSE on the whole training dataset is expensive in terms of computing resources because the training dataset has many events.

The validation dataset enables to monitor the learning curve of the neural network, in particular to make sure that the model does not over-fit the features of the training dataset. We also use the Mean Absolute Error (MAE) metric on the validation dataset. The MAE gives us an estimation of the resolution in centimeters in the detector.

These two metrics, MSE and MAE, computed on the validation dataset enable us to understand if the model is under-fitting, over-fitting or correctly fitting the data. Over-fitting happens when the predictive model describes too well the fluctuations of the training set rather than the general tendency. The model cannot generalize. Under-fitting happens when the predictive model cannot detect correlations of the training set. It induces a bias on the training set, and consequently also on the validation set. A good fitting model does not suffer from either a large variance or a large bias. A balance must be reached between the complexity of the data and the power of the model. An example of these fitting behaviors is showed in Figure VII.7.

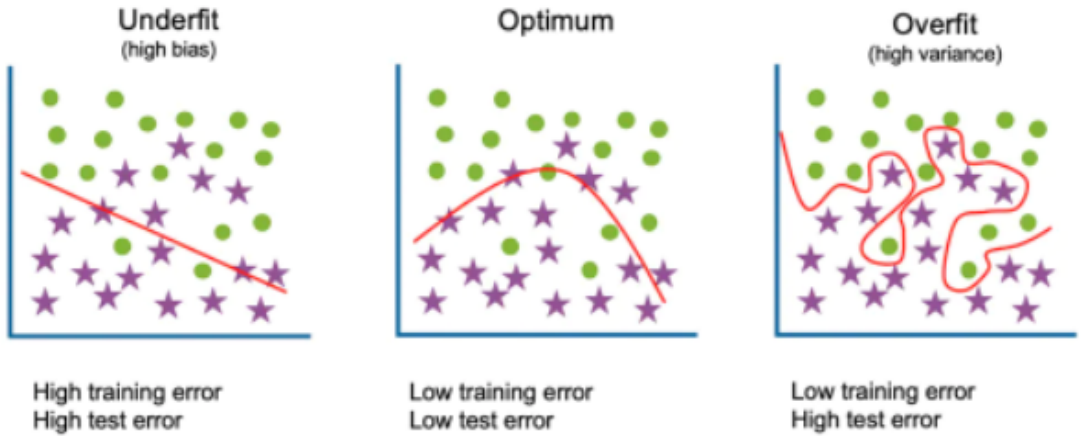

Figure VII.7 – Example of under-fitting, optimal fitting and over-fitting from [210].

These fitting behaviors can be diagnosed by visualizing the training and validation loss in order to optimize the model and its fitting. As schemed in Figure VII.8, under-fitting is

characterized by a high training loss and over-fitting by a good training loss but a raising validation loss. We will use the tensorboard package [211] to visualize theses losses during the training.

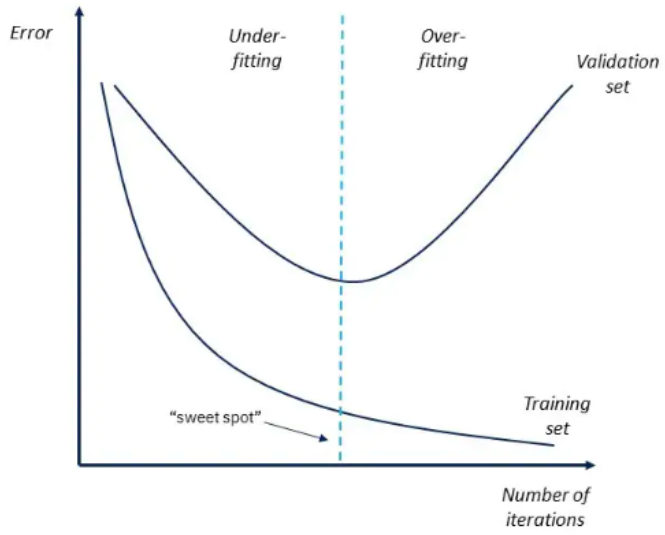

Figure VII.8 – Scheme of the fitting behaviors depending on the training and validation loss, from [210].

At the end, predictions are performed by applying the trained model on the prediction set returning a triplet (X, Y, Z) of the predicted position.

^{83m}Kr can be used in place of Monte-Carlo data as this source will be uniformly distributed inside the detector for calibration purposes.

There exists a large variety of supervised methods in machine learning. We however need a model that can handle a multi-output target (X, Y, Z), several features (8280 channels) and a medium-size training set (10^4 to 10^5 events). In addition we look for pattern recognition as photo-electron distributions look like pictures. Consequently, the most appropriate tool is the convolution neutral networks (CNN) which is known to be efficient with image and pattern recognition. We used the pytorch [211] and pytorch-lightning [212] packages for the implementation.

VII.2.1 Pre-processing of the data

The first step is to convert the data into readable objects for the neural network structure. Hence, we create 3D arrays for each event. It allows to have two (X, Y) planes, top and bottom, each consisting of 70 PDMs X and Y positions. Each position in (X, Y) is mapped with its coinciding PDM giving 70×70 arrays for each plane. In DarkSide-20k, these PDMs will be disposed as an octagon inscribed inside the 70×70 array. Consequently, positions of the (2×70×70) arrays outside the detector, so above the edge of the octagon, are filled with -1 values to show that it is outside the volume of the detector.

Then, each position was filled with the number of photo-electrons detected by its associated PDM. In the end, for each event, we have an 'image' of the detected photo-electrons in each plane that will be used as input data for the convolution neural network (cf. example in Figure VII.9).

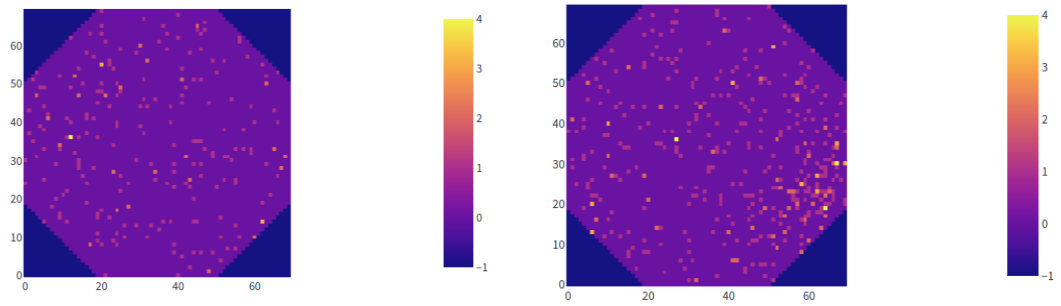

(a) (b)

Figure VII.9 – Data input of CNN for event 10 of simulated MC data highlighted (a) top and (b) bottom planes. The color scale represents the number of photo-electrons detected in each (X, Y) PDM. The x and y axis scales give the identification number of the position of the different (X, Y) positions inside a 70×70 array.

VII.2.2 CNN Model

Convolutional neural networks (CNN) were introduced in 1995 by LeCun and Bengio [213]. It is a class of artificial multilayered neural networks based on convolutions instead of matrix multiplications in at least one of their layers. They were designed to learn spatial patterns through back-propagation of the error gradient and are consequently vastly used for image recognition. They are typically composed by four kind of layers: convolutional layers, pooling layers, non-linear layers and fully connected layers.

- Convolutional layers analyse the input layers and detect the presence of features. These layers perform a convolution between the input matrix and a kernel that slides through the input matrix to produce a representation of the image (activation map) giving the kernel response to each spatial position in the image. The kernel size is set depending on the image size and is usually equal to 3.

- Pooling layers reduce the data dimensions by statistically combining a cluster of nearby neurons into one in the next layer. The size of the cluster must be tuned, but usually it combines small clusters such as 3x3. Several polling functions are possible as for instance the L2 norm, the average or the maximum output of the cluster. Its role is to reduce the image size while keeping its essential features.

- Non linear layers can be placed after convolution layers to break linearity. Several activation functions can be used, one of the most used is the ReLU (Rectified Linear Unit) which keeps only positive neurons.

- Fully connected layers are at the end of the network. They simply consist in matrix multiplications followed by an activation function (*i.e.* ReLU) to classify or perform

a regression. The output is a vector of the size of the expected output for a regression and for a classification, of the number of classes with the probability that the image belongs to each of them.

A scheme of the architecture of a basic network is given in Figure VII.10.

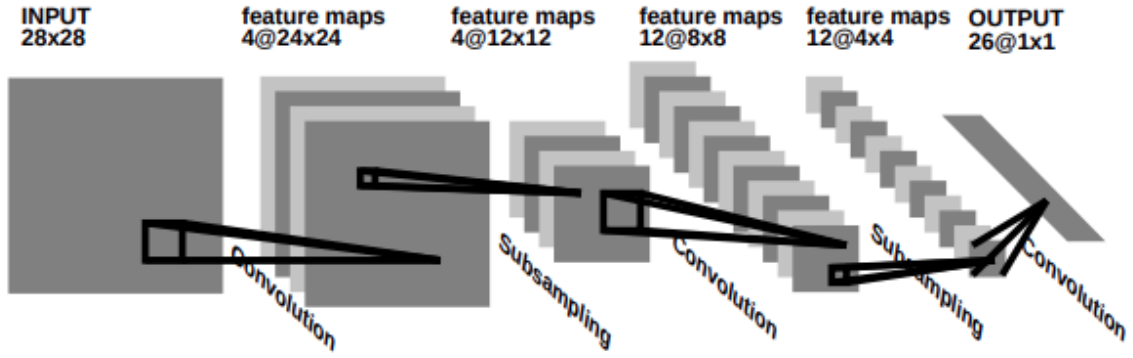

Figure VII.10 – Scheme of the architecture of a basic CNN [213].

Five to twenty five layers are usually used for pattern recognition. In our case, we use a well-known architecture, a deep residual learning network, ResNet-18 [214] with 18 internal layers. Residual neural networks are part of the CNN family but used in addition to convolutional layers residual building blocks of the previous layers to form a network. Indeed, to solve more complex problems by adding more and more layers inside a classical CNN network, it actually becomes more difficult to train the network and to get a good accuracy. It was developed in 2015 by [214].

Instead of relying on a traditional gradient descent on the MSE to decrease the loss function, we use a Stochastic Gradient Descent to optimize the loss function. The Gradient Descent is an optimisation algorithm which minimize the loss function in an iterative way. In the case of the Stochastic Gradient Descent, in each iteration, instead of taking the whole training dataset only a few samples are randomly sampled. The number of samples taken from the training dataset to compute the gradient is called a batch. An epoch is the number of times the learning algorithm go through the whole training dataset. Finally, iterations are the number of batches necessary to complete an epoch.

VII.2.3 Results

We use a training set of 9×10^4 events and a validation one of 1×10^4 for a uniform sample of 50 keV electrons. It allows to find a good fitting behavior: the training loss and the validation loss are decreasing to reach a common value, a MAE near 20 cm. We then train and validate with an uniform sample of 8 keV electrons with 1×10^5 training events and 1×10^4 validation events. This time the training MAE decreases more slowly and its validation reaches only around 60 cm, showing that the pattern recognition is harder and that we are at the limit of the capability of the CNN to converge. Last, we test a training sample of uniform 50 keV electrons events and validation of uniform 8 keV electrons events. The result is the worse, with a validation MAE around 90 cm

which shows slightly over-fitting, but mostly the limit of the algorithm (cf. Figure VII.11).

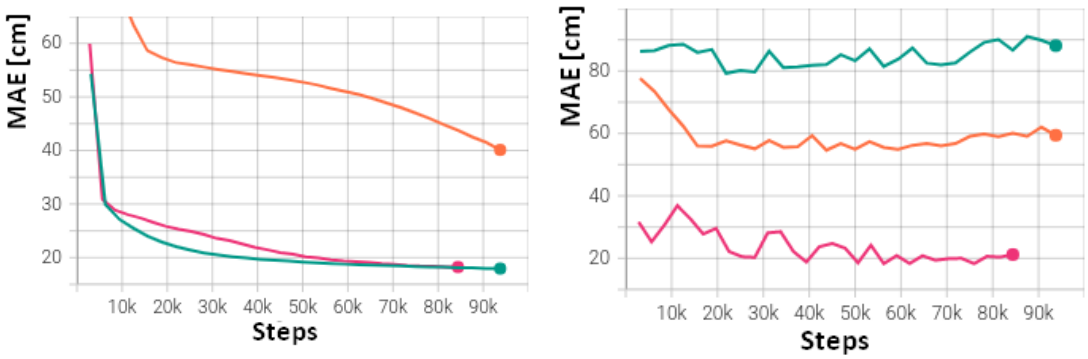

(a) (b)

Figure VII.11 – (a) Training and (b) Validation loss (MAE) depending on the iteration from tensorboard for 3 different samples. Pink: train/validation sets at 50 keV; Orange: train/validation sets at 8 keV; Green: train at 50 keV and validation at 8 keV. See text for more details.

Looking at the performance, *i.e.* the validation loss (Figure VII.11b), we find a factor 1.5 in resolution between the train/validation at mixed energy and the train/validation at 8 keV and a factor 4.5 between the train/validation at mixed energy and the train/validation at 50 keV. This is due to the fact that the pattern is less featured at lower energies, becoming more and more indistinguishable from dark noise, so it is harder for the model to generalize when given a training at a higher energy. If we look at both train and validation sets at the same energy, we see that the resolution decreases while the energy raises (factor 3 between 50 keV and 8 keV).

This is also visible if we look at the RMS between true and reconstructed positions for the uniformly distributed validation sets (cf. Figure VII.12). While the precision does not seem to be highly dependant of the XY position, it is however driven by the Z one. For both 8 and 50 keV samples, we find, in agreement with previous observations, a worse precision on the central part of the TPC. However, at 8 keV, this degradation is generalized to almost the whole Z range, with resolutions from 50 to 140 cm. For the 50 keV, the resolution is smaller, from 15 to 30 cm depending on Z. With the mixed train/validation, results are highly biased: the algorithm is no longer able to generalize. Using the same energy, or close energies, in the train, validation and prediction sets are hence necessary. It however gives better results at high energies.

Consequently, we train the CNN at 20 and 30 keV in addition to the already trained 8 and 50 keV to see the evolution of the performance with the energy. Each time we use a G4DS simulation of 10^5 events for the training and 10^4 events for the validation. Training and validation curves are showed in Figure VII.13. In Figure VII.14, we see that the resolution does not improve in a linear way when the energy raises. Good resolution is obtained for 20, 30 and 50 keV (respectively around 20, 25 and 30 cm) while the one for 8 keV is degraded (around 60 cm). This is due to patterns becoming too faint at this energy to be still distinguishable one from another based on their input position.

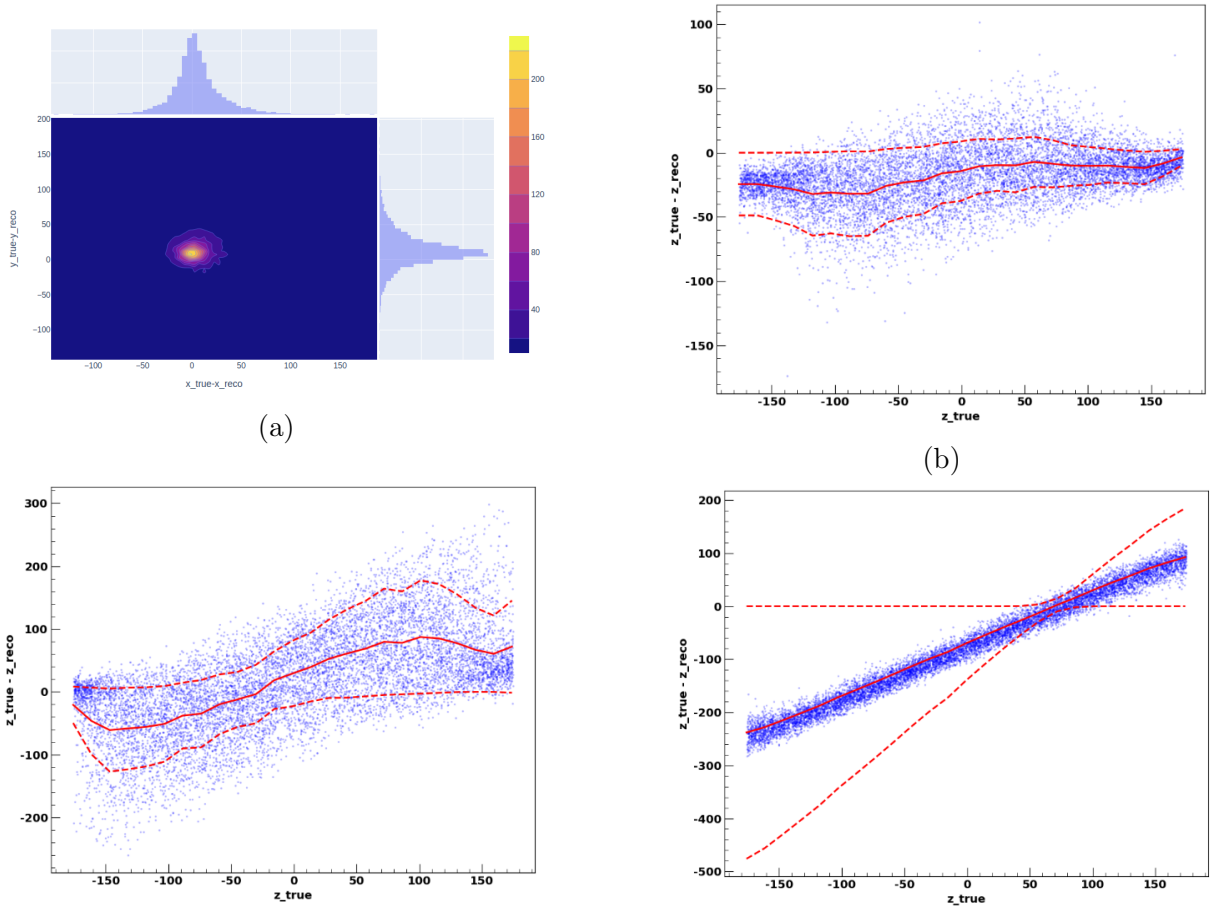

(a) (b) (c) (d)

Figure VII.12 – Difference between true and reconstructed values for (a) X and Y position at 50 keV train/validation, (b) Z position at 50 keV train/validation, (c) Z position 8 keV train/validation and (d) Z position 50 keV train / 8 keV validation where the algorithm does not converge. The solid red line is the mean of the distribution while dashed lines show the mean ± RMS.

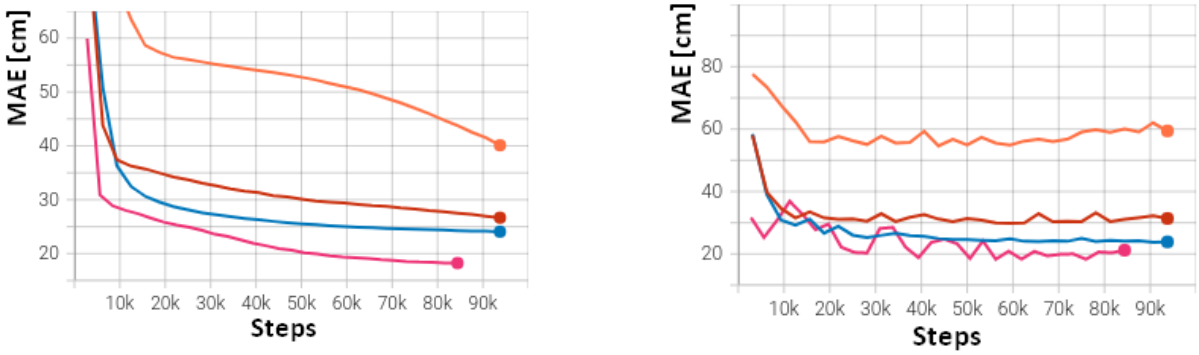

(a) (b)

Figure VII.13 – (a) Training and (b) Validation loss (MAE) depending on the iteration from tensorboard for 4 different energies for the train/validation sets. Pink: 50 keV; Dark Blue: 30 keV; Red: 20 keV; Orange: 8 keV. See text for more details.

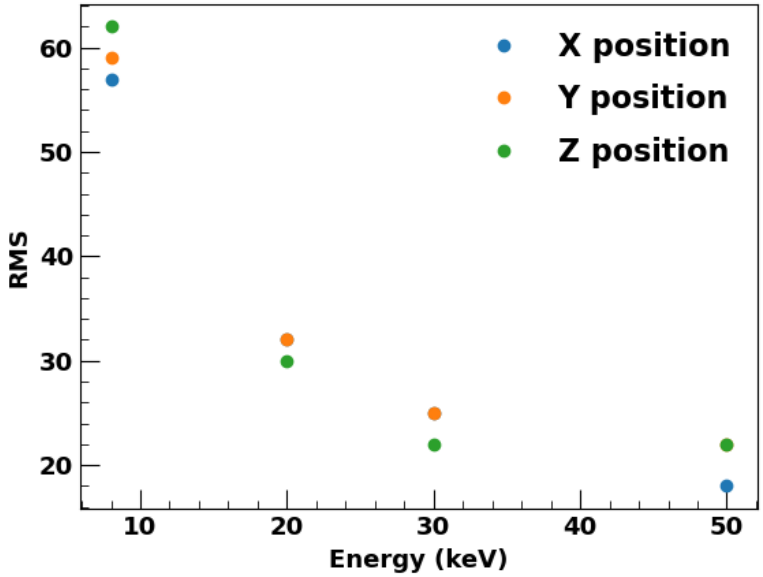

Figure VII.14 – Performance of the X, Y and Z position reconstruction in terms of RMS depending on the energy using the CNN algorithm on 10^4 uniformly distributed events at each energy.

Table VII.4 – RMS of the s_1 reconstructed X, Y and Z positions using a CNN, developed in the text, for several input positions computed at 50 keV and 8 keV. Training and validation are done at the same energy than the samples on which predictions are performed.

	50 keV				8 keV			
Input XYZ [cm]	X RMS	Y RMS	Z RMS	Full RMS	X RMS	Y RMS	Z RMS	Full RMS
0 0 0	43	47	28	32	60	63	60	51
0 0 130	9	13	13	10	43	43	98	48
0 0 -130	15	19	37	19	50	56	102	57
0 -130 0	40	25	29	25	58	121	66	70
0 -130 130	10	14	13	11	42	88	105	59
0 -130 -130	12	28	35	23	43	90	88	54
125 125 0	58	62	35	43	119	105	62	81
125 125 130	11	17	24	15	90	79	114	71
125 125 -130	20	28	17	19	66	54	56	42

We also compute the RMS of the predictions and their biases for each position component performed for the previous 9 configurations at 50 keV and 8 keV in order to further be able to compare with the results obtained with the KDE (Table VII.4 and Table VII.5 respectively). We see that the total RMS for train and validation at 50 keV or train and validation at 8 keV gives results in the expected order of magnitude (cf. Figure VII.11 and Figure VII.12). We still observe the same degradation of resolution and increase of the bias in the center of the detector and in the edges of the XY plane.

Table VII.5 – Biases of the s_1 reconstructed X, Y and Z positions using a CNN, developed in the text, for several input positions computed at 50 keV and 8 keV. Training and validation are done at the same energy than the samples on which predictions are performed.

	50 keV			8 keV		
Input XYZ [cm]	X Bias	Y Bias	Z Bias	X Bias	Y Bias	Z Bias
0 0 0	16	24	11	3	20	19
0 0 130	2	11	9	5	18	76
0 0 -130	5	11	29	1	17	84
0 -130 0	13	5	12	1	103	25
0 -130 130	1	10	9	7	57	79
0 -130 -130	2	26	33	2	53	59
125 125 0	46	54	26	103	87	31
125 125 130	8	15	21	67	53	91
125 125 -130	19	27	13	49	39	22

VII.2.4 Comparison to Unsupervised Learning

Looking at the performance of uniformly distributed events all over the TPC at different energies (Figure VII.15), we see that the overall performance of the CNN is largely superior to the KDE: around 3 times better for 50 keV and around 1.5 times better for 8 keV. Consequently, for the s_1 position reconstruction the CNN algorithm improves notably the performance compared to unsupervised methods as the KDE.

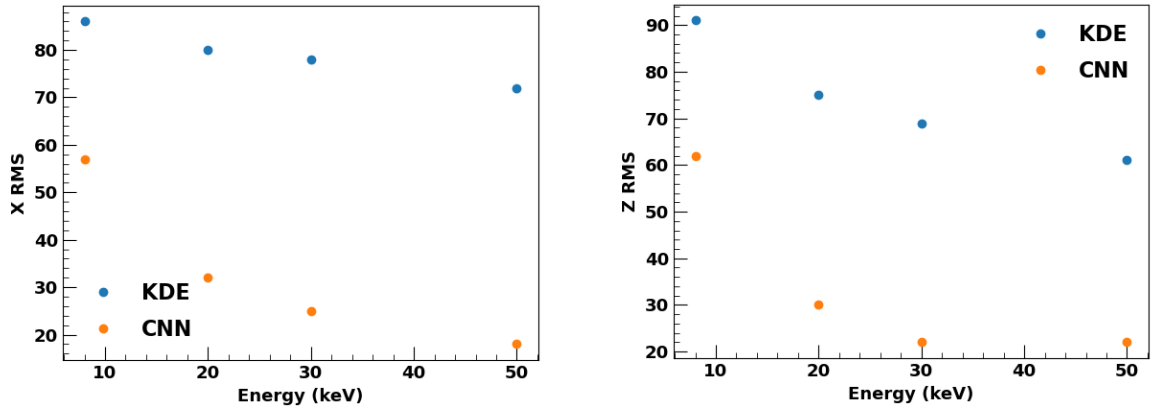

(a) (b)

Figure VII.15 – Compared performance of (a) X (Y is similar), and (b) Z position reconstruction in terms of RMS depending on the energy using either the KDE or CNN algorithm on 10^4 uniformly distributed events at each energy.

In conclusion, a proposal based on this study would be to use the CNN with several training sets at different energies.

VII.3 Extension to Real Data

From previous sections, we found that the best option for s_1 position reconstruction is to use the developed CNN with training and validation sets at different energies in order to have the best resolution.
This means that in practice, we could train and validate using the Monte-Carlo simulation we already used, and this at an extended number of energies in the range of interest. This would however means that the neural network is only trained with simulated data.

Another option based on real data for the training, consists of using ^{83m}Kr calibration data (41.5 keV electrons) to train and validate the CNN. This is a reliable source for the CNN as for a 50-100 Hz ^{83m}Kr source we will have 5-10$\times 10^6$ events per day which will give enough statistics. In addition, it is an internal calibration source, and so we can have spatially uniformly distributed events in the detector. The only drawback is that it is a mono-energetic source.
Consequently, we will develop in this section a strategy to mimic the calibration data distribution at different energies by 1/ scaling in an uniformly random way the light yield of ^{83m}Kr and 2/ adding uniformly and randomly missing dark noise events.

VII.3.1 Scaling Algorithm

We produce 10^4 uniformly distributed events of fake ^{83m}Kr calibration data using G4DS multi-event generator (2 electrons of respectively 10 keV and 31.5 keV). We also generate 10^4 uniformly distributed electron events with G4DS at respectively 8, 20 and 30 keV to serve as benchmarks for the scaling procedure which is as follows:

1. We retrieve the true s_1 energy of generated distributions to compute the scaling factor (f_{xkeV}) between the ^{83m}Kr source energy (E_0) and the target energies at x keV, x = {8, 20, 30} keV (E^{e-}_{xkeV}):

$$f_{xkeV} = E_0 / E^{e-}_{xkeV} \tag{VII.2}$$

2. We scale the initial ^{83m}Kr distribution number of photo-electrons for each event by dividing by the scaling factor f_{xkeV}. Looking at the number of photo-electrons difference between the benchmark sample at a given energy and the scaled sample at the same energy, we see that there is an excess of photo-electrons in the benchmark sample compared to the scaled one (Figure VII.16). We also see that when the energy is decreasing, the offset to zero of the difference is increasing, meaning that the excess of photo-electrons of the benchmark sample is increasing. This phenomena is due to the fact that when we scale the number of photo-electrons, we scale the signal and the noise. However, the dark noise amount is the same at each energy. Hence, the discrepancy between both samples is due to missing dark noise events in the scaled sample.

3. Consequently, for each event we add randomly in active channels synthetic dark noise events to compensate the loss due to the scaling. This amount of dark noise events will be measurable in tiles in the future experiment. For now, we compute it by taking the number of missing events of Figure VII.16, respectively around 192,

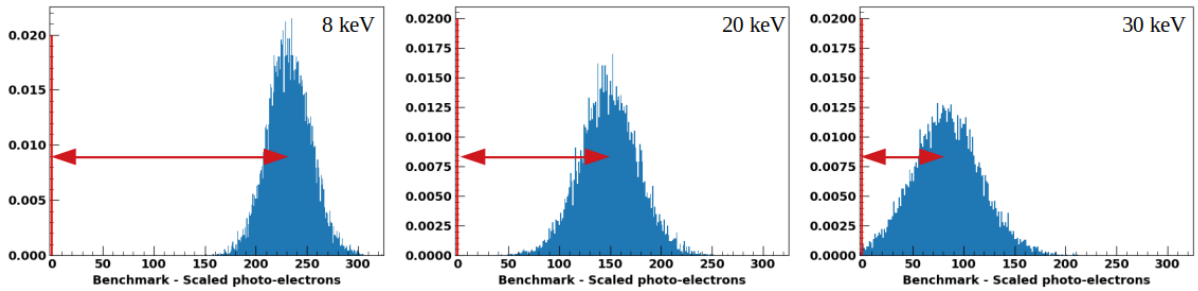

Figure VII.16 – Density of the difference in each channel of photo-electrons between the benchmark and scaled ^{83m}Kr samples **without any dark noise addition**, for events at 8, 20 and 30 keV. The target is a density centered in zero, the offset is thus highlighted by a red arrow.

124 and 69 photo-electrons/events at 8, 20 and 30 keV. Then, by looking at the difference between the scaled and dark noise distribution and the benchmark one, we see that the average is now statistically centered around zero (Figure VII.17).

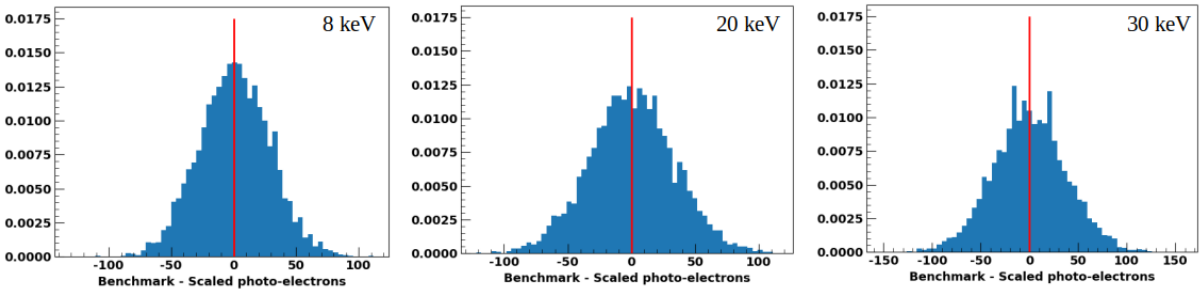

Figure VII.17 – Density of the difference of photo-electrons for each channel between the benchmark and scaled ^{83m}Kr samples **with synthetic dark noise addition**, for events at 8, 20 and 30 keV. The distribution is centered on zero, highlighting the consistency between both samples.

Using this method, we generate uniformly distributed samples for the training set with 10^5 events and for the validation set with 10^4 events at 8, 20 and 30 keV. These samples are then going through the standard pre-processing steps developed in Section VII.2.1 before applying the CNN model developed in Section VII.2.2.

We test the performance of the model on three different configurations in order to check the validity of this scaling method. At each energy, 1/ we use a training, validation and prediction set from the scaling of ^{83m}Kr, 2/ we use a training and validation set from the scaling of ^{83m}Kr and a prediction set with an electron sample and, 3/ we use a training, validation and prediction set with electron samples.

In all cases, the training sets have 10^5 events while validation and prediction sets have 10^4 events. As the scaling procedure of ^{83m}Kr should be mimicking the shape of an electron signal, we should have similar results in terms of resolution for the three configurations. It is indeed what we observe in Table VII.6, with however a slight degradation in the lower energy range due to the rough modeling of the noise. The scaling gives anyway sufficiently close resolution compared to the benchmark case to be validated for further

use.

Table VII.6 – Prediction RMS for 8, 20, 30 keV for three different training/validation/prediction scenarios (cf. text).

RMS (cm)	8 keV	20 keV	30 keV
Training/Validation: scaled ^{83m}Kr Prediction: scaled ^{83m}Kr	61	34	27
Training/Validation: scaled ^{83m}Kr Prediction: electron	63	35	27
Training/Validation: electron Prediction: electron	68	36	27

VII.3.2 CNN Performance

Thanks to the procedure presented in the previous section, we can train the reconstruction procedure with real data. Consequently, to evaluate the performance of the model, we use uniformly distributed training and validation sets from the scaling procedure of ^{83m}Kr and prediction events from simulated electron events.
Training and validation losses for the initial ^{83m}Kr sample at 41.5 keV and scaled samples at 30, 20 and 8 keV are shown on Figure VII.18.

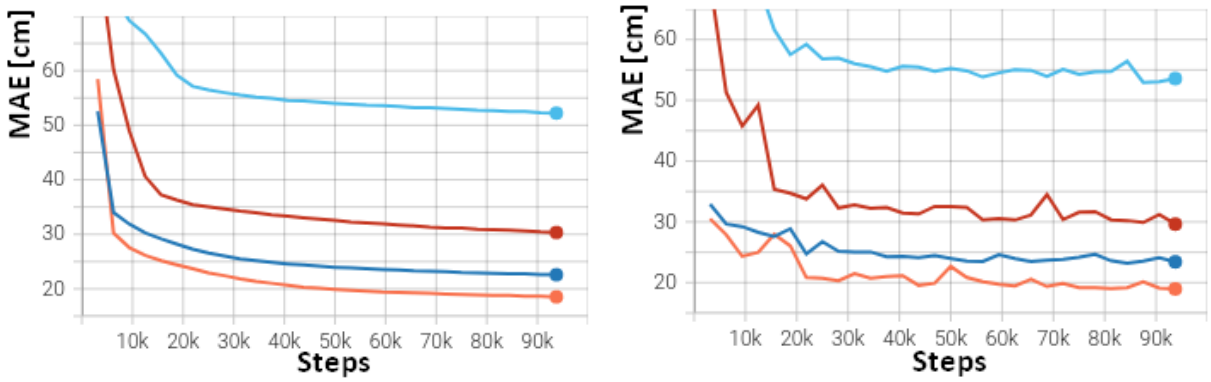

(a) (b)

Figure VII.18 – (a) Training and (b) Validation loss (MAE) depending on the iteration from Tensorboard for 4 different energies. Orange: ^{83m}Kr train/validation sets at 41.5 keV; Dark blue: ^{83m}Kr train/validation sets scaled at 30 keV; Red: ^{83m}Kr train/validation sets scaled at 20 keV; Cyan: ^{83m}Kr train/validation sets scaled at 8 keV. See text for more details.

Table VII.7 – RMS and bias for 8, 20, 30 and 41.5 keV for each s_1 X, Y and Z components for training/validation sets based on ^{83m}Kr and prediction sets based on electron events.

	8 keV			20 keV			30 keV			41.5 keV		
	X	Y	Z	X	Y	Z	X	Y	Z	X	Y	Z
RMS [cm]	54	54	58	31	31	29	25	24	21	14	14	16
Bias [cm]	10	13	6	4	5	2	4	2	2	2	1	2

Looking at the resolution for each component at each energy (Table VII.7), we see that we obtain a good resolution in the highest energy range while it goes up to 55 cm for the lowest energy range.

Similarly, the bias is very small, around 1 to 2 cm, in the highest energy range and it increases to reach 6 to 13 cm in the lowest energy range (Table VII.7). This is highlighted by the distributions of the bias contours for X and Y positions of Figure VII.19. It visually shows the similar behavior between X and Y, very small biases for the reconstructed position in X and Y and a bias increase and resolution decrease at lower energies.

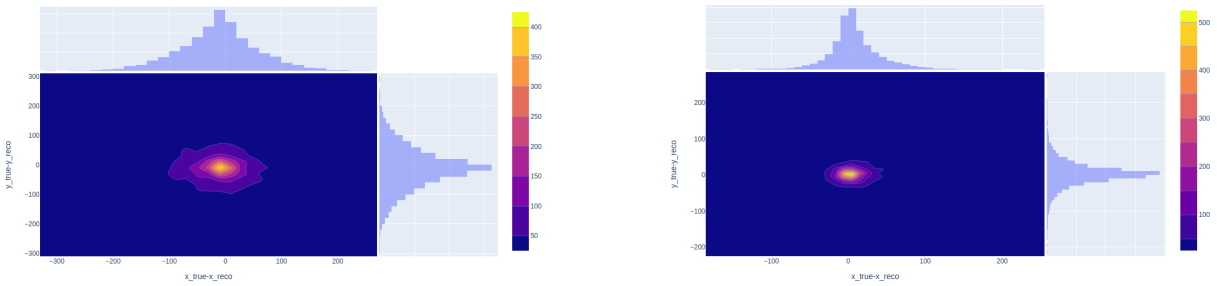

(a) (b)

Figure VII.19 – Contours in number of events of the difference between true and reconstructed X and Y positions for (a) 8 keV and (b) 30 keV. Marginal plots are histograms of the number of events in both axis.

We also look at the behavior of the reconstructed position resolution in Z (Figure VII.20). In this case, depending on the true Z position, the true minus reconstructed Z position is not constant. This effect is stronger in the lower energy range, where signals are fainter (smaller SNR).

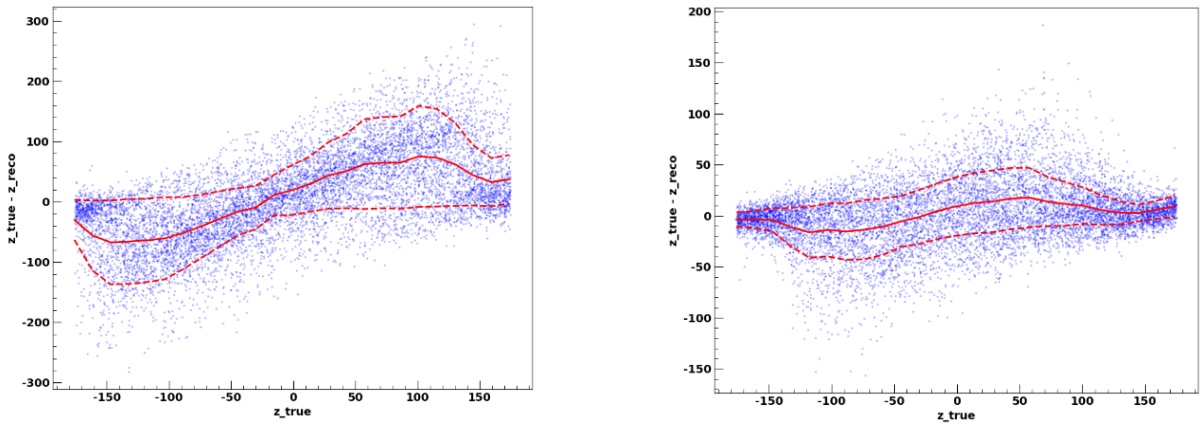

(a) (b)

Figure VII.20 – Distribution of the difference between true and reconstructed Z position depending on the true Z position for (a) 8 keV and (b) 30 keV. The solid red line represents the mean of the distribution and the dashed red lines correspond to the resolution.

We could correct the bias in the reconstructed Z determination by subtracting the mean of the true minus reconstructed Z position at each true Z to every sample at the true Z

(Figure VII.21). Recomputing the mean of the sample, we are now centered in zero at all true Z. This gives us a model-based correction that could be applied to the results of the model depending on Z to further improve the accuracy of the result. The RMS is however still worse in the lower energy range, as expected following previous results.

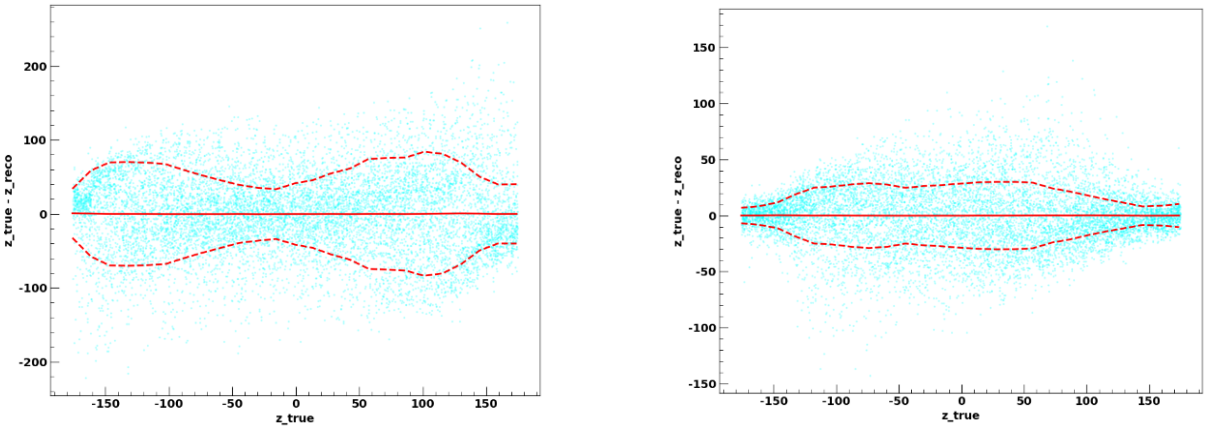

(a) (b)

Figure VII.21 – Distribution of the difference between true and corrected by the mean of Figure VII.20 reconstructed Z positions depending on the true Z position for (a) 8 keV and (b) 30 keV. The solid red line represents the mean of the distribution and the dashed red lines correspond to the resolution.

VII.3.3 Smearing Impact

For the training and validation datasets, the true XY position associated to a calibration ^{83m}Kr event will be inferred from the s_2 XY reconstruction. This last is implemented in the simulation for DarkSide-20k and gives a maximum RMS of 5 cm.
Consequently, we test the impact of Gaussian smearings of X and Y, centered on their respective true value and with a standard deviation of 5 cm.

We use uniformly distributed training, validation and prediction datasets from the scaling procedure of ^{83m}Kr at 30, 20 and 8 keV. We compare the same datasets with and without the smearing due to the s_2 position reconstruction. RMS of the prediction in each case are reported in Table VII.8. The difference between both is in average of 1 cm of RMS. This smearing has consequently a negligible effect on the performance of this algorithm.

Table VII.8 – Prediction RMS for 8, 20, 30 keV for ^{83m}Kr scaled events with and without XY smearing. More details on the data samples in the text.

RMS (cm)	8 keV	20 keV	30 keV
Training/Validation/Prediction: scaled ^{83m}Kr	61	34	27
Training/Validation/Prediction: **smeared** scaled ^{83m}Kr	62	35	28

VII.4 Conclusion

Using a CNN model, we were able to find an efficient way to perform s_1 position reconstruction based on the training of the model that is function of the energy of the event. This hence requires to train the model at the different energies of the energy range of interest.

This reconstruction can be applied directly on real data, using uniformly distributed ^{83m}Kr calibration data to train the algorithm at different energies. Given that ^{83m}Kr energy is at 41.5 keV, we developed a scaling procedure allowing to mimic consistently lower energy signals to be able to make the training on them.

Finally, the resolution found for this method for s_1 reconstruction goes from around 15 to 60 cm depending on the energy, in the energy range of interest.

Chapter VIII

S1-S2 Association

> Nothing revives the past so completely as a smell that was once associated with it.
>
> Vladimir Nabokov (1926)

The long electron drift time in DarkSide-20k TPC (3.5 ms), the residual activity of 39Ar in the liquid argon bulk and the background coming from materials surrounding the target, will produce a large number of events in the TPC with a pile-up probability of ∼42%. The rejection of pile-up events would result in an important loss of lifetime for DarkSide-20k.

The algorithms developed in Chapter VII are then fundamental to minimize such a loss. The combination of the precise recombination of the position of s_2 ($\leq$ 5 cm) with the one from s_1 (few tens of cm), allows to associate event by event s_1 and s_2 pulses.

In this chapter we will test the performance of the s1 - s2 association based on simulated DarkSide-20k data and on the expected reconstruction performances. This will be done by simulating mixed events in a same time window (gate) composed by a nuclear recoil from a WIMP scattering and electronic recoils induced by sources of background in DarkSide-20k: ^{39}Ar and external γ (Section VIII.1).
We will then apply some standard selection cuts (Section VIII.2.1) and will compute the resulting pile-up with WIMPs probability inside the detector (Section VIII.3). Finally, in Section VIII.4, we will estimate the performance of the s_1 and s_2 association based on signal and detector physical properties and its effect on the pile-up.

VIII.1 Data Preparation

We simulate a sample of events containing, for each data taking gate, a WIMP and background deposits assuming the rates expected in DarkSide-20k. For WIMPs, we use uniformly distributed samples with 10 keVnr energy. For the background, G4DS samples from γ background from the different materials are simulated (Table VIII.1). The ^{39}Ar sample with an activity estimated at 0.73±0.11 mBq/kg [113] is accounted for. The total expected rate of electronic recoil background inside the TPC for ^{39}Ar is 36 Hz.

The DUNE cryostat foam provides a small contribution to the background inside the inner veto and the TPC (cf. Section II.3). We consider the non-secular equilibrium of ^{238}U by splitting the chain in three parts: the upper (from $^{238}_{92}$U to $^{226}_{88}$Ra - 6 isotopes), the middle (from $^{222}_{88}$Ra to $^{214}_{84}$Po - 7 isotopes) and the lower (from $^{210}_{82}$Pb to $^{210}_{84}$Po - 3 isotopes). The ^{232}Th has 10 isotopes in its chain, ^{235}U has 11 isotopes, and all the other radio-nucleides considered decay in a stable isotope. Each rate is multiplied by the number of isotopes corresponding to its radio-nucleide to get the contribution of the whole decay chain.

Then, considering 1000 gates of length $t_g = 12$ ms, WIMP and background samples are mixed together accordingly to the corresponding rate. We consider WIMP as the primary source which triggers the gate. The primary event occurs at 4 ms from the beginning of the gate (cf. scheme Figure VIII.1). The background is generated following a Poisson statistic with a parameter $\lambda = r_i \times t_g$, r_i being its rate.

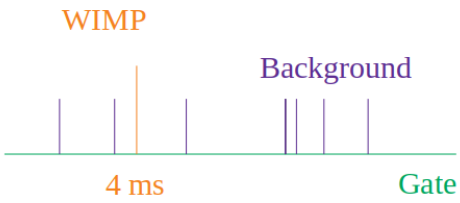

Figure VIII.1 – Scheme of the mixing between a WIMP and background inside a given time gate.

Table VIII.1 – γ and ^{39}Ar rates expected for DarkSide-20k background budget inside the TPC and the inner veto.

Positions	**γ rate [Hz]** TPC	Inner veto
TPC PDM	35.5	13.3
Veto PDM	2.5	50.4
Gd Acrylic	10.4	21.2
Titanium Vessel	0.47	27.2
Cryostat	0.03	2.7
Total γ rate	48.9	114.8
^{39}Ar rate [Hz]	36	26
γ + ^{39}Ar rates	84.9	140.8

Each gate, composed by a WIMP and background, is reconstructed using standard G4DS reconstruction that combines together deposits that are very close one to another, and so, are indistinguishable.

VIII.2 Toy Reconstruction

Once the samples of WIMPs and backgrounds are simulated and mixed, we reconstruct physical variables using a toy reconstruction based on the resolutions obtained with the

reconstruction framework. We use this method to estimate the performance of association of s_1 and s_2 as it is much faster and less demanding in terms of computing resources than performing the full reconstruction of s_1 and s_2 pulses.

VIII.2.1 Procedure

From G4DS true information of each deposit, we reconstruct variables of interest: position, energy, time etc. We also distinguish between events occurring inside the TPC and events in the inner veto.
Inside the TPC, the time of the deposits correspond to the s_2 pulses time. s_2 pulses arriving within a time difference below 200 ns are grouped together. For each group, we associate only one s_1. These groups are called clusters (cf. schemes Figure VIII.2). We also reconstruct s_1 pulses.

Then, for each gate, we store the pulse id, type (s_1 or s_2), pdg code, material in which it was deposited, inner veto or TPC, true and reconstructed X, Y, Z, energy, time, f_x. Lasts variables are defined in the paragraphs below.

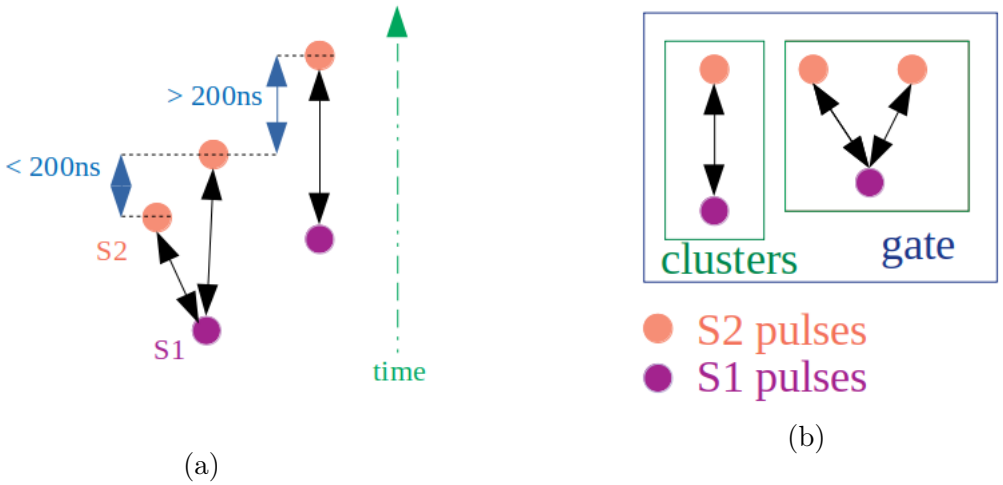

(a) (b)

Figure VIII.2 – Schemes of (a) the association of pulses into clusters based on the time condition between s_2's (cf. text) and (b) examples of clusters present inside a time gate.

Position reconstruction. For this study we do not run the full reconstruction but we associate the reconstructed position of s_1 by randomly generating a position from a distribution centred in the true position of the recoil and with the resolution from the CNN method described in Chapter VII.

The XY resolution of s_2 pulses is 5 cm. For s_1 pulses inside the TPC, the resolution is parameterized as a function of the recoil energy and the position by using samples of recoils with energies of 8, 20, 30 and 41.5 keV distributed uniformly inside the TPC. For each energy, we compute the mean difference between the true and reconstructed position. Then, we correct the reconstructed position by the observed bias and we retrieve the RMS

of the corrected distribution as the resolution. For more details on this part, please refer to Chapter VII. To cover the whole energy and position range, we interpolate it on a 2D grid. Maps of the X, Y and Z resolution depending on the energy are shown on Figure VIII.3. The resolution obtained for s_1 and s_2 pulses by applying this method is shown in Figure VIII.4.

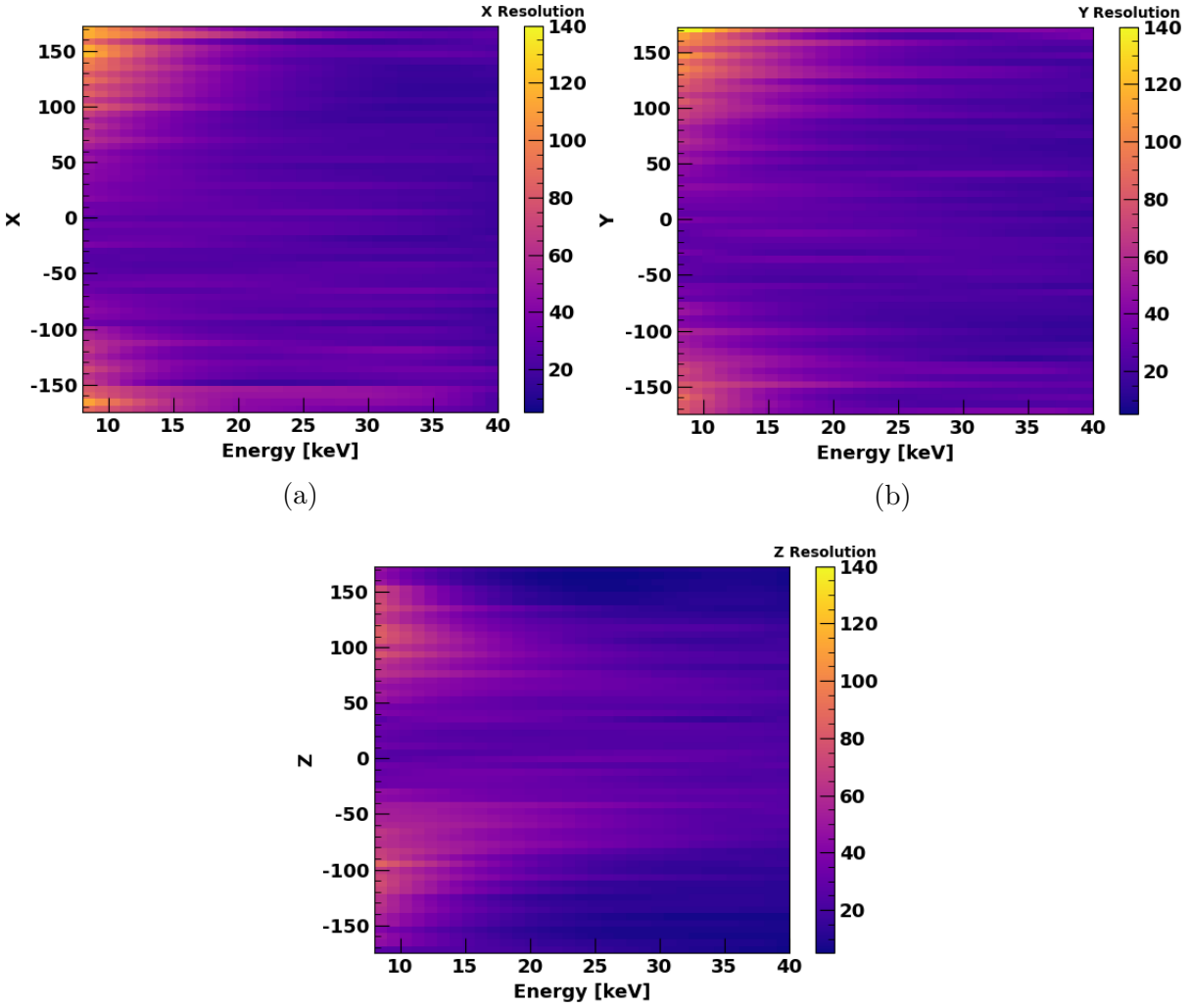

(a) (b)

(c)

Figure VIII.3 – Resolution on each component of the s_1 position depending on the position component and the energy based on interpolated results from the CNN presented in Chapter VII. The binning creates small discontinuities of the resolution in some X or Y bins which are only a plotting artifact.

Energy reconstruction. We calculate the number of photo-electrons in s_1 and s_2 [110] and generate their associated reconstructed variables assuming a Gaussian smearing.

Time-related variables. Concerning the time reconstruction, we assume that there are no biases and we take the G4DS time as the one for s_1 pulses. For s_2 pulses, the time is obtained summing the drift time to the true time. Time distributions are shown

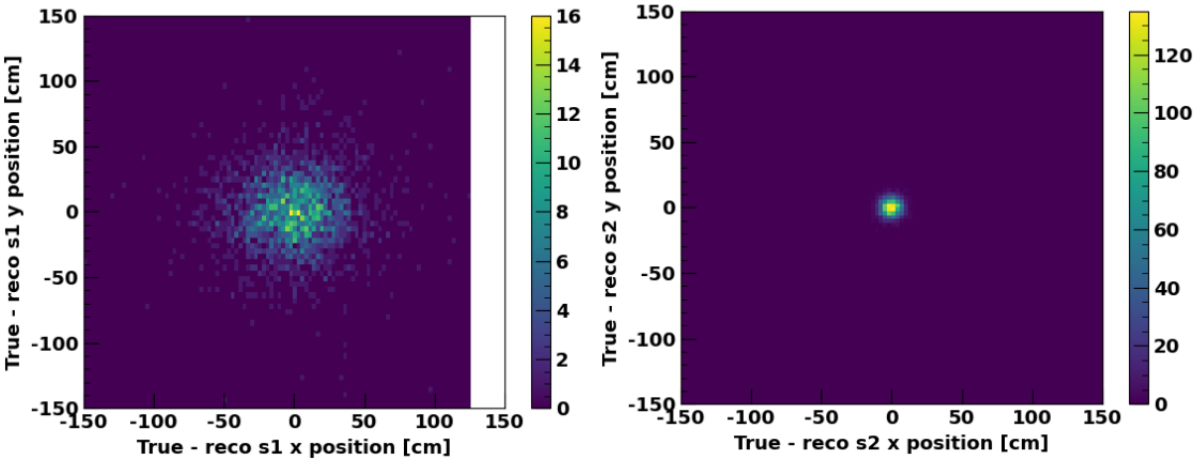

(a) (b)

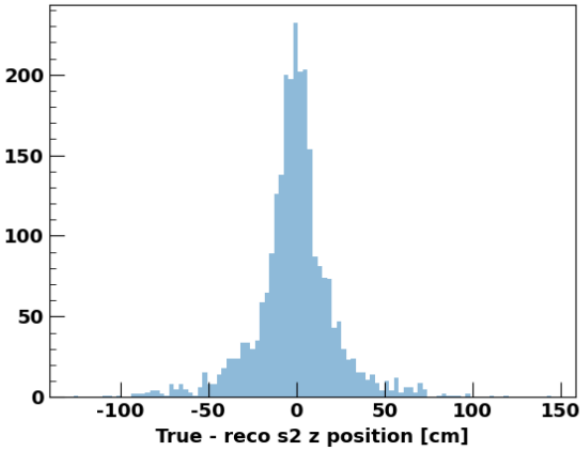

(c)

Figure VIII.4 – True - reconstructed position (a) XY for s_1, (b) XY for s_2 and (c) Z for s_1 and s_2.

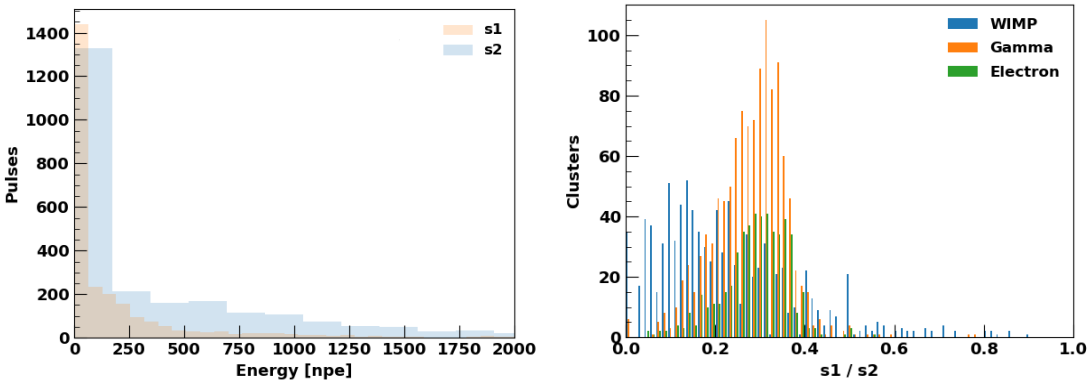

(a) (b)

Figure VIII.5 – (a) Reconstructed energy of s_1 and s_2 pulses and (b) Ratio of s_1 over s_2 depending on the particle type.

in Figure VIII.6a where the spike in time for s_1 is due to the fact that all WIMPs are produced at the same time.
Then we also create a proxy of f_{190}, called f_x, by looking at the fraction of energy in the deposit due to a nuclear recoil. f_x distribution is shown on Figure VIII.6b.

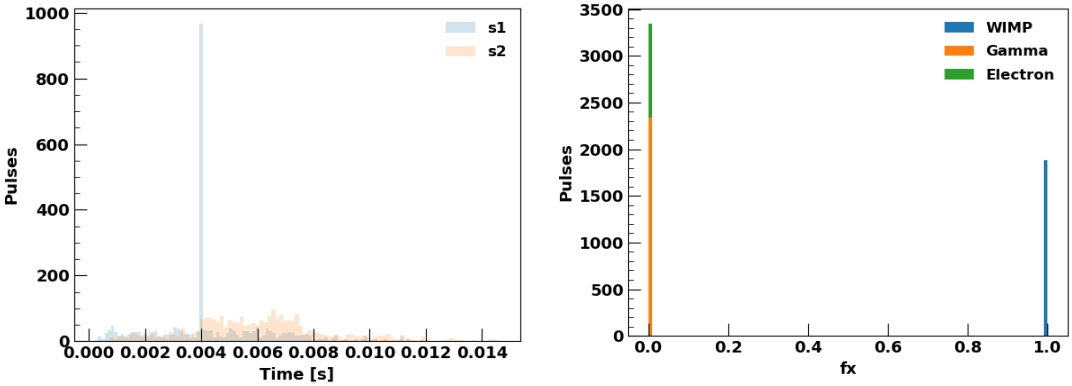

(a) (b)

Figure VIII.6 – (a) Time of s_1 and s_2 pulses and (b) f_x depending on the particle type.

VIII.2.2 Selection cuts

As we consider pulses deposited inside the TPC, we start by selecting only clusters that are in the TPC. We generate 1000 WIMPs recoils. Inside these gates, 343 gates are WIMPs only while the residual 657 gates contain background events as well.

We generate gates of 12 ms much larger than the maximum drift time in the TPC (3.5 ms). Thus, we split the gate into sub-gates if two s_1's are separated by more than the maximum drift time. In such case, one of the sub-gate is necessarily composed of background pulses (only one WIMP event per gate). After this operation, 537 sub-gates contain WIMPs only and the residuals are in pile-up with either a TPC background or a veto event.

Then, the information contained in the inner veto allows to remove background pulses that are detected in coincidence by the TPC and the inner veto. A coincidence is considered when there is an s_1 pulse in the TPC and a pulse in the inner veto above 200 keV within a time delay below 800 μs. For such coincidence, we cut the s_1 and its associated s_2 inside the TPC. This operation can remove WIMP events, and so we loss gates. After this step, we have 942 gates, 521 with WIMPs only and the remaining 421 with WIMPs and background events.

The evolution of the number of gates depending on whether there are background events inside the gates is summarized in Figure VIII.7 along with the evolution of the difference between the number of s_2 and the number of s_1 which shows the progressive removal of multi-scatter background clusters.

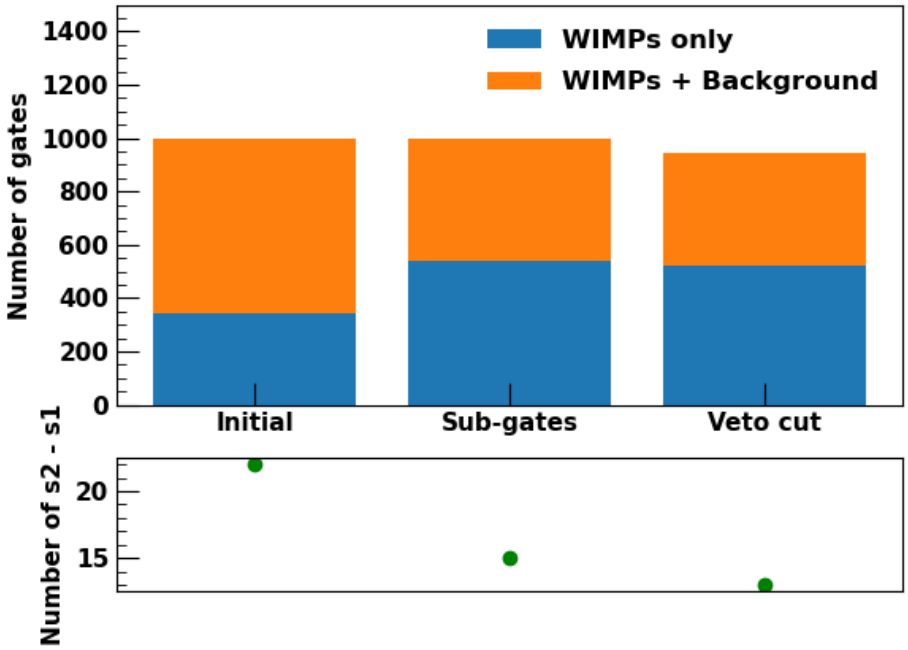

Figure VIII.7 – (top) Number of gates with WIMPs only and WIMPs + background, (bottom) Evolution of the difference between the number of s_2 and the number of s_1, along the different steps of data preparation.

VIII.3 Pile-up

In addition to the association of s_1 and s_2 pulses that will be performed in the following section, we evaluate at this stage the expected pile-up in the detector. It is an important variable as it defines the dead time between the acquisition of different pulses and hence the fraction of signal that we may loose. We consider the pile-up as the coexistence in the same gate of pulses of WIMP and background. We distinguish between three different kind of pile-up:

- **TPC pile-up.** We consider only pulses occurring inside the TPC. It is computed such as: 1 - (number of gates with WIMPs only in the TPC / the total number of gates with WIMPs).
- **Veto pile-up.** We consider WIMPs pulses occurring inside the TPC as well as pulses in the inner veto that are in coincidence with WIMPs TPC pulses. It is computed such as: number of gates with WIMPs in the TPC and background in the inner veto in coincidence divided by the total number of gates with WIMPs
- **Global pile-up.** It is computed as the number of gates for which at least one of the above conditions is fulfilled divided by the total number of gates with WIMPs.

The results are summarized in Table VIII.2.

Table VIII.2 – Impact of the different selection and cuts on pile-up percentages.

	Initial	Sub-gates	Veto cut
TPC Pile-up [%]	65.7	46.3	47.9
Veto Pile-up [%]	11.5	8.7	0
Global Pile-up [%]	67.1	49.0	47.9

VIII.4 S_1-S_2 association

In Section VIII.1 and Section VIII.2.1, we produced a sample of clusters of s_1 and s_2 pulses for which we know notably the position, energy and time. Here, we assess the performance of associating pulses on the basis of reconstructed variables.

In each gate other than s_1+s_2 only, we associate pulses based on the following conditions:

- The distance XY between two pulses is below 80 cm,
- $|\Delta t - \Delta Z/v_{drift}|$ between two pulses is below 1 ms,

The optimization of both the distance and time thresholds is performed based on the number of false positives, the number of true WIMPs over generated, the number of remaining background clusters and the percentage of clusters with one WIMP pulse, and more than two WIMPs pulses (Figure VIII.8). Based on these 5 parameters, we maximize the number of true WIMPs and minimize all the other variables. The best compromise is for a time threshold of 1 ms and a distance threshold of 80 cm.

We also add an s_2/s_1 cut: inside the pulses of a sub-gate, if there is only one combination of s_1 + s_2 pulses that satisfies s_2 / $s_1 < 27$ then we associate both pulses together. The new associations are from now on defined as reconstructed clusters.

Figure VIII.9 shows the impact of the s_2/s_1 threshold value on the same five parameters (number of false positives, number of true WIMPs over generated, number of remaining background clusters and percentage of clusters with one WIMP pulse, and more than two WIMPs pulses). The best performance is obtained for a cut at 27. It increases the percentage of true WIMPs over generated by 3.6%.

Finally, each time, for each sub-gate we only store reconstructed clusters with two pulses, as multi-scatters are suppressed. Looking more into details, reconstructed clusters depending on their number of pulses are shown in Figure VIII.10. As expected, reconstructed clusters with more than 2 pulses contain only background pulses and a fraction of WIMP events are lost as their s_1 and s_2 pulses are not matched together (cluster with only one pulse).

We evaluate the fraction of selected true clusters that are not matched correctly (false positives), the percentage of true WIMPs over generated and the percentage of remaining background clusters in the TPC. Their values are summarized in Table VIII.3.

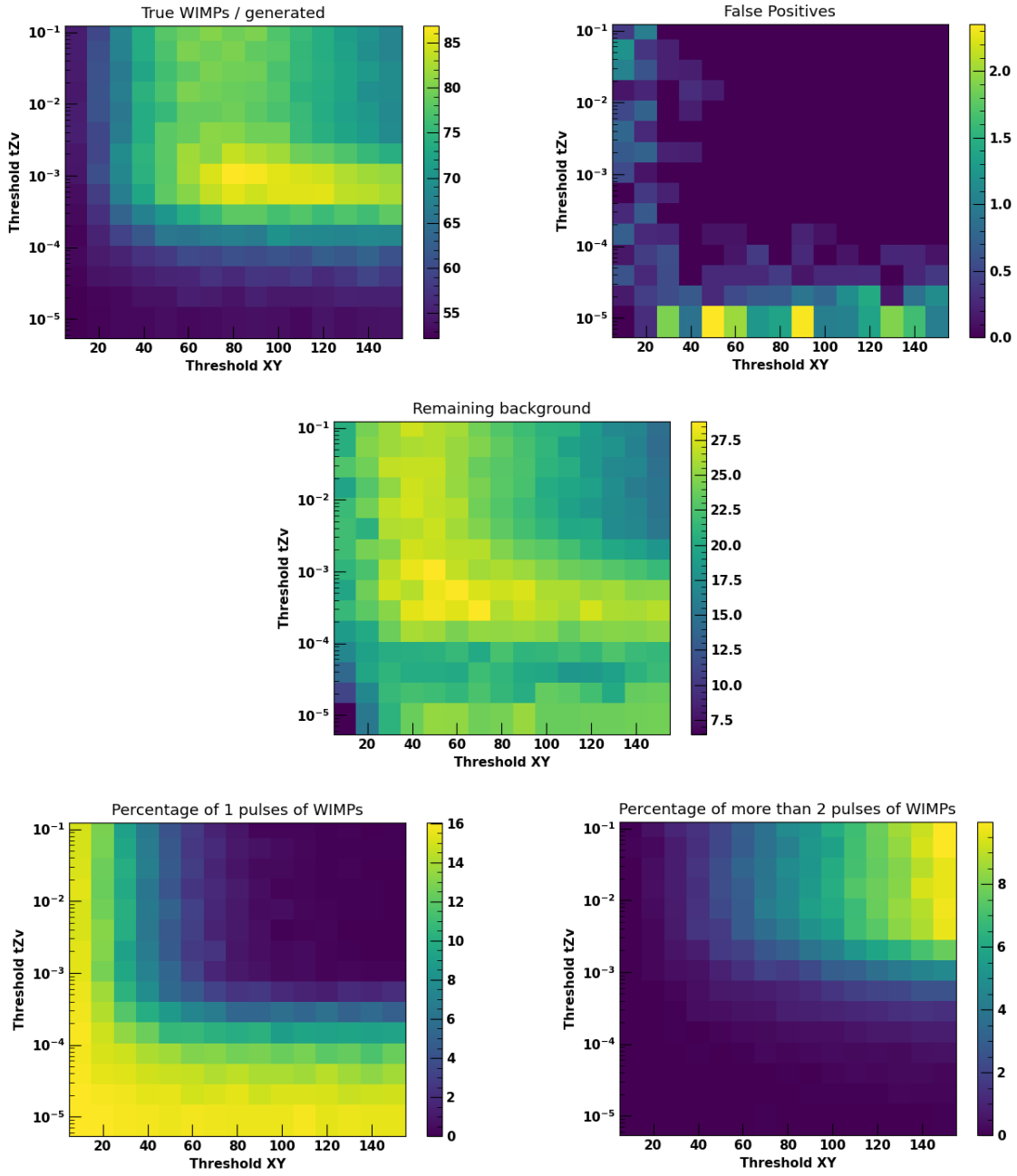

Figure VIII.8 – Maps of the threshold value for the XY cut [cm] and the time cut (tZv) [s] depending on percentages of the true number of WIMPs over generated, the number of false positives, the remaining background clusters and the number of WIMPs pulses inside clusters (either 1 or more than 2). For the first three variables we also apply the two pulses cut. The s_2/s_1 cut is not applied (cf. upper part of Table VIII.3).

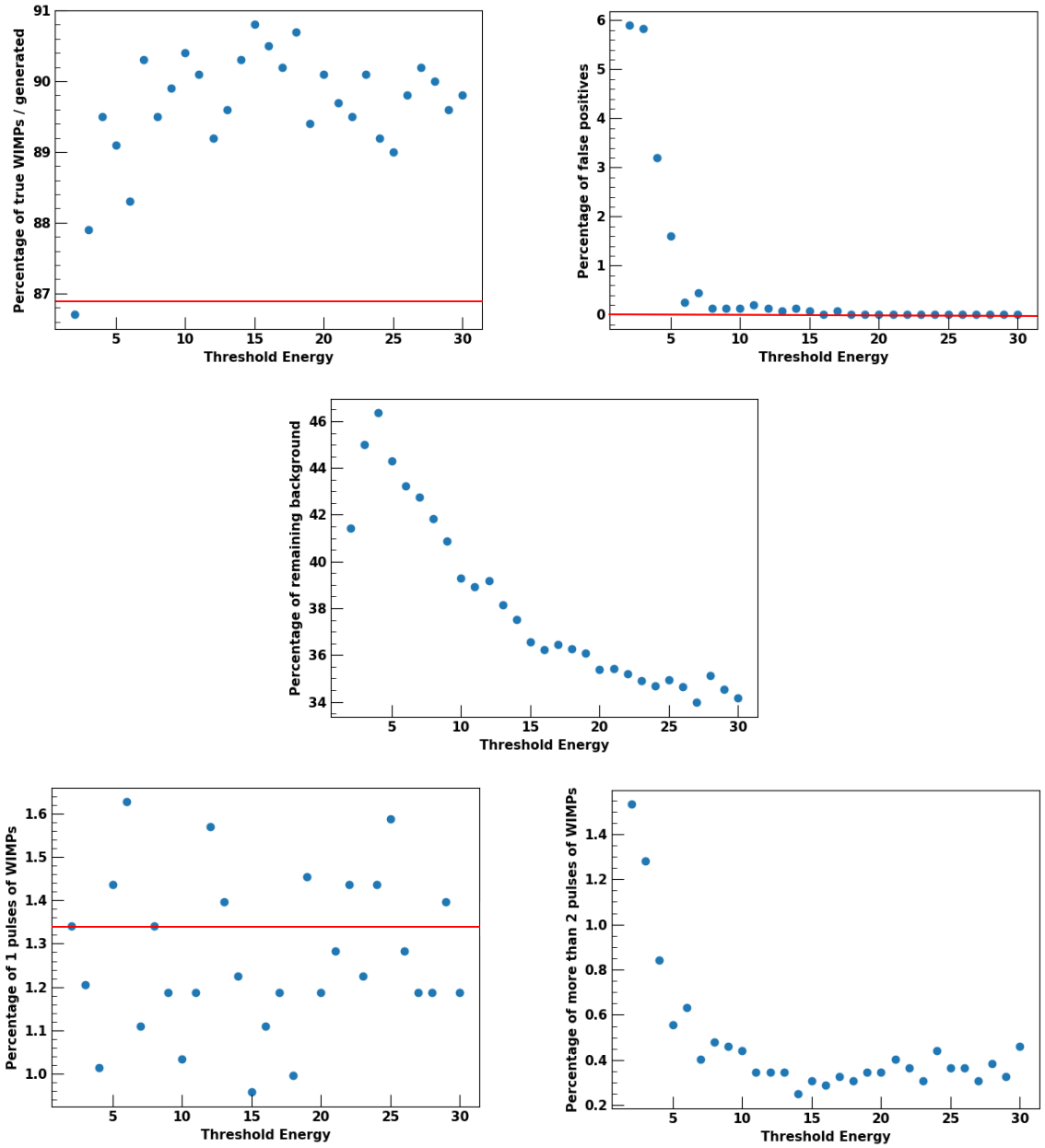

Figure VIII.9 – Evolution of the percentages of the true number of WIMPs over generated, the number of false positives, the remaining background clusters and the number of WIMPs pulses inside clusters (either 1 or more than 2) depending on the threshold on the s_2/s_1 cut with a threshold on the XY of 80 cm and on the time of 1 ms (cf. lower part of Table VIII.3). The two pulses cut was only applied on the first three variables. The red line shows the value obtained without the s_2/s_1 cut. For the remaining background, the line is below the range of obtained values, at 26.11%, and for more than 2 WIMPs pulses in a reconstructed cluster, it is slightly above at 1.64%.

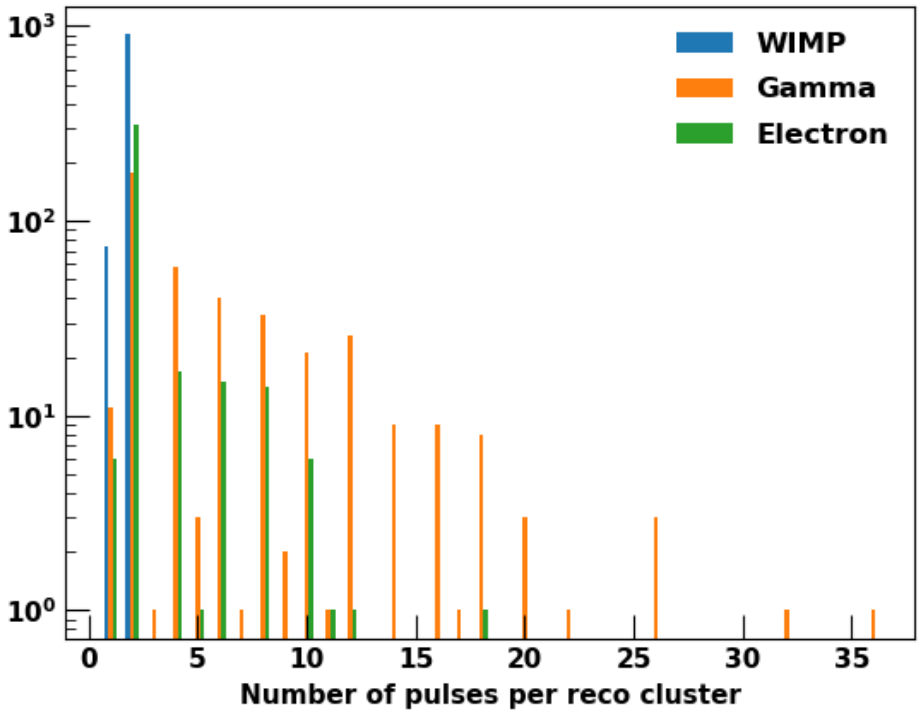

Figure VIII.10 – Number of pulses per reconstructed clusters depending on the particle type.

Table VIII.3 – Performance of the s_1-s_2 association by sequentially applying the cuts, without (up) and with (down) the s_2/s_1 cut.

	Position and Time Cuts	Two Pulses Cut
False positives [%]	1.87	0.00
True WIMPs over generated [%]	97.80	86.90
Remaining background clusters [%]	39.92	26.11

	Position and Time Cuts	s_2/s_1 Cut	Two Pulses Cut
False positives [%]	1.87	2.10	0.00
True WIMPs over generated [%]	97.80	97.80	90.20
Remaining background clusters [%]	39.92	42.97	33.97

Finally, this approach enables to have zero false positives. In addition, we reconstruct correctly about 90% of the WIMPs when applying all cuts. Hence, this procedure allows to reduce the dead-time from 48% to 10 %.

VIII.5 Conclusion

This approach first allowed to evaluate the pile-up with WIMPs inside the detector. Comparing the pile-up induced by the inner veto and induced by the TPC, it occurred that it is mainly driven by the TPC. After applying the different cuts that will be also applied on real data, we estimated a pile-up of around 48%. It is an important quantity, but is in line with what is expected.

Then, based on a simulation of a sample of WIMP and background following the expected rate distribution of DarkSide-20k, an effective toy reconstruction and the physical properties of the pulses, we were able to estimate the performance of the s_1-s_2 association to around 90% of true WIMPs rightly associated without any false positives. Hence, this procedure allows to reduce the dead-time inside the detector down to 10%.

Conclusion

With only indirect evidences from astrophysical observations and cosmological measurements, dark matter precise nature is one of the biggest puzzle in cosmology and fundamental physics. The DarkSide experiment aims at its direct detection using a dual-phase LAr TPC. In the previous stage, DarkSide build a 50 kg active mass detector (DarkSide-50) which allowed to set the best limits in the 1.8 and 6 GeV/c^2 WIMP mass range. The collaboration is now building a 50 ton active mass detector with the potential to increase the sensitivity up to the neutrino floor.

The first part of this thesis, based on DarkSide-50 data, described my contributions to the re-analysis of the backgrounds and refinements of the detector response, which allowed to improve the low-mass dark matter limits by about a factor 10 compared to the previous analysis and to set the best limits in the 40 MeV/c^2 to 3.6 GeV/c^2 WIMP mass range. I also describe alternative dark matter candidate models, such as keV-sterile neutrinos and galactic and solar ALPs, and associated limits. A preliminary analysis of the search of an annual modulation with DarkSide-50 data hinted at a rejection of the DAMA/LIBRA claim at more than 3σ.

The second part of this thesis was focused on the reconstruction and simulation software of DarkSide-20k. I first describe the development of the reconstruction software based on a custom single photo-electron (hit) finder which demonstrated to be very effective. The stability of the reconstruction software was validated with simulation and data from small scale set-ups. Then, based on the reconstructed variables, we were able to prepare additional tools for the future experiment:

- The study of the gas pocket thickness is an important aspect as it is required to be stable along the entire data taking. To monitor it, we implemented a tool based on the fit of the ionisation signal pulse shape. This approach was tested on real data from the ReD experiment. Although this approach is not able to result in an absolute measurement of the gas pocket thickness it enables a relative measurement along the plane.

- The sensitivity strongly depends on the acceptance of WIMPs defined by the pulse shape discrimination method. We then developed a toy Monte-Carlo package to assess the impact of the detector parameters on the pulse shape discrimination. This allowed to drive optimizations for the detector design.

- Given the large volume of DarkSide-20k and the consequently high rate of expected events, one of the main challenges will be the minimization of the pile-up effect. A strategy relies on the correct association between scintillation and ionisation signals, even in presence of pile-up. For that, we developed a CNN that can be tuned on

real calibration data and can reconstruct the scintillation signal position with a precision around 15 to 60 cm depending on the energy. Thanks to this reconstruction, we associated correctly around 90% of WIMPs scintillation and ionisation signals together without any false positive. From an initial pile-up in the detector of around 48%, it allowed reducing it at around 10%.

DarkSide-20k is starting its construction this year and its data taking in planned for 2025. In ten years of data-taking, DarkSide-20k expects to be sensitive to cross-sections of 6.3×10^{-48} cm^2 for the 90% CL exclusion and 2.1×10^{-47} cm^2 for the 5σ discovery at a WIMP mass of 1 TeV/c^2. With its full volume, it almost reaches the neutrino floor with 4.6×10^{-48} cm^2 for the 90% C.L. exclusion and 1.5×10^{-47} cm^2 for the 5σ discovery. And maybe a nice discovery on the way!

Appendix

A Résumé pédagogique en français

A.1 Qu'est-ce que la matière noire ?

Au début du XXème siècle, et plus précisément en 1932, l'astronome hollandais Jan Hendrick Oort étudiait le décalage entre la fréquence des ondes stellaires à l'émission et à la réception (communément appelé effet Doppler) près du plan galactique de la Voie Lactée [1]. On appelle plan galactique le plan dans lequel se trouve la vaste majorité des étoiles de la galaxie. Se faisant, il observa que la force gravitationnelle, c'est-à-dire l'interaction responsable de l'attraction des corps massifs, dues aux masses lumineuses, c'est-à-dire aux masses qu'il pouvait voir, était trop faible pour maintenir les étoiles dans la trajectoire observée. Il postula alors l'existence d'une matière massique invisible localisée dans le plan galactique. En ajoutant cette matière, la masse totale de la galaxie était alors suffisante pour expliquer sa dynamique en suivant les modèles physiques de l'époque.

Peu après, en 1933, un autre astronome, Fritz Zwicky qui s'intéressait à la dispersion des vitesses des galaxies dans le cluster Coma observa le même déficit entre la masse visible et la masse prédite par les modèles [2] [3]. En continuité du travail de Oort, Vera Rubin et ses collaborateurs étudièrent la vitesse de rotation de 60 galaxies isolées et parvinrent à la même conclusion [4]. D'autres indices venant de mesures astrophysiques et de la cosmologie vinrent de même appuyer l'hypothèse de cette masse dite manquante [7] [9] [10] [12] [15] [19].

Cette matière inconnue, n'émettant pas de lumière et présente dans le plan galactique, fut appelée matière noire. Grâce aux observations, nous savons également qu'elle est cinq fois plus abondante que la matière baryonique, c'est-à-dire cinq fois plus abondante que la matière composant toutes les structures observables de notre Univers (planètes, étoiles, galaxies, etc) [6] [18], soit 80% de la matière de l'Univers. Elle n'interagit que par gravitation avec le reste de la matière [6], se déplace à des vitesses très inférieures à la vitesse de la lumière [20] [21], interagit faiblement avec elle même [6] et ne possède pas de charge électrique [19]. Cette matière serait également stable, c'est-à-dire qu'elle ne se désintégrerait pas en d'autres particules ou alors qu'elle mettrait un temps supérieur à l'âge de l'Univers pour le faire [22].

Plusieurs particules hypothétiques sont en lice pour prétendre à cette masse manquante. Les plus prometteuses sont les WIMPs [37] [38], les ALPs [52] [53] et les neutrinos stériles [65] [68]. Ces particules ont de nombreuses propriétés et caractéristiques. Elle ont en commun de répondre aux exigences attendues des particules de matière noire établies au

paragraphe précédent.
Il existe cependant une autre possibilité qui nierait la présence d'une matière additionnelle. En effet, cette question de la masse manquante pourrait également être due à une mauvaise compréhension de la physique et donc, à des imprécisions dans les modèles théoriques [82] [83] [87]. Dans cette thèse nous nous intéresserons uniquement aux candidats de type particule.

A.2 DarkSide ou l'art de diffuser les particules dans l'argon

Afin de tenter de détecter cette matière noire, plusieurs expériences ont vu le jour. L'expérience DarkSide est l'une d'entre elles. Elle possède plusieurs détecteurs dont le but est soit d'être le plus sensible possible à la matière noire et plus particulièrement aux WIMPs, soit de tester de nouvelles méthodes de détection pour cela. Tous les détecteurs de l'expérience DarkSide ont au coeur de leur dispositif expérimental une Chambre à Projection Temporelle (TPC). Il s'agit d'un type de technologie qui permet de reconstruire en trois dimensions les positions et énergies d'interaction des particules à l'intérieur d'un volume, dans notre cas un volume d'argon liquide, soumis à un champ électrique et dans certains cas magnétique. DarkSide n'utilise que des champs électriques car, comme nous l'avons vu précédemment, la matière noire n'a pas de charge et un champ magnétique n'aurait donc aucune influence sur les particules. En effet, un champ magnétique courbe les particules chargées de façon différente selon le signe positif ou négatif de leur charge.

Lorsqu'une particule de matière noire entre dans le détecteur elle interagit avec un noyau d'argon par diffusion. En plus de déposer de l'énergie dans le détecteur, cela entraîne également toute une chaîne de réaction sur les atomes d'argon qui produit notamment des électrons qui vont dériver à cause du champ électrique vers le haut de la TPC. Ils atteignent alors une poche d'argon gazeux située en haut du détecteur. À cet endroit ces électrons vont de nouveau provoquer un dépôt d'énergie qui sera mesuré. Les deux dépôts d'énergie vont nous permettre de déterminer si la particule qui a traversé le détecteur est bien une particule de matière noire ou s'il s'agit d'une particule parasite. En effet, un des grands enjeux de ce type d'expérience est de rejeter toutes les particules autres que la matière noire et qui viennent de l'environnement proche comme des confins de l'Univers. Même les composants de l'expérience ont leur propre radioactivité qui contribue à ce qu'on appelle communément le bruit de fond. Pour réduire toutes ces sources de bruits de fond, et plus particulièrement celles qui laissent des signaux similaires à ceux de la matière noire dans le détecteur, ces derniers sont placés dans des laboratoires souterrains et possèdent des dispositifs de blindage qui permettent de stopper la très grande majorité du bruit de fond. Le reste est modélisé et supprimé lors des analyses.

Dans cette thèse nous nous intéressons à quatre détecteurs. DarkSide-50 est actuellement le détecteur le plus sensible aux WIMPs de faibles masses [101]. Proto-0 est un prototype du prochain détecteur - DarkSide-20k - qui sera encore plus sensible à la matière noire car il possédera un volume plus important dans lequel les particules de matière noire pourront interagir (20 tonnes à la place de 50 kg). Ce changement d'échelle n'est possible qu'en améliorant de façon significative les technologies de détection. Proto-0 a pour objectif de tester certaines de ces technologies et d'initier la mise en place d'un logiciel de reconstruction, c'est-à-dire d'un logiciel qui permettra de passer des mesures de signaux dans le détecteur à des quantités physiques utilisables pour la détection de la matière

noire. Finalement, le quatrième détecteur, ReD a pour objectif de tester une autre façon de détecter les particules de matière noire.

A.3 Objectifs de cette thèse

Cette thèse s'inscrit au sein de la collaboration DarkSide dont le but est de détecter la matière noire. Mon objectif principal au sein de cette collaboration a été de contribuer à l'analyse des données et au développement des logiciels de reconstruction de données et de modélisation. En pratique, cela s'est traduit par diverses contributions à chacune des quatre expériences décrites dans la section précédente.
Dans le cadre de DarkSide-50, j'ai contribué à la calibration et ré-analyse des bruits de fond dans le détecteur afin d'améliorer la sensibilité de l'expérience aux WIMPs de basses masses avec ou sans effet Migdal. De plus, j'ai implémenté et testé plusieurs autres modèles de matière noire : les ALPs solaires et galactiques ainsi que les neutrinos stériles dans l'intervalle de masse candidat à la matière noire. Finalement, j'ai recherché une modulation annuelle dans les données, autre signature de la matière noire. Les résultats principaux sont exposés Section A.4.

Dans le cadre de Proto-0, ReD et de la future expérience DarkSide-20k, j'ai contribué à la mise en place des logiciels de reconstruction de données et de modélisation (cf. Section A.5). Une fois les données reconstruites, j'ai réalisé une étude de l'épaisseur de la poche de gaz à l'interieur du détecteur de l'experience ReD dans le but de suivre son évolution au cours de la prise de données (cf. Section A.6).
J'ai également participé à la mise en place du futur logiciel de reconstruction de l'expérience DarkSide-20k et notamment aux modélisations ayant pour but de tester la sensibilité du futur détecteur contrainte par l'efficacité de la discrimination par forme d'impulsion dont nous discuterons Section A.7. Finalement, j'ai mis en place une méthode de reconstruction de la position d'interaction de la matière noire dans le détecteur, dite s_1, grâce à des réseaux de neurones convolutifs (Section A.8) permettant d'associer ce signal à sa contrepartie s_2 dans le détecteur et ainsi de réduire la perte de données due à l'empilement des signaux (Section A.9).

A.4 Recherche de WIMPs, d'ALPs et de neutrinos stériles

DarkSide-50 a été conçu pour la recherche de WIMPs. Il est cependant également intéressant d'étudier sa sensibilité à d'autres candidats tels que les ALPs et les neutrinos stériles. La signature des particules recherchées est un spectre en énergie. Les modèles implémentés doivent donc donner l'allure de ce spectre en énergie, c'est-à-dire du nombre d'évènements en fonction de l'énergie pour chaque candidat. Cette signature est ensuite comparée aux données prises par l'expérience. Dans le cas où aucun évènement n'est détecté, il est tout de même possible de contraindre l'espace des paramètres. Il suffit d'enlever la partie correspondant aux paramètres qui auraient donné un signal visible dans le détecteur. Cela revient à tracer une limite dans l'espace des paramètres, limite se trouvant entre la zone rejetée et celle des possibles.

Pour calculer ces spectres, et donc le nombre d'évènements en fonction de l'énergie dans le détecteur, nous avons besoin de connaître le flux de matière noire arrivant sur Terre, la section efficace entre la matière noire et l'argon et la quantité d'atomes d'argon sur

laquelle les particules de matière noire peuvent interagir. Il est également nécessaire de connaître les distortions venant du détecteur qui déforment les spectres et changent donc légèrement la signature recherchée. Pour chaque type de particules candidates, c'est ce spectre prenant en compte les effets du détecteur qui est ensuite comparé aux données qui ont été acquises. Aucun des modèles existants n'a aboutit sur une détection directe de matière noire. Il a par contre été possible de tracer des limites dans chaque cas.

Contrairement aux WIMPs basses masses, étude qui avait déjà été faite par la collaboration et qui a été affinée par un jeu de donnée plus large et une maîtrise des bruits de fonds plus poussée, les limites sur les ALPs et les neutrinos stériles ne donnent pas de meilleurs résultats que d'autres expériences utilisant le même type de méthodes expérimentales.

A.5 Reconstruire la physique à partir de signaux lumineux

Pour étudier divers modèles de matière noire, comme vu à la section précédente, il est nécessaire de reconstruire précisément l'énergie déposée dans le détecteur pour chacun des évènements à partir des signaux lumineux mesurés en sortie. Afin d'automatiser cette reconstruction, nous avons mis au point un logiciel adapté aux technologies et conditions expérimentales des détecteurs. Ainsi, pour les expériences Proto-0 et ReD, nous avons développé une nouvelle version de ce logiciel, adaptée à l'apport de nouvelles technologies, et qui sert de base pour développer celui de DarkSide-20k, actuellement en cours.

J'ai participé à plusieurs étapes de cette reconstruction des données. Tout d'abord, la détection et la séparation des pics dans les données qui sont le résultat des interactions dans le détecteur. Ensuite la calibration laser qui sert à évaluer la réponse d'un seul photo-électron dans le détecteur. Pour cela, un signal laser pulsé est envoyé dans la TPC. Le signal laser a un pic en charge pour un, deux, trois, etc, photo-électrons. En faisant un ajustement de chacun de ces pics nous trouvons une relation linéaire entre le gain en charge et le nombre de photo-électrons émis. Il est également possible de déterminer d'autres variables d'ajustement telle que la variance ou encore le niveau d'occupation laser dans le détecteur.

Nous avons vu que la matière noire dépose deux signaux différents dans le détecteur que l'on appelle respectivement s_1 et s_2 et qu'il faut donc identifier dans les fenêtres de prise de données à partir des pics détectés afin connaître leurs caractéristiques. Pour cela, nous avons mis au point un algorithme de regroupement qui va sélectionner les évènements s_1 et s_2 en se basant dans les deux cas sur les caractéristiques physiques connues de ces signaux.

Nous pouvons finalement évaluer la résolution des signaux obtenus ainsi que la performance de la procédure de reconstruction. Grâce à l'algorithme de détection de pics nous avons notamment amélioré la résolution et permis d'atteindre une efficacité de reconstruction au dessus de 95% en l'absence de bruit dans le détecteur.
Cette reconstruction nous a également permis de mettre en place des variables physiques pertinentes qui nous permettent ensuite d'étudier différents phénomènes physiques et de pouvoir étudier la sensibilité à la matière noire.

A.6 De l'intérêt de l'épaisseur de la poche de gaz

A l'intérieur des TPCs à dual phase, la phase gazeuse est un élément clé qui se doit de rester stable tout au long de la prise de données. Cependant, il n'est pas possible de mesurer directement son épaisseur. Ainsi, un outil de diagnostic a été mis en place pour en faire un suivi tout au long de la prise de données.

Cette étude est basée sur des données de l'expérience ReD sur lesquelles nous avons utilisé un modèle théorique pré-existant qui permet de mesurer la forme de l'impulsion du signal d'ionisation (s_2). Un des paramètres de ce modèle est le temps de dérive dans la poche de gaz. En multipliant par la vitesse, que nous avons également calculé, il est donc possible de retrouver l'épaisseur. Les incertitudes liées au modèle ont été extensivement mesurées à l'aide de différents outils de simulation.

Il s'avère qu'en appliquant le modèle et ses incertitudes aux données de ReD, la poche de gaz reste relativement uniforme dans le détecteur en suivant les tendances spatiales attendues au vu de sa configuration. Cependant, la valeur absolue de la poche de gaz est largement supérieure à ce qui est mécaniquement possible dans le détecteur. Ainsi cet outil peut être utilisé de façon relative pour observer les variations dans le temps et dans l'espace. Des améliorations doivent toutefois être mises en place pour avoir accès à la valeur absolue.

A.7 PSD et sensibilité dans DarkSide-20k

Un des atouts de l'expérience DarkSide, possible grâce à l'utilisation de l'argon liquide, est la possibilité de réaliser des analyses sans bruit de fond. Ceci est réalisable notamment grâce à une technique qui s'appelle la discrimination par forme d'impulsion (PSD). Cette technique permet de séparer les reculs électroniques, qui sont le bruit de fond majoritaire, des reculs nucléaires effectués par les particules de matière noire. Ainsi, il est possible de délimiter une région dans l'espace des paramètres de la PSD dans laquelle tout signal enregistré est un signal de matière noire. La taille et la position de cette région aura donc une influence directe sur la sensibilité de l'expérience.

Pour correctement utiliser la PSD, il est primordial d'avoir correctement reconstruit les données. En effet la PSD est basée sur la mesure différentielle du temps de détection des photons. Ainsi, il est nécessaire d'avoir des mesures précises d'arrivés des signaux ainsi qu'une bonne séparation entre eux. Par ailleurs, il est également important de prendre en compte les différents bruits de fond du détecteur et notamment ceux dus à la détection des photons.

Ainsi, pour le prochain détecteur, DarkSide-20k, le design doit permettre d'obtenir une très bonne sensibilité et donc une excellente PSD. Par conséquent, nous avons mis en place un logiciel de simulation de cette dernière qui nous a permis de réaliser plusieurs études sur l'impact de certains paramètres et scénarios de conception pour DarkSide-20k donnant ainsi des éléments de réponse pour la mise en place de l'expérience à venir.

A.8 Comment retrouver la position de S_1 ?

L'expérience DarkSide-20k sera constituée d'une TPC de taille telle qu'il sera primordial d'associer correctement les signaux s_1 et s_2 sous peine d'éliminer à tort une partie non négligeable de véritables évènements. Pour réaliser cette association, il est nécessaire d'avoir plusieurs informations dont les positions en XYZ de s_1 et de s_2.

Pour reconstruire la position de s_1 l'information principale provient des distributions de photo-électrons provenant des dépôts d'énergie par scintillation qui sont mesurés par les plans de détection en haut et en bas du détecteur. En fonction du motif observé sur chacun des plans, il est possible de déterminer la position d'où ils proviennent.

Deux méthodes ont été implémentées. La première est basée sur des barycentres et densités de présence pour XY et sur une calibration du rapport haut/bas pour Z. Cette méthode n'était pas la plus probante, particulièrement pour les énergies les plus basses quand le bruit de fond est très important par rapport au signal.

La seconde méthode, plus probante, est basée sur des réseaux de neurones convolutifs. Elle a permis de mettre au point une méthode de reconstitution qui nécessite d'entraîner le réseaux de neurones sur des évènements dont la position est connue, c'est-à-dire de lui faire apprendre les motifs attendus pour chaque position. Il faut pour cela disposer de données uniformément dispersées dans le détecteur et en nombre important, supérieur à 10^5 évènements. Il est possible d'utiliser soit des données simulées, soit des données de calibration.
Cette méthode fonctionne correctement uniquement en entraînant le modèle à la même énergie que celle pour laquelle la position des évènements est recherchée. Ainsi, il faut entraîner le modèle à plusieurs énergies. Or, les données de calibrations ne sont disponibles qu'à une seule énergie, en haut de la gamme d'intêret. Un algorithme de mise à l'échelle a été implémenté pour résoudre ce problème.
Finalement, cette méthode permet d'avoir de bonnes résolutions dans la reconstruction de la position de s_1, entre 15 et 60 cm, avec les meilleurs performances en haut de la gamme d'énergie (environ 40 keV) et les pires en bas (environ 8 keV).

A.9 Association des signaux S_1 et S_2

Il a été mentionné à la section précédente la nécessité associer correctement les signaux s_1 et s_2 afin de diminuer la perte de véritables évènements qui seraient temporellement superposés dans le détecteur. Nous avons donc évalué la performance de l'association entre ces deux signaux.

Pour cela, des fenêtres temporelles de prise de données ont été simulées. Elles contiennent des échantillons combinant WIMPs et bruits de fond selon les taux attendus dans l'expérience DarkSide-20k. Ces données ont été reconstruites à l'aide d'un outil de reconstruction effectif basé sur les performances du logiciel de reconstruction de DarkSide-20k. Les évènements obtenus ont été sélectionnés de la même façon qu'ils le seront dans DarkSide-20k. Sur l'ensemble de données résultantes, l'empilement à l'intérieur du détecteur, c'est-à-dire la proportion de fenêtres temporelles dans laquelle se trouve à la fois une WIMP et du bruit de fond, a été évalué à environ 48%. Cette proportion est importante à connaître

car elle permet d'évaluer le temps mort et donc la perte de données résultante dans le détecteur.

L'association des signaux s_1 et s_2 est ensuite effectuée sur cet échantillon de données en suivant les propriétés physiques des signaux. La performance de cette association est bonne : 90% des WIMPs sont associées correctement, sans aucun faux positif. Ainsi, il ne reste que 10% des cas dans lesquels il reste de l'empilement. Cette procédure permet donc de réduire de façon considérable la perte d'évènements dans le futur détecteur.

Bibliography

[1] J. H. Oort. The force exerted by the stellar system in the direction perpendicular to the galactic plane and some related problems. *Bulletin of the Astronomical Institutes of the Netherlands*, 6:249, Aug 1932.

[2] F. Zwicky. Die Rotverschiebung von extragalaktischen Nebeln. *Helvetica Physica Acta*, 6:110–127, Jan 1933.

[3] F. Zwicky. On the Masses of Nebulae and of Clusters of Nebulae. *The Astrophysical Journal*, 86:217, Oct 1937.

[4] Vera C. Rubin. Dark matter in spiral galaxies. *Scientific American*, 248(6):96–109, 1983.

[5] A. Einstein. Lens-like action of a star by the deviation of light int the gravitational field. *Science*, 84(2188):506–507, 1936.

[6] Richard Massey, Thomas Kitching, and Johan Richard. The dark matter of gravitational lensing. *Reports on Progress in Physics*, 73(8):086901, 2010.

[7] Dennis Walsh, Robert F Carswell, and Ray J Weymann. 0957+ 561 a, b: twin quasistellar objects or gravitational lens? *Nature*, 279(5712):381–384, 1979.

[8] Katherine Garrett and Gintaras Duda. Dark matter: A primer. *Advances in Astronomy*, 2011:1–22, 2011.

[9] Anton G. Bergmann, Vahe Petrosian, and Roger Lynds. Gravitational Lens Models of Arcs in Clusters. *The Astrophysical Journal*, 350:23, Feb 1990.

[10] Douglas Clowe and et al. A direct empirical proof of the existence of dark matter. *The Astrophysical Journal*, 648(2):L109–L113, Aug 2006.

[11] Marusa Bradac and et al. Dark matter and baryons in the x-ray luminous merging galaxy cluster rx j1347. 5–1145. *The Astrophysical Journal*, 681(1):187, 2008.

[12] D. Harvey and et al. The nongravitational interactions of dark matter in colliding galaxy clusters. *Science*, 347(6229):1462–1465, Mar 2015.

[13] Alain Coc and Elisabeth Vangioni. Primordial nucleosynthesis. *International Journal of Modern Physics E*, 26(08):1741002, Aug 2017.

[14] N. Jarosik and et al. Seven-year wilkinson microwave anisotropy probe(wmap) observations: Sky maps, systematic errors, and basic results. *The Astrophysical Journal Supplement Series*, 192(2):14, Jan 2011.

[15] Richard H. Cyburt. Primordial nucleosynthesis for the new cosmology: Determining uncertainties and examining concordance. *Physical Review D*, 70(2):023505, 2004.

[16] Joseph Silk. Cosmic black-body radiation and galaxy formation. *Astrophysical Journal*, 151:459, February 1968.

[17] R.A. Sunyaev and Ya. B. Zeldovich. Small-scale fluctuations of relic radiation. *Astrophysics and Space Science*, 7(1):3–19, April 1970.

[18] Planck Collaboration. Planck 2018 results. vi. cosmological parameters. *Astronomy & Astrophysics*, 641:A6, sep 2020.

[19] G. F. Smoot and et al. Structure in the COBE Differential Microwave Radiometer First-Year Maps. *Astrophysical Journal Letters*, 396:L1, Sep 1992.

[20] P. J. E. Peebles. Large-scale background temperature and mass fluctuations due to scale-invariant primeval perturbations. *Astrophysical Journal, Part 2 - Letters to the Editor*, 263:L1–L5, Dec 1982.

[21] M. Davis and et al. The evolution of large-scale structure in a universe dominated by cold dark matter. *Astrophysical Journal*, 292:371–394, May 1985.

[22] Thomas Hambye. On the stability of particle dark matter, 2010.

[23] Robert J. Scherrer and Michael S. Turner. On the Relic, Cosmic Abundance of Stable Weakly Interacting Massive Particles. *Phys. Rev. D*, 33:1585, 1986. [Erratum: Phys.Rev.D 34, 3263 (1986)].

[24] Mark Srednicki, Richard Watkins, and Keith A. Olive. Calculations of Relic Densities in the Early Universe. *Nucl. Phys. B*, 310:693, 1988.

[25] P. Agnes and et al. First results from the darkside-50 dark matter experiment at laboratori nazionali del gran sasso. *Physics Letters B*, 743:456–466, Apr 2015.

[26] Keith Bechtol and et al. Dark matter science in the era of lsst, 2019.

[27] E. Aprile and et al. Light dark matter search with ionization signals in xenon1t. *Physical Review Letters*, 123(25), Dec 2019.

[28] B. Paczynski. Gravitational Microlensing by the Galactic Halo. *The Astrophysical Journal*, 304:1, May 1986.

[29] Kim Griest. Galactic Microlensing as a Method of Detecting Massive Compact Halo Objects. *Astrophysical Journal*, 366:412, Jan 1991.

[30] P. Tisserand and et al. Limits on the macho content of the galactic halo from the eros-2 survey of the magellanic clouds. *Astronomy and Astrophysics*, 469(2):387–404, April 2007.

[31] Ya. B. Zel'dovich and I. D. Novikov. The Hypothesis of Cores Retarded during Expansion and the Hot Cosmological Model. *Astronomicheskii Zhurnal*, 43:758, Jan 1966.

[32] Stephen Hawking. Gravitationally collapsed objects of very low mass. *Monthly Notices of the Royal Astronomical Society*, 152(1):75–78, 1971.

[33] Bernard Carr, Florian Kuhnel, and Marit Sandstad. Primordial black holes as dark matter. *Physical Review D*, 94(8), 2016.

[34] Sebastien Clesse and Juan Garcia-Bellido. Seven hints for primordial black hole dark matter. *arXiv:1711.10458 [astro-ph, physics:gr-qc, physics:hep-th]*, 2018.

[35] V. De Luca, G. Franciolini, P. Pani, and A. Riotto. Primordial black holes confront ligo/virgo data: current situation. *Journal of Cosmology and Astroparticle Physics*, 2020(06):044–044, Jun 2020.

[36] Bernard Carr and et al. Primordial black hole constraints for extended mass functions. *Physical Review D*, 96(2):023514, 2017.

[37] Marc Schumann. Direct detection of WIMP dark matter: Concepts and status. *Journal of Physics G: Nuclear and Particle Physics*, 46(10), 2019.

[38] Jonathan L. Feng. Dark matter candidates from particle physics and methods of detection. *Annual Review of Astronomy and Astrophysics*, 48(1):495–545, 2010.

[39] Graciela Gelmini and Paolo Gondolo. Dm production mechanisms, 2010.

[40] Gianfranco Bertone and Dan Hooper. History of dark matter. *Reviews of Modern Physics*, 90(4), Oct 2018.

[41] Laura Baudis. The search for dark matter. *European Review*, 26(1):70–81, Dec 2017.

[42] G. Aad and et. Search for dark matter in events with a hadronically decaying w or z boson and missing transverse momentum in pp collisions at $\sqrt{s} = 13$ tev with the atlas detector. *Phys. Rev. Lett.*, 112:041802, Jan 2014.

[43] Stefano Giagu. WIMP Dark Matter Searches With the ATLAS Detector at the LHC. *Front. in Phys.*, 7:75, 2019.

[44] David Vannerom. Dark Matter searches with CMS. *PoS*, DIS2019:111, 2019.

[45] Fiorenza Donato. Indirect searches for dark matter. *Phys. Dark Univ.*, 4:41–43, 2014.

[46] Jan Conrad and Olaf Reimer. Indirect dark matter searches in gamma and cosmic rays. *Nature Phys.*, 13(3):224–231, 2017.

[47] M. N. Mazziotta. Indirect searches for dark matter with the fermi lat instrument. *International Journal of Modern Physics A*, 29(22):1430030, Aug 2014.

[48] S. Desai and et al. Search for dark matter wimps using upward through-going muons in super-kamiokande. *Phys. Rev. D*, 70:083523, Oct 2004.

[49] K. Choi and et al. Search for neutrinos from annihilation of captured low-mass dark matter particles in the sun by super-kamiokande. *Phys. Rev. Lett.*, 114:141301, Apr 2015.

[50] K. Abe and et al. Indirect search for dark matter from the galactic center and halo with the super-kamiokande detector. *Physical Review D*, 102(7), Oct 2020.

[51] P.A. Zyla and et al. (Particle Data Group). Review of Particle Physics. *PTEP*, 2020(8):083C01, 2021.

[52] Roberto D Peccei and Helen R Quinn. Cp conservation in the presence of pseudoparticles. *Physical Review Letters*, 38(25):1440, 1977.

[53] Roberto D Peccei. The strong cp problem and axions. In *Axions*, pages 3–17. Springer, 2008.

[54] Frank Wilczek. Nobel lecture: Asymptotic freedom: From paradox to paradigm. *Reviews of Modern Physics*, 77(3):857, 2005.

[55] Leanne D Duffy and Karl Van Bibber. Axions as dark matter particles. *New Journal of Physics*, 11(10):105008, 2009.

[56] A.R. Zhitnitsky. On Possible Suppression of the Axion Hadron Interactions. (In Russian). *Sov. J. Nucl. Phys.*, 31:260, 1980.

[57] Michael Dine, Willy Fischler, and Mark Srednicki. A Simple Solution to the Strong CP Problem with a Harmless Axion. *Phys. Lett. B*, 104:199–202, 1981.

[58] Jihn E. Kim. Weak-interaction singlet and strong cp invariance. *Phys. Rev. Lett.*, 43:103–107, Jul 1979.

[59] Mikhail A. Shifman, A.I. Vainshtein, and Valentin I. Zakharov. Can Confinement Ensure Natural CP Invariance of Strong Interactions? *Nucl. Phys. B*, 166:493–506, 1980.

[60] N. Du and et al. Search for invisible axion dark matter with the axion dark matter experiment. *Physical Review Letters*, 120(15), Apr 2018.

[61] T. Braine and et al. Extended search for the invisible axion with the axion dark matter experiment. *Physical Review Letters*, 124(10), Mar 2020.

[62] P. Brun and et al. A new experimental approach to probe qcd axion dark matter in the mass range above 40 μev. *The European Physical Journal C*, 79(3), Mar 2019.

[63] M. Tanabashi and et al. (Particle Data Group). Review of particle physics. *Phys. Rev. D*, 98:030001, Aug 2018.

[64] Simon DM White, Carlos S Frenk, and Marc Davis. Clustering in a neutrino-dominated universe. *The Astrophysical Journal*, 274:L1–L5, 1983.

[65] R. Adhikari and et al. A white paper on kev sterile neutrino dark matter. *Journal of Cosmology and Astroparticle Physics*, 2017(01):025–025, Jan 2017.

[66] A. Boyarsky and et al. Sterile neutrino dark matter. *Progress in Particle and Nuclear Physics*, 104:1–45, Jan 2019.

[67] Alexey Boyarsky, Oleg Ruchayskiy, and Mikhail Shaposhnikov. The role of sterile neutrinos in cosmology and astrophysics. *Annual Review of Nuclear and Particle Science*, 59(1):191–214, Nov 2009.

[68] Matteo Leo and et al. The effect of thermal velocities on structure formation in n-body simulations of warm dark matter. *Journal of Cosmology and Astroparticle Physics*, 2017(11):017–017, Nov 2017.

[69] Aurel Schneider and et al. Warm dark matter does not do better than cold dark matter in solving small-scale inconsistencies. *Monthly Notices of the Royal Astronomical Society: Letters*, 441(1):L6–L10, Mar 2014.

[70] Miguel D. Campos and Werner Rodejohann. Testing kev sterile neutrino dark matter in future direct detection experiments. *Physical Review D*, 94(9), Nov 2016.

[71] J. N. Abdurashitov and et al. First measurements in search for kev sterile neutrino in tritium beta-decay in the troitsk nu-mass experiment. *JETP Letters*, 105(12):753–757, Jun 2017.

[72] Susanne Mertens and et al. A novel detector system for katrin to search for kev-scale sterile neutrinos. *Journal of Physics G: Nuclear and Particle Physics*, 46(6):065203, May 2019.

[73] T. Lasserre and et al. Direct search for kev sterile neutrino dark matter with a stable dysprosium target, 2016.

[74] Brandon M. Roach and et al. Nustar tests of sterile-neutrino dark matter: New galactic bulge observations and combined impact. *Physical Review D*, 101(10), May 2020.

[75] Jonathan L. Feng, Arvind Rajaraman, and Fumihiro Takayama. Superweakly interacting massive particles. *Physical Review Letters*, 91(1), Jul 2003.

[76] Edward W. Kolb, Daniel J. H. Chung, and Antonio Riotto. Wimpzillas!, 1998.

[77] Jonathan L Feng, Arvind Rajaraman, and Fumihiro Takayama. Superweakly interacting massive particle dark matter signals from the early universe. *Physical Review D*, 68(6):063504, 2003.

[78] Riccardo Catena and Laura Covi. Susy dark matter(s). *The European Physical Journal C*, 74(5), May 2014.

[79] Eric Kuflik and et al. Phenomenology of elder dark matter. *Journal of High Energy Physics*, 2017(8), Aug 2017.

[80] Yonit Hochberg and et al. Strongly interacting massive particles through the axion portal. *Phys. Rev. D*, 98(11):115031, 2018.

[81] Marco Battaglieri and et al. Us cosmic visions: New ideas in dark matter 2017: Community report, 2017.

[82] Mordehai Milgrom. A modification of the newtonian dynamics as a possible alternative to the hidden mass hypothesis. *The Astrophysical Journal*, 270:365–370, 1983.

[83] JD Beckenstein. Modified gravity vs dark matter: Relativistc theory for mond. *PoS*, page 012, 2004.

[84] Jean-Philippe Bruneton and et al. Reconciling mond and dark matter? *Journal of Cosmology and Astroparticle Physics*, 2009(03):021, 2009.

[85] Chiu Man Ho, Djordje Minic, and Y Jack Ng. Cold dark matter with mond scaling. *Physics Letters B*, 693(5):567–570, 2010.

[86] Jean-Philippe Bruneton and Gilles Esposito-Farese. Field-theoretical formulations of mond-like gravity. *Physical Review D*, 76(12):124012, 2007.

[87] Mordehai Milgrom. Mond theory. *Canadian Journal of Physics*, 93(2):107–118, 2014.

[88] Katherine Freese, Mariangela Lisanti, and Christopher Savage. Colloquium: Annual modulation of dark matter. *Reviews of Modern Physics*, 85(4):1561–1581, Nov 2013.

[89] R. Bernabei and et al. New results from dama/libra. *The European Physical Journal C*, 67(1-2):39–49, Mar 2010.

[90] C. E. Aalseth and et al. Results from a search for light-mass dark matter with ap-type point contact germanium detector. *Physical Review Letters*, 106(13), Mar 2011.

[91] G. Adhikari and et al. Search for a dark matter-induced annual modulation signal in nai(tl) with the cosine-100 experiment. *Physical Review Letters*, 123(3), Jul 2019.

[92] F. Mayet and et al. A review of the discovery reach of directional dark matter detection. *Physics Reports*, 627:1–49, Apr 2016.

[93] S. Ahlen and et al. The case for a directional dark matter detector and the status of current experimental efforts. *International Journal of Modern Physics A*, 25(01):1–51, Jan 2010.

[94] DarkSide Collaboration. Argon tpc. `http://darkside.lngs.infn.it/argon-tpc/`, October 2020.

[95] ArDM Collaboration. Experiment website, scintillation and ionisation detection methods. `http://darkmatter.ethz.ch/`, October 2019.

[96] The DarkSide collaboration. Calibration of the liquid argon ionization response to low energy electronic and nuclear recoils with DarkSide-50. *Physical Review D*, 104(8), oct 2021.

[97] P. Agnes and et al. Separating 39Ar from 40Ar by cryogenic distillation with aria for dark matter searches. *The European Physical Journal C*, 81(4), apr 2021.

[98] P. Agnes and et al. Results From the First Use of Low Radioactivity Argon in a Dark Matter Search. *Phys.Rev.D*, 93(8):081101, 2016.

[99] J. Angle and et al. First results from the xenon10 dark matter experiment at the gran sasso national laboratory. *Physical Review Letters*, 100(2), Jan 2008.

[100] P. Agnes and et al. Darkside-50 532-day dark matter search with low-radioactivity argon. *Phys. Rev. D*, 98:102006, Nov 2018.

[101] P. Agnes and et al. Low-mass dark matter search with the darkside-50 experiment. *Phys. Rev. Lett.*, 121:081307, Aug 2018.

[102] G. Bellini and et al. Cosmogenic backgrounds in borexino at 3800 m water-equivalent depth. *Journal of Cosmology and Astroparticle Physics*, 2013(08):049–049, aug 2013.

[103] G. Alimonti and et al. The borexino detector at the laboratori nazionali del gran sasso. *Nuclear Instruments and Methods in Physics Research Section A: Accelerators, Spectrometers, Detectors and Associated Equipment*, 600(3):568–593, Mar 2009.

[104] Borexino collaboration. Search for electron antineutrino interactions with the borexino counting test facility at gran sasso. *The European Physical Journal C*, 47(1):21–30, May 2006.

[105] P. Agnes and et al. The veto system of the darkside-50 experiment. *Journal of Instrumentation*, 11(03):P03016–P03016, Mar 2016.

[106] G. Zuzel and et al. The DarkSide Experiment: Present Status and Future. In *2nd International Conference on Particle Physics and Astrophysics*, volume 798, Moscow, Russia, October 2016.

[107] The DarkSide Collaboration. The electronics and data acquisition system of the darkside dark matter search, 2015.

[108] L. W. Kastens and et al. Calibration of a liquid xenon detector withkr83m. *Physical Review C*, 80(4), Oct 2009.

[109] P. Agnes and et al. Calis - a calibration insertion system for the darkside-50 dark matter search experiment. *Journal of Instrumentation*, 12(12):T12004–T12004, Dec 2017.

[110] P. Agnes and et al. Measurement of the liquid argon energy response to nuclear and electronic recoils. *Physical Review D*, 97(11), Jun 2018.

[111] T. Alexander and et al. Observation of the dependence on drift field of scintillation from nuclear recoils in liquid argon. *Physical Review D*, 88(9), Nov 2013.

[112] H. Cao and et al. Measurement of scintillation and ionization yield and scintillation pulse shape from nuclear recoils in liquid argon. *Phys. Rev. D*, 91:092007, May 2015.

[113] The Global Argon Dark Matter Collaboration. Darkside-20k technical design report. Technical report, The Global Argon Dark Matter Collaboration, 2021.

[114] Frank Simon. Silicon photomultipliers in particle and nuclear physics. *Nuclear Instruments and Methods in Physics Research Section A: Accelerators, Spectrometers, Detectors and Associated Equipment*, 926:85–100, May 2019.

[115] Sense light. Technical note: An introduction to the silicon photomultiplier. Technical report, Sense light, 2011.

[116] Robert Klanner. Characterisation of sipms. *Nuclear Instruments and Methods in Physics Research Section A: Accelerators, Spectrometers, Detectors and Associated Equipment*, 926:36–56, May 2019.

[117] E. Garutti and Yu. Musienko. Radiation damage of sipms. *Nuclear Instruments and Methods in Physics Research Section A: Accelerators, Spectrometers, Detectors and Associated Equipment*, 926:69–84, May 2019.

[118] L Gallego and et al. Modeling crosstalk in silicon photomultipliers. *Journal of Instrumentation*, 8(05):P05010–P05010, may 2013.

[119] Fabio Acerbi and et al. Cryogenic characterization of fbk hd near-uv sensitive sipms. *IEEE Transactions on Electron Devices*, 64(2):521–526, Feb 2017.

[120] K.D. Nakamura and et al. Angular dependence of columnar recombination in high pressure xenon gas using time profiles of scintillation emission. *Journal of Instrumentation*, 13(07):P07015–P07015, Jul 2018.

[121] D R Nygren. Columnar recombination: a tool for nuclear recoil directional sensitivity in a xenon-based direct detection WIMP search. *Journal of Physics: Conference Series*, 460:012006, oct 2013.

[122] The ReD Collaboration. Recoil directionality (red) project. *Recoil directionality proposal to CSN5 2015*, 2015.

[123] P. Agnes and et al. Performance of the red tpc, a novel double-phase lar detector with silicon photomultiplier readout. *The European Physical Journal C*, 81(11), Nov 2021.

[124] Bianca Bottino. *Dark matter search with liquid argon in DarkSide: results with scientific and technological prototypes.* PhD thesis, University of Genoa, 2019.

[125] Simone Sanfilippo. *Dark matter direct detection with the Dark Side project. ReD: an experiment to probe the recoil directionality in liquid argon.* PhD thesis, Universita degli Studi Roma Tre, 2020.

[126] A. G. Santos-Ocampo and D. C. Conway. $\frac{L}{K}$-capture ratio and $\frac{E_L}{E_K}$ for ar^{37}. *Phys. Rev.*, 120:2196–2200, Dec 1960.

[127] P. W. Dougan, K. W. D. Ledingham, and R. W. P. Drever. The l/k-capture ratio of argon 37. *The Philosophical Magazine: A Journal of Theoretical Experimental and Applied Physics*, 7(75):475–482, 1962.

[128] D. Totzek and K. Hoffmann. L/k-einfangverhältnis von65zn. *Zeitschrift für Physik*, 205:137–144, 1967.

[129] D E Cullen. Program relax: A code designed to calculate atomic relaxation spectra of x-rays and electrons. March 1992.

[130] Dermott E. Cullen. A survey of atomic binding energies for use in epics2017. Technical Report IAEA-NDS-0224, IAEA, 2018.

[131] Xavier Mougeot. Towards high-precision calculation of electron capture decays. *Applied Radiation and Isotopes*, 154:108884, December 2019.

[132] J. Thomas and D. A. Imel. Recombination of electron-ion pairs in liquid argon and liquid xenon. *Phys. Rev. A*, 36:614–616, Jul 1987.

[133] Doke Tadayoshi and et al. Let dependence of scintillation yields in liquid argon. *Nuclear Instruments and Methods in Physics Research Section A: Accelerators, Spectrometers, Detectors and Associated Equipment*, 269(1):291–296, 1988.

[134] Fedor Bezrukov, Felix Kahlhoefer, and Manfred Lindner. Interplay between scintillation and ionization in liquid xenon dark matter searches. *Astroparticle Physics*, 35(3):119–127, Oct 2011.

[135] H. Ryssel and H. Glawischnig. Ion implantation techniques. 1982.

[136] T. H. Joshi and et al. First measurement of the ionization yield of nuclear recoils in liquid argon. *Phys. Rev. Lett.*, 112:171303, May 2014.

[137] P. Agnes and et al. Search for low-mass dark matter wimps with 12 ton-day exposure of darkside-50, 2022.

[138] Leendert Hayen and et al. High precision analytical description of the allowed β spectrum shape. *Reviews of Modern Physics*, 90(1), Mar 2018.

[139] S. Agostinelli et al. GEANT4–a simulation toolkit. *Nucl. Instrum. Meth. A*, 506:250–303, 2003.

[140] Andrzej K. Drukier, Katherine Freese, and David N. Spergel. Detecting cold dark-matter candidates. *Phys. Rev. D*, 33:3495–3508, Jun 1986.

[141] J. Binney and S. Tremaine. Galactic dynamics: Second edition. *Princeton University Press*, 2008.

[142] Gianfranco Bertone. *Particle Dark Matter: Observations, Models and Searches*. Cambridge University Press, 2010.

[143] J. D. Lewin and P. F. Smith. Review of mathematics, numerical factors, and corrections for dark matter experiments based on elastic nuclear recoil. *Astropart. Phys.*, 6:87–112, 1996.

[144] E. Aprile and et al. Low-mass dark matter search using ionization signals in xenon100. *Phys. Rev. D*, 94:092001, Nov 2016.

[145] R. Agnese and et al. Search for low-mass weakly interacting massive particles with supercdms. *Phys. Rev. Lett.*, 112:241302, Jun 2014.

[146] W. Zhao and et al. Search of low-mass wimps with a p-type point contact germanium detector in the cdex-1 experiment. *Phys. Rev. D*, 93:092003, May 2016.

[147] Andi Tan and et al. Dark matter results from first 98.7 days of data from the pandax-ii experiment. *Phys. Rev. Lett.*, 117:121303, Sep 2016.

[148] R. Agnese and et al. Low-mass dark matter search with CDMSlite. *Physical Review D*, 97(2), jan 2018.

[149] E. Behnke and et al. Final results of the picasso dark matter search experiment. *Astroparticle Physics*, 90:85–92, 2017.

[150] D. S. Akerib and et al. Results from a search for dark matter in the complete lux exposure. *Phys. Rev. Lett.*, 118:021303, Jan 2017.

[151] Q. Arnaud and et al. First results from the news-g direct dark matter search experiment at the lsm. *Astroparticle Physics*, 97:54–62, 2018.

[152] A. Aguilar-Arevalo and et al. Results on low-mass weakly interacting massive particles from an 11 kg d target exposure of damic at snolab. *Phys. Rev. Lett.*, 125:241803, Dec 2020.

[153] A.H. Abdelhameed and et al. First results from the cresst-iii low-mass dark matter program. *Physical Review D*, 100(10), Nov 2019.

[154] C. Amole and et al. Dark matter search results from the complete exposure of the pico-60 c_3f_8 bubble chamber. *Phys. Rev. D*, 100:022001, Jul 2019.

[155] E. Aprile and et al. First dark matter search results from the xenon1t experiment. *Phys. Rev. Lett.*, 119:181301, Oct 2017.

[156] E. Aprile and et al. Search for light dark matter interactions enhanced by the migdal effect or bremsstrahlung in xenon1t. *Physical Review Letters*, 123(24), Dec 2019.

[157] CRESST Collaboration. Results on low mass wimps using an upgraded cresst-ii detector. *The European Physical Journal C*, 74(12), dec 2014.

[158] C. E. Aalseth, P. S. Barbeau, J. Colaresi, J. I. Collar, J. Diaz Leon, J. E. Fast, N. E. Fields, T. W. Hossbach, A. Knecht, M. S. Kos, and et al. Cogent: A search for low-mass dark matter usingp-type point contact germanium detectors. *Physical Review D*, 88(1), Jul 2013.

[159] R Bernabei and et al. New results from dama/libra. *The European Physical Journal C*, 67(1):39–49, 2010.

[160] F. Ruppin and et al. Complementarity of dark matter detectors in light of the neutrino background. *Physical Review D*, 90(8), Oct 2014.

[161] A. B. Migdal. Ionization of atoms accompanying α-and β-decay. *J. Phys. USSR*, 4:449, 1941.

[162] Masahiro Ibe and et al. Migdal effect in dark matter direct detection experiments. *Journal of High Energy Physics*, 2018:1–36, 2017.

[163] Nicole F. Bell and et al. Migdal effect and photon bremsstrahlung in effective field theories of dark matter direct detection and coherent elastic neutrino-nucleus scattering. *Physical Review D*, 101(1), Jan 2020.

[164] Musaab Al-Bakry and et al. A Search for Low-mass Dark Matter via Bremsstrahlung Radiation and the Migdal Effect in SuperCDMS. *arXiv*, 3 2022.

[165] Yue Meng and et al. Dark matter search results from the pandax-4t commissioning run. *Physical Review Letters*, 127(26), Dec 2021.

[166] D. S. Akerib and et al. First searches for axions and axion-like particles with the LUX experiment. *Physical Review Letters*, 118(26):261301, 2017.

[167] NIST. Atomic spectra database, nist standard reference database 78, 2019. `https://www.nist.gov/pml/atomic-spectra-database`.

[168] K. Arisaka and et al. Expected sensitivity to galactic/solar axions and bosonic super-WIMPs based on the axio-electric effect in liquid xenon dark matter detectors. *Astroparticle Physics*, 44:59–67, 2013.

[169] R.J. Creswick and et al. Theory for the direct detection of solar axions by coherent primakoff conversion in germanium detectors. *Physics Letters B*, 427(3-4):235–240, May 1998.

[170] CAST collaboration. Search for 14.4 kev solar axions emitted in the m1-transition of 57fe nuclei with cast. *Journal of Cosmology and Astroparticle Physics*, 2009(12):002–002, Dec 2009.

[171] Shigetaka Moriyama. Proposal to search for a monochromatic component of solar axions using 57fe. *Phys. Rev. Lett.*, 75:3222–3225, Oct 1995.

[172] Javier Redondo. Solar axion flux from the axion-electron coupling. *Journal of Cosmology and Astroparticle Physics*, 2013(12):008, dec 2013.

[173] Maxim Pospelov, Adam Ritz, and Mikhail B. Voloshin. Bosonic super-WIMPs as keV-scale dark matter. *Physical Review D*, 78(11):115012, 2008.

[174] YS Yoon and et al. Search for solar axions with csi (tl) crystal detectors. *Journal of High Energy Physics*, 2016(6):11, 2016.

[175] The XENON100 Collaboration. First axion results from the XENON100 experiment. *Physical Review D*, 90(6):062009, 2014.

[176] N. Abgrall and et al. New limits on bosonic dark matter, solar axions, pauli exclusion principle violation, and electron decay from the majorana demonstrator. *Phys. Rev. Lett.*, 118:161801, Apr 2017.

[177] Changbo Fu and et al. Limits on axion couplings from the first 80-day data of PandaX-II experiment. *Physical Review Letters*, 119(18):181806, 2017.

[178] Christopher S. Reynolds and et al. Astrophysical limits on very light axion-like particles from chandra grating spectroscopy of NGC 1275. *The Astrophysical Journal*, 890(1):59, feb 2020.

[179] Francesco Capozzi and Georg Raffelt. Axion and neutrino bounds improved with new calibrations of the tip of the red-giant branch using geometric distance determinations. *Phys. Rev. D*, 102:083007, Oct 2020.

[180] Mengjiao Xiao and et al. Betelgeuse constraints on coupling between axion-like particles and electrons, 2022.

[181] A.V. Derbin and et al. New limit on the mass of 14.4-kev solar axions emitted in an m1 transition in 57fe nuclei. *Physics of Atomic Nuclei*, 74:596–602, 2011.

[182] E. Aprile and et al. Excess electronic recoil events in xenon1t. *Phys. Rev. D*, 102:072004, Oct 2020.

[183] T. Aralis and et al. Constraints on dark photons and axionlike particles from the supercdms soudan experiment. *Phys. Rev. D*, 101:052008, Mar 2020.

[184] N. Viaux and et al. Neutrino and axion bounds from the globular cluster m5 (ngc 5904). *Phys. Rev. Lett.*, 111:231301, Dec 2013.

[185] Ricardo Z. Ferreira, M. C. David Marsh, and Eike Müller. Do direct detection experiments constrain axionlike particles coupled to electrons? *arXiv:2202.08858 [hep-ex, physics:hep-ph]*, February 2022.

[186] Shin'ichiro Ando and Alexander Kusenko. Interactions of keV sterile neutrinos with matter. *Physical Review D*, 81(11):113006, 2010.

[187] Miguel David Campos Vidal. *Phenomenology and Models of Dark Matter and Neutrinos*. PhD thesis, University of Heidelberg, 2018.

[188] A.D. Dolgov. Neutrinos in cosmology. *Physics Reports*, 370(4-5):333–535, nov 2002.

[189] Chudaykin, Anton. kev sterile neutrino with large mixing angle is still alive. *EPJ Web Conf.*, 191:08003, 2018.

[190] Carlos A. Arguelles, Vedran Brdar, and Joachim Kopp. Production of keV sterile neutrinos in supernovae: New constraints and gamma-ray observables. *Physical Review D*, 99(4), feb 2019.

[191] G. J. Gounaris, E. A. Paschos, and P. I. Porfyriadis. Electron spectra in the ionization of atoms by neutrinos. *Physical Review D*, 70(11), Dec 2004.

[192] Carlos Bunge, J.A. Barrientos, and Annik Vivier-bunge. Roothaan-hartree-fock ground-state atomic wave-functions - slater-type orbital expansions and expectation values for z=2-54. *Atom. Data Nucl. Data Tables*, 53:113–162, 01 1993.

[193] Jo Bovy and Scott Tremaine. On the local dark matter density. *The Astrophysical Journal*, 756(1):89, Aug 2012.

[194] E Holzschuh and et al. Search for heavy neutrinos in the β-spectrum of 63ni. *Physics Letters B*, 451(1):247–255, 1999.

[195] J. L. Mortara and et al. Evidence against a 17 kev neutrino from ^{35}S beta decay. *Phys. Rev. Lett.*, 70:394–397, Jan 1993.

[196] Stefan Schonert and et al. Experimental limits for heavy neutrino admixture deduced from Lu-177 beta decay and constraints on the life time of a radiative neutrino decay mode. *Nucl. Phys. B Proc. Suppl.*, 48:201–203, 1996.

[197] E. Aprile and et al. Search for event rate modulation in xenon100 electronic recoil data. *Physical Review Letters*, 115(9), Aug 2015.

[198] K. Abe and et al. Direct dark matter search by annual modulation with 2.7 years of xmass-i data. *Physical Review D*, 97(10), May 2018.

[199] Marc Lavielle. Statistics in action with r - non linear regression. `http://sia.webpopix.org/nonlinearRegression.html#statistical-tests-for-the-model-parameters`, February 2019.

[200] Sture Holm. A simple sequentially rejective multiple test procedure. *Scandinavian Journal of Statistics*, 6(2):65–70, 1979.

[201] Pauli Virtanen and et al. SciPy 1.0: Fundamental Algorithms for Scientific Computing in Python. *Nature Methods*, 17:261–272, 2020.

[202] P. Agnes and et al. Electroluminescence pulse shape and electron diffusion in liquid argon measured in a dual-phase tpc. *Nuclear Instruments and Methods in Physics Research Section A: Accelerators, Spectrometers, Detectors and Associated Equipment*, 904:23–34, Oct 2018.

[203] Yichen Li and et al. Measurement of longitudinal electron diffusion in liquid argon. *Nuclear Instruments and Methods in Physics Research Section A: Accelerators, Spectrometers, Detectors and Associated Equipment*, 816:160–170, 2016.

[204] A. Buzulutskov and et al. Revealing neutral bremsstrahlung in two-phase argon electroluminescence. *Astroparticle Physics*, 103:29–40, Dec 2018.

[205] Chengliang Zhu. *Study of Argon Electroluminescence Light Yield using Data from DarkSide-50*. PhD thesis, Princeton University, 2018.

[206] D. V. Hinkley. On the ratio of two correlated normal random variables. *Biometrika*, 56(3):635–639, 1969.

[207] P. Agnes and et al. Simulation of argon response and light detection in the darkside-50 dual phase tpc. *Journal of Instrumentation*, 12(10):P10015–P10015, Oct 2017.

[208] F. Pedregosa and et al. Scikit-learn: Machine learning in Python. *Journal of Machine Learning Research*, 12:2825–2830, 2011.

[209] James Gareth and et al. *An introduction to statistical learning*, volume 112. Springer, 2013.

[210] IBM Cloud Education. Overfitting. `https://www.ibm.com/cloud/learn/overfitting`, March 2021.

[211] Adam Paszke and et al. Pytorch: An imperative style, high-performance deep learning library. In H. Wallach, H. Larochelle, A. Beygelzimer, F. d'Alché-Buc, E. Fox, and R. Garnett, editors, *Advances in Neural Information Processing Systems 32*, pages 8024–8035. Curran Associates, Inc., 2019.

[212] William Falcon and The PyTorch Lightning team. PyTorch Lightning, 3 2019.

[213] Yann LeCun and Yoshua Bengio. Convolutional networks for images, speech, and time series. *The handbook of brain theory and neural networks*, 3361(10):1995, 1995.

[214] Kaiming He and et al. Deep residual learning for image recognition. *CoRR*, abs/1512.03385, 2015.

List of Figures

List of Tables